A Field Dislocation Mechanics Approach To Emergent Properties In Two-Phase Nickel-Based Superalloys

By

James Jordan Little

A thesis submitted to the University of Birmingham for the degree of DOCTOR OF ENGINEERING

School of Metallurgy and Materials

College of Engineering and Physical Sciences

University of Birmingham

March 2019

UNIVERSITY OF BIRMINGHAM

University of Birmingham Research Archive

e-theses repository

Abstract

The objective of this study is the development of a theoretical framework for treating the flow stress response of two-phase alloys as emergent behaviour arising from fundamental dislocation interactions. To this end a field dislocation mechanics (FDM) formulation has been developed to model heterogeneous slip within a computational domain representative of a two-phase nickel-based superalloy crystal at elevated temperature. A transport equation for the statistically stored dislocation (SSD) field is presented and implemented within a plane strain finite element scheme. Elastic interactions between dislocations and the microstructure are explicitly accounted for in this formulation. The theory has been supplemented with constitutive rules for dislocation glide and climb, as well as local cutting conditions for the γ' particles by the dislocation field. Numerical simulations show that γ' precipitates reduced the effective dislocation mobility by both acting as discrete slip barriers and providing a drag effect through line tension. The effect of varying microstructural parameters on the crystal deformation behaviour is investigated for simple shear loading boundary conditions. It is demonstrated that slip band propagation can be simulated by the proposed FDM approach. Emergent behaviour is predicted and includes: domain size yield dependence (Hall-Petch relationship), γ' volume fraction yield dependence (along with more complex γ' dispersion-related yield and post-yield flow stress phenomena), and hardening related to dislocation source distribution at the grain boundary. From these simulations, scaling laws are derived. Also, the emergence of internal back stresses associated with non-homogeneous plastic deformation is predicted. Prediction of these back stresses, due to sub-grain stress partitioning across elastic/plastic zones, is an important result which can provide useful information for the calibration of phenomenological macroscale models. Validation for the presented model is provided through comparison to experimental micro-shear tests that can be found in published literature.

Acknowledgements

Contents

Chapter 1

Introduction

"The general feature exposed by the electron microscopic observations is that work hardened dislocation structures are heterogeneous on a mesoscopic scale. This set two new problems for the theory: to deduce the flow stress from the starting point of a given observed heterogeneous structure; and to explain the formation of these structures and their evolution with plastic strain. The first of these has proved to be the easier and more fully developed." - Alan Cottrell [1]

1.1 Heterogeneity in Micro-scale Plasticity

Plastic deformation of precipitate strengthened alloys is fundamentally heterogeneous due to localised plastic shear propagating along crystallographic slip systems that activate non-uniformly under a given applied stress field. These regions, termed 'slip bands', are not uniformly distributed within the material grains at the microscale, and their spatial distribution means that the localisation of strain varies from grain to grain. Furthermore, dislocation slip, the cause of these plastic shear bands within a material, may be obstructed by second phase features such as the precipitate distribution in nickel-based superalloys [2]. The resultant state is that microstructural features will control the number and position of the shear bands, causing them to evolve in a non-uniform way across a deforming volume. Observations of this heterogenity have been made in literature, for example, using High Resolution EBSD and Digital Image correlation for the polycrystaline superalloys René 88DT [3] and Udimet 720Li [4].

At present, a popular approach to modelling plasticity in metallic systems, at length scales where individual grains are spatially resolved, is to employ crystal plasticity (CP). The various CP formulations reported in the literature focus on the development of the constitutive description of the shear rates on active slip systems. Within these constitutive descriptions the key length scale dependencies, such as grain size or precipitate spacing, are 'hard-wired' into the models. Such an approach has limitations on the ability to truly predict component behaviour, since model parameters are then calibrated to experimental data. Furthermore, current CP formlations are not capable of modelling the heterogeneous nature of slip at the grain length scale. Fundamentally the component-level behaviour of alloys arises from the complex interactions between dislocations and the material microstructure. These interactions enter due to the elastic fields associated with the dislocations and the presence of precipitates, as well as grain boundaries. It follows that a potentially fruitful way of treating macroscale properties, such as the yield strength and work hardening, is to model them as emergent phenomena. In this way, scaling laws may be derived that explicitly connect dislocation-microstructure interactions to macroscale behaviour. These, in turn, may be used to inform/develop higher length scale models of plasticity for finite element (FE) component-level analysis.

1.2   Aims of this Work

The current work aims to develop a Field Dislocation Mechanics (FDM) formulation for the evolution of deformation slip bands arising from the transport of the dislocation field, and in particular, to develop a theory of heterogeneous slip relevant to typical precipitate strengthened nickel-based superalloys, from which the macroscale behaviour may be derived from the dislocation/microstructure interactions. For the latter, the presence of the intermetallic γ' precipitates will influence the development of the deformation slip bands. A modelling capability for handling these interactions at the scale of the grains is important for the ability to derive component-level properties. This will be achieved by constructing a series of representative volume elements (RVEs) that are representative of γ' strengthened nickel-based superalloys used in turbine disc applications. Through homogenisation of predicted microscale mechanical fields the macroscale flow stress responses of the simulated material domains were obtained. Such a procedure has been used in this work to

extract emergent behaviour, such as yield stress dependency on grain size, and the development of back stresses associated with the development of slip bands.

With the above in mind the individual targets of this work are to:

- Develop a transport equation for the field of statistically stored dislocations (SSDs) within a domain

- Determine appropriate interaction and mobility terms for dislocations within a precipitate strengthened nickel-base superalloy

- Implement the equation set within a finite element (FE) model, tracking SSD density and velocity as state variables and determining the resultant plastic deformation and microstress states

- To study numerically dislocation-microstructure interactions predicted by the theory and understand component-level flow stress behaviour in terms of these interactions, i.e., as emergent phenomena.

- Provide benchmarking for the developed model through comparison to micro-shear tests of a CMSX-4 type alloy available in the literature

To begin a brief review of the necessary literature concerning superalloy deformation behaviour, dislocation theory and applied dislocation models will be presented in Chapter 2. This will be followed by a comprehensive development of the proposed FDM formulation from basic dislocation theory in Chapter 3. This is followed by Chapter 4 which focuses on application of the FDM to nickel-based superalloys. Details of the numerical implementation within the FE model shall follow this in Chapter 5. Full-field simulation results are presented in Chapter 6 for pure-γ microstructure and Chapter 7 for $\gamma - \gamma'$ microstructure, encompassing both predicted flow stress responses and strain maps showing slip band development, finishing with a a benchmarking comparison against experiment. The discussion is widened to encompass emergence of internal backstresses within the RVE in Chapter 8, where the separated stress evolution in elastic and plastic domains is considered for selected cases. The discussion ends with a final round-up and quantification of the microstructure to macro-property relations that emerge from the fundamental dislocation reactions in Chapter 9. Key conclusions and areas for future research are given in Chapter 10.

Chapter 2

Literature Review

2.1 Nickel-based Superalloy Overview

2.1.1 Brief introduction to Nickel-based Superalloys

The term "superalloy" is a classification of alloy defined by its high concentration of either nickel, iron or cobalt and good high temperature properties under high load [5]. Showing good all-round resistance to static, fatigue and creep loading, nickel-based superalloys have become the alloy of choice for use within gas turbine engines where internal conditions can be severe [6]. These alloys are well suited for use within turbine engines where components may be required to tolerate localised temperatures of up to 1200°C approaching a homologous temperature of ~ 0.9 [7]. Titanium alloys could not be expected to survive these temperatures in service due to much poorer oxidation resistance, but nickel-based superalloys may resist this deterioration through the formation of protective Al_2O_3 / Cr_2O_3 scales [8].

Progress in superalloy development from the 1960s has brought about signifcant improvements to fuel efficiency within gas turbine engines as polycrystal superalloys were succeeded by first directionally solidified and then single-crystal alloys [9], allowing the engines to run at higher temperature. The newer single crystal alloys have generally demonstrate a much greater creep strength, which also improves component life within engines allowing longer service [10].

At the crystal structural level nickel-based superalloys comprise of a Face Centred Cubic (FCC)

disordered matrix, referred to as the gamma phase (γ), and precipitates with an ordered $L1_2$ structure based on Ni$_3$(Al,Ti). This second phase is known as gamma-prime (γ'), which forms a coherent interface with very similar lattice parameters ($\sim 0.1\%$) to the matrix, allowing energetically favouable precipitation throughout the matrix [6] [11]. Although coherent, with closely aligned $\langle 110 \rangle$ slip directions, the γ' phase has a larger Burgers vector due to the larger space between repeating atomic arrangement. This precipitate acts as a barrier to dislocation slip (discussed later), providing the primary strengthening mechanism at high temperature conditions. Another observed phase is gamma double prime (γ'') caused by Body Centred Tetragonal (BCT) ordering of Ni$_3$Nb. This phase can provide a nickel-based superalloy with high strength up until $\sim 650°$C where it begins to break down [12]. This γ'' phase will not be considered within this work as the temperature range of interest is higher than its stable range.

2.1.2 γ/γ' microstructures

The distribution of γ' precipitates within a disc superalloy is typically described by a size distribution with three modal sizes, the particles associated with each mode are known as: fine *tertiary* particles (<50nm), intermediate *secondary* particles (50-400nm) and much larger *primary* particles (>400nm) [13]. A good example of the distinct particles sizes that can be observed is found in the work of Anderson *et al.* [14], created with scanning electron backscatter micrographs of heat treated nickel-based superalloy IN738LC: this is reproduced in Fig. 2.1.1. Precipitate distributions and morphologies such as these are specific to a given alloy following its precise thermal history.

A high energy state exists due to the presence of matrix-particle interfaces within the lattice. This state is larger for smaller particles with a high surface area to volume ratio, and thus diffusive processes are inclined to lower this state through *coarsening* a particle structure [15] [16]. This term describes the growth of larger particles at the expense of the smaller particles, and is also known as *Ostwald ripening*. In most alloy systems the γ' shape is observed to be equiaxed and to take spherical shape for small particles, with more cuboidal shapes found within the primary size range [15][17].
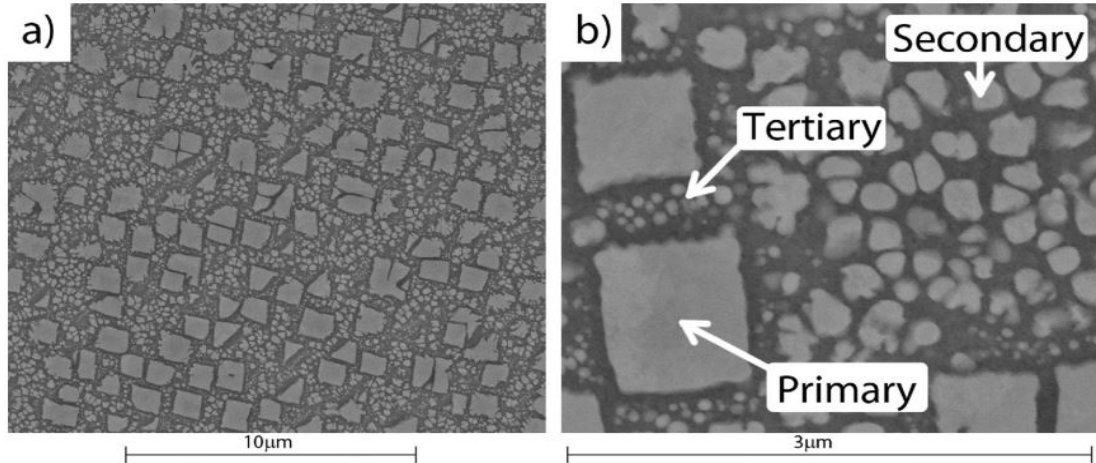
Figure 2.1.1: Representation of different particle sizes for alloy IN738LC in the post- heat treatment condition [14].

In 1959 Lifshitz and Slyozov defined a critical length dimension, x, above which particles grow and below which they dissolve away for a supersaturated solution undergoing internal diffusion processes [18]. The particle growth laws they predicted gave rise to the burgeoning field of precipitate modelling which can later be used to inform alloy design [15][14][17].

The gamma prime dispersion may be controlled through heat treatments designed to push particle growth in a particular direction [19]. Disc alloys typically have complex thermal histories to evolve the trimodal particle dispersion from which they gain their creep resistance properties and fatigue strength [20][21]: the primary particles are typically found at the grain boundaries, while the secondary and tertiary particles are transgranular. These heat treatments involve aging alloys for a number of hours at high temperature before quenching rapidly to lock in a particular precipitate microstructure. The size, distribution and shape of particles has been shown to be sensitive to the cooling rate from the solvus temperature [22]. For some turbine discs the bore and rim regions can undergo separate heat treatments (utilising heat sinks) to secure desirable properties in these areas. The bore region will experience a greater stress state so requires good tensile properties and fatigue resistance, while the rim is closer to the high temperature gas and must resist creep and thermal gradients. To this end, dual microstructure heat treatments (DMHT) can be used to produce fine grains with fine particles at the bore, and coarse grains with coarser particles at the rim [23][24].

11

An example of the particle-coarsening effect induced by heat treatment can be found in the work of A. Sato [8], who produced scanning electron micrographs of high chromium nickel-superalloy SCA425+ at different stages during a range of treatments. These images, reproduced in Fig. 2.1.2, show the large γ' particles coarsening with increasing temperature and hold time. The distribution develops to a unimodal state by sub-figure (h).
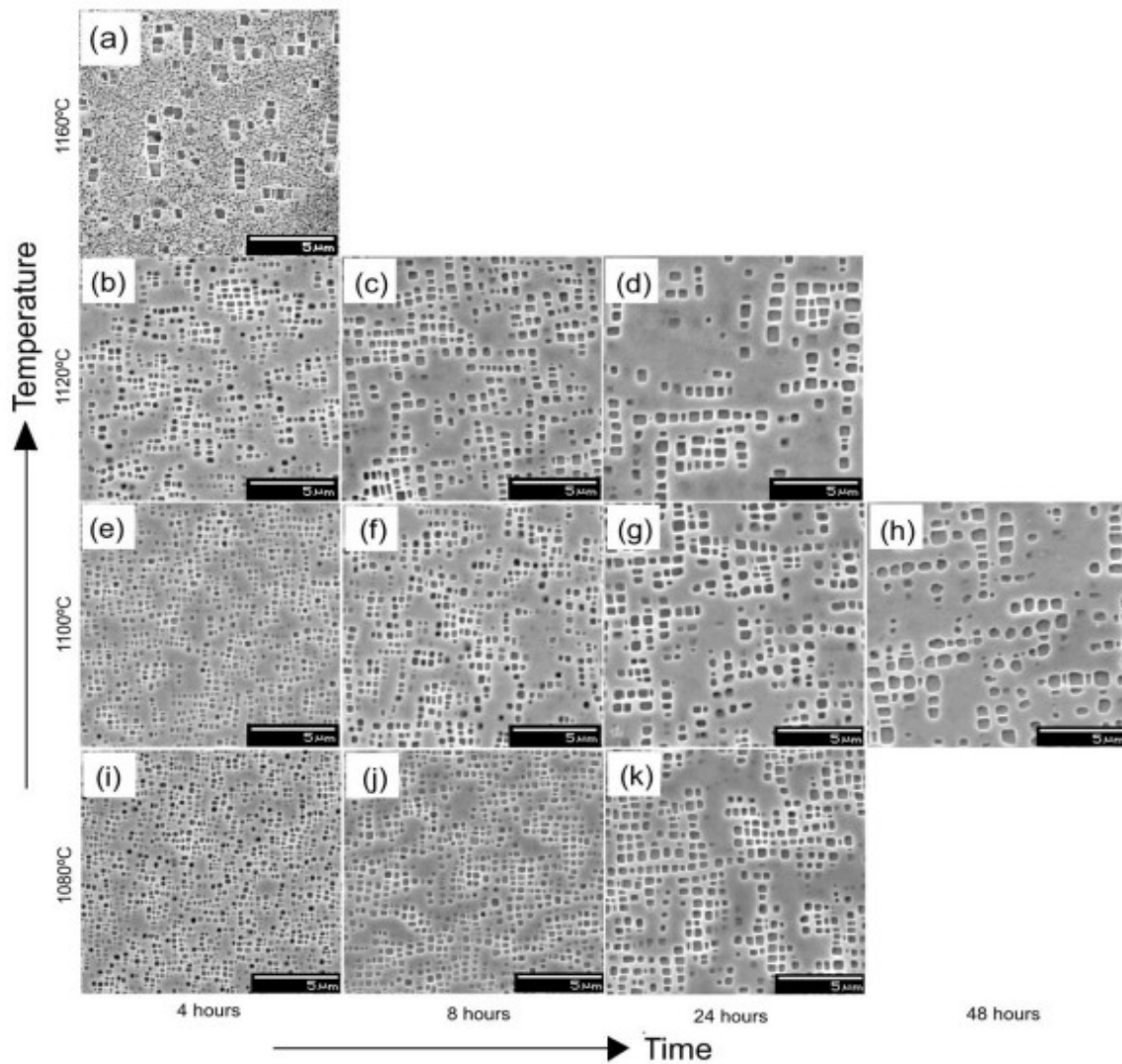
Figure 2.1.2: Primary particle growth in SCA425+ Nickel-Superalloy for different indicated first-stage heat treaments [8].

2.1.3   Characterising deformation

Plastic deformation in nickel-based superalloys is inherently heterogeneous due to plastic slip activity being confined to specific crystallographic planes and directions. These slip systems will activate preferentially according to the resolved shear stress upon them, which in turn will depend upon crystal orientation. This leads to a state where non-uniform distribution of slip activity will naturally occur [25].

Recent Digital Image Correlation (DIC) performed on high-resolution SEM images, both in-situ and post-situ, has observed slip bands distributed heterogeneously throughout samples of deforming nickel-based superalloys at room temperature [3][26][27][28]. Stinville *et al.* [3], observing superalloy Rene 88DT, found localised strain upon {111} planes near and parallel to annealing twin boundaries. In similar observations of Udimet 720Li Larrouy *et al.* [4] have noted that when intense slip bands meet a grain boundary with limited slip transmission then significant lattice rotations can occur. This gives rise to high stress concentrations in a small volume at the boundary, which will act as an initiation point for fatigue cracks.
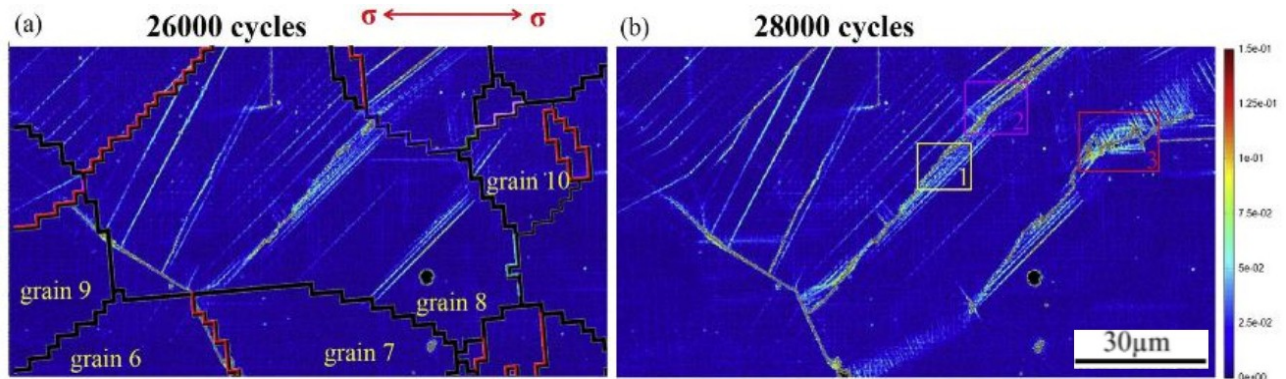
Figure 2.1.3: Strain maps created using DIC for polycrystalline powder-HIPed disc alloy LSHR, showing max shear strain ϵ_{xy}^{max}. Both images share the same scale bar. [28].

Fig. 2.1.3, produced by R. Jiang *et al.* [28], neatly maps the dislocation shear bands developing across the width of a number of grains within a polycrystaline disc alloy with increasing fatigue cycles. This result shows both the non-uniform distribution of slip bands generally across the de-

forming grain and the preferential formation of new slip bands next to existing bands (towards the right hand side of grain 8).

Within the single crystal superalloy CMSX-4, B. Chen *et al.* [27] have produced single-slip deformation through careful control of the sample orientation during fatigue bending. This is reproduced in Fig. 2.1.4, where the highly localised strain is shown to develop considerably with increasing peak applied force (ranging 2000N-2900N). Again new slip bands are shown predominantly to form adjacent to existing bands. Recreation of this type of behaviour from underlying dislocation-stress field interactions could be considered a good initial test for a new heterogeneous dislocation model under development.
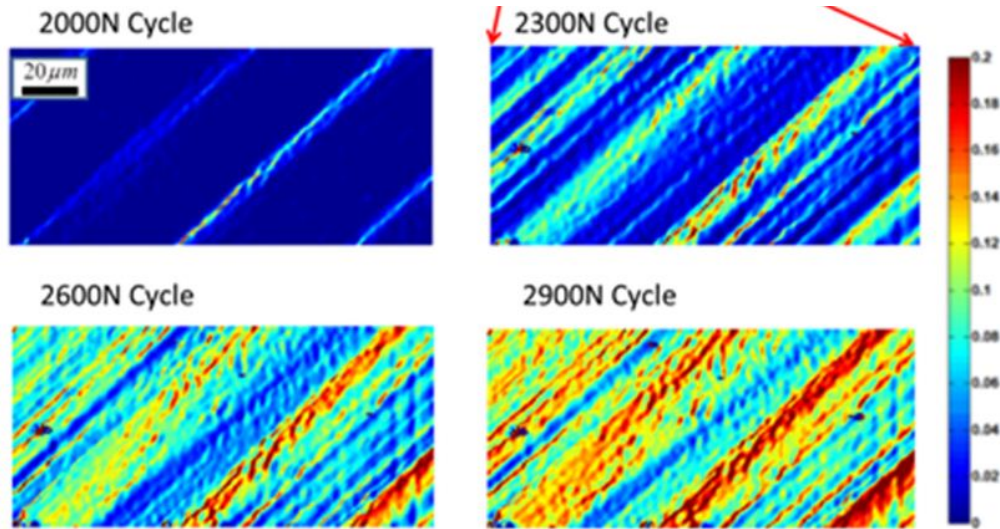
Figure 2.1.4: Strain maps created using DIC for single-crystal CMSX-4, showing lateral strain ϵ_{xx}. Each image shares the same scale bar. [27].

A significant barrier to slip transfer is caused by γ' particles inhibiting slip. These particle obstacles may be overcome through particle cutting (shearing), the mechanism of which is discussed later, but which will occur at stress thresholds defined by the particle size and spacing [29]. Examples of particle shearing may be observed using SEM on post-situ samples: this was carried out by M. Preuss *et al.* [30] and the result is reproduced in Fig. 2.1.5. Here secondary particles are seen to have been sheared by slip along a {111} plane, occurring at $\sim 45°$ to the tensile loading axis.

14

Fine tertiary particles may also be seen in the interstitial space between the larger particles.
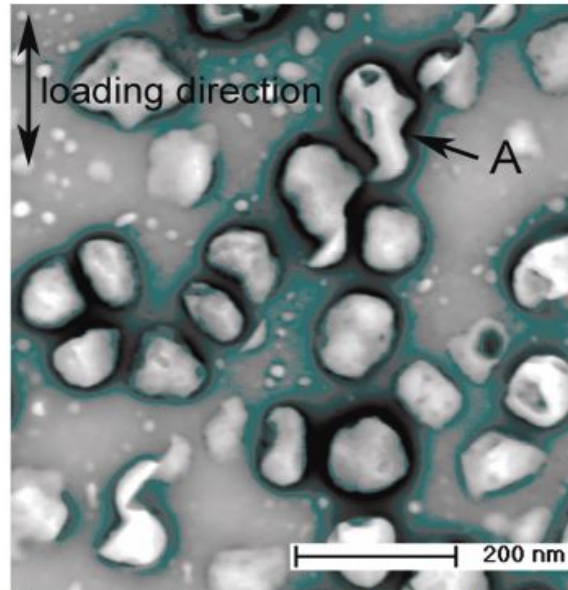
Figure 2.1.5: SEM micrograph of RR1000 nickel-based superalloy after loading, showing precipitates clearly being sheared at $\sim 45°$ to the loading axis [30]

2.1.4   Influence of particle dispersions on emergent properties

Solid-solution strengthening and precipitate strengthening are mechanisms by which nickel-based superalloys gain their characteristic strength and therefore become appropriate for use within gas turbine engines. Both rely on restricting dislocation movement within the lattice; the former through the introduction of new alloying elements that produce local strain fields and the latter through creation of precipitate dispersions that act as hard obstacles [6][31]. Here the strengthening from γ' particles will be considered.

The heat treatments mentioned in Section 2.1.2 are used to create desirable particle distributions within a given alloy. As such, much work has gone into quantifying the link between macroscale properties and given precipitate parameters. Sondhi *et al.* [19] have observed that the coarsening of bimodal particle distributions to remove tertiary particles will cause a loss of creep strength. In the same work investigation into tensile/compression behaviour found that plastic deformation was mainly confined within the matrix, which already contains compressive internal stress that was

put down to volumetric mismatch between the phases. This led to markedly higher yield stress in tension than in compression.

M. Preuss *et al.* [30] have studied the effect of secondary γ' particle size on flow stress for samples of RR1000 polycrystalline superalloy with carefully controlled unimodal microstructures of mean radius: 40nm (fine), 60nm (medium) and 75nm (coarse). The findings for tensile loading were that the fine particles provided higher yield stress at all temperatures, but that the strength difference was particularly prominent at higher temperatures ($\sim 750°$C). These results are displayed in Fig. 2.1.6.
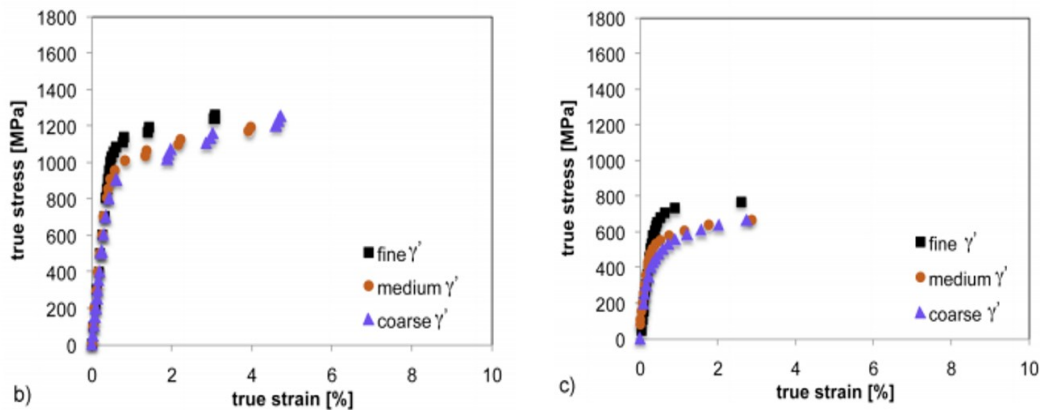
Figure 2.1.6: Flow stress of polycrystal RR1000 superalloy with unimodal secondary distribution with different mean radius: fine - 40nm radius, medium - 60nm radius, coarse - 75nm radius. Left hand side at 500°C and right hand side at 750°C [30]

Begining with Kocks [32] in 1967 efforts have also been made to model the particle strengthening effect. The basis of these models was to capture the relationship between the local cutting threshold of particles within a distribution and the macroscale critical flow stress of a volume. Kocks argued that one of the most important parameters in such a model must be the distibution of local flow stresses at each particle, which would give a flow stress curve its characteristic yield. With the increase in available computing power, later simulations began to apply dislocation dynamics rather than constitutive models, initially in 1D [33], followed by 2D [2] [34] and specifically for nickel-based superalloys [35]. All of these models include a random distribution of particles with a

threshold stress value for cutting.

More intuitive relations could be supposed by taking the average particle radius and spacing and assuming that the averaged cutting threshold may be representative of the macro-scale yield property. Equations relating the volume fraction, particle radius and threshold cutting stress are defined for a lattice square spacing of uniform particles in [6] (p78 & p81). This approach may be useful as a fast first approximation, but does not account for any of the localised stress fields of dislocations and so cannot be relied upon as an accurate prediction of yield.

2.1.5 Deformation in CMSX-4 type alloys under shear loading

While this work will predominantly consider the behaviour of a non-specific nickel-based superalloy with generalised precipitate microstructures, a comparison to experiments upon the real alloy ERBO/1 will also be considered. As such a brief summary of this pedigree of alloy will follow.

ERBO/1 is a CMSX-4 type alloy that has undergone a specifc heat treatment to promote creep resistance [36]. CMSX-4 is a well known second generation nickel-based superalloy designed for increased high-temperature capability over first generation predecessors, due the additional 3% composition of Rhenium [37]. In practice the alloy has peak operation temperature of at least 1163°C making it appropriate for hot-section rotative components within gas-turbine engines [38]. The nominal chemistry is provided in Table 2.1.1.

Table 2.1.1: Nominal composition of CMSX-4 alloy [39]

Element	Cr	Co	W	Re	Mo	Al	Ti	Ta	Hf	Ni
Weight %	6.5	9.6	6.4	3.0	0.6	5.6	1.0	6.5	0.1	Balance

CMSX-4 typically shows microstructural heterogeneities following casting which spawn from segregation of dendritic and interdendritic regions during solidifcation [40]. To attempt to homogenise the as-cast material complex heat treatments are applied to dissolve the larger eutectics and arrive at a final microstructure with ~70% volume fraction of γ' (i.e ERBO/1). The microstrucutre following such an optimised treatment is show in Fig. 2.1.7. In this state the precipitate distribution exists as cuboidal particles and have been characterised in ERBO/1 as

having an edge length scatter of between 50-750nm and a γ-channel scatter of between 15-125nm [41]. The average edge length in this instance was 442nm and the channel width was 65nm. Even following the homogenisation treatments differences between the microstructure of the dendritic and interdendritic regions remain, with γ' volume fractions of $72\pm1\%$ and $77\pm1\%$ being observed post-treatment [42].
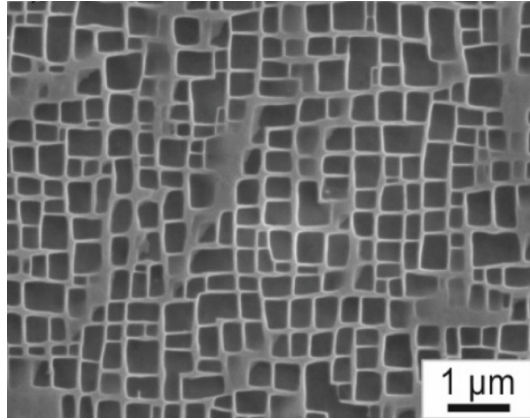
Figure 2.1.7: γ/γ' microstructure of ERBO/1 following optimised heat treatment [40]

Laplanche et al [41] have studied room temperature shear deformation of ERBO/1 in configurations promoting single, double and multiple (eight) slip system deformation. For microsamples loaded at constant strain rate, the characteristic early stage deformation feature was a minor deviation from elastic behaviour before total yield. This deviation was associated with in-grown dislocations upon the {111} glide planes gliding across the wider γ-channels ($\sim$125nm), equivalent to a slip distance of 180nm. The shear stress τ_{el} at which this feature occurred did not differ between dendritic and interdendritic regions, leading the authors to believe that γ-channel width (and not total volume fraction) dominated this behaviour. Following yield, subsequent strain hardening was observed before sudden deformation events (SDEs) occured, causing large plastic strains and shear steps in the samples. The SDE intervals were interpreted to be due to the γ-channel dislocations bowing out and cutting through the precipitate particles at shear stress τ_{SDE}: this released large amount of dislocations as the particles were sheared. The largest SDEs were observed in single slip setups, where τ_{SDE} was also the largest. The double-slip setup saw smaller, but evident, plastic slip events and generally lower yield stresses due to the additional capacity for plastic slip. The setup with eight slip systems active saw no SDEs as the slip systems did not align with the axis of shear

loading, thus the plastic deformation was spread more evenly and could not lead to a large localised event. The dominant deformation mode was due to particle shearing for every tested orientation.

2.2   Dislocations and Plasticity

2.2.1   Dislocations within crystals

In metals there are two main methods of plastic deformation: twinning and dislocation glide. The first is a process by which the crystal arrangement flips along a twinning boundary to become a mirror image of the arrangement on the other side. This effectively means that a new separate crystal is formed with coincident lattice points along the boundary. Twinning is normally associated with low temperature deformation, in materials with low stacking fault energy, and occurs in cubic and hexagonal crystals alike [43]. The second is the sole form considered in this work and involves dislocation slip along atomic planes.

Dislocations exist as line defect symmetry faults within a periodic crystal. This defect causes a physical displacement of lattice points in a direction which is denoted by the Burgers vector $\underline{b}$. As illustrated in Fig. 2.2.1, the vector may be determined by drawing a closed circuit (Burgers circuit) around an area of lattice without a dislocation then observing the non-closure condition of the same circuit when dislocation content is added. Vector $\underline{b}$ will act to close the circuit. A dislocation line also has a directional component given by the line tangent vector $\underline{\xi}$ at each point upon the line. The combination of these vectors may describe any local point upon a dislocation line [43][44][45].

Two pure forms of dislocation are identified, depending on if the $\underline{b}$ and $\underline{\xi}$ vectors are perpendicular or parallel; these are termed edge type and screw type respectively. It can be mathematically convenient to consider the forms in isolation; however in reality dislocation will generally exist as closed loops containing components of both type. The edge type dislocation refers to the situation when an extra half-plane of atoms exists within a crystal section. The point at which the half-plane ends and gives way to the original crystal structure is the point of maximum lattice distortion and is termed the dislocation core, see Fig. 2.2.1. Graphically an edge dislocation can be represented by

19

⊥ if the half plane extends upwards from the core location and ⊤ if it extends downwards. A screw dislocation does not involve an extra plane of atoms, but rather the twisting of an existing perfect lattice region so that the area above a given line of atoms is displaced in a direction parallel to the line while the area below is displaced anti-parallel. This type of dislocation will not be considered within the current work.
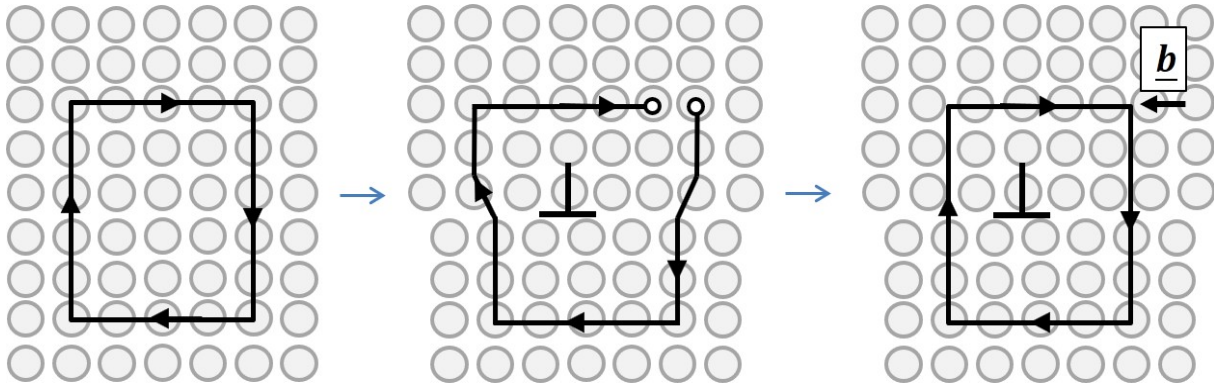
Figure 2.2.1: Burgers circuit drawn around a lattice before and after the introduction of a single edge dislocation. Burgers vector $\underline{b}$ is required to close the circuit containing the dislocation.

Dislocations exist and move upon the close-packed planes of a crystal, called the glide planes or slip planes. In the case of FCC nickel-based alloys these are the four $\{111\}$ planes, e.g. a plane defined by normal vector $\underline{n} = [111]$. Each plane has three close-packed $\langle 110 \rangle$ slip directions, along which a dislocation may travel, which is parallel with the dislocation Burgers vector $\underline{b}$. For the $\underline{n}$ plane one such direction could be given by $\underline{s} = [\bar{1}10]$. Finally the dislocation line itself will lie parallel with the line tangent vector $\underline{\xi}$, which is perpendicular to the other two. This is illustrated in Fig. 2.2.2 for a single $\{111\}$ plane. In total three slip directions upon four planes gives a family of twelve slip systems for the FCC unit cell.
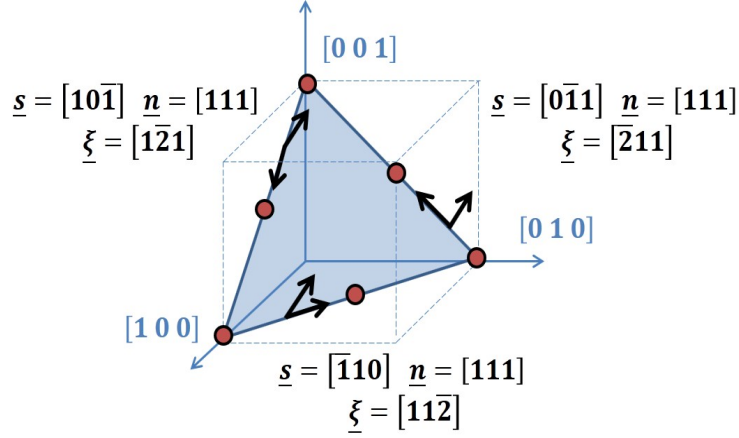
Figure 2.2.2: The three slip systems (and accompanying direction vectors) upon a $\{111\}$ plane in an FCC crystal.

2.2.2 Dynamics of dislocations

Dislocation slip (or *glide*) involves the dislocation line moving along a glide plane in direction $\underline{s}$, displacing the material in its wake by $\underline{n}$ as it moves to a new lattice site. The dislocation moves stepwise one Burgers vector at a time, minimising the number of atomic bonds that need to be broken during transport. The motion is activated by shear stresses resolved along the slip plane. Typically a slipping dislocation will move until an obstruction checks the motion and prevents further shearing [25][45].

Dislocation glide velocity has been described with numerous relationships to shear stress [44][46][47], some of the simplest being

$$v_g \;=\; \left(\frac{\tau b}{B}\right) \quad [44] \tag{2.2.1}$$

$$v_g \;=\; \left(\frac{\tau}{\tau_0}\right)^{m} \quad [46] \tag{2.2.2}$$

$$v_g = \begin{cases} \text{sign } \tau(|\tau| - \hat{\tau})b + Tk & \text{, for } |\tau| > \hat{\tau} \\ 0 & \text{, for } |\tau| \leqslant \hat{\tau} \quad [48] \end{cases} \tag{2.2.3}$$

$$v_g = \frac{\tau b}{B} + \frac{\mathbb{T}cos(\theta)}{B}\frac{\partial \theta}{\partial X} \quad [48] \tag{2.2.4}$$

where τ is critically resolved shear stress, B is a drag coefficient, τ_0 and m are characteristic material constants, $\hat{\tau}$ is the shear yield stress, $\mathbb{T}$ is line tension, and θ is the angle between tangent ξ and an axis X_1. The first of these, containing the linear relationship to applied force τb scaled by a drag coefficient, is often associated with the lattice self-friction or phonon drag. More dislocation mobility and velocity terms are found in the works cited in Section 2.3.3.

Further to glide, there is also an out-of-plane movement available to the dislocation termed dislocation climb. This mechanism involves the migration of vacancies within the crystal lattice towards the dislocation core by diffusion. When a vacancy reaches the dislocation, the dislocation may move in the $\underline{s}$ direction up or downwards by a single plane. As vacancy diffusion is a slow and thermally activated process, movement by climb is not so rapid as dislocation glide, often occurring orders of magnitude slower. Nevertheless, over long timescales or at extreme temperatures the mechanism allows dislocations to overcome obstacles in the lattice by climbing planes until there is no longer an obstruction [44][45].

2.2.3 Dislocation interactions

Dislocations-dislocation interactions

The distortion created by the presence of a dislocation within a lattice creates a displacement field that emanates from a dislocation line, decaying as a function of distance. This was laid out in Mura's formula given by eqn. (2.2.9) in the next section. The displacement gives rise to a stress field with well-defined shape [49][44], determined early in the 20th century, and a magnitude determined through material specific stiffness constants. The standard stress field equations are covered within the FDM application section of this work (see eqn 4.3.3) and so will not be unnecessarily repeated here, however field shape is illustrated in Fig. 2.2.3. Between dislocations of the same sign (e.g. two positive edge dislocations) these fields are repulsive in the shear direction and so concentrations of dislocations upon a slip plane will attempt to diffuse away from each other. When shear stress is externally applied to a system, dislocations will tend to pile-up against each other with predictable distribution shape depending on the density of dislocations present [50][51]. Given enough time to move, dislocations will tend towards an arrangement that provides the lowest stress state, in some cases forming sub-grain dislocation cell structures [52][53]. Dislocation stress fields

may also cause a dislocation pinning effect when low-stress regions occur in a grain [54].

The force $\underline{f}$ upon a dislocation segment caused by stress $\underline{\sigma}$ is given by the Peach-Koehler relationship [44]

$$\underline{f} = \underline{\xi} \times (\underline{\sigma} \cdot \underline{b}) \tag{2.2.5}$$
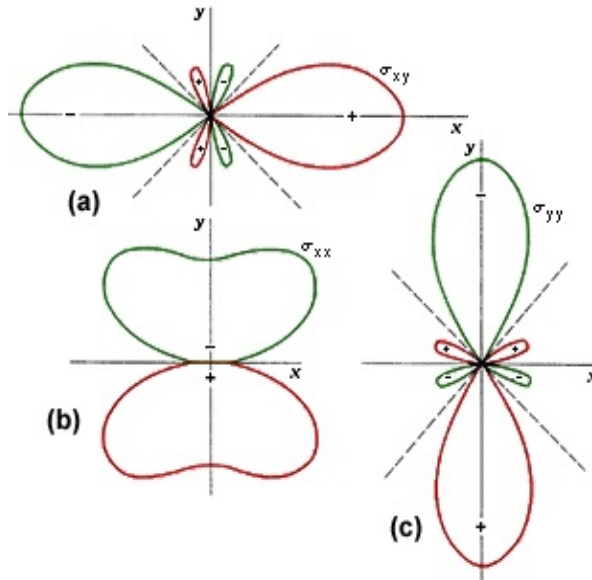
Figure 2.2.3: Illustration of the three components of the stress field for a straight edge-type dislocation at the origin, with green and red indicating tensile or compressive stress [55].

Dislocation-environment interactions

Dislocation mobility may be reduced by the presence of hard obstacles to slip in the form of grain-boundaries, dislocations upon other slip systems or second-phase microstructure. In the case of nickel-based superalloys the main slip-limiting factor is the presence of γ' particles, which act as barriers to dislocation slip until the local stress reaches a critical condition for which the dislocation may make the energetically unfavourable advancement. This leaves the precipitate particle sheared [6]. The full mechanism by which this occurs is discussed later in Section 4.4.

Before the particles are sheared a dislocation line under applied stress may begin to bow out

between two points that are pinning it. This pinning has been shown to cause a line tension (restorative force) which acts against further bowing. From a dynamics point of view this effectively provides a drag on the dislocation slip velocity in the bowing regions [56][57]. Line tension is further discussed in Section 4.3.2.

At a grain boundary slip transmission to another grain is possible if the orientation of the two grains is close, as observed at the top of grain 8 in Fig. 2.1.3. When this orientation does not allow the slip systems of the two grains to align, then the grain boundary becomes a hard barrier to slip [58]. Dislocations under shear stress will pile-up against this type of boundary, which can cause a considerable stress concentration at the grain wall and eventually form crack tips [59][60].

A Frank-Read source is created when a dislocation segment bows out between two pinning points until the line folds back on itself forming a new self-contained dislocation loop while preserving the original segment between the pinning points [49][61]. In this manner many dislocation loops may be created from a single source given enough applied shear stress to cause extensive dislocation bowing. This point is normally modelled with a threshold stress value for critical bowing [62]. A source that begins to generate dislocations is said to have "activated". Similar generation mechanisms may apply wherever dislocations can be pinned. R. A. Varin et al [63] have identified grain boundary sources as a key source of plasticity in polycrystals.

2.2.4   Continuum dislocation theory

In 1952 J. F. Nye [64] introduced the second rank dislocation density tensor $\underline{\underline{\alpha}}$ to describe the combined dislocation state from multiple dislocations averaged over a volume. This was given by

$$\underline{\underline{\alpha}} \;=\; n\,\underline{b}\,\underline{\xi} \tag{2.2.6}$$

for one dislocation type, where n is the number of dislocations. For multiple dislocation types a summation is carried out with different n for each type. This was related to an associated curvature tensor $\underline{\underline{\kappa}}$ within the volume through

$$\underline{\underline{\kappa}} \;=\; \underline{\underline{\alpha}}^{T} \;-\; \frac{1}{2} tr(\underline{\underline{\alpha}}) \tag{2.2.7}$$

Bilby *et al.* [65] built upon this by extending the Burgers circuit formally to a continuum of dislocations and defining the generation of deformation as applied to an undeformed reference crystal state. This was especially useful a decade later in 1968 when E. H. Lee suggested the decomposition of deformation into separate plastic and elastic components [66] [67]: with the plastic deformation gradient tensor $\underline{\underline{F}}^{(p)}$ first applied to the reference crystal to form an intermediate plastically deformed state, then the elastic deformation deformation gradient tensor $\underline{\underline{F}}^{(e)}$ applied to complete the deformation.

$$\underline{\underline{F}} = \underline{\underline{F}}^{(e)} \cdot \underline{\underline{F}}^{(p)} \tag{2.2.8}$$

Mura [68] proposed a theory for calculating the distortion at point $\underline{x}$ from a moving, continuous dislocation field at $\underline{x}'$ through integrating the distortion components from dislocation segments around a line integral of the dislocation loops of length L. The Mura formula [69] was then given (in index notation) by:

$$\beta_{ji}(\underline{x}) = \int_L \epsilon_{jnh} \, C_{pqmn} \, G_{ip,q}(\underline{x} - \underline{x}') \, b_m \, \xi_h \, dl(\underline{x}') \tag{2.2.9}$$

where $\underline{\underline{\beta}}$ is the displacement gradient tensor, $\underline{\underline{\underline{C}}}$ is the material stiffness tensor, $\underline{\underline{G}}$ is the Green's function which gives the field shape (and the subscripts are indices for the tensor operation order). Within this relationship it is shown that

$$\underline{\underline{\alpha}} = -\underline{\nabla} \times \underline{\underline{\beta}} \tag{2.2.10}$$

Much of the continuum theory for dislocation evolution within a volume that is recognisable today was put down by Soviet-Ukranian physicist A. M. Kosevich, from 1965 onwards [70] [71]. Beginning with an arbitrary contour drawn around a single dislocation loop he developed, at length, a wave equation for continuity. This assumed the general dislocation density tensor moving as a continuous field which could flux through a given contour and would cause deformation in an isotropic medium. The final equation for a scalar dislocation density ρ evolving over time t was [70]

$$\frac{\partial \rho}{\partial t} + \frac{\partial}{\partial \boldsymbol{r}}(\rho V_0) + \frac{\partial}{\partial r_m}(\rho v_m) = 0 \tag{2.2.11}$$

where V_0 is the slip velocity, $\boldsymbol{r}$ is a spatial coordinate, r_m is the dislocation length and v_m is the material velocity during deformation. In England, N. Fox [72] undertook similar work at this time, considering infinitesimal strains and producing continuity equation $\dot{\rho} + \rho \, \partial_m v_m = 0$. Equations of

25

this type underpin most Field Dislocation Mechanics models.

More recently, as increased computer processing power has allowed solutions to these wave equations to be iterated relatively cheaply, there has been further advancement of the theory. El-Azab [73] has looked into the boundary conditions of the dislocation dynamics problem, treating dislocation microstructure as a defect field interacting with applied elastic stress fields and boundary conditions at the edges of the volume. This edge was taken as either a free surface or the edge of a small volume in a larger volume deforming homogeneously. For single crystals it was found to be important to consider the effect of *surface dislocations* (at the edge of crystal) which may form large steps when stored at the boundary (*surface dislocations* are described in [74]).

Follow-up work by Acharya *et al.* [75] developed a theory of Crystal Plasticity based upon the instantaneous distribution of dislocation density. This was further improved through consideration of the dislocation driving force [76] and plausible boundary conditions [77] setting up a closed set of equations for the dynamics of a continuous dislocation system, the implementation of which will be discussed in Section 2.3.3.

2.3　Computational Material Modelling

2.3.1　Constitutive models

Constitutive models mathematically describe how materials will respond to given applied loading conditions. In modern times this is obviously processed digitally. Computational modelling of the stress state evolution across a domain may be achieved, provided well-defined external boundary conditions for a domain, using one of a number of time-iterative solvers. Common commercially available software packages such as Abaqus Unified FEA (previously ABAQUS) [78] and DEFORM-3D [79] provide stress solutions to material modellers using Finite Element Analysis: whereby a domain is discretised with a fine mesh and the stress equilibrium is solved for each element of the mesh [80]. The FE domain may be termed the Representative Volume Element (RVE) of the modelled material.

The use of internal state variables, which may be ascribed to elements as a group or individually, can allow microstructural parameters to be tracked locally as a response to local conditions [81]. In 1981 Mecking and Kocks [82] suggested the use of a mechanical threshold stress, applied to all elements, which would describe the stress at yielding if no thermal effects were assumed (i.e the yield stress at 0K) for use in capturing the strain hardening effect.

Since these early days, constitutive models concerned with plastic flow now contain many more microstructural state variables [83][84][85][86], most with their own independent evolution rate and all of which will contribute to a final equation for the plastic strain rate $\underline{\dot{\varepsilon}}^{(p)}$ [87]. As total strain rate $\underline{\dot{\varepsilon}}$ is given by the sum of the elastic $\underline{\dot{\varepsilon}}^{(e)}$ and plastic contributions: $\underline{\dot{\varepsilon}} = \underline{\dot{\varepsilon}}^{(e)} + \underline{\dot{\varepsilon}}^{(p)}$, then the stress rate is given by

$$\underline{\dot{\sigma}} = \underline{\underline{C}} : (\underline{\dot{\varepsilon}} - \underline{\dot{\varepsilon}}^{(p)}) \tag{2.3.1}$$

Amongst the examples is a strong tendency towards models that predict creep rates in order to estimate the potential life of high-cost aerospace turbine components. In this regard in 2004, H. C. Basoalto *et al.* introduced coarsening of the γ' precipitate, mobile dislocation density evolution and development of grain boundary cavities as state variables for a constitutive model for creep in Nickel-based Superalloys. Backstress evolution between particles and matrix was also incorporated,

building on the formulation laid down by J. C. Ion *et al.* in 1986 [88]. The basic relation for a homogenised backstress σ_b within a volume, and its place in the plastic strain evolution, was described by:

$$H = \frac{\sigma_b}{\sigma}, \quad \dot{H} = \left(\frac{h}{\sigma}\right)\left(\frac{H}{H^*}\right)\dot{\varepsilon}^{(p)} \tag{2.3.2}$$

$$\dot{\varepsilon}^{(p)} = \dot{\varepsilon}_0^{(p)} \sinh\left(\frac{\sigma(1-H)}{\sigma_0}\right) \tag{2.3.3}$$

where H is the normalised backstress, and h, H^* and $\dot{\varepsilon}_0^{(p)}$ are functions of material constants such as particle fraction. Using this type of model predictions for creep rate and creep fracture strain could be extracted.

2.3.2 Deformation kinematics - CP

Great efforts within the material modelling community have been applied towards the prediction of component-level flow stress behaviour from the deformation of individual grains using Crystal Plasticity (CP) approaches [89][90][91][92]. The CP formulations require the value of plastic shear rate upon active slip systems to be defined by constitutive descriptions. These descriptions, as considered above, may be based on empirical or phenomenological state variable evolution theories, ideally accounting for the evolution of scalar dislocation density upon a plane and subsequent interaction with microstructure within the grain. Within CP formulations the plastic shear rate $\dot{\gamma}$ is related to plastic deformation through

$$\underline{\underline{L}}^{(p)} = \dot{\underline{\underline{F}}}^{(p)} \cdot \underline{\underline{F}}^{(p)-1} = \sum_{k=1}^{N} \dot{\gamma} \, \underline{s} \, \underline{n} \tag{2.3.4}$$

where $\underline{\underline{L}}^{(p)}$ is the plastic velocity gradient tensor and N is the number of active slip planes. From this point multiple methods may be taken to arrive at the associated stress state, one of these combines eqn (2.3.4) with (2.2.8) to determine the elastic deformation gradient. This may be related to the elastic strain and stress within the RVE respectively through

$$\underline{\underline{\varepsilon}}^{(e)} = \frac{1}{2}\left(\underline{\underline{F}}^{(e)T} \cdot \underline{\underline{F}}^{(e)} - \underline{\underline{\mathbb{I}}}\right) \tag{2.3.5}$$

$$\underline{\underline{\sigma}} = \underline{\underline{\underline{C}}} : \underline{\underline{\varepsilon}}^{(e)} \tag{2.3.6}$$

where $\underline{\underline{\mathbb{I}}}$ is the identity tensor [91]. An alternative relation uses the symmetric stretch component of $\underline{\underline{L}}^{(p)}$ to determine the stress increment between steps [89].

For the case of Keshavarz and Ghosh [91] a hierarchical framework has been used to bridge length scales between the polycrystal and sub-grain domains (see Fig. 2.3.1). Information from lower-scale models with discrete particle microstructure informed the γ channel width and grain boundary spacing, which was used to inform the state variables for the higher-scale homogenised grain model. This setup is commonly termed Multi Scale Modelling.
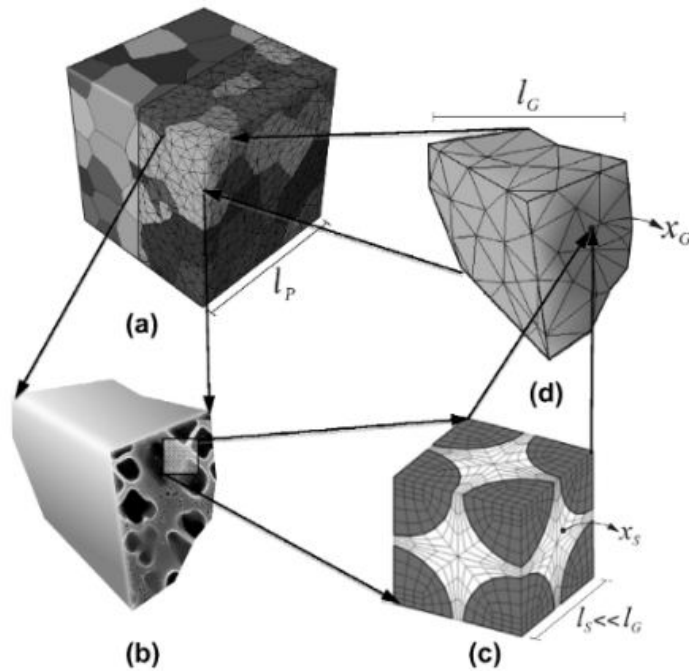
Figure 2.3.1: Multiple scales of a Crystal Plasticity finite element model for Ni-based superalloys showing: a) Polycrystal microstructure, b&c) Sub-grain γ' particles d) The homogenised FE model for a single grain [91].

Macroscale behaviour is obtained through homogenisation across an RVE composed of an aggregate of grains subjected to appropriate boundary conditions. However, limitations exist with current CP formulations which may prove significant to the development of component-level constitutive models. Firstly, the highly heterogeneous and localised nature of slip band evolution (shown in Section 2.1.3) is not attended to, meaning backstresses caused by associated localised strains are not directly included (unless through phenomenolgical Fredrick-Armstrong description [93]).

Secondly CP formulations do not directly account for elastic interactions between dislocations and microstructure of discrete geometry (i.e grain boundary seperation and particle distributions). Such reactions are likely to cause emergent properties on the macroscale.

2.3.3   Modelling dislocation dynamics

Discrete Dislocation Dynamics - DDD

Plasticity as emerging directly from dislocation interactions has provided a well-trodden research ground since the early 1990's. Discrete dislocation dynamics has proven useful in determining the wider behaviour of collections of dislocations; this is accomplished through discretising individual dislocation lines into segments and processing long-range interactions from each segment explicitly [94][95][62][96][97]. Such models require accurate description of individual dislocation velocities with relation to local stress states.

Pioneers in the field include Van Der Giessen and Needleman [94] who created a planar model containing discrete dislocation points which could form order from initial homogeneous arrangement. Flow stress curves could also be derived from this domain, showing jerky behaviour associated with large slip events: these are shown in Fig. 2.3.2. Further applications to 3D domains have been made in order to capture hardening effects through jog-formation and cross slip [96] (though models have historically been limited to high strain rates $\sim 10\mathrm{s}^{-1}$, domain sizes of $\sim 10\mu\mathrm{m}$ and low dislocation content due to significant CPU requirements).

In 2012 work by Huang *et al.* [97] looked at DDD within single crystal nickel-based superalloys. Simulations results were produced for the uniaxial loading ($1\mathrm{s}^{-1}$) of a small domain RVE ($< 500\mathrm{nm}$) representative of CMSX-4 alloy containing a single γ' particle. The *gamma* channel width was altered in this model, producing the expected result that lower channel width led to a higher predicted flow stress for the RVE. Realistic yield strengths were achieved through the threshold for particle cutting.
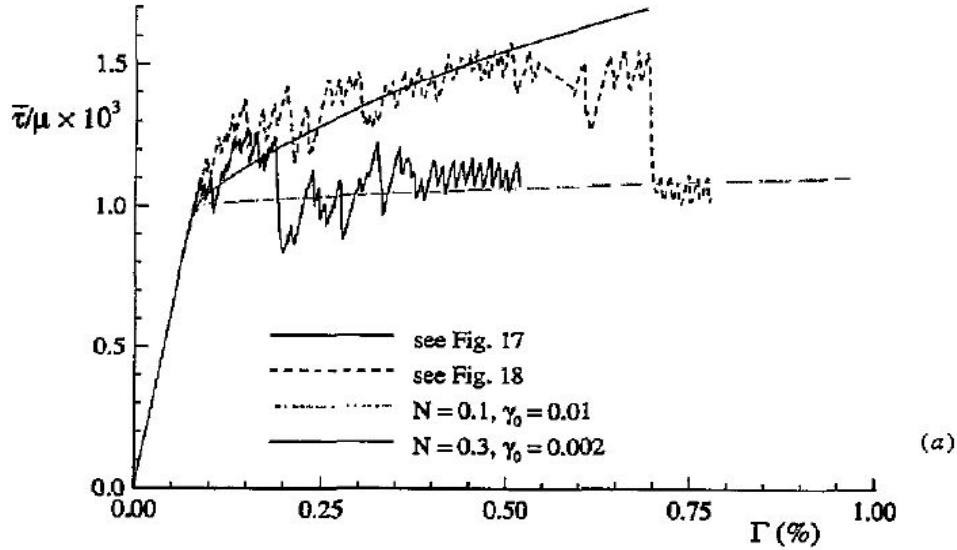
Figure 2.3.2: Jerky flow stress curves produced by Van Der Giessen and Needleman's planar discrete dislocation model, emerging through internal dislocation reactions, vs the smooth curves produced by early continuum model with different hardening parameters [94]

Mobile and sessile dislocation populations may be separately considered through these methods. However, when applied only to single slip scenarios H. Mughrabi [98] has shown that geometrically necessary dislocations (GNDs) are not required to predict macroscopic flow stress. The contribution of GNDs becomes non-zero but small, he argues, when more slip systems are included.

Continuum Dislocation Dynamics - CDD

By contrast Continuum Dislocation Dynamics (CDD) - a term used interchangeably with Field Dislocation Mechanics (FDM) - is inherently able to handle much larger dislocation content through homogenisation into a singular scalar dislocation density value for each spatial element in the model. The ability to resolve more localised heterogeneous phenomena may be maintained by using appropriately small element dimensions. Roy and Acharya [99] have implemented their equation set from [77] within a FE model to simulate a 1 μm grain representative of aluminium under simple shear (strain rate $1s^{-1}$). Attention was drawn to the low processing time for CDD compared to DDD, predicting this model to be faster by a factor of ~ 40. Density within this model, however, evolved as an amorphous mass within the grain, leaving considerable room for improvement in

intergranular strain localisation.

This work has been continued into the 2000's [48][100][101][102][103][104][105] with additions often added to retain some semblance of short-range interactions (that are lost through homogenisation) by tracking local line tension and curvature within an element (as in eqn (2.2.4)). Considerable mention must go to Hochrainer *et al.* [102] who in 2014 advanced a hd-CDD theory (higher dimensional CDD) to include the scalar curvature associated with the density at each element (this is sometimes referred to as 2.5D CDD theory in literature). In this work short simulations were carried out over 13.5μs, viewing a uniform distribution of dislocation loops top-down upon a slip plane during deformation, tracking the density to its inevitable pile-up against zero-flux boundaries. Further simulations recreated compression tests of a nickel micro-pillar with "six" active slip systems, producing a predicted flow stress curve - although it should be noted that the six systems response was created by only one CDD simulation which represented plasticity on multiple planes. Amongst others *anisotropic dislocation mobilities* were discussed as a key area for future work in this field. Dislocation patterning has been investigated amongst these works, albeit with a minimal model [103] not designed to recreate realistic patterns, and which has formed only "blobs" (to quote the authors) of dislocation density in heterogeneous internal patterns. The hd-CDD theory was governed by:

$$\frac{\partial \rho}{\partial t} \;=\; -\nabla \cdot (v\underline{\boldsymbol{\kappa}}) \;+\; vq \tag{2.3.7}$$

where v is the magnitude of dislocation velocity (with sign), $\underline{\boldsymbol{\kappa}}$ is the dislocation density vector (which may contain information about dislocation character) and q is the scalar curvature density.

In 2015 Sandfeld *et al.* [106] performed side-by-side comparisons of consistent discrete and continuum models, finding that the continuum model, carefully designed with appropriate boundary conditions, could accurately resolve almost the same detail as the discrete simulation, but at much lower processing costs. The paper argues that computing costs scale with the square of the number of dislocation segments present in 3D DDD simulations, but have no such processing increase in CDD. In the same year Xia and El-Azab [53] implemented a continuum formulation for density evolution within a finite element solver to simulate cross-slip within single crystal copper (5μm^3). These 3D simulations produced flow stress curves and dislocation cell patterning, though there was

no investigation into the effect of localised plastic strains.

Recently in 2017 Wu *et al.* [107][108] have used 2D continuum dislocation dynamics coupled with a phase-field model of particle growth to look into plasticity and precipitate coarsening during deformation of nickel-based superalloys. Discrete particle morphologies are included within a 2.5 μm domain; however localised slip bands are not specifically investigated. The simple linear drag velocity from eqn (2.2.1) is implemented, with the shear stress amended by backstress terms compensating for short range interactions.

Phase Field Dislocation Dynamics (PFDD) is also used to model physical behaviour through evolving scalar parameters. Here it is assumed that plastic strain is related directly to the number of gliding dislocations through [109]

$$\varepsilon_{ij}^{(p)} \; = \; \frac{1}{2} \; \sum_{k=1}^{N} b \; \xi_k \; \delta_m (s_i^k n_j^k + s_j^k n_i^k) \tag{2.3.8}$$

where δ_m is the Dirac delta function upon slip plane m.

In 2016 Zeng *et al.* [110] modelled the transmission of single pure dislocations across FCC elemental boundaries (i.e Ni-Cu) using PFDD, finding screw dislocations require less shear stress to transmit. Fig. 2.3.3 shows snapshots from this work effectively modelling a single slip band in 2D.
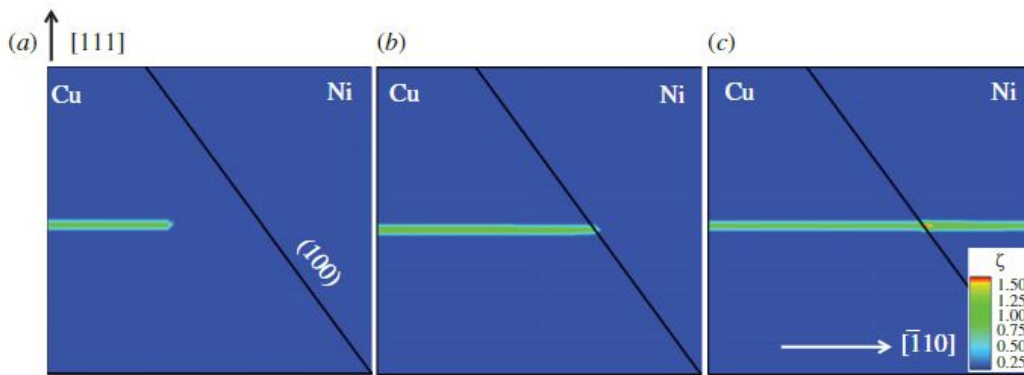
Figure 2.3.3: Single dislocation modelled travelling across a Cu-Ni boundary in 2D using PFDD [110].

The gap within the literature, therefore, appears to be that strain localisation due to well-defined slip bands has not been thoroughly investigated through a field (continuum) dislocation dynamics model, particularly not within multi-phase microstuctures that can affect the band evolution. Furthermore, specific application of continuum models to nickel-based superalloy systems with realistic microstructures, for the purpose of macro-property prediction for different internal parameters, has not to the author's knowledge been assessed (though discrete modelling in [97] has shown potential in small domains).

Note: Shear band strain localisation has been found previously investigated within literature on FE models [111]; however this was in regard to Bulk Metalic Glasses deforming through amorphous plasticity. Shear bands patterning and avalanche rates were predicted for a dimensionless domain under pure and simple-shear loading conditions.

Chapter 3

Field Dislocation Mechanics I: General Formulation

In this chapter a mathematical framework is developed to describe the evolution of the statisically stored dislocation state within a system. The proposed theory follows from the work of Basoalto [112] and Basoalto and Little 2019 [113], which seeks to develop a field dislocation mechanics description rooted in metallurgical physics.

Note on mathematical representation: For clarity the equations in this section have been duplicated in both vector notation (left hand side) and index notation (right hand side). For longer equations, when space will not neatly permit both forms, the index notation has been preferred.

3.1 Development of General Theory

3.1.1 The Burgers Vector

The deformation of a domain from an initial state Ω_0 to a final state Ω_F is described by the mapping $\underline{\underline{F}}$, also known as the deformation gradient tensor. This deformation may be decomposed into separate plastic and elastic contributions [66][67], making use of an intermediate configuration Ω_P concerned with advection of the dislocation field in the lattice. As depicted in Fig. 3.1.1, the map from $\Omega_0 \rightarrow \Omega_P$ is given by $\underline{\underline{F}}^{(p)}$, which leaves the lattice structure unchanged. The second mapping $\Omega_P \rightarrow \Omega_F$ is given by $\underline{\underline{F}}^{(e)}$, which elastically distorts the lattice and arrives at the final

state. These tensors are related by

$$\underline{\underline{F}} = \underline{\underline{F}}^{(e)} \cdot \underline{\underline{F}}^{(p)} \qquad\qquad F_{ik} = F_{ij}^{(e)} F_{jk}^{(p)} \qquad\qquad (3.1.1)$$

The evolution of the dislocation field will be calculated between the initial and intermediate sate.

Consider a material domain defined by the set of points $\Omega_0 = \{\underline{X} \in \mathbb{R}^3\}$. Within this domain let a dislocation loop be defined by the set of points $\mathcal{L} = \{\underline{q} \in \mathbb{R}^3 \mid \underline{q} = (q_1, q_2, q_3)\}$, where a loop segment may described by line tangent vector $\underline{\xi}$, slip direction $\underline{s}^*$ and slip plane normal $\underline{n}$. A contour C may be arbitrarily drawn around a section of the loop, such that the dislocation penetrates the surface of the contour S. An element of this contour has a tangent vector $\underline{t}$ and unit normal $\underline{m}$. The points upon the dislocation line may be parameterised into points p on a second line I, such that $\psi : I \to \mathcal{L}$, where $I \subset \mathbb{R}$, $p \in I$ and $\underline{q} = \underline{q}(\underline{p})$. A deformation within this domain will cause a displacement $\underline{u}^{(p)}$ which translates an initial point at $\underline{X}$ to a new point at $\underline{x}$. The graphical representation of this setup is presented in Fig. 3.1.2.
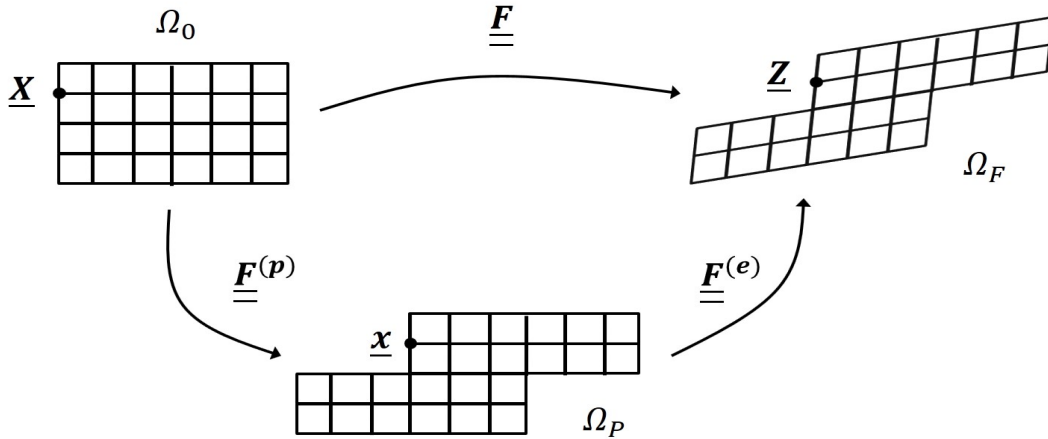
Figure 3.1.1: Mapping between undeformed and deformed lattice configurations.

The total Burger's vector $\underline{B}$ within a contour is defined as the sum of the enclosed displacements $d\underline{u}^{(d)}$ within (where basis vectors are labelled $\underline{e}_*$):

$$\underline{B} = \int_c d\underline{u}^{(d)} \qquad\qquad B_i \, \underline{e_i} = \int_c du_i \, \underline{e_i}$$
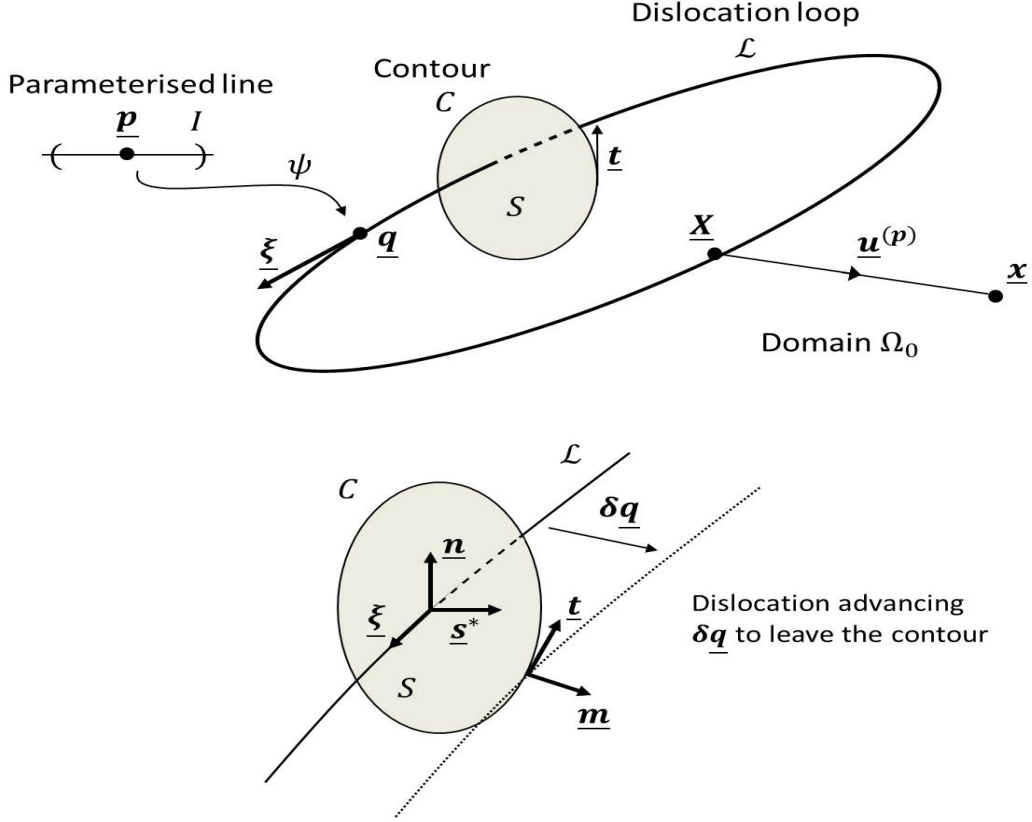
Figure 3.1.2: Dislocation loop with accompanying contour and vectors.

If the coordinates of the reference (undeformed) system are given by $\underline{X}$, then the integral may be rewritten as follows

$$\int_c d\underline{u}^{(d)} = \int_c d\underline{u}^{(d)} \cdot \frac{d\underline{X}}{d\underline{X}}$$
$$= \int_c \frac{d\underline{u}}{d\underline{X}}^{(d)} \cdot d\underline{X}$$
$$= \int_c (\underline{\nabla}\, \underline{u}^{(d)}) \cdot d\underline{X}$$
$$= \int_c \underline{\underline{\beta}}^{(d)} \cdot d\underline{X}$$

$$\int_c du_i\; \boldsymbol{e_i} = \int_c du_i \cdot \frac{dX_k}{dX_k}\; \boldsymbol{e_i}$$
$$= \int_c \left(\frac{du_i}{dX_k}\; \boldsymbol{e_i}\; \boldsymbol{e_k}\right) \cdot (dX_k\; \boldsymbol{e_k})$$
$$= \int_c (\partial_k u_i^{(d)} \boldsymbol{e_i}\; \boldsymbol{e_k}) \cdot (dX_k\; \boldsymbol{e_k})$$
$$= \int_c \beta_{ik}^{(d)}\; dX_k\; \boldsymbol{e_i}$$

Where $\underline{\underline{\beta}}^{(d)}$ is the displacement gradient tensor

$$\underline{\underline{\beta}}^{(d)} = \underline{\nabla}\, \underline{u}^{(d)} \qquad\qquad \beta_{ik}^{(d)} = \partial_k u_i^{(d)} \qquad\qquad (3.1.2)$$

Applying Stoke's theorem can convert the contour integral into a surface integral. This surface $d\underline{S}$ will now describe a membrane penetrated by the dislocation lines, causing the contained displace-

ment field

$$\int_c \underline{\underline{\boldsymbol{\beta}}}^{(d)} \cdot d\underline{\boldsymbol{X}} \;=\; \iint_s \left(\boldsymbol{\nabla} \times \underline{\underline{\boldsymbol{\beta}}}^{(d)}\right) \cdot d\underline{\boldsymbol{S}} \qquad\qquad \int_c \beta_{ik}^{(d)} \; dX_k \;=\; \iint_s \epsilon_{pkm} \; \partial_m \; \beta_{ik}^{(d)} \; dS_p$$

Here the Nye (1953) dislocation density tensor $\underline{\underline{\boldsymbol{\alpha}}}$ may be introduced

$$\iint_s \left(\boldsymbol{\nabla} \times \underline{\underline{\boldsymbol{\beta}}}^{(d)}\right) \cdot d\underline{\boldsymbol{S}} = \iint_s \underline{\underline{\boldsymbol{\alpha}}} \cdot d\underline{\boldsymbol{S}} \qquad \iint_s \epsilon_{pkm} \; \partial_m \; \beta_{ik}^{(d)} \; dS_p = \iint_s \alpha_{ip} \; dS_p \qquad (3.1.3)$$

This tensor may be defined equivalently as a measure of distortion within a domain, using the curl of the displacement gradient tensor

$$\underline{\underline{\boldsymbol{\alpha}}} \;=\; \left(\boldsymbol{\nabla} \times \underline{\underline{\boldsymbol{\beta}}}^{(d)}\right) \qquad\qquad \alpha_{ip} \;=\; \epsilon_{pkm} \; \partial_m \; \beta_{ik}^{(d)}$$

or as a measure of amount of dislocation within a system, using a count of the dislocation quantity within that domain

$$\underline{\underline{\boldsymbol{\alpha}}} \;=\; \rho \, \underline{\boldsymbol{b}} \otimes \underline{\boldsymbol{\xi}} \qquad\qquad \alpha_{ip} \;=\; \rho \, b_i \, \xi_p \qquad (3.1.4)$$

where ρ is the scalar dislocation density within a domain and b is the Burgers vector of a single dislocation.

The important finding from this arrangement is that the total Burgers vector across a surface is given by the integral of the density tensor at that surface

$$\underline{\boldsymbol{B}} = \iint_s \underline{\underline{\boldsymbol{\alpha}}} \cdot d\underline{\boldsymbol{S}} \qquad\qquad B_i = \iint_s \alpha_{ip} \; dS_p \qquad (3.1.5)$$

This relationship is the starting point for the continuum model used in this work.

3.1.2 Evolution of Burgers Vector through the Time Derivative

The aim of this section is to derive the transport equation for a continuous field of dislocations. The approach follows that proposed by Basoalto [112]. From eqn (3.1.5), the rate of change in the

Burgers vector is given by

$$\underline{\dot{B}} = \frac{d}{dt} \iint_s \underline{\underline{\alpha}} \cdot d\underline{S} \qquad\qquad \dot{B}_i = \frac{d}{dt} \iint_s \alpha_{ip} \, dS_p$$

and exchanging the integral and derivative operations gives the following

$$\underline{\dot{B}} = \iint_s \left\{ \underline{\underline{\alpha}} \cdot \underline{\dot{S}} + \underline{\underline{\dot{\alpha}}} \cdot d\underline{S} \right\} \qquad\qquad \dot{B}_i = \iint_s \left\{ \alpha_{ip} \, \dot{S}_p \ + \ \dot{\alpha}_{ip} dS_p \right\} \qquad (3.1.6)$$

To proceed the quantities $\underline{\dot{S}}$ and $\underline{\underline{\dot{\alpha}}}$ need to be determined.

Surface Element Evolution - $\underline{\dot{S}}$

With reference to Fig. 3.1.1, plastic deformation gradient is defined by

$$\underline{\underline{F}}^{(p)} = \frac{\partial \underline{x}}{\partial \underline{X}} \qquad\qquad F_{mp}^{(p)} = \frac{\partial x_m}{\partial X_p}$$

Using Nanson's formula [114] the change between the reference state $d\underline{S}^{(0)}$ and the intermediate state $d\underline{S}$ of an area element is given by

$$d\underline{S} = |\underline{\underline{F}}^{(p)}| \ \underline{\underline{F}}^{(p)-T} \cdot d\underline{S}^{(0)} \qquad\qquad dS_p = |\underline{\underline{F}}^{(p)}| \ F_{pm}^{(p)-T} \ dS_m^{(0)} \qquad (3.1.7)$$

it follows that the rate of change of an infinitesimal area element dS in the intermediate configuration is

$$\dot{S}_p = |\underline{\underline{\dot{F}}}^{(p)}| \ F_{pm}^{(p)-T} \ dS_m^{(0)} + |\underline{\underline{F}}^{(p)}| \ \dot{F}_{pm}^{(p)-T} \ dS_m^{(0)} \qquad (3.1.8)$$

The rate of change of the Jacobian $|\underline{\underline{\dot{F}}}^{(p)}|$ vanishes since the volume is conserved during dislocation slip.

By definition the deformation gradient tensor is orthogonal, i.e.,

$$\underline{\underline{F}}^{(p)} \cdot \underline{\underline{F}}^{(p)-1} \ = \ \underline{\underline{\mathbb{I}}} \qquad\qquad F_{im}^{(p)} \ F_{mj}^{(p)-1} \ = \ \delta_{ij} \qquad (3.1.9)$$

where $\underline{\underline{\mathbb{I}}}$ is the identity tensor. Taking the time derivative of this expression gives

$$\underline{\underline{\dot{F}}}^{(p)} \cdot \underline{\underline{F}}^{(p)-1} + \underline{\underline{F}}^{(p)} \cdot \underline{\underline{\dot{F}}}^{(p)-1} \ = \ 0 \qquad\qquad \dot{F}_{im}^{(p)} \ F_{mj}^{(p)-1} + F_{im}^{(p)} \ (\dot{F}_{mj}^{(p)-1}) = \ 0$$

Noting the definition of the plastic velocity gradient tensor as $L_{ij}^{(p)} = \dot{F}_{im}^{(p)} F_{mj}^{(p)-1}$ (see eqn (2.3.4)) the terms may be rearranged to give an expression for $\dot{\underline{\underline{F}}}^{(p)-T}$

$$\underline{\underline{L}}^{(p)} + \underline{\underline{F}}^{(p)} \cdot \dot{\underline{\underline{F}}}^{(p)-1} = 0 \qquad\qquad L_{ij}^{(p)} + F_{im}^{(p)} (\dot{F}_{mj}^{(p)-1}) = 0$$

$$\underline{\underline{F}}^{(p)-1} \cdot \underline{\underline{L}}^{(p)} + \underline{\underline{F}}^{(p)-1} \cdot \underline{\underline{F}}^{(p)} \cdot \dot{\underline{\underline{F}}}^{(p)-1} = 0 \qquad\qquad L_{ij}^{(p)} F_{qi}^{(p)-1} + F_{im}^{(p)} F_{qi}^{(p)-1} (\dot{F}_{mj}^{(p)-1}) = 0$$

$$\underline{\underline{F}}^{(p)-1} \cdot \underline{\underline{L}}^{(p)} + \mathbb{I} \cdot \dot{\underline{\underline{F}}}^{(p)-1} = 0 \qquad\qquad L_{ij}^{(p)} F_{qi}^{(p)-1} + \delta_{mq} (\dot{F}_{mj}^{(p)-1}) = 0$$

$$\underline{\underline{F}}^{(p)-1} \cdot \underline{\underline{L}}^{(p)} + \dot{\underline{\underline{F}}}^{(p)-1} = 0 \qquad\qquad L_{ij}^{(p)} F_{qi}^{(p)-1} + (\dot{F}_{qj}^{(p)-1}) = 0$$

$$\dot{\underline{\underline{F}}}^{(p)-1} = -\underline{\underline{F}}^{(p)-1} \cdot \underline{\underline{L}}^{(p)} \qquad\qquad (\dot{F}_{jq}^{(p)-T}) = -L_{ji}^{(p)T} F_{iq}^{(p)-T}$$

and the indices can be relabelled to fit with eqn (3.1.8), with n chosen as the arbitrary repeating index.

$$\dot{F}_{pm}^{(p)-T} = -L_{pn}^{(p)T} F_{nm}^{(p)-T} \tag{3.1.10}$$

Entering eqn (3.1.10) into (3.1.8) gives

$$\dot{\underline{S}} = -|\underline{\underline{F}}^{(p)}| \, d\underline{S}^{(0)} \cdot \underline{\underline{F}}^{(p)-1} \cdot \underline{\underline{L}}^{(p)} \qquad\qquad \dot{S}_p = -|\underline{\underline{F}}^{(p)}| \, L_{pn}^{(p)T} F_{nm}^{(p)-T} \, dS_m^{(0)} \tag{3.1.11}$$

This allows eqn (3.1.7) to be substituted in

$$\dot{\underline{S}} = -d\underline{S} \cdot \mathbb{I} \cdot \underline{\underline{L}}^{(p)} \qquad\qquad\qquad \dot{S}_p = - L_{pn}^{(p)T} \, dS_n$$

$$\dot{\underline{S}} = - d\underline{S} \cdot \underline{\underline{L}}^{(p)} = - \underline{\underline{L}}^{(p)T} \cdot d\underline{S} \qquad\qquad \dot{S}_p = - L_{pn}^{(p)T} \, dS_n \tag{3.1.12}$$

Rate of change of the Burgers vector

The definition of surface evolution determined in eqn (3.1.12) may now be reinserted into the Burgers rate integral eqn (3.1.6) to give

$$\dot{B}_i = \iint_s \{ - \alpha_{ip} \ L_{pn}^{(p)T} \ dS_n \ + \ \dot{\alpha}_{ip} \ dS_p \}$$

$$\dot{B}_i = \iint_s \dot{\alpha}_{ip} \ dS_p \ - \ \iint_s \alpha_{ip} \ L_{pn}^{(p)T} \ dS_n$$

The repeating indices of the right-hand term can now be relabelled to complement the left-hand integral

$$\dot{B}_i = \iint_s \dot{\alpha}_{ip} \ dS_p \ - \ \iint_s \alpha_{in} \ L_{np}^{(p)T} \ dS_p$$

$$\underline{\dot{\underline{B}}} = \iint_s \{ \underline{\dot{\underline{\alpha}}} \ - \ \underline{\underline{\alpha}} \cdot \underline{\underline{L}}^{(p)T} \} \cdot d\underline{S} \qquad \dot{B}_i = \iint_s \{ \dot{\alpha}_{ip} - \ \alpha_{in} \ L_{np}^{(p)T} \} \ dS_p \qquad (3.1.13)$$

This equation, now fully expanded, is the first of two definitions for the Burgers rate. It will act as one side of the equation for continuity of the system.

3.1.3   Deformation Kinematics of the Dislocation Field

An expression connecting plastic velocity gradient $\underline{\underline{L}}^{(p)}$ (defined in eqn (2.3.4)) and the dislocation density tensor will now be derived.

The plastic displacement of material points at $\underline{X}$ by a single dislocation of Burgers vector $\underline{b} = b \ \underline{s}^*$ may be given by

$$\delta \underline{u}^{(p)}(\underline{X}) \ = \ \frac{\delta q}{d} \ \underline{b} \ H(\underline{X} \cdot \underline{n}) \qquad\qquad \delta u_i^{(p)} \ = \ \frac{\delta q}{d} \ b_i \ H(X_k n_k) \qquad (3.1.14)$$

where δq refers to a small advancement of a dislocation line and d is the mean free path for slip. When the dislocation advances this path length then $\delta q = d$ and the material at $\underline{X}$ is displaced by a single Burgers vector

$$\delta \underline{u}^{(p)}(\underline{X}) \ = \ \underline{b} \ H(\underline{X} \cdot \underline{n}) \qquad\qquad \delta u_i^{(p)} \ = \ b_i \ H(X_k n_k)$$

where $H(\underline{X} \cdot \underline{n})$ is a Top Hat (boxcar) function describing the region above the slipped surface S, and $\underline{n}$ is the plane normal. The function is defined such that $H(\underline{X} \cdot \underline{n}) = 1$ for $\underline{X}$ between

$q \rightarrow q + \delta q$ and $\underline{\boldsymbol{X}} \cdot \underline{\boldsymbol{n}} \geq 0$, else $H(\underline{\boldsymbol{X}} \cdot \underline{\boldsymbol{n}}) = 0$.

The local plastic displacement gradient associated with such a displacement is therefore

$$\underline{\boldsymbol{\nabla}}\, \delta\underline{\boldsymbol{u}}^{(p)} \;=\; \underline{\boldsymbol{b}}\,\underline{\boldsymbol{n}}\,\delta(S - \underline{\boldsymbol{X}}) \qquad\qquad \partial_k u_i^{(p)} \;=\; b_i\,n_k\,\delta(S - X_k) \qquad (3.1.15)$$

where $\delta(.)$ is the Dirac delta function.

The volume average of the plastic part of the displacement gradient is then given by

$$\langle \underline{\boldsymbol{\nabla}}\, \delta\underline{\boldsymbol{u}}^{(p)} \rangle \;=\; \frac{1}{V(\Omega)} \iiint_\Omega \underline{\boldsymbol{b}}\,\underline{\boldsymbol{n}}\,\delta(S - \underline{\boldsymbol{X}})\,d^3X \qquad \langle \partial_k u_i^{(p)} \rangle \;=\; \frac{1}{V(\Omega)} \iiint_\Omega b_i\,n_k\,\delta(S - X_k)\,d^3X$$

$$(3.1.16)$$

where the volume average of the Dirac delta function picks out only the slipped surface

$$\iiint_\Omega \delta(S - \underline{\boldsymbol{X}})\,d^3X \;=\; \iint_S dS \qquad\qquad (3.1.17)$$

and the slipped area may in turn be described by the total length of the dislocation line $\mathcal{L}$ multiplied by the distance advanced δq

$$\iint_S dS \;=\; \oint_{\mathcal{L}} \delta q(p)\,\|\underline{\boldsymbol{t}}(p)\|\,dp \;=\; \delta q\,\mathcal{L} \qquad\qquad (3.1.18)$$

Applying eqns (3.1.17) and (3.1.18) sequentially to eqn (3.1.16) gives

$$\langle \underline{\boldsymbol{\nabla}}\, \delta\underline{\boldsymbol{u}}^{(p)} \rangle \;=\; \frac{\underline{\boldsymbol{b}}\,\underline{\boldsymbol{n}}}{V(\Omega)}\,\delta q\,\mathcal{L} \qquad\qquad \langle \partial_k u_i^{(p)} \rangle \;=\; \frac{b_i\,n_k}{V(\Omega)}\,\delta q\,\mathcal{L}$$

where the scalar dislocation density may be introduced as $\rho = \mathcal{L}/V(\Omega)$, the normal vector can be defined by the right handed set $\underline{\boldsymbol{n}} = \underline{\boldsymbol{\xi}} \times \underline{\boldsymbol{s}}^*$ and the definition of $\underline{\underline{\boldsymbol{\alpha}}}$ from eqn (3.1.4) has been used

$$\langle \underline{\boldsymbol{\nabla}}\, \delta\underline{\boldsymbol{u}}^{(p)} \rangle \;=\; \underline{\boldsymbol{b}}\,(\underline{\boldsymbol{\xi}} \times \underline{\boldsymbol{s}}^*)\,\rho\,\delta q \qquad\qquad \langle \partial_k u_i^{(p)} \rangle \;=\; b_i\,\epsilon_{kmn}\,\xi_m\,s_n^*\,\rho\,\delta q$$

$$= \underline{\underline{\boldsymbol{\alpha}}} \times \delta\underline{\boldsymbol{q}} \qquad\qquad\qquad\qquad = \epsilon_{kmn}\,\alpha_{im}\,\delta q_n$$

Finally, taking the rate of change of this quantity, a definition for the plastic velocity gradient is formed

$$\langle \underline{\boldsymbol{\nabla}}\, \dot{\underline{\boldsymbol{u}}}^{(p)} \rangle \;=\; \underline{\underline{\boldsymbol{L}}}^{(p)} \qquad\qquad \langle \partial_k u_i^{(p)} \rangle \;=\; L_{ik}^{(p)}$$

$$\therefore \qquad \underline{\underline{\boldsymbol{L}}}^{(p)} \;=\; \underline{\underline{\boldsymbol{\alpha}}} \times \dot{\underline{\boldsymbol{q}}} \qquad\qquad \therefore \qquad L_{ik}^{(p)} \;=\; \epsilon_{kmn}\,\alpha_{im}\,\dot{q}_n \qquad (3.1.19)$$

where $\dot{\underline{\boldsymbol{q}}}$ denotes the dislocation velocity, given by the rate of change of the coordinates of a point on the dislocation line.

3.1.4 The Dislocation Flux

Considering a group of dislocation lines crossing a contour element of length dl, the local rate of change of the Burgers vector $d\dot{\underline{B}}$ will be scaled by the density of dislocations crossing $(\dot{\underline{q}} \cdot \underline{m}) \, \rho \, dl$.

$$d\dot{\underline{B}} \;=\; \underline{b} \, (\dot{\underline{q}} \cdot \underline{m}) \, \rho \, dl \qquad\qquad d\dot{B}_i = b_i \, (\dot{q}_k m_k) \, \rho \, dl \qquad\qquad (3.1.20)$$

The contour is set such that the unit vector $\underline{m}$ is related to the dislocation tangent and contour tangent through a right-handed set (see Fig. 3.1.2)

$$\underline{m} = \underline{t} \times \underline{\xi} \qquad\qquad m_i = \epsilon_{inp} \, t_n \xi_p$$

And this identity may be applied to form

$$d\dot{\underline{B}} \;=\; \underline{b} \;\; \dot{\underline{q}} \cdot (\underline{t} \times \underline{\xi}) \, \rho \, dl \qquad\qquad d\dot{B}_i = b_i \, \dot{q}_k \, (\epsilon_{knp} \, t_n \, \xi_p) \, \rho \, dl$$

$$\;=\; \underline{b} \;\; \dot{\underline{q}} \cdot (\underline{dl} \times \underline{\xi}) \, \rho \qquad\qquad = b_i \, \dot{q}_k \, (\epsilon_{knp} \, dl_n \, \xi_p) \, \rho$$

Here a cyclic permutation can reorder the triple product so that it matches with the form of the dislocation density tensor definition in eqn. (3.1.4).

$$d\dot{\underline{B}} \;=\; \rho \, \underline{b} \;\; \underline{\xi} \cdot (\dot{\underline{q}} \times \underline{dl}) \qquad\qquad d\dot{B}_i = b_i \, \epsilon_{pkn} \, \dot{q}_k \, dl_n \, \xi_p \, \rho$$

$$\;=\; \rho \, \underline{b} \;\; (\underline{\xi} \times \dot{\underline{q}}) \cdot \underline{dl} \qquad\qquad = b_i \, \epsilon_{npk} \, \xi_p \, \dot{q}_k \, dl_n \; \rho \qquad (3.1.21)$$

$$\;=\; (\underline{\underline{\alpha}} \times \dot{\underline{q}}) \cdot \underline{dl} \qquad\qquad = \epsilon_{npk} \, \alpha_{ip} \, \dot{q}_k \, dl_n$$

The total Burger vector flux across the contour C is therefore

$$\dot{\underline{B}} = \int_c (\underline{\underline{\alpha}} \times \dot{\underline{q}}) \cdot \underline{dl} \qquad\qquad \dot{B}_i = \int_c \epsilon_{npk} \, \alpha_{ip} \, \dot{q}_k \, dl_n$$

where the definition for $\underline{\underline{L}}^{(p)}$ in eqn (3.1.19) may be inserted

$$\dot{\underline{B}} = \int_c \underline{\underline{L}}^{(p)} \cdot \underline{dl} \qquad\qquad \dot{B}_i = \int_c L_{in}^{(p)} \, dl_n \qquad\qquad (3.1.22)$$

Stoke's theorem may be applied again on the contour integral of the flux, to convert this to a surface integral.

$$\dot{\underline{B}} = \iint_s (\underline{\nabla} \times \underline{\underline{L}}^{(p)}) \cdot d\underline{S} \qquad\qquad \dot{B}_i = \iint_s \epsilon_{lnm} \, \partial_m \, L_{in}^{(p)} \, dS_l \qquad (3.1.23)$$

As before, this surface is a hypothetical membrane pierced by dislocation tangent lines as they traverse the crystal. This equation is the second definition for the Burgers vector evolution and so acts as the second side of the continuity equation.

3.1.5 Transport Equation of the Dislocation Field

From eqns (3.1.13) and (3.1.23), the following holds

$$\iint_s \left\{ \dot{\alpha}_{ip} - \alpha_{in} \, L_{np}^{(p)T} \right\} \, dS_p = \iint_s \epsilon_{lnm} \, \partial_m \, L_{in}^{(p)} \, dS_l$$

As the domains of integration are identical then the contents of the integral must be equal

$$\dot{\alpha}_{ip} - \alpha_{in} \, L_{np}^{(p)T} = \epsilon_{pnm} \, \partial_m \, L_{in}^{(p)} \tag{3.1.24}$$

This is the transport equation of the dislocation density tensor within a system. If all transport terms are moved to the left side then any source or sink terms for dislocation density may be added or subtracted to the right hand side to balance the equation

$$\underline{\dot{\underline{\alpha}}} - \underline{\underline{\alpha}} \cdot \underline{\underline{L}}^{(p)T} - \underline{\nabla} \times \underline{\underline{L}}^{(p)} = \underline{\dot{\underline{G}}}^{+} - \underline{\underline{A}}^{-}$$

$$\dot{\alpha}_{ip} - \alpha_{in} \, L_{np}^{(p)T} - \epsilon_{pnm} \, \partial_m \, L_{in}^{(p)} = G_{ip}^{+} - A_{ip}^{-} \tag{3.1.25}$$

in this instance $\underline{\dot{\underline{G}}}^{+}$ and $\underline{\underline{A}}^{-}$ are tensors describing the generation and annihilation of dislocations.

3.2 Elastic interactions from the Dislocation field

Elastic distortions $\underline{\underline{\beta}}^{(d)}$ created by the presence of a dislocation field will give rise to an associated stress field $\underline{\underline{\pi}}^{(d)}$ through the stiffness relationship

$$\underline{\underline{\pi}}^{(d)} = \underline{\underline{C}} : \underline{\underline{\beta}}^{(d)} \tag{3.2.1}$$

where $\underline{\underline{C}}$ is the fourth rank stiffness tensor of the material.

It is desirable then that a direct relation between the dislocation density tensor and the dislocation stress be determined. This can be achieved using Mura's (1963) formula [69] for elastic distortion at position $\underline{X}$ arising from the contributions of points $\underline{X}'$ along dislocation line L, this is often represented in literature as:

$$\beta_{ji}(\underline{X})[\underline{e}_i \, \underline{e}_j] = \oint_L \epsilon_{jnk} \, C_{pqmn} \, G_{ip,q}(\underline{X} - \underline{X}') \, b_m \, t_k \, dl(\underline{X}')[\underline{e}_i \, \underline{e}_j] \tag{3.2.2}$$

44

where $\underline{\underline{G}}$ is a Green's function for isotropic elasticity. The notation $G_{ip,q}$ refers to the gradient of the Green's function, taken such that $\boldsymbol{\nabla}\,\underline{\underline{G}} \equiv G_{ip,q}\,[\underline{e}_i \otimes \underline{e}_p] \otimes [\underline{e}_q]$. Making use of the dot-cross operator $\dot{\times}$; defined such that $(\underline{a}\,\underline{b})\dot{\times}(\underline{c}\,\underline{d}) = (\underline{a}\cdot\underline{c})(\underline{b}\times\underline{d})$; it is possible to write eqn (3.2.2) in vector notation:

$$\underline{\underline{\beta}}(\underline{X}) = \oint_L \boldsymbol{\nabla}\,\underline{\underline{G}}(\underline{X}-\underline{X}')\;:\;\underline{\underline{\underline{C}}}\;\dot{\times}\;(\underline{b}\,\underline{t})\;dl(\underline{X}')$$

The full form of $\underline{\underline{G}}$ is given by

$$\underline{\underline{G}}(\underline{X}-\underline{X}') \;=\; \frac{1}{8\pi\mu}\Big[\underline{\underline{\mathbb{I}}}\,\nabla^2 R \;-\; \frac{1}{2(1-\nu)}\,\boldsymbol{\nabla}\,\boldsymbol{\nabla}R\Big] \tag{3.2.3}$$

where μ is the shear modulus, $\underline{\underline{\mathbb{I}}}$ is identity, ν is Poisson's ratio and $R = \|\,\underline{X}-\underline{X}'\,\|$. The points $\underline{X}$ and $\underline{X}'$ exist within the domain Ω.

In order to homogenise the Mura formula it is beneficial to consider a dislocation distribution within a small volume element $\omega \subset \Omega$ centred at $\underline{X}$, with volume $\delta V_\omega(\underline{X})$. This volume surrounds a dislocation segment of length δl. A dislocation distribution function $\underline{D}(\underline{X})$ may be introduced across Ω such that the dislocation content at point $\underline{X}$ is described by

$$\underline{D}(\underline{X}) = \underline{b}\,\delta(\underline{X}-\underline{X}')$$

if a single dislocation is present. The Dirac delta function equals 1 whenever the point $\underline{X}$ falls on a dislocation line, and 0 otherwise. For a number of parallel dislocations (with the same Burgers vector) at the same point, the distribution function becomes a sum across these dislocations

$$\underline{D}(\underline{X}) = \sum_{k=1}^{N}\underline{b}\,\delta(\underline{X}-\underline{X}'^{\,k}) \tag{3.2.4}$$

where N is the number of dislocations and k is the index for the different dislocation lines.

The volume average of the distribution function over small element ω becomes

$$\langle\underline{D}(\underline{X})\rangle_\omega = \frac{\underline{b}}{\delta V_\omega(\underline{X})}\sum_{k=1}^{N}\iiint_\omega \delta(\underline{X}-\underline{X}'^{\,k})\,d^3\underline{X} \tag{3.2.5}$$

For straight parallel dislocation segments on the same slip plane the coordinates along a dislocation segment will vary in only one dimension, collapsing the volume integral into a line integral along the segment length δl, i.e:

$$\iiint_\omega \delta(\underline{\boldsymbol{X}} - \underline{\boldsymbol{X}}'^{\,k}) \, dX_1 \, dX_2 \, dX_3 \;=\; \int_{\delta l} \delta(\underline{\boldsymbol{X}} - \underline{\boldsymbol{X}}'^{\,k}) \, dX_3 \;=\; \delta l \qquad (3.2.6)$$

Using this equivalence eqn (3.2.5) becomes

$$\langle \underline{\boldsymbol{D}}(\underline{\boldsymbol{X}}) \rangle_\omega = \frac{\underline{\boldsymbol{b}} \, N(\underline{\boldsymbol{X}}) \, \delta l}{\delta V_\omega(\underline{\boldsymbol{X}})} \;=\; \underline{\boldsymbol{b}} \, \rho(\underline{\boldsymbol{X}}) \qquad (3.2.7)$$

where the scalar dislocation density $\rho(\underline{\boldsymbol{X}})$ is introduced as the total length of dislocation contained in element ω.

If Mura's formula is now considered for a number of identical dislocations N, following line L

$$\underline{\underline{\boldsymbol{\beta}}}(\underline{\boldsymbol{X}}) = \oint_L \underline{\boldsymbol{\nabla}} \, \underline{\underline{\boldsymbol{G}}}(\underline{\boldsymbol{X}} - \underline{\boldsymbol{X}}') \; : \; \underline{\underline{\underline{\boldsymbol{C}}}} \overset{.}{\times} (N \underline{\boldsymbol{b}} \, \underline{\boldsymbol{t}}) \, dl(\underline{\boldsymbol{X}}')$$

then the distortion at $\underline{\boldsymbol{X}}$ contributed by a line segment at point $\underline{\boldsymbol{X}}'$ is

$$\delta \underline{\underline{\boldsymbol{\beta}}}(\underline{\boldsymbol{X}} - \underline{\boldsymbol{X}}') = \underline{\boldsymbol{\nabla}} \, \underline{\underline{\boldsymbol{G}}}(\underline{\boldsymbol{X}} - \underline{\boldsymbol{X}}') \; : \; \underline{\underline{\underline{\boldsymbol{C}}}} \overset{.}{\times} (N(\underline{\boldsymbol{X}}') \, \underline{\boldsymbol{b}} \, \underline{\boldsymbol{t}}(\underline{\boldsymbol{X}}')) \, \delta l(\underline{\boldsymbol{X}}') \qquad (3.2.8)$$

Using the definition in eqn (3.2.7) the distribution function may now be introduced, allowing the distortion from volume element ω to be calculated

$$\delta \underline{\underline{\boldsymbol{\beta}}}(\underline{\boldsymbol{X}} - \underline{\boldsymbol{X}}') = \underline{\boldsymbol{\nabla}} \, \underline{\underline{\boldsymbol{G}}}(\underline{\boldsymbol{X}} - \underline{\boldsymbol{X}}') \; : \; \underline{\underline{\underline{\boldsymbol{C}}}} \overset{.}{\times} (\langle \underline{\boldsymbol{D}}(\underline{\boldsymbol{X}}') \rangle_\omega \, \underline{\boldsymbol{t}}(\underline{\boldsymbol{X}}')) \, \delta V_\omega(\underline{\boldsymbol{X}}')$$

and the expression for dislocation density to be introduced

$$\delta \underline{\underline{\boldsymbol{\beta}}}(\underline{\boldsymbol{X}} - \underline{\boldsymbol{X}}') = \underline{\boldsymbol{\nabla}} \, \underline{\underline{\boldsymbol{G}}}(\underline{\boldsymbol{X}} - \underline{\boldsymbol{X}}') \; : \; \underline{\underline{\underline{\boldsymbol{C}}}} \overset{.}{\times} \underline{\underline{\boldsymbol{\alpha}}}(\underline{\boldsymbol{X}}') \, \delta V_\omega(\underline{\boldsymbol{X}}') \qquad (3.2.9)$$

$$\underline{\underline{\boldsymbol{\alpha}}}(\underline{\boldsymbol{X}}') \;=\; \langle \underline{\boldsymbol{D}}(\underline{\boldsymbol{X}}) \rangle_\omega \, \underline{\boldsymbol{t}}(\underline{\boldsymbol{X}}') \qquad (3.2.10)$$

The total dislocation stress at $\underline{\boldsymbol{X}}$ relates to the sum of the distortions from all other points in the Ω domain, indexed as $\underline{\boldsymbol{X}}'^{\,m}$

$$\underline{\underline{\boldsymbol{\pi}}}^{(d)}(\underline{\boldsymbol{X}}) = \underline{\underline{\underline{\boldsymbol{C}}}} : \sum_{m \in \Omega} \delta \underline{\underline{\boldsymbol{\beta}}}(\underline{\boldsymbol{X}} - \underline{\boldsymbol{X}}'^{\,m})$$

$$\underline{\underline{\boldsymbol{\pi}}}^{(d)}(\underline{\boldsymbol{X}}) = \sum_{m \in \Omega} \underline{\underline{\underline{\boldsymbol{C}}}} : \underline{\boldsymbol{\nabla}} \, \underline{\underline{\boldsymbol{G}}}(\underline{\boldsymbol{X}} - \underline{\boldsymbol{X}}'^{\,m})) : \underline{\underline{\underline{\boldsymbol{C}}}} \overset{.}{\times} \underline{\underline{\boldsymbol{\alpha}}}(\underline{\boldsymbol{X}}'^{\,m})) \, \delta V_\omega(\underline{\boldsymbol{X}}'^{\,m})) \qquad (3.2.11)$$

46

If all volumes δV_ω are the same, then taking the limit $\delta V_\omega \to 0$ forms the integral

$$\underline{\underline{\boldsymbol{\pi}}}^{(d)}(\underline{\boldsymbol{X}}) = \iiint_\Omega \underline{\underline{\boldsymbol{C}}} : \boldsymbol{\nabla}\,\underline{\underline{\boldsymbol{G}}}(\underline{\boldsymbol{X}} - \underline{\boldsymbol{X}}') : \underline{\underline{\boldsymbol{C}}} \, \dot{\times} \, \underline{\underline{\boldsymbol{\alpha}}}(\underline{\boldsymbol{X}}'))\ dV$$

$$\underline{\underline{\boldsymbol{j}}}(\underline{\boldsymbol{X}} - \underline{\boldsymbol{X}}') \; = \; \underline{\underline{\boldsymbol{C}}} : \boldsymbol{\nabla}\,\underline{\underline{\boldsymbol{G}}}(\underline{\boldsymbol{X}} - \underline{\boldsymbol{X}}') : \underline{\underline{\boldsymbol{C}}} \tag{3.2.12}$$

where the third rank tensor $\underline{\underline{\boldsymbol{j}}}(\underline{\boldsymbol{X}} - \underline{\boldsymbol{X}}')$ is introduced to collect material specific terms.

The dislocation stress field may now be directly defined at any point in a domain by a function of the dislocation density at all other points

$$\underline{\underline{\boldsymbol{\pi}}}^{(d)}(\underline{\boldsymbol{X}}) = \iiint_\Omega \underline{\underline{\boldsymbol{j}}}(\underline{\boldsymbol{X}} - \underline{\boldsymbol{X}}') \, \dot{\times} \, \underline{\underline{\boldsymbol{\alpha}}}(\underline{\boldsymbol{X}}'))\ dV \tag{3.2.13}$$

Chapter 4

Field Dislocation Mechanics II: Application to Nickel-based Superalloys

This chapter will apply the general FDM formulation to the specific case of a nickel-based super-alloy material deforming under plane strain conditions. Plane strain simplifications for the SSD density $\underline{\underline{\alpha}}$, dislocation velocity and stress fields, and interaction with appropriate microstructural features will all be considered. Finally the integration within a crystal plasticity formulation is described.

Note: The contributions from geometrically necessary dislocations (GNDs) are omitted from this work, but will provide grounds for future extension of this model. It is assumed that for the single crystal, single-slip arrangement in this work the GND effect would be minimal as the deformation gradients on a slip plane are not severe. This assumption is later discussed in Section 9.3.

4.1 Adapting the Transport Equation to Plane Strain

This section will see the FDM transport equation simplified to 2D plane strain conditions. The plane of interest is the X_1 - X_2 plane. The out-of-plane strain components are all removed apart from ε_{33}, which is also small enough to be negligible.

It has been stated earlier in eqn (3.1.4) that the dislocation density tensor can be defined as

$$\underline{\underline{\alpha}} = \rho\, \underline{b} \otimes \underline{\xi} \qquad\qquad \alpha_{ip} = \rho\, b_i\, \xi_p$$

in the general case. However if only edge type dislocations are considered with tangent vector parallel to the X_3 axis then the equations can be reduced to a 2D form. All Burgers vectors are set parallel to the X_1 axis, meaning the system contains density that evolves along a single slip plane (aligned to this axis). This gives the dislocation density the parameters:

$$\underline{b} = [b\ 0\ 0]$$

$$\underline{\xi} = [0\ 0\ 1]$$

$$\underline{\underline{\alpha}} = \rho \begin{bmatrix} 0 & 0 & b \\ 0 & 0 & 0 \\ 0 & 0 & 0 \end{bmatrix} \qquad\qquad \alpha_{13} = \rho\, b \qquad\qquad (4.1.1)$$

Here it can be seen that the $\underline{\underline{\alpha}}$ tensor is reduced to a single component α_{13}. As the Burgers magnitude will be constant upon a single slip system then the dislocation density is now described by a scalar field $\rho(\underline{X})$. A graphical representation of the dislocation alignment is shown in Fig. (4.1.1), with the slip velocity vector $\dot{q}_1$ indicated.
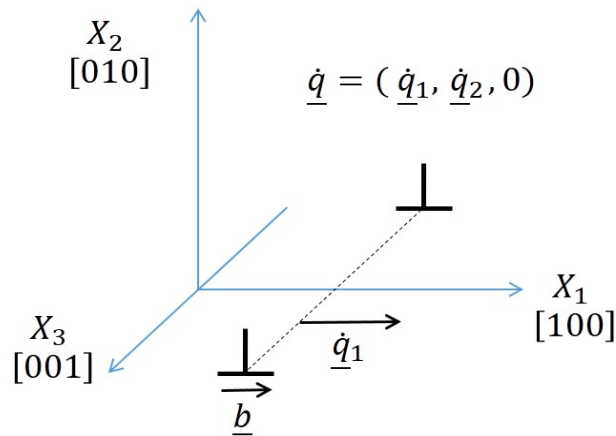
Figure 4.1.1: Geometry of a single straight edge dislocation within the model.

If the density tensor in the general form eqn (3.1.24) is replaced with α_{13} then a scalar continuity equation can be developed

$$\frac{\partial \alpha_{13}}{\partial t} \ - \ \alpha_{13} \ L_{33}^{(p)} \ - \ \epsilon_{3nm} \ \partial_m \ L_{1n}^{(p)} \ = \ 0$$

As there is no velocity in the X_3 direction within the plane strain setup then $L_{33}^{(p)} = 0$

$$\frac{\partial \alpha_{13}}{\partial t} \ - \ \epsilon_{3nm} \ \partial_m \ L_{1n}^{(p)} \ = \ 0 \tag{4.1.2}$$

It now remains to evaluate the flux tensor in plane strain. This involves first calculating the value of the curl of the dislocation flux in general space, then reducing to the scalar setup.

Expanding the Dislocation Flux Term

Expanding the dislocation flux term fully using the definition $L_{ik}^{(p)} \ = \ \epsilon_{kmn} \ \alpha_{im} \ \dot{q}_n$ from eqn (3.1.19) gives the following components:

$$L_{11}^{(p)} \ = \ \alpha_{12} \ \dot{q}_3 \ - \ \alpha_{13} \ \dot{q}_2$$
$$L_{12}^{(p)} \ = \ \alpha_{13} \ \dot{q}_1 \ - \ \alpha_{11} \ \dot{q}_3$$
$$L_{13}^{(p)} \ = \ \alpha_{11} \ \dot{q}_2 \ - \ \alpha_{12} \ \dot{q}_1$$
$$L_{21}^{(p)} \ = \ \alpha_{22} \ \dot{q}_3 \ - \ \alpha_{23} \ \dot{q}_2$$
$$L_{22}^{(p)} \ = \ \alpha_{23} \ \dot{q}_1 \ - \ \alpha_{21} \ \dot{q}_3$$
$$L_{23}^{(p)} \ = \ \alpha_{21} \ \dot{q}_2 \ - \ \alpha_{22} \ \dot{q}_1$$
$$L_{31}^{(p)} \ = \ \alpha_{32} \ \dot{q}_3 \ - \ \alpha_{33} \ \dot{q}_2$$
$$L_{32}^{(p)} \ = \ \alpha_{33} \ \dot{q}_1 \ - \ \alpha_{31} \ \dot{q}_3$$
$$L_{33}^{(p)} \ = \ \alpha_{31} \ \dot{q}_2 \ - \ \alpha_{32} \ \dot{q}_1$$

Meaning that for the plane strain setup in eqn (4.1.1), where $\dot{q}_3 = 0$, only two terms survive

$$L_{11}^{(p)} \ = \ - \ \alpha_{13} \ \dot{q}_2$$
$$L_{12}^{(p)} \ = \ \ \ \alpha_{13} \ \dot{q}_1$$

Expanding the curl of the flux tensor using placeholder tensor $A_{ip} = \epsilon_{pnm}\,\partial_m\,L_{in}^{(p)}$ gives the following components:

$$A_{11} = \partial_3\,L_{12}^{(p)} - \partial_2\,L_{13}^{(p)}$$

$$A_{12} = \partial_1\,L_{13}^{(p)} - \partial_3\,L_{11}^{(p)}$$

$$A_{13} = \partial_2\,L_{11}^{(p)} - \partial_1\,L_{12}^{(p)}$$

$$A_{21} = \partial_3\,L_{22}^{(p)} - \partial_2\,L_{23}^{(p)}$$

$$A_{22} = \partial_1\,L_{23}^{(p)} - \partial_3\,L_{21}^{(p)}$$

$$A_{23} = \partial_2\,L_{21}^{(p)} - \partial_1\,L_{22}^{(p)}$$

$$A_{31} = \partial_3\,L_{32}^{(p)} - \partial_2\,L_{33}^{(p)}$$

$$A_{32} = \partial_1\,L_{33}^{(p)} - \partial_3\,L_{31}^{(p)}$$

$$A_{33} = \partial_2\,L_{31}^{(p)} - \partial_1\,L_{32}^{(p)}$$

As only $L_{11}^{(p)}$ and $L_{12}^{(p)}$ exist, and because the spatial differential in the third direction has no value (i.e $\partial_3 = 0$), this leaves only

$$A_{13} = \partial_2\,L_{11}^{(p)} - \partial_1\,L_{12}^{(p)}$$

$$\epsilon_{3nm}\,\partial_m\,L_{1n}^{(p)} = A_{13} = -\,\partial_1\,(\alpha_{13}\,\dot{q}_1) - \partial_2\,(\alpha_{13}\,\dot{q}_2) \qquad (4.1.3)$$

The Plane Strain Scalar Continuity Equation

Now the expanded flux term in eqn (4.1.3) can be inserted into eqn (4.1.2)

$$\frac{\partial\alpha_{13}}{\partial t} + \partial_1\,(\alpha_{13}\,\dot{q}_1) + \partial_2\,(\alpha_{13}\,\dot{q}_2) = 0$$

substituting for the scalar density introduces the Burgers magnitude to every term. As this is a constant for a single dislocation variety then it has no effect on the continuity.

$$b\,\frac{\partial\rho}{\partial t} + b\,\partial_1\,(\rho\,\dot{q}_1) + b\,\partial_2\,(\rho\,\dot{q}_2) = 0$$

$$\frac{\partial\rho}{\partial t} + \partial_1\,(\rho\,\dot{q}_1) + \partial_2\,(\rho\,\dot{q}_2) = 0$$

Using the chain rule and collecting terms now gives a more concise form:

$$\frac{\partial\rho}{\partial t} + \underline{\boldsymbol{\nabla}}\cdot(\underline{\dot{q}}\,\rho) = 0 \qquad\qquad \frac{\partial\rho}{\partial t} + \partial_k\,(\dot{q}_k\,\rho) = 0 \qquad (4.1.4)$$

This equation now describes the transport of a field of parallel dislocations within a 2D plastic state. It requires only the input of the dislocation velocity field within the domain and the boundary conditions associated with the environment in order to function as a model for dislocation behaviour.

4.2   Dislocation Velocity Contributions

4.2.1   Separation into principle directions

The 2D system and reference frame outlined in the previous section allows the dislocation velocity term $\underline{\dot{q}}$ to be split into the perpendicular components of glide $\underline{v}_g$ and climb $\underline{v}_g$ which are aligned with the principle axes of the coordinate system, $\underline{e}_1$ and $\underline{e}_2$. By expanding the divergence term within eqn (4.1.4) the scalar value of the glide and climb velocity can then be associated with the differential in each direction.

$$\underline{\dot{q}} \ = \ \underline{v}_g \ + \ \underline{v}_c \ = \ v_g \ \underline{e}_1 \ + \ v_c \ \underline{e}_2$$

$$\frac{\partial \rho}{\partial t} \ + \ \frac{\partial(\rho v_g)}{\partial x_1} \ + \ \frac{\partial(\rho v_c)}{\partial x_2} \ = \ 0 \tag{4.2.1}$$

Similarly the motive force upon the dislocation $\underline{\boldsymbol{f}}^{mot}$ can be split into components f_1^{mot} and f_2^{mot}, resolved in the principle directions. The term *motive force* is used to discern the force that is driving dislocation movement after factors such as line-tension drag and internal stress fields are accounted for. f_1^{mot} arises from shear stresses upon the slip plane, while f_2^{mot} is normal to the plane. The full derivation of these forces within the current work is provided in Section (4.3.2), but it is sufficient here to assume this as the resultant force upon the dislocation.

4.2.2   Glide Velocity

The dislocation glide velocity can be calculated assuming one of two mobility conditions: either a lattice phonon drag based mobility or a jog-controlled mobility. Both velocities are functions of f_1^{mot}, but each applies within a different shear stress regime. The largest drag contribution will supersede the smaller, meaning that the lowest calculated velocity should be used within the continuity equation.

The lattice vibration/phonon drag coefficient B can be approximated through molecular dynamics simulations or inferred from experimental observations of in-situ deformation, with varying degrees of agreement in the literature [50][53][115][116][117]. This drag coefficient is also expressed as a mobility factor M which linearly relates the force on the dislocation to a free-glide velocity v_g^{phonon} following:

$$v_g^{phonon} = M \, f_1^{mot} \quad , \quad M = \frac{1}{B} \qquad (4.2.2)$$

Molecular dynamics simulations by Dongsheng Li et al [115] have produced values of $M \approx 2800 \text{Pa}^{-1}\text{s}^{-1}$ ($B = 3.57\text{x}10^{-4}\text{Pa s}$) at room temperature, for a Fe-Ni alloy with 20% nickel composition. The trend for this alloy system assumed a reduction in mobility as temperature or % nickel composition increased. Urabe and Weertman [116] undertook experiments on similar FCC single crystal iron samples in the mid 1970s, where rapid stress pulses were used to spur dislocation movement and the distances travelled during the pulse duration were converted into mobility measurements. At room temperature a value of $M = 2940 \text{Pa}^{-1}\text{s}^{-1}$ ($B = 3.4\text{x}10^{-4}\text{Pa s}$) was determined.

Another method for predicting the phonon drag is derived from the Debye frequency of the lattice. The Debye frequency of a crystal is given by [118]

$$\nu_{Debye} = \nu_{sound} \left(\frac{3}{4\pi\Omega_{atom}} \right)^{\frac{1}{3}} \qquad (4.2.3)$$

where ν_{Debye} is the Debye frequency of the lattice, v_{sound} is the speed of sound in the material and Ω_{atom} is the atomic volume. The drag coefficient B is then calculated by [119]

$$B = \frac{k_B T}{\Omega_{atom}\nu_{Debye}} \qquad (4.2.4)$$

where k_B is the Boltzman constant and T is the material temperature. This equation calculates a mobility of $M = 5076 \text{Pa}^{-1}\text{s}^{-1}$ ($B = 1.97\times10^{-4} \text{ Pa s}$) at 973K for a CMSX-6 type superalloy, using the material parameters from Section 5.5. This value is almost double the simulated/measured values quoted above, however the predicted dislocations velocities for each value fall within the expected orders of magnitude found within literature [25]. For an applied stress of 200MPa the molecular dynamics value would give dislocation velocity of 142.2 ms^{-1}, the experimentally observed value would give dislocation velocity of 149.4 ms^{-1} and the calculated value would give dislocation velocity of 258.1 ms^{-1}.

Noted CDD modeller Thomas Hochrainer has discussed dislocation mobility in a recent paper [120], he writes frankly "*Another open problem is the form of the mobility function which remains on the level of an educated guess so far.*". The author goes on to suggest that a dimensionless prefactor with a narrow range could be used to adjust the dislocation mobility as required to yield smooth transition to plastic flow around the yield stress.

The jog-controlled velocity is derived from the diffusion of jogs through the lattice. Jogs on a dislocation gliding on the $\langle \bar{1}10 \rangle \{111\}$ system will not have a burgers vector parallel with the slip direction and therefore will not easily undergo slip. Vacancy diffusion is required to move these jogs. Smaller jog spacing means there will be a greater number of jogs per unit length and more vacancy diffusion is required to move a given length of dislocation line, thus a lower line velocity v_g^{jog} is calculated. The relationship has an exponential form [44][121]

$$v_g^{jog} \;=\; \frac{4\pi D_s}{h_{jog}} \; exp\Big(\frac{f_1^{mot} \, b\lambda_{jog}}{k_B T} - 1\Big) \tag{4.2.5}$$

where D_s is the diffusion coefficient, b is the magnitude of the burgers vector, λ_{jog} is the jog spacing and h_{jog} is the mean jog height (taken here as the close-packed inter-plane spacing for FCC $h_{jog} = \frac{\sqrt{2}}{\sqrt{3}}b$). The diffusion coefficient may be determined for a given temperature using an Arrenhius relationship:

$$D_s \;=\; D_{s,0} \; exp\Big(\frac{-Q}{RT}\Big) \tag{4.2.6}$$

where $D_{s,0}$ is the maximal diffusion coefficient at infinite temperature, Q is the activation energy and R is the molar gas constant.

Having calculated both potential velocities at any given instant, a Heaviside function is used to determine the value which shall be used within the continuity equation:

$$v_g = \begin{cases} v_g^{jog} & , \quad \text{if } \; v_g^{jog} \leq v_g^{phonon} \\ v_g^{phonon} & , \quad \text{if } \; v_g^{jog} > v_g^{phonon} \end{cases}$$

In practice this means that for low shear stresses the jog-controlled term initially dominates, causing very low v_g^{jog} velocities in the flat region before the exponential function curves. As the stress

increases the exponential function approaches an asymptote and the velocities rapidly increase, surpassing the v_g^{phonon} velocities calculated for the internal lattice drag method. From this point onwards the lattice drag is preferred as the dominant drag system. Fig. 4.2.1 provides the calculated velocities vs shear stress for a nickel-based superslloy with a range of jog-spacings at 700^oC, the latter Fig. 4.2.2 shows the same data with a different scale (materials parameters for the alloy can be found in Section (5.5.2)). Fig. 4.2.3 shows an example of the resultant velocity profile chosen within single phase $\lambda_{jog} = 300b$ simulations. A similar velocity profile has been presented by Gurrutxaga-Lerma et al [122] in a comprehensive discussion of dislocation mobility regimes.
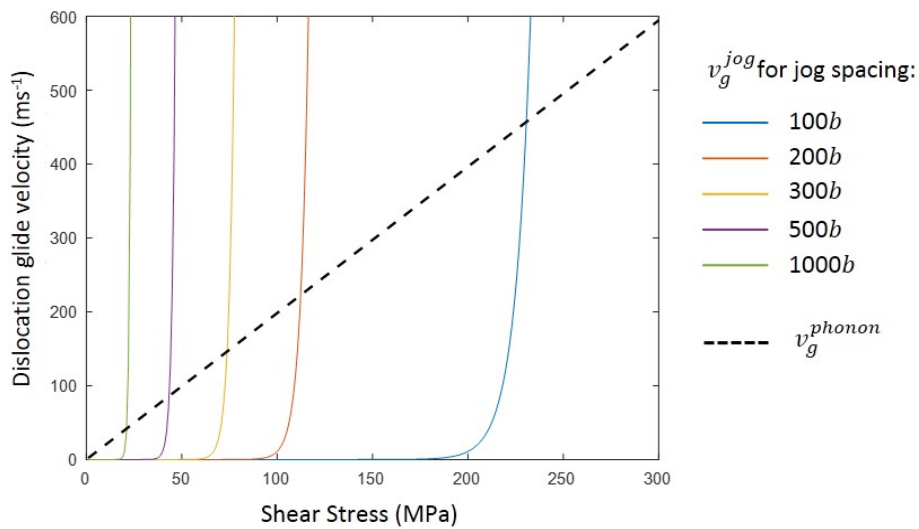
Figure 4.2.1: Plot showing Shear Stress vs Velocity of Dislocations at 700^oC. Coloured lines indicate the jog-controlled velocities for different jog spacings while the dotted line is the phonon-drag controlled velocity.
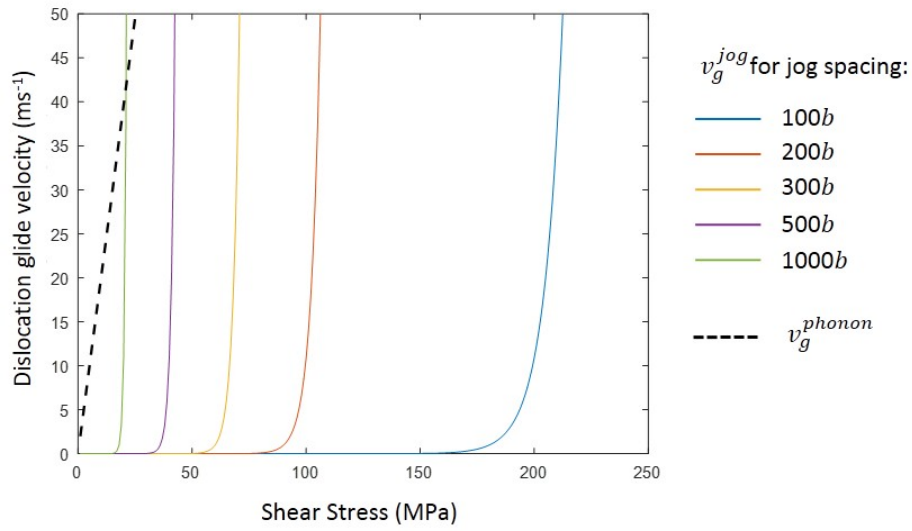
Figure 4.2.2: Plot showing Shear Stress vs Velocity of Dislocations at 700^oC. Coloured lines indicate the jog-controlled velocities for different jog spacings while the dotted line is the phonon-drag controlled velocity.
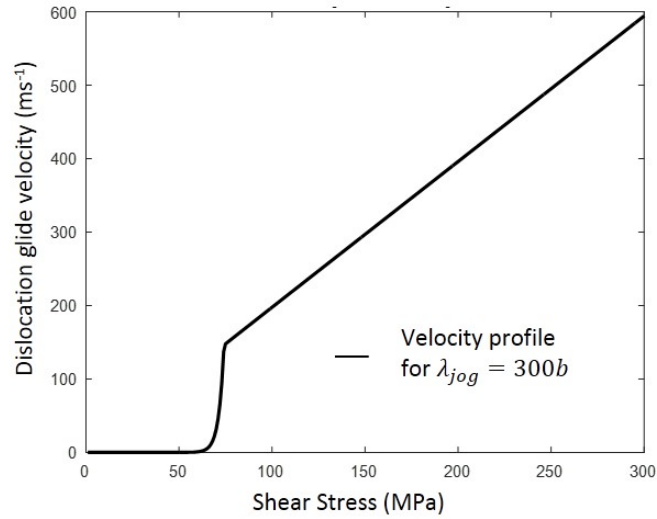

Figure 4.2.3: Plot showing glide velocity profile used within single-phase simulations with $\lambda_{jog} = 300b$.

4.2.3 Climb Velocity

The mechanism for dislocation climb is vacancy driven, requiring an unoccupied lattice site to migrate towards the bottom of the extra atomic plane that makes-up an edge dislocation. This effectively causes the half-plane to move 'upward' one atomic spacing perpendicular to the glide direction.

The physical mechanism has been defined in terms of the concentration gradients of vacancies moving from the bulk material and towards dislocation cores. In this way the crystal attempts to minimise the Gibbs free energy, giving the basis for the diffusion driven climb velocity term within the model [25]

$$v_c \; = \; \frac{4\pi}{b} \; D_v \; \left[exp\Big(\frac{f_2^{mot} \; \Omega_{atom}}{b \; k_B \; T}\Big) \; - \; 1 \right] \tag{4.2.7}$$

where D_v is the vacancy diffusivity of the material and Ω_{atom} the vacancy/atomic volume. The vacancy diffusivity can be found through the Arrhenius relationship with the self-diffusivity constant $D_{s,0}$.

$$D_v \; = \; D_{s,0} \; exp\Big(- \frac{Q}{k_B T}\Big) \tag{4.2.8}$$

where Q is the activation energy for diffusion ($\sim 310 \; kJ$).

Though the climb velocity has strong temperature dependency, it will generally be orders of magnitude lower than the glide velocity.

4.3 Calculation of the 2D Stress Field

Within this model the stress at an element of the FDM domain has two contributing terms. The first contribution is that which a Finite Element (FE) solver calculates from the deformation gradients using the CP formulation (i.e the deformation kinematics from the applied boundary conditions and moving dislocation field). The second accounts for dislocation interactions required to correctly evaluate the transport equation, this contribution must be handled explicitly (via the internal dislocation stress fields) and is not part of traditional CP. This stress formulation is typical in literature concerning both discrete and continuous dislocation modelling [94][123][124][125]. The terms add linearly as they are both expressed in the same plane strain reference frame.

The local stress required to solve the FE boundary value problem $\underline{\underline{\pi}}^{\infty}$ can be extracted from the FE solver and mapped directly to the FDM material point for each timestep in an iterative scheme. The local internal dislocation stress field $\underline{\underline{\pi}}^d$ is independent of applied conditions, and must be calculated from the current dislocation positions at the start of each increment. The traditional stress symbol "$\underline{\underline{\sigma}}$" will be reserved for the macro-scale stress state of the domain, while the current "$\underline{\underline{\pi}}$" nomenclature will refer to a local stress or *microstress* state.

The stress from a field of dislocation density was discussed in Section 3.2 for a generalised 3D system. In that case the stress was determined by a third rank tensor acting upon the dislocation density field. For a simplified 2D system containing only parallel edge dislocations, however, the stress at $\underline{X}$ due to dislocations at $\underline{X}_0$ may be described by a scalar material constant A, scalar density ρ and a second rank tensor describing the field shape $\underline{\underline{g}}$.

$$\underline{\underline{\pi}}^d(\underline{X}) \;=\; -A \, \rho(\underline{X}_0) \, \underline{\underline{g}}(\underline{X} - \underline{X}_0) \tag{4.3.1}$$

$$A \;=\; \frac{\mu b}{2\pi(1 - \nu)} \tag{4.3.2}$$

where μ is the shear modulus of the material and ν is the Poissons ration. This relationship and the field shapes for screw and edge-type dislocations are well known to literature [44][49][126].

Taking the standard formulas for an edge dislocation in Cartesian coordinates, where $\underline{X} = (x, y)$ and $\underline{X}_0 = (x_0, y_0)$, the individual terms of the tensor are described in 2D by

$$g_{11}(\underline{X} - \underline{X}_0) = (y - y_0) \frac{3(x - x_0)^2 + (y - y_0)^2}{((x - x_0)^2 + (y - y_0)^2)^2}$$

$$g_{22}(\underline{X} - \underline{X}_0) = (y - y_0) \frac{(x - x_0)^2 - (y - y_0)^2}{((x - x_0)^2 + (y - y_0)^2)^2}$$

$$g_{12}(\underline{X} - \underline{X}_0) = g_{21}(\underline{X} - \underline{X}_0) = (x - x_0) \frac{(x - x_0)^2 - (y - y_0)^2}{((x - x_0)^2 + (y - y_0)^2)^2}$$

$$g_{13} = g_{23} = g_{31} = g_{32} = 0$$

$$g_{33}(\underline{X} - \underline{X}_0) = v \, (g_{11}(\underline{X} - \underline{X}_0) + g_{22}(\underline{X} - \underline{X}_0)) \tag{4.3.3}$$

Combining eqns (4.3.1), (4.3.2) and (4.3.3) will describe the stress field at all points $\underline{X}$ within the domain, emitted from a single location $\underline{X}_0$. A surface integral may be used to sum for the total

field at $\underline{X}$ emitted from every other point within the domain. The fields are then layered atop one another to find the complete internal stress field (as illustrated in Fig. 4.3.1).

$$\underline{\underline{\pi}}^d(\underline{X}) \;=\; A \; \iint \rho(\underline{X_0}) \, \underline{\underline{g}}(\underline{X} - \underline{X_0}) \; d^2\underline{X_0} \tag{4.3.4}$$

The total local stress on a dislocation at each element location $\underline{X}$ is given by the sum of externally applied, $\underline{\underline{\pi}}^\infty$, and internal dislocation, $\underline{\underline{\pi}}^d$, stress contributions

$$\underline{\underline{\pi}}(\underline{X}) \;=\; \underline{\underline{\pi}}^\infty(\underline{X}) + \underline{\underline{\pi}}^d(\underline{X}) \tag{4.3.5}$$
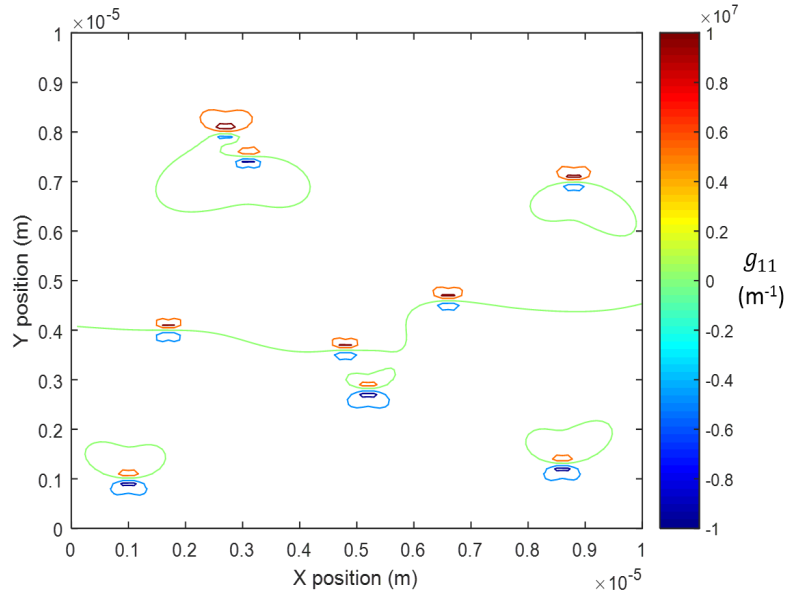
Figure 4.3.1: Plotting the g_{11} component of the g-field for nine random points of dislocation density within a 10 μm domain. The emitted fields sums into a continuous description across the domain.

4.3.1 Force on the dislocation field

The force acting on a dislocation within an element is found using the Peach-Koehler relationship [126]

$$\underline{f}^\infty(\underline{X}) \;=\; \underline{\xi} \times (\underline{\underline{\pi}}^\infty(\underline{X}) \cdot \underline{b})$$
$$\underline{f}^d(\underline{X}) \;=\; \underline{\xi} \times (\underline{\underline{\pi}}^d(\underline{X}) \cdot \underline{b})$$
$$\underline{f}(\underline{X}) \;=\; \underline{f}^\infty(\underline{X}) \;+\; \underline{f}^d(\underline{X}) \tag{4.3.6}$$

59

where $\underline{\xi}$ and $\underline{b}$ are the line tangent and Burgers vectors within the simulation reference frame.

No out-of-plane force vector along $\underline{e}_3$ will exist for the chosen dislocation type (eqn 4.1.1), leaving:

$$\underline{f}^\infty(\underline{X}) \;=\; f_1^\infty \; \underline{e}_1 \;+\; f_2^\infty \; \underline{e}_2$$

$$\underline{f}^d(\underline{X}) \;=\; f_1^d \; \underline{e}_1 \;+\; f_2^d \; \underline{e}_2$$

From these force components the local glide and climb velocities can be determined.

4.3.2 Line tension force from dislocation pinning

A commonly observed phenomenon of dislocation dynamics is the pinning effect caused by inhomogeneities in the crystal matrix as they obstruct sections of a dislocation line. When a section of dislocation line is pinned, the unpinned sections may continue to move, bowing out between obstructions. This causes the dislocation line to curve and introduces a restorative force due to line tension, which acts to stop further bowing [6] [56]. This line tension must be overcome before a bowing dislocation segment can advance. Causes of pinning may generally include precipitate phases in the bulk material in the form of particles or lathes; grain or sub-grain boundaries between non-complimentary orientations and entanglement with fellow dislocation lines on different slip systems.

In the case of nickel-based superalloys, the γ' phase particles provide a significant pinning effect. As such, before introducing the discrete particles to the 2D domain (in Section 5.4.3) and considering the cutting mechanism, it is important to appreciate the out-of-plane effect of the non-resolved particles. These obstacles exist outside of the resolved plane, meaning the individual interactions cannot be addressed and the effect must be approximated through a mean-field drag term. This term supposes a hypothetical curvature κ of the dislocation line segment between the out-of-plane pinning points, from this curvature a line tension is derived and then applied as a drag force $\underline{f}^{lt}$ against the motion of the dislocation.

This drag force works only in the glide direction and is given by

$$\underline{f}^{lt} \;=\; \mathbb{T}\kappa \; \underline{e}_1 \;=\; f_1^{lt} \; \underline{e}_1 \tag{4.3.7}$$

where $\mathbb{T}$ is a material-specific tension approximated by $\mathbb{T} \approx \frac{1}{2}\mu b^2$.

Curvature is calculated for all elements within the domain at the start of each timestep using the geometrical relations of the circle segment bounded by a dislocation line arcing between two pinning points. The pinning point spacing is given by λ_{pin} and may take values of either the edge-to-edge particle spacing or the grain size depending on criteria that will be discussed later.

Deriving the dislocation curvature

Consider two pinning points lying upon an axis described by coordinate x, as illustrated in Fig. 4.3.2. A dislocation bowing between these points will originally be flat with the axis before each point on the line begins to displace away from its original position by displacement $u(x)$. The force required to cause this displacement is
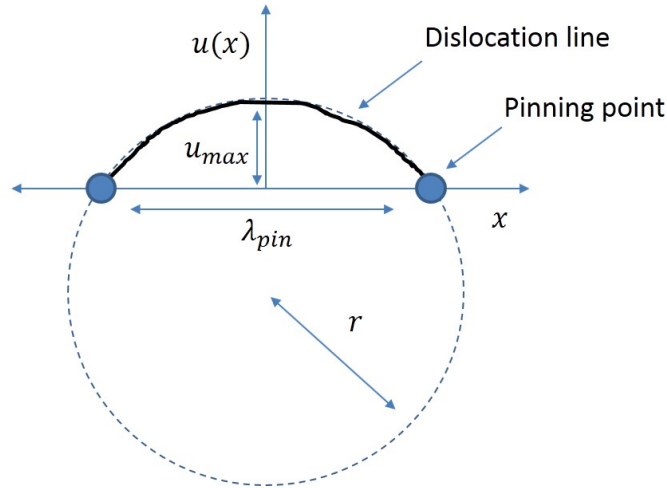
Figure 4.3.2: Illustration of geometry for calculating hypothetical curvature and drag effects caused by dislocations bowing between pinning points

$$f_1 = -\mathbb{T}\,\frac{\partial^2 u}{\partial x^2}$$

From this the equation for the displacement at each point along the axis can be found

$$\frac{\partial^2 u}{\partial x^2} = -\frac{f_1}{\mathbb{T}}$$
$$\frac{\partial u}{\partial x} = -\frac{f_1}{\mathbb{T}} x + c$$
$$u(x) = -\frac{f_1}{2\mathbb{T}} x^2 + c x + a \tag{4.3.8}$$

where c and a are integration constants. Inserting the edge of the curve limits $x = \frac{-\lambda_{pin}}{2}$ and $x = \frac{\lambda_{pin}}{2}$ into the function for u is known to give zero displacement:

$$0 = -\frac{f_1}{2\mathbb{T}} \left(\frac{\lambda_{pin}}{2}\right)^2 + c \left(\frac{\lambda_{pin}}{2}\right) + a \tag{4.3.9}$$
$$0 = -\frac{f_1}{2\mathbb{T}} \left(\frac{-\lambda_{pin}}{2}\right)^2 + c \left(\frac{-\lambda_{pin}}{2}\right) + a \tag{4.3.10}$$

Taking eqn (4.3.10) from eqn (4.3.9) can determine the value of the constants

$$c = 0$$
$$a = \frac{f_1}{2\mathbb{T}} \left(\frac{\lambda_{pin}}{2}\right)^2$$

Applying these to eqn (4.3.8) gives:

$$u(x) = -\frac{f_1}{2\mathbb{T}} x^2 + \frac{f_1}{2\mathbb{T}} \left(\frac{\lambda_{pin}}{2}\right)^2$$
$$u(x) = -\frac{f_1}{2\mathbb{T}} \left(\frac{\lambda_{pin}^2}{4} - x^2\right) \tag{4.3.11}$$

As maximum displacement u_{max} occurs when $x = 0$, then this displacement is found to be

$$u_{max} = \frac{f_1 \lambda_{pin}^2}{8\mathbb{T}} \qquad u_{max} = \frac{(f_1^\infty + f_1^d) \lambda_{pin}^2}{8\mathbb{T}} \tag{4.3.12}$$

Considering the circle upon which the pinning points and dislocation line lie, in Fig. 4.3.2, then the chord length is equivalent to the pinning spacing. The sagitta is given by U_{max} and will therefore change with the applied force f_1. Knowing both the chord and the sagitta, known geometrical relations may be applied in order to calculate the radius r of the circle, and therefore the curvature of the dislocation segment.

$$r = \frac{u_{max}}{2} + \frac{\lambda_{pin}^2}{8 \, u_{max}} \tag{4.3.13}$$
$$\kappa = \frac{1}{r} \tag{4.3.14}$$

62

Applying the line tension drag force

In this framework the pinning spacing has a number of potential contributors. For a perfect defect-free homogeneous matrix the spacing is set to default to the dimension of the domain λ_{grain}. When gamma prime particles are introduced to a matrix, the average spacing of the large secondary particles λ_L or small tertiary particles λ_s may be used as the pinning point spacing. The smaller of the available spacings is the appropriate choice for such calculations, as smaller spacings will lead to a greater drag effect and supersede the effect of the others. When included, the tertiary γ' normally account for the smallest pinning spacing, however it is important to note that high stresses the particles can be sheared and so lose their effect as obstacles in the mean-field calculations. It is therefore necessary to change the pinning point spacing dynamically with the local stress conditions in the model.

If the forces required to cut a tertiary or secondary particle are f_{tert} and f_{sec} respectively, then the choice of pinning point spacing to use in eqns (4.3.12) and (4.3.13) is given by a logical function relating to the domain of the simulation in question. The functions (listed below) are formulated so that when reading from top to bottom the first applicable case should be chosen.

For a pure-matrix simulation:

$$\lambda_{pin} = \lambda_{grain}$$

For a simulation with a unimodal particle distribution (in this example only secondaries):

$$\lambda_{pin} = \begin{cases} \lambda_L & \text{, if} \quad f_1^\infty + f_1^d < f_{sec} \\ \lambda_{grain} & \text{, else} \end{cases}$$

For a bimodal secondary and tertiary particle distribution:

$$\lambda_{pin} = \begin{cases} \lambda_s & \text{, if} \quad \lambda_s \le \lambda_L \quad \text{and } f_1^\infty + f_1^d < f_{tert} \\ \lambda_L & \text{, if} \quad f_1^\infty + f_1^d > f_{tert} \text{ and } f_1^\infty + f_1^d < f_{sec} \\ \lambda_{grain} & \text{, else} \end{cases} \tag{4.3.15}$$

The combination of forces from external conditions, internal dislocation stress fields and line tension drag gives the resultant force contribution that drives the dislocation motion. This force will be

termed the *motive force* $\underline{\boldsymbol{f}}^{mot}$ as it pertains only to the local force moving the dislocations within an element.

$$\underline{\boldsymbol{f}}^{mot}(\underline{\boldsymbol{x}}) \;=\; f_1^{mot}\;\underline{\boldsymbol{e}_1}\;+\;f_2^{mot}\;\underline{\boldsymbol{e}_2}$$

$$f_1^{mot} \;=\; f_1^\infty\;+\;f_1^d\;-\;f_1^{lt}$$

$$f_2^{mot} \;=\; f_2^\infty\;+\;f_2^d \tag{4.3.16}$$

As the line tension drag force is acting as a response to an applied force trying to push a dislocation between two pinning points, it is not physically possible for it to exceed the force being applied. To guard against this eventuality the condition $f_1^{mot} = 0$ is applied for elements where $f_1^\infty + f_1^d \;<\; f_1^{lt}$. This stops the line tension from erroneously reversing the direction of motion and instead creates a situation where dislocation motion will cease if the line tension cannot be overcome.

Figure 4.3.3 illustrates how the motive force vector varies for a dislocation in a domain with and without a particle field, when moving under three different applied external forces. The topmost image depicts the hypothetical interaction with the non-resolved particles, while the bottommost image shows the corresponding information handled by the model. The effect of jogs, grain boundaries and further particles sizes are omitted for simplicity. Situation A considers a dislocation travelling unperturbed through a matrix without particles under some force $f^\infty{}_{[1]}$. Situation B introduces a particle field where the line tension drag exceeds $f^\infty{}_{[1]}$ and so stops the dislocation. Situation C applies a larger force $f^\infty{}_{[2]}$, such that the line tension can be overcome and the dislocation can bow between the particles and progress onwards (experiencing the drag term). Situation D further increases the external force to $f^\infty{}_{[3]}$, which is greater than the cutting threshold for the particle distribution, meaning the particles are sheared and no longer act as pinning points or impose a line tension.
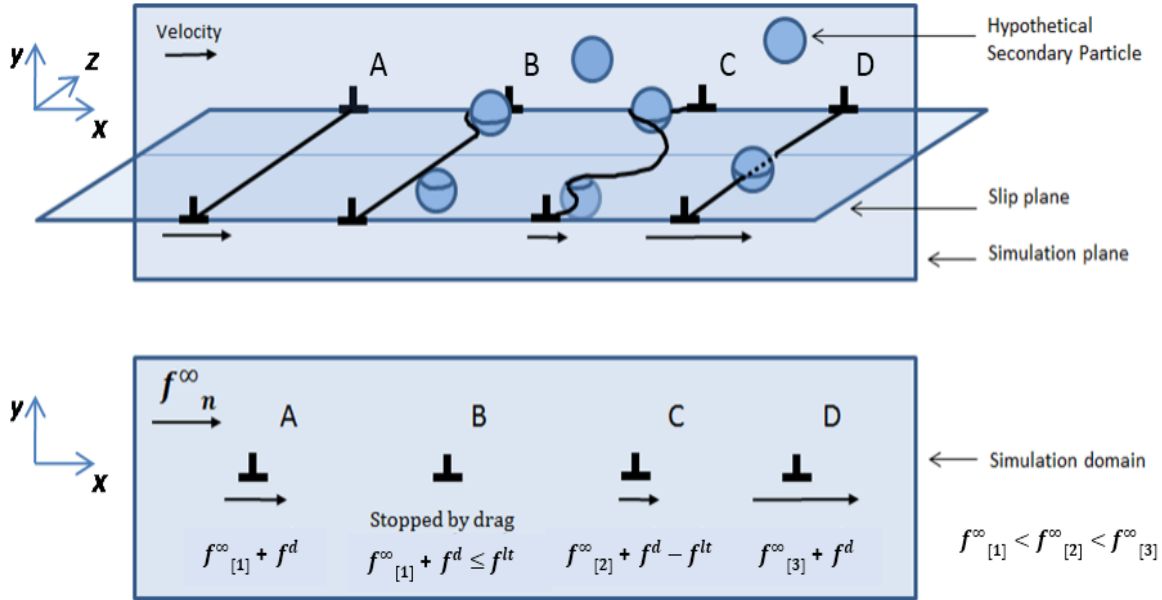
Figure 4.3.3: An illustration of four potential conditions within the model, determined by the applied force and the particle field present. The resultant motive force vector appears below the dislocation as the black arrow.

The motive force components acting within an element are fed into the appropriate glide and climb velocity equations (4.2.2), (4.2.5) or (4.2.7) in order to find the velocities for the dislocation density. In this way the velocity of the density changes in real time as a response to the local conditions and environment. These values may then be implemented within the finite difference scheme in order to advect the density around the domain.

4.4 Shearing of γ' Precipitates

4.4.1 Background to the precipitate strengthening effect

The gamma γ matrix and gamma prime γ' precipitate phases of nickel-base superalloys have a coherent crystal structure, meaning the precipitate slip systems are closely aligned to the parent matrix ($\pm$ 0.1 % [11]). This allows dislocations to move between phases without the creation of a residual dislocation or complex Burgers vector reactions; the only obstruction to slip transfer is the necessary creation of an anti-phase boundary (APB) within the particle.

The matrix phase is a disordered FCC arrangement with randomly distributed constituent atoms across the lattice sites, while the precipitate is an ordered FCC with the nickel atoms taking the face centre positions and either aluminium or titanium taking the corners. As the ordered γ' has a larger distance between repeating elements in the slip driection, the Burgers vector (while complimentary to the direction of the matrix vector) is larger by a factor of $\sim \times 2$. A single matrix dislocation moving into the precipitate is therefore not enough to slip the more ordered structure by a full Burgers vector and so instead creates a high-energy situation with an APB between the slipped and non-slipped regions. A second matrix dislocation following the first can restore order to the precipitate and eliminate the APB [6] [127].

In the γ' phase the energy per unit area required to create an anti-phase boundary e_{apb} is ~ 0.2 Jm^{-2}, typically this prevents shearing until high stress regimes, when dislocations push on particle surfaces with considerable force. The energy barrier allows the precipitate phase to be used to delay yield by effectively acting as a barrier to plastic flow, causing dislocation pile-up. When a matrix dislocation manages to pass through the cross-section of a particle the particle is said to be "sheared" or "cut".

4.4.2 Approach to modelling particle shear

The model for shearing a precipitate particle involves equivalating the work done in advancing a dislocation line to the energy required to create the associated area of APB. Only the first of a pair of shearing dislocation is considered in this model, for it is this dislocation that comes up against the energy barrier while the second has an energetically favourable progression as it restores the crystal to the lower energy state.

The work done δW in moving a dislocation segment of length L is given by

$$\delta W \;=\; \tau \, b \, L \, \delta q \tag{4.4.1}$$

where τ is the shear stress along the plane and δq is displacement of the dislocation into the particle.

The energy deficit δE for the creation of an APB is given by

$$\delta E \;=\; 2R \, e_{apb} \, \delta q \tag{4.4.2}$$

where particle cross sections are modelled as squares with R as the radius. Thus $2R\delta q$ is the area of an APB surface. Fig. (4.4.1) illustrates the set-up graphically.
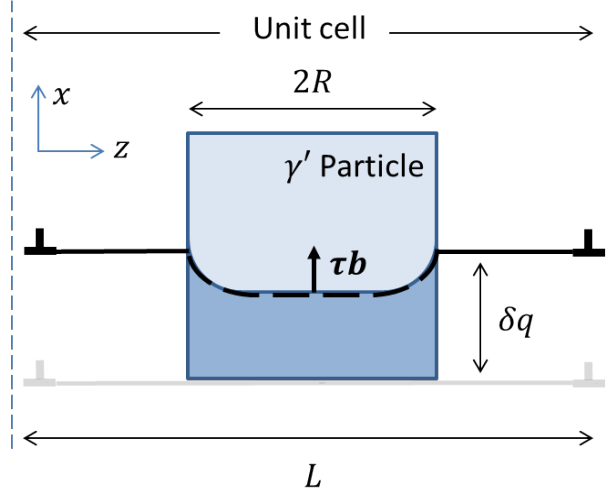

Figure 4.4.1: Cutting of a single particle - Single dislocation waiting at particle face (grey) moving distance δq to new location (black) and creating an area of APB (dark blue)

Singular size distribution of particles

A particle distribution of average radius $\hat{r}$ may be described by two particle spacings: the edge-to-edge spacing λ and the centre-to-centre spacing λ^*. The two are related simply via $\lambda^* = 2\,\hat{r} + \lambda$.

Taking the average centre-to-centre spacing λ^* of these particles as the dislocation segment length, and using the average particle radius $\hat{r}$ for the distribution, it is possible to create a repeating unit cell to model cutting events. Fig. (4.4.2) depicts the centre-to-centre spacing and the small lateral displacement that creates the repeating cell (two equivalent cells are labelled). With $L = \lambda^*$ and $R = \hat{r}$ and setting $\delta W = \delta E$, the condition for cutting a given particle may be obtained.

$$\tau\, b\, \lambda^*\, \delta q \;=\; 2\,\hat{r}\, e_{apb}\, \delta q \tag{4.4.3}$$

This means the shear stress threshold τ_{cut} above which a particle can be cut is given by

$$\tau_{cut} \;\geq\; \frac{2\,\hat{r}\, e_{apb}}{b\, \lambda^*} \tag{4.4.4}$$

67
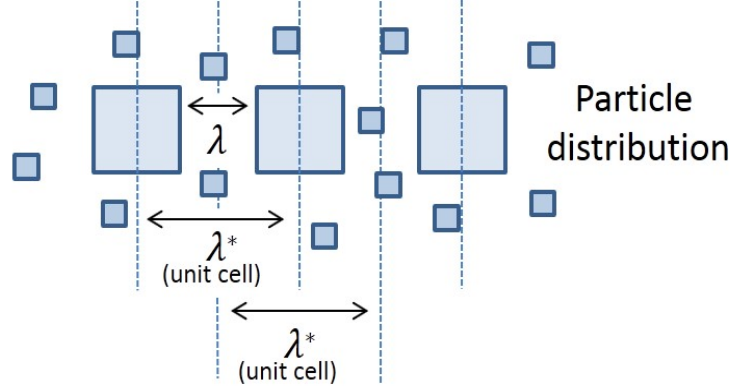
Figure 4.4.2: Distribution of larger secondary particles with interstitial smaller tertiary particles.

Multi-modal size distribution of particles

When multiple particle sizes are introduced to a domain then it is necessary to calculate the total contribution of interstitial particles which would be cut during the cutting of a larger particle. This is accomplished by assuming that both particles sizes will be encountered across the line segment L, and during the advancement δq_2 through a secondary particle the dislocation line will move a uniform δq_3 through any tertiaries encountered.

If the larger particles are taken to be secondary particles of radius $\hat{r}_2$ with centre-to-centre spacing λ_2^* and the smaller are taken as tertiaries with corresponding parameters $\hat{r}_3$ and λ_3^* then the work done in advancing the dislocation line across the secondary unit cell has the same form as eqn (4.4.1):

$$\delta W \ = \ \tau \, b \, \lambda_2^* \, \delta q_2 \tag{4.4.5}$$

where the larger spacing is used as the dislocation segment length.

The APB energy term appears as before, but with an additional term to account for the effect of a number of tertiaries δN_3 which exist in the gaps between secondaries. Fig. (4.4.3) illustrates the situation.

$$\delta E \ = \ 2 \, \hat{r}_2 \, e_{apb} \, \delta q_2 \ + \ 2 \, \hat{r}_3 \, e_{apb} \, \delta q_3 \, \delta N_3 \tag{4.4.6}$$

68

The number of tertiaries encountered by the line segment is calculated from the relative spacing information

$$\delta N_3 = \frac{\lambda_2^*}{\lambda_3^*} \tag{4.4.7}$$

Thus the energy term becomes

$$\delta E = 2 \, \hat{r}_2 \, e_{apb} \, \delta q_2 + 2 \, \hat{r}_3 \, e_{apb} \, \delta q_3 \, \frac{\lambda_2^*}{\lambda_3^*}$$

$$= 2 \, e_{apb} \left[\hat{r}_2 \, \delta q_2 + \hat{r}_3 \, \delta q_3 \, \frac{\lambda_2^*}{\lambda_3^*} \right] \tag{4.4.8}$$

and the work - energy balance is

$$\tau \, b \, \lambda_2^* \, \delta q_2 = 2 \, e_{apb} \left[\hat{r}_2 \, \delta q_2 + \hat{r}_3 \, \delta q_3 \, \frac{\lambda_2^*}{\lambda_3^*} \right] \tag{4.4.9}$$

giving the cutting threshold for combined secondaries and interstitial tertiaries as

$$\tau_{cut} = \frac{2 \, e_{apb}}{b} \left[\frac{\hat{r}_2}{\lambda_2^*} + \frac{\hat{r}_3}{\lambda_3^*} \frac{\delta q_3}{\delta q_2} \right] \tag{4.4.10}$$

It is assumed for this model that the shearing displacement into the secondaries and the tertiaries is approximately equal, meaning $\delta q_2 \approx \delta q_3$ and the stress threshold for cutting the larger particle in a bimodal distribution is just the linear addition of the effects of two unimodal distributions:

$$\tau_{cut} = \frac{2 \, e_{apb}}{b} \left[\frac{\hat{r}_2}{\lambda_2^*} + \frac{\hat{r}_3}{\lambda_3^*} \right] \tag{4.4.11}$$
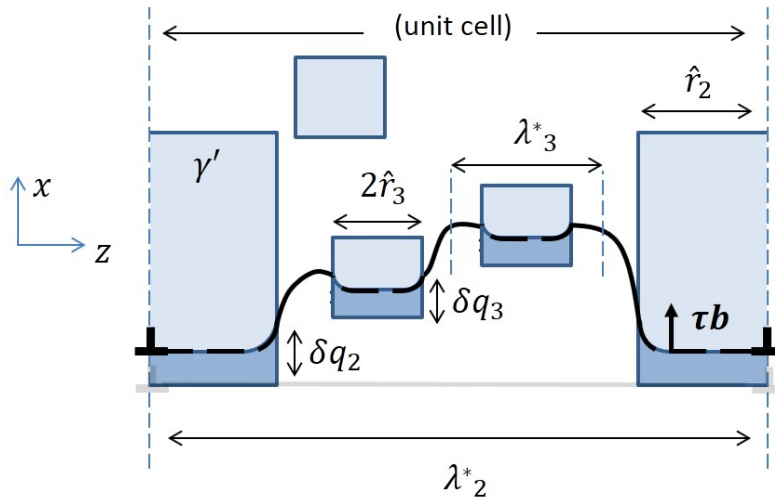
Figure 4.4.3: Cutting of a multiple particles - Single dislocation waiting at large particle face (grey) moving distance δq to new location (black) and creating an area of APB (dark blue)

Considering now the forces acting upon a dislocation, the local cutting condition becomes

$$f_1^{mot} \geq 2 \, e_{apb} \left[\frac{\hat{r}_2}{\lambda_2^*} + \frac{\hat{r}_3}{\lambda_3^*} \right] \tag{4.4.12}$$

More information on the implementation of this cutting condition is covered in the discussion of environmental boundary conditions in Section 5.4.3.

4.5   Reaction Terms

The terms $\dot{G}^+$ and $\dot{A}^-$ in eqn (3.1.25) have been neglected for simplicity during the adaptation to plane strain in Section 4.1. Perfect conservation of dislocation density has been assumed such that the continuity equation balances against a net flux of zero across the domain (with 0 appearing on the right hand side of most equations). This balance can be altered *reaction terms*, which account for dislocation density entering and leaving the domain. The scope of these terms could potentially cover a broad spectrum of dislocation source/sink mechanisms, but essentially rely on separate functions for the addition or removal of density in a local area.

Within this work the $\dot{G}^+$ term refers to the generation of dislocation density at a source location using the mechanism of a Frank-Read source [44][128]. The generation conditions for a given source at location $\underline{x}$ are taken from the work of Benzerga *et al.* in 2004 [123]

$$\dot{G}^+(\underline{X}) = \rho_{source} \, \Gamma^{n,+}(\underline{X}, \tau, l_{FR}) \tag{4.5.1}$$

with l_{FR} as Frank-Read source length, $\Gamma^{n,+}$ as the frequency of generation and ρ_{source} as the amount of density introduced in each generation.

Source generation frequency is given by the inverse of the nucleation time t_{nuc}, which in turn is approximated by the time taken for a dislocation to bow out to a critical distance y^* between two obstacles separated by l_{FR}, as shown in Figure 4.5.1. The critical distance is here set to $\frac{l_{FR}}{2}$:

$$\Gamma^{n,+}(\underline{X}, \tau, l_{FR}) = \frac{1}{t_{nuc}}$$
$$t_{nuc} = \frac{y^*}{v_g} = \frac{l_{FR}}{2 \, v_g} \tag{4.5.2}$$

The threshold stress at which source activation occurs, τ_{gen}, is given by
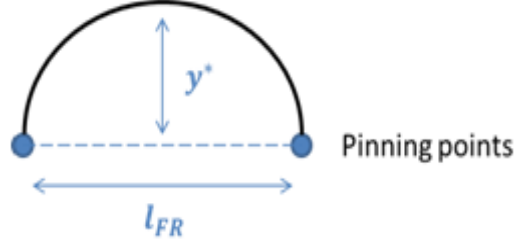
Figure 4.5.1: A new dislocation bowing between two pinning points.

$$\tau_{gen} = \alpha \frac{G \, |\boldsymbol{b}|}{l_{FR}} \tag{4.5.3}$$

where G is the shear modulus of the material and α is a constant (here $\alpha = 0.25$).

Annihilation of dislocations may occur when opposite-signed dislocation density is present upon the same node. In this instance a fraction of the density is removed from the simulation according to a constant that describes the probability of annihilation occurring P_{ann} (between two dislocations within the interaction distance associated with a single node). The positive and negative density can be described by $\rho^{+,n}(\boldsymbol{X})$ and $\rho^{-,n}(\boldsymbol{X})$ respectively.

$$\dot{A}^-(\boldsymbol{X}) = P_{ann} \, \rho^{+,n}(\boldsymbol{X}) \, \rho^{-,n}(\boldsymbol{X}) \tag{4.5.4}$$

The simulations within this work will contain only positive edge statisically stored dislocations (SSDs), thus $\rho^{-,n}(\boldsymbol{X}) = 0$ at all times.

4.6 Crystal Plasticity Framework for the UMAT subroutine

A crystal plasticity framework may be used to determine the stress within an element of a FE model. Recalling eqn (2.3.6), the definition of the stress at a point $\boldsymbol{X}$ is a function of the local elastic strain $\underline{\underline{\varepsilon}}^{(e)}(\boldsymbol{X})$ at that point

$$\underline{\underline{\pi}}^{\infty}(\boldsymbol{X}) = \underline{\underline{\boldsymbol{C}}} : \underline{\underline{\varepsilon}}^{(e)}(\boldsymbol{X}) \tag{4.6.1}$$

It follows that the elastic strain field $\underline{\underline{\varepsilon}}^{(e)}$ must be defined at all points for each increment within the FE solver. As all the tensors in the CP equations have a spatial dependency, the notation $*(\boldsymbol{X})$ will henceforth be dropped.

Using the definition for the Green-Langrangian strain tensor, elastic strain can be expressed in terms of the elastic deformation gradient $\underline{\underline{F}}^{(e)}$:

$$\underline{\underline{\varepsilon}}^{(e)} = \frac{1}{2}\left(\underline{\underline{F}}^{(e)T}\,\underline{\underline{F}}^{(e)} - \underline{\underline{\mathbb{I}}}\right) \tag{4.6.2}$$

where $\underline{\underline{\mathbb{I}}}$ is the second-order identity matrix.

The elastic component $\underline{\underline{F}}^{(e)}$ can be separated from the total deformation gradient tensor $\underline{\underline{F}}$ using the principle of Lee decomposition:

$$\underline{\underline{F}} = \underline{\underline{F}}^{(e)} \cdot \underline{\underline{F}}^{(p)} \qquad \rightarrow \qquad \underline{\underline{F}}^{(e)} = \underline{\underline{F}} \cdot \underline{\underline{F}}^{(p)-1} \tag{4.6.3}$$

where $\underline{\underline{F}}^{(p)}$ is the plastic deformation gradient tensor.

The finite element software automatically finds the total deformation gradient $\underline{\underline{F}}$ at each new time increment, leaving only the plastic component $\underline{\underline{F}}^{(p)}$ to be determined in order to find the updated stress state. The output from the FDM formulation can be used to find this unknown quantity.

The dislocation density and glide velocity at a given location produce the local plastic shear rate $\dot{\gamma}$ during each FDM timestep

$$\dot{\gamma}(\underline{X}) \;=\; b\,\rho(\underline{X})\,v_g(\underline{X}) \tag{4.6.4}$$

These shear rates may be averaged across a larger FE timestep using eqn (5.4.1), to produce the FE shear rate $\dot{\gamma}_{abq}$.

The sum of the plastic shear rates upon each of the different slip systems gives the plastic velocity gradient tensor $\underline{\underline{L}}^{(p)}$

$$\underline{\underline{L}}^{(p)} \;=\; \sum_{m=1,12} \dot{\gamma}_{abq}{}^m\,\underline{s}^m \otimes \underline{n}^m \tag{4.6.5}$$

where $\underline{s}^m$ and $\underline{n}^m$ are the slip and normal unit vectors for the slip system denoted by the index m. Of the twelve available primary slip systems in a FCC crystal, the $\langle\bar{1}10\rangle$ direction on the (111) plane is the only system considered for the plane strain implementation. The slip and normal vectors

expressed within this reference frame are $\underline{s} = [1\ 0\ 0]$ and $\underline{n} = [0\ 1\ 0]$, meaning that only the shear component $L_{12}^{(p)}$ of the plastic velocity gradient is non-zero (see Fig. 5.2.3)

$$\underline{\underline{L}}^{(p)} = \begin{bmatrix} 0 & \dot{\gamma}_{abq} & 0 \\ 0 & 0 & 0 \\ 0 & 0 & 0 \end{bmatrix}$$

and consequently all plastic deformation has only shear components.

The plastic velocity gradient tensor may also be expressed through the plastic deformation gradient

$$\underline{\underline{L}}^{(p)} = \dot{\underline{\underline{F}}}^{(p)} \cdot \underline{\underline{F}}^{(p)-1} \tag{4.6.6}$$

The rate of change $\dot{\underline{\underline{F}}}^{(p)}$ can be approximated using the change of value between the previous timestep $\underline{\underline{F}}_0^{(p)}$ and the current timestep $\underline{\underline{F}}_1^{(p)}$

$$\dot{\underline{\underline{F}}}^{(p)} \approx \frac{\underline{\underline{F}}_1^{(p)} - \underline{\underline{F}}_0^{(p)}}{\Delta t_{abq}} \tag{4.6.7}$$

Inserting eqn (4.6.7) into eqn (4.6.6) and rearranging allows the updated plastic deformation gradient to be calculated from the plastic velocity gradient

$$\underline{\underline{F}}_1^{(p)} = \underline{\underline{F}}_0^{(p)} \left(\Delta t_{abq} \underline{\underline{L}}^{(p)} + \underline{\underline{\mathbb{I}}} \right) \tag{4.6.8}$$

The initial value of $\underline{\underline{F}}_0^{(p)}$ before deformation has started may be taken as identity, as the simulations will begin in a state without plastic deformation. The instantaneous value of $\underline{\underline{L}}^{(p)}$ is calculated directly from eqn (4.6.5) and the sequence may be iterated for each FE timestep.

The updated $\underline{\underline{F}}_1^{(p)}$ can then be fed back into eqn (4.6.3) and (4.6.2) in order to receive the updated elastic strain state and solve for the stress of the system.

73

Chapter 5

Numerical Implementation

5.1 Constitutive Model Framework and Boundary Value Problem

This section presents a summary of the constitutive framework and boundary value problem (BVP) which will be solved. The following sections will focus on the numerical implementation and parameter identification.

The spatial/temporal evolution of dislocation density within the crystal lattice is determined using eqns (3.1.19), (3.1.25) and (4.5.1). The dislocation velocity $\dot{\underline{q}}$ will evolve according to the local motive force using eqns (3.2.12), (4.3.7) and (4.3.16), where this force takes contributions from the applied stress $\underline{\underline{\pi}}^{(\infty)}$, internal dislocation stress fields $\underline{\underline{\pi}}^{(d)}$ and dislocation line tension $\underline{f}^{lt}$. The dislocation transport equations are:

$$\dot{\underline{\underline{\alpha}}} \; = \; \underline{\underline{\alpha}} \cdot (\underline{\underline{\alpha}} \times \dot{\underline{q}})^T \; + \; \underline{\nabla} \times (\underline{\underline{\alpha}} \times \dot{\underline{q}}) \; + \; \dot{\underline{\underline{G}}}^+ \tag{5.1.1}$$

$$\dot{\underline{q}} \; = \; \dot{\underline{q}}(\underline{f}^{mot}, \underline{X})$$

$$\underline{f}^{mot} = \underline{f} - \underline{f}^{lt}$$

$$\underline{f} \; = \; \underline{t} \; \times \left(\; \underline{\underline{\pi}}^{(\infty)}(\underline{X}) + \underline{\underline{\pi}}^{(d)}(\underline{X}) \; \right) \cdot \underline{b}$$

$$\underline{\underline{\pi}}^{(d)}(\underline{X}) = \iiint_{\Omega} \underline{\underline{\underline{j}}}(\underline{X} - \underline{X}') \overset{.}{\times} \underline{\underline{\alpha}}(\underline{X}') \; dV \tag{5.1.2}$$

The deformation kinematics and stress update are calculated using eqns (3.1.19), (4.6.1) and (4.6.2):

$$\underline{\underline{L}}^{(p)} \;=\; \underline{\underline{\alpha}} \times \underline{\dot{q}} \;=\; \sum_{m=1,12} \dot{\gamma}_{abq}{}^{m} \; \underline{s}^{m} \otimes \underline{n}^{m}$$

$$\underline{\underline{L}}^{(p)} \;=\; \underline{\dot{\underline{F}}}^{(p)} \cdot \underline{\underline{F}}^{(p)-1} \;, \qquad \underline{\underline{F}}^{(e)} = \underline{\underline{F}} \cdot \underline{\underline{F}}^{(p)-1}$$

$$\underline{\underline{\pi}}^{(\infty)}(\underline{X}) \;=\; \frac{1}{2}\, \underline{\underline{C}} : \left(\underline{\underline{F}}^{(e)T} \cdot \underline{\underline{F}}^{(e)} - \underline{\underline{\mathbb{I}}} \right)$$

The microscale fields are assumed to satisfy quasi-equilibrium conditions:

$$\underline{\nabla} \cdot \underline{\underline{\pi}}^{(\infty)} \;=\; 0 \qquad (\forall\, \underline{X} \in \Omega)$$

Te present study will focus on shear modes of deformation (as described in Section 5.2.1). Thus the BVP is subject to the following boundary conditions:

$$\underline{\dot{u}} \;=\; \underline{\dot{u}}^{(\infty)} \quad (\forall\, \underline{X} \in \partial\Omega)$$

It was shown through Sections 4.1 and 4.5 that within the 2D plane strain setup, using single slip and positive edge dislocations without any dislocation sink terms, eqn (5.1.1) becomes the scalar density evolution (of SSDs):

$$\frac{\partial \rho}{\partial t} \;+\; \underline{\nabla} \cdot (\underline{\dot{q}}\, \rho) \;=\; \dot{G}^{+} \tag{5.1.3}$$

This is the equation which will be solved at each node within the spatial domain.

The plane-strain setup also allows the stress field in eqn (5.1.2) to reduce to the 2D form given in Section 4.3

$$\underline{\underline{\pi}}^{(d)}(\underline{X}) \;=\; A \; \iint \rho(\underline{X}') \; \underline{\underline{g}}(\underline{X} - \underline{X}') \; d^{2}\underline{X} \tag{5.1.4}$$

The implementation of the FDM code, the UMAT and the Abaqus FE model will now be expanded upon.

75

5.2 RVE Finite Element Implementation

A finite difference (FD) scheme has been developed to solve the transport equation numerically for the dislocation density tensor and has been coupled to the commercial finite element software ABAQUS v6.13-1 through a user-defined material subroutine (UMAT).

The UMAT outputs the stress state in the current configuration and the stiffness tangent matrix. These are calculated from the material constitutive descriptions which must be specified. At the start of each increment input to the routine includes: the increment time Δt, element temperature T, element deformation gradient tensor at the start of the increment $\underline{\underline{F}}_0$, element deformation gradient tensor at the end of the increment $\underline{\underline{F}}_1$ and the range of chosen state variables.

In this setup the model requires a state variable for the shear rate $\dot{\gamma}$ to be calculated for each increment. This variable can be used within the CP calculations to define the plastic deformation state. A bespoke FORTRAN code was created to handle the FD scheme for dislocation transport; this code was called through a second routine, URDFIL, which can access the state variable values of all elements at the end of each step.

Within this routine the FDM code takes the current increment stress state as an input, allowing the dislocation state to evolve for a single timestep and the shear rate to be calculated. The shear rate is saved to the COMMON memory block which is shared between subroutines and is available for the UMAT to call at the start of the next increment. The process is mapped out graphically in Fig. 5.2.1.

As well as the shear rate the COMMON block also carries other variables from the FDM code which are not of direct use in calculations, but which may be of interest when visualised using the ABAQUS viewer (i.e dislocation density, source location etc.). These are saved as state variables on entering the UMAT on the next increment.
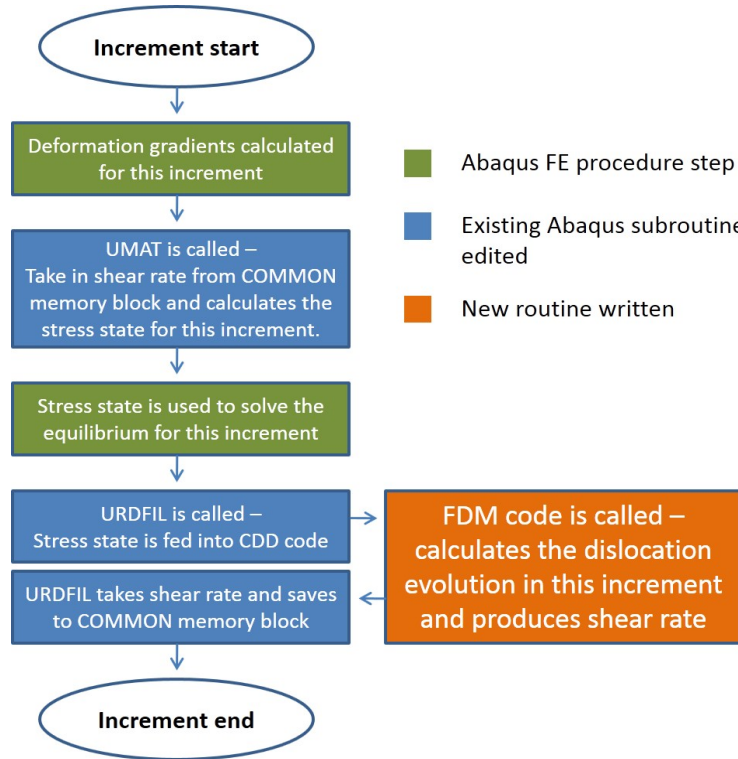
Figure 5.2.1: Flow chart for a single time increment of the FE-FDM model.

5.2.1 RVE model and boundary conditions

In the present study RVEs subject to plane strain conditions have been set up with ABAQUS. The domain size and shape was chosen to match the grains of a disc nickel-based superalloy, which typically lie in the range 5-50 μm [13][129], with the average grain shape being equiaxed. A square domain was deemed a reasonable 2D approximation, and side lengths in this work range from 5-30 μm.

The grain was meshed using equally sized tetragonal plane strain elements with reduced integration points (of type CPEG4R). This element type was appropriate for 2D displacement analysis using a UMAT. The enhanced hourglass control and discontinuous analysis options were used to assist in convergence.

With attention to the typical trade-off between element density and processing time, a mesh was selected that would resolve both secondary particles and slip bands but still remain coarse enough

to run simulations to a reasonable strain ($\sim 5\%$) in a cluster wall time of less than fourteen days. A typical slip band width of approximately 100nm has been observed in nickel-based superalloys during the SEM analysis of tensile [130] or compressive [131] tests, and previous CDD simulations have used 100nm as a slip band width for simulations of aluminium crystals [132]. As such a 100nm grid division was employed for the presented simulations, such that a 5 μm grain would contain 2,500 elements.

The following boundary conditions were imposed on the computational domain to reproduce a simple shear mode of deformation: for nodes along $y = 0$ the displacements $u_1 = u_2 = 0$; for nodes along $y = Y_0$ the displacement $u_2 = 0$ and the imposed velocity V_1^{app}, where X_0 and Y_0 are the lateral and vertical side lengths of the domain respectively. The strain rate is given by $\dot{\epsilon} = \dfrac{V_1^{app}}{Y_0}$. This is depicted in Fig. 5.2.2 for $Y_0 = X_0 = 10\mu m$.
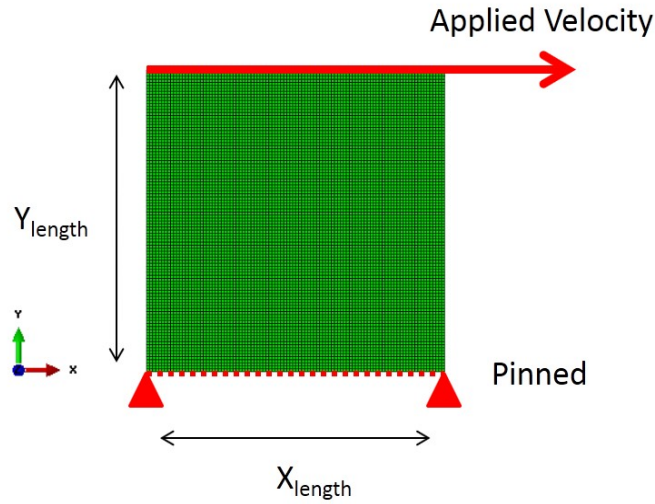

Figure 5.2.2: Boundary conditions applied within Abaqus.

The counterpart nodes of the left- and right-hand sides, where $x = 0$ and $x = X_0$, were linked via a Periodic Boundary Condition (PBC) for displacement. This ensured homogeneous stress fields during elastic deformation by preventing stress concentrations around the pinned corner nodes. In Abaqus this setup is achieved via an intermediary Reference Point node, to which the displacement of both counterpart nodes is linked using an equation constraint.
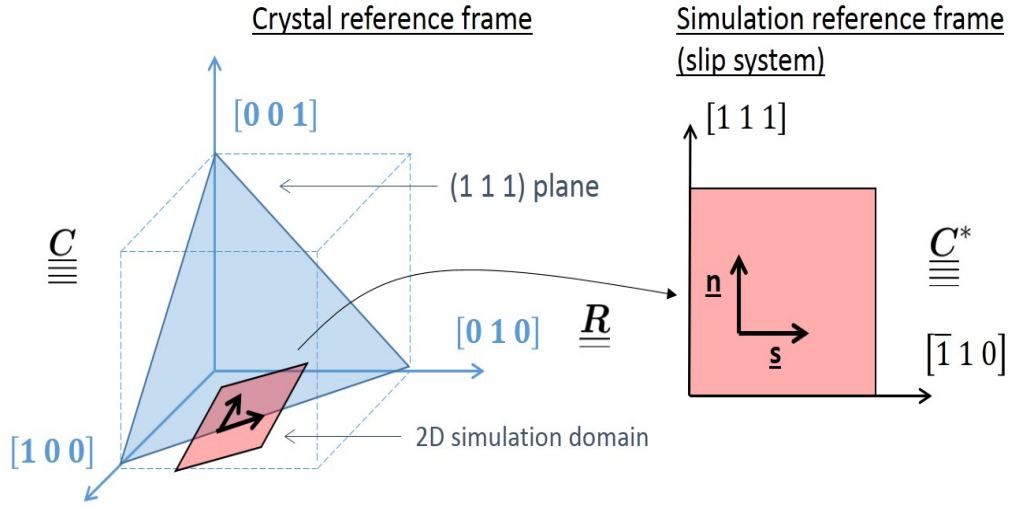
Figure 5.2.3: Indication of the FDM simulation plane within the standard Crystal reference system

Crystallographically, the planes of both the Abaqus domain and the FDM domain are identical and regard a surface described by the plane normal $[11\overline{2}]$. This vector is also the tangent vector for the straight edge-type dislocations within the simulations, meaning an element of dislocation density represents a quantity of dislocations viewed end on. The x-axis of the plane is aligned with the slip direction $[\overline{1}10]$ and the y-axis is aligned with the slip plane normal $[111]$. This is useful in that it confines glide and climb only to the x and y directions respectively (covered in Section 5.3.1). Fig. 5.2.3 illustrates this arrangement more clearly, with the simulation plane depicted as the pink square membrane through which dislocations can penetrate.

Stiffness constants were required to be expressed within the simulation reference frame. To accomplish this a rotation matrix $\underline{\underline{R}}$ was calculated

$$\underline{\underline{R}} = \begin{bmatrix} -\frac{1}{\sqrt{2}} & \frac{1}{\sqrt{3}} & \frac{1}{\sqrt{6}} \\ \\ \frac{1}{\sqrt{2}} & \frac{1}{\sqrt{3}} & \frac{1}{\sqrt{6}} \\ \\ 0 & \frac{1}{\sqrt{3}} & -\frac{2}{\sqrt{6}} \end{bmatrix} \tag{5.2.1}$$

This matrix was applied to the elastic stiffness constants $\underline{\underline{\underline{C}}}$ so that the tensor could be expressed within the desired orientation as $\underline{\underline{\underline{C}}}^*$. This requires the operation

$$\underline{\underline{\underline{C}}}^* = \underline{\underline{R}} \cdot \underline{\underline{R}} \cdot \underline{\underline{\underline{C}}} \cdot \underline{\underline{R}}^T \cdot \underline{\underline{R}}^T \tag{5.2.2}$$

The $\underline{\underline{\underline{C}}}^*$ constants were used for all elastic calculations within the UMAT.

5.3 Solving PDEs Numerically with Finite Difference

The handling of the dislocation density fields within this model is achieved using the Finite Difference (FD) method. The Partial Differential Equations (PDEs) that make up the continuity equation are approximated and then rearranged to produce the dislocation density locations at future times.

5.3.1 Discretising the domain and approximating the differentials

The continuity equation

$$\frac{\partial \rho}{\partial t} + \underline{\nabla} \cdot (\underline{\dot{q}}\, \rho) = 0$$

from eqn (4.1.4) refers to the evolution of a closed system with pre-existing density. As the computer cannot solve the equation analytically, in order to find the solution at time t_2, first the state at a given time t_1 must be known and then a numerical scheme must be chosen to iterate forward/backwards.

To iterate temporally, the time differential for a variable can be broken into a function of the states before and after a short time interval Δt has elapsed. These density states are given by ρ_t and $\rho_{t+\Delta t}$ respectively.

$$\frac{\partial \rho}{\partial t} \approx \left(\frac{\rho_{t+\Delta t} - \rho_t}{\Delta t} \right) \tag{5.3.1}$$

To iterate spatially first the divergence operator must be expanded into its x and y components

$$\underline{\nabla} \cdot (\underline{\dot{q}}\, \rho) = \frac{\partial(\dot{q}_x \rho)}{\partial x} + \frac{\partial(\dot{q}_y \rho)}{\partial y} \tag{5.3.2}$$

Then the spatial domain must be discretised into a grid of known spacing. In this case a uniform grid was chosen, with spacing Δx in the horizontal dimension and Δy in the vertical dimension.

The local information (dislocation density etc.) that exists for each grid location is stored within the computer memory as a 2D array with indices $[j, i]$. The array is set up such that the i index scans across the array locations in the x-direction, the j scans in the y-direction, and the coordinate location is merely the index multiplied by the grid spacing.

$$\underline{x} = [x, y] \quad \rightarrow \quad \underline{x} = x_{[i]} \underline{e_1} + y_{[j]} \underline{e_2}$$

$$\underline{\dot{q}} = \underline{\dot{q}}(\underline{x}) \quad \rightarrow \quad \underline{\dot{q}} = \dot{q}_{x[j,i]} \underline{e_1} + \dot{q}_{y[j,i]} \underline{e_2}$$

$$\rho = \rho(\underline{x}) \quad \rightarrow \quad \rho = \rho_{[j,i]} \tag{5.3.3}$$

With this discretisation in place, a number of schemes are available for approximating spatial differentials in eqn (5.3.2). Each scheme will calculate the spatial gradient at a point in the same manner, using the values of surrounding array points to approximate the gradient over short distances. The degree of accuracy in this approximation can differ according to the points used.

The simplest approximation, analogous to the temporal approximation in eqn (5.3.1), would involve looking at the array value at $[j, i]$ and one other neighbouring point $[j, i - 1]$. The value change between these points can give an estimate of the gradient of a function, as long as the function is continuous.

$$\frac{\partial(\dot{q}_x \rho)}{\partial x}\bigg|_{[j,i]} \approx \frac{\dot{q}_{x[j,i]} \rho_{[j,i]} - \dot{q}_{x[j,i-1]} \rho_{[j,i-1]}}{\Delta x} \tag{5.3.4}$$

This is termed a backwards two-point scheme. *Backwards* refers to the fact that the neighbouring point $[j, i - 1]$ has been chosen in the negative x direction. *Two-point* refers to the number of array locations sampled within the scheme. FD schemes can be either forward facing, backward facing or two-sided depending on the points chosen. One scheme may suit a particular function more than another due to the characteristics of the chosen function. For example, for a very smooth continuous function it can be desirable to sample multiple points to improve the accuracy of the approximation. In general this is a way to lower the error associated with the final value [133]. However, for a jagged function in which the values change abruptly near the location of interest then the same approximation could sample an area of points much wider than a sharp feature and so the approximation would not provide an accurate local gradient measurement.

Substituting the temporal and spatial differentials into the continuity equation, and solving for

$\rho_{t+\Delta t}$, provides the updated dislocation density value at location $[j, i]$ after a short interval. If this calculation is performed at all locations then the dislocation density across the entire domain is updated and the quantity is said to have advected across the domain (at velocity $\underline{\dot{q}}$).

Depending on the advection direction of the density there is a preferable direction for the spatial FD scheme to face, in order to produce a better approximation. Backwards differencing is preferred when the direction of travel is in the positive direction along a principal axis and forward differencing is preferred when the travel is in a negative direction. In the case of an edge dislocation within a crystal it is possible for the direction of movement to be either positive or negative, as its velocity has been shown to depend upon the forces applied to it. These forces may also flip direction as a reaction to applied or internal stresses during the course of a FE simulation; therefore using a uni-directional scheme would not be appropriate to model this behaviour. To allow for this dynamic behaviour an *Upwind* approach was chosen. The upwind method switches between forward and backward schemes depending on the direction of travel, a decision which can be made simply by inspection of the sign of the velocity vector at the point of interest; this guarantees the best approximation under the local conditions.

For this model the forward and backward three-point schemes were found to be most appropriate for advection of dislocation density across the bulk material. Trials found this approximation best conserved the total density over long distances of advection and was less prone to numerical instability forming unwanted density spikes. The three-point scheme weights the contribution of different local points with a numerical constant and samples over a distance of $2\Delta x$ or $2\Delta y$. As the majority of motion within this model is in the positve direction then only the backwards differencing equations are displayed below:

$$\frac{\partial(\dot{q}_x\rho)}{\partial x}\bigg[_{j,i}\bigg] \approx \frac{3\,\dot{q}_x{\big[_{j,i}\big]}\,\rho{\big[_{j,i}\big]}\,-\,4\,\dot{q}_x{\big[_{j,i-1}\big]}\,\rho{\big[_{j,i-1}\big]}\,+\,\dot{q}_x{\big[_{j,i-2}\big]}\,\rho{\big[_{j,i-2}\big]}}{2\Delta x}$$

$$\frac{\partial(\dot{q}_y\rho)}{\partial y}\bigg[_{j,i}\bigg] \approx \frac{3\,\dot{q}_y{\big[_{j,i}\big]}\,\rho{\big[_{j,i}\big]}\,-\,4\,\dot{q}_y{\big[_{j-1,i}\big]}\,\rho{\big[_{j-1,i}\big]}\,+\,\dot{q}_y{\big[_{j-2,i}\big]}\,\rho{\big[_{j-2,i}\big]}}{2\Delta y} \tag{5.3.5}$$

Substituting eqns (5.3.1), (5.3.2) and (5.3.5) into continuity eqn (4.1.4) gives

$$\frac{\rho_{t+\Delta t[j,i]} - \rho_{t[j,i]}}{\Delta t} + \left(\frac{3\,\dot{q}_{x[j,i]}\,\rho_{t[j,i]} - 4\,\dot{q}_{x[j,i-1]}\,\rho_{t[j,i-1]} + \dot{q}_{x[j,i-2]}\,\rho_{t[j,i-2]}}{2\Delta x} \right)$$

$$+ \left(\frac{3\,\dot{q}_{y[j,i]}\,\rho_{t[j,i]} - 4\,\dot{q}_{y[j-1,i]}\,\rho_{t[j-1,i]} + \dot{q}_{y[j-2,i]}\,\rho_{t[j-2,i]}}{2\Delta y} \right) = 0 \qquad (5.3.6)$$

Solving for local $\rho_{t+\Delta t}$ gives the final equation for updating the density each iteration

$$\rho_{t+\Delta t[j,i]} = \rho_{t[j,i]} - \Delta t \left(\frac{3\,\dot{q}_{x[j,i]}\,\rho_{t[j,i]} - 4\,\dot{q}_{x[j,i-1]}\,\rho_{t[j,i-1]} + \dot{q}_{x[j,i-2]}\,\rho_{t[j,i-2]}}{2\Delta x} \right)$$

$$- \Delta t \left(\frac{3\,\dot{q}_{y[j,i]}\,\rho_{t[j,i]} - 4\,\dot{q}_{y[j-1,i]}\,\rho_{t[j-1,i]} + \dot{q}_{y[j-2,i]}\,\rho_{t[j-2,i]}}{2\Delta y} \right) \qquad (5.3.7)$$

This equation may estimate the evolution of dislocation density across the regular grid (left-hand side), using the state of the current system as input (right-hand side). Once an estimation is made the dislocation state can be recycled into the equation again, using the new velocity fields, until the required time period has been achieved through small timesteps.

Examples of different schemes are displayed graphically in Fig. 5.3.1. The point of interest in each case is denoted by a black dot and any points included in the gradient approximation (the reference domain) are highlighted as circles. Case A shows the Two-Point backwards scheme in the x direction around $\rho_{t[5,2]}$. Case B shows the Three-Point backwards scheme in the x direction around $\rho_{t[5,3]}$, while case C shows the same scheme in y direction around $\rho_{t[7,4]}$. Case D shows the combined possible reference domains (red or black), around $\rho_{t[5,6]}$, for the Three-Point Upwind Scheme used in this model.

NOTE: The narrower two-point schemes of the type in eqn (5.3.4) were used at hard boundaries and obstacles. These were implemented in the same way as the three-point schemes, but were necessary due to the large discontinuity of the density function across these barriers. As discussed, highly localised phenomena require a smaller reference domain for an accurate gradient estimation. It is also significant that at the edges of the grid the upwind behaviour was dropped, such that the scheme might always look inwards and not search for points outside of the domain.
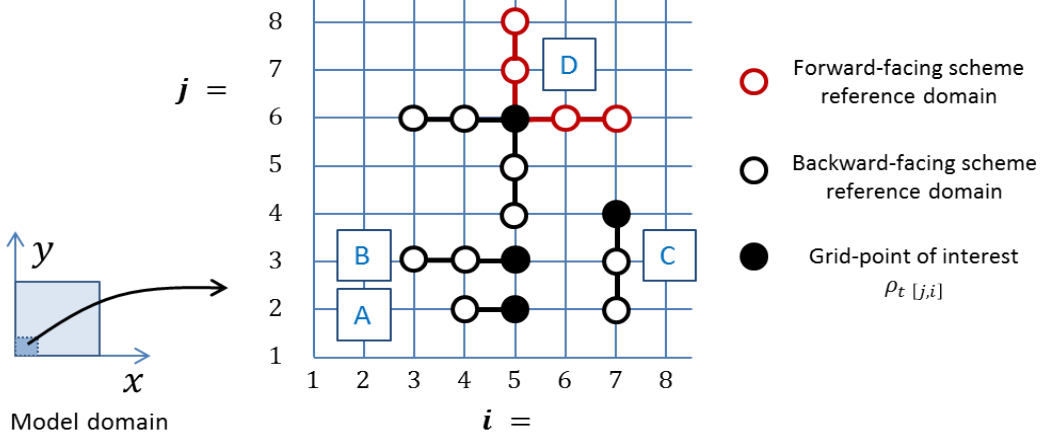
Figure 5.3.1: Discretised grid showing the reference domain for the spatial gradient calculation used in different FD schemes.

5.3.2 Error tolerance and iteration within Fortran

With the variable update equation having been derived in the previous section it remains for the iterating process to be set up within a computational environment: stepping forward through time steadily with a new prediction of a future state after interval Δt. This is achieved within a Fortran environment by setting up two nested loops for the indicies i and j which calculate the updated values for the entire grid. The loops contain logical operators to check the direction of the velocity at each grid location and choose the x and y FD scheme direction and type appropriately.

As the accuracy of the differential approximations is not known then eqn (5.3.7) may not just be applied once per timestep without check, in case the approximation errors build up to a large extent and invalidate the future predictions of the model. Instead it is necessary to check that the change in value at a grid-point after each time increment $\rho_\Delta^{\%}$ does not exceed a chosen error tolerance e_{tol}.

$$\rho_{\Delta[j,i]}^{\%} = \frac{\rho_{t+\Delta t[j,i]} - \rho_{t[j,i]}}{\rho_{t+\Delta t[j,i]}} \tag{5.3.8}$$

If the change in value is very large, and greater than the tolerance value, it can be a sign that the mobile quantity (the dislocation density) is moving too fast to be properly modelled by the FD equations; that the differential approximations are over-estimating and not properly capturing the dynamic system. In this eventuality both the timestep and the grid spacing may be altered

84

in order to bring the $\rho_\Delta^\%$ below tolerance and to an acceptable value for progression to the next step.

The current model utilises a dynamic time step for instances when tolerance is breached. After the initial update attempt is made the new values in the grid are checked using eqn (5.3.8) and if the change is greater than the allowed tolerance at any grid-point then the time step is halved and loops are reset with the original values. This is repeated until every $\rho_{\Delta[j,i]}^\%$ is less than e_{tol} and the FD subroutine can close, passing on the updated values and timestep.

The ideal value of e_{tol} was determined through trials using a 1D version of the dislocation continuity equation in a $10\mu m$ domain. This experiment found the value of 1E-4 was appropriate to prevent numerical instability. Such instabilities are immediately evident when viewing a plotted 1D function, appearing as jerky linear regions within the otherwise smooth function. The unstable regions may begin as small patches of "noise", but locally these have much larger gradients than the smooth areas and the oscillating nature introduces a positive/negative gradient flip for adjacent points. In practice this means that small errors quickly influence neighbouring regions, introducing errors to the gradient approximation of neighbouring points and travelling across the grid with successive iterations until the function is lost to the noise.

Similarly, the Gauss-Seidel iterative method was found to give the best results in a 1D testing environment. This method acknowledges the fact that during the progress of a FD loop some regions of the grid may be updated while other regions are yet to be calculated; it then states that any updated values for a current time step may be used in the approximation of the gradients for the remaining grid points [133].

This is achieved computationally through initialising $\rho_{t+\Delta t[j,i]} = \rho_{t[j,i]}$ at the start of each timestep, and then proceeding into the update loop with equation:

$$\rho_{t+\Delta t[j,i]} = \rho_{t+\Delta t[j,i]} - \Delta t \left(\frac{3\,\dot{q}_{x[j,i]}\,\rho_{t+\Delta t[j,i]} - 4\,\dot{q}_{x[j,i-1]}\,\rho_{t+\Delta t[j,i-1]} + \dot{q}_{x[j,i-2]}\,\rho_{t+\Delta t[j,i-2]}}{2\Delta x} \right)$$

$$- \Delta t \left(\frac{3\,\dot{q}_{y[j,i]}\,\rho_{t+\Delta t[j,i]} - 4\,\dot{q}_{y[j-1,i]}\,\rho_{t+\Delta t[j-1,i]} + \dot{q}_{y[j-2,i]}\,\rho_{t+\Delta t[j-2,i]}}{2\Delta y} \right) \quad (5.3.9)$$

This method coped adequately with the advection of the large ($\sim 10^{14}$) density values contained within this model as well as velocities from 0 - 1000 ms^{-1}.

5.3.3   Avoiding density conservation problems

One significant problem that is encountered when using Finite Difference Methods to model dislocation density is keeping the density contained within a slip plane if that plane is inclined away from the axis of the grid.

A physical dislocation system has glide and climb movements confined to perpendicular directions and along paths which can be considered perfectly straight within the plastic domain. This setup lends itself well to the FD grid system if the velocities are defined parallel to the grid axes and the two relative velocities may be progressed in separate terms. In practice this means that for instances where climb is negligible then the gliding dislocation density (having only velocity in the x-direction) will remain constrained within a single row of the grid and not leave the slip plane. Similarly for an element containing dislocation density that is climbing the side of an obstacle (with no glide velocity), all the density is constrained to a single column in the grid and does not progress along the slip plane. The movements are progressed discretely and the density is well conserved by the 1D nature of travel.

If the slip direction is set at an angle to the x-axis then the glide velocity has both x and y components. The density then travels across the grid points in a diagonal manner, passing density to adjacent i and j locations simultaneously, best approximating the route of a slip plane which does not necessarily line up with the majority of the FD gridpoints (see Fig. 5.3.2). Density can only be passed along rows and up or down columns of the grid; in this way for each timestep the majority of the density will advect along the required path; however a small amount of density will be passed into locations that do not lie upon the plane. This is an error associated with the non-conformity of the velocity vector and the grid points. The errant density in these locations will then be advected with the same velocity during the next step, such that a proportion will be moved even further from the original slip plane. The process continues for each timestep such that the density will appear to diffuse slightly from the desired slip plane. This numerical diffusion,

separate from the diffusion terms found within the governing equation, is a feature of the gridded FD method and, while acceptable for some unconstrained cases (i.e. modelling of gas diffusing through free space), it is not desirable in such a highly constrained system as dislocation dynamics.
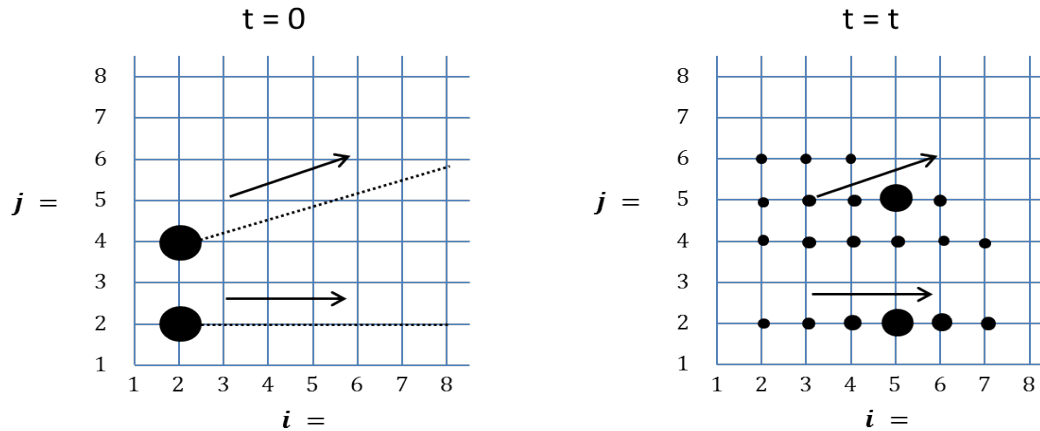

Figure 5.3.2: Illustration of the errors inherent in using a slip direction that is non-complementary with the FD grid.

In this work, choosing to investigate a single slip system aligned with the x axis of the grid simplifies the velocity components of eqn (5.3.9) to $\dot{q}_x = v_g$ and $\dot{q}_y = v_c$, which prevents these approximation errors and keeps the density conserved upon the slip plane.

5.4 Environmental Boundary Conditions For FDM

The boundary conditions within the Abaqus model can be used to simulate a range of experimental testing conditions for the external nodes of the single grain domain. Further internal microstructure boundary conditions can disrupt the dislocation flow and influence the plastic deformation within the domain. Together these conditions (along with the material constants used) will define the material stress response.

5.4.1 Applied strain rate and timesteps

In Section 5.2.1 the external boundary conditions have been described for the recreation of simple shear testing along the x-axis. For the chosen slip system and corresponding model plane these conditions promote the maximum shear stress σ_{12} that can be obtained through deformation, which in turn causes greater dislocation activity through increased generation and dislocation driving force f_1.

The applied velocity V on the top face of the domain has been set as an exponent of 10 multiplied by the height Y_0 of the domain, so that the strain rate $\dot{\epsilon} = \dfrac{V}{Y_0}$ itself becomes an exponent of 10. For $Y_0 = 5\mu$m a strain rate of $\dot{\epsilon} = 0.1$ s^{-1} is achieved by applying $V = 0.5\ \mu$ms^{-1} to the top face.

The current work contains simulations for strain rates of 0.01 s^{-1} - 100 s^{-1}. These values, while somewhat higher than the values typically experienced during the manufacturing or operating conditions of a nickel-based superalloy, were chosen due to limitations imposed by the timestep requirements of the FDM code (which have been noted in the literature for similar models [96]). The continuum dislocation dynamics and reactions from Sections 4.2 and 4.3 both occur over a very short length and time scale, forcing a much lower timestep than the Abaqus FE deformation.

Consider an element of dislocation density, within a 5 μm grain, experiencing a (high shear stress) phonon drag-controlled velocity of 500 ms^{-1}. The density would travel a 5 μm distance in 10 ns. This would mean the system would require a timestep of less than 10 ns in order to resolve details of the intermediate journey and prevent the density crossing the length of the grain in a single step. Furthermore, to resolve progress and interaction of the dislocation field between discrete particles spaced 100 nm apart a timestep of 0.2 ns or lower is required. The rapid acceleration of dislocations has been remarked upon by Gurrutxaga-Lerma et al [122] where simulations have shown dislocations reach speeds of $\sim$3000ms^{-1} in times increments under 10^{-12}s.

In this work the FDM code starts with an initial timestep of 2 ns which changes dynamically with the velocity of the dislocations, down to a minimum of 0.005 ns.

The Abaqus UMAT is not similarly restrictive regarding the selection of an appropriate timestep. The equations for stress evolution (detailed in Section 4.6) require only the value of the shear rate during a given time interval in order to progress to the next step, and so the Abaqus FE section of the model may run at a larger timestep of Δt_{abq}. The shear rate $\dot{\gamma}_{abq}$ over this time period may be calculated as the sum of the shear increments from the FDM timesteps divided by the larger Abaqus timestep.

$$\dot{\gamma}_{abq} = \sum_{t=0}^{\Delta t_{abq}} \frac{\dot{\gamma} \, \Delta t}{\Delta t_{abq}} \tag{5.4.1}$$

This split timestep allows the model to save a significant amount of computational walltime and calculation by reducing the number of calls to the FE solver. However, for simulations modelling a long time period, the speed of the simulations is still limited by the smaller FDM timestep. For this reason the relatively high strain rates were investigated in this work, bringing down the total simulation time and allowing simulations to progress to an appreciable amount of total strain before hitting a walltime limit.

5.4.2 Edge conditions

At the left and right edges of the domain, within the FE setup, Periodic Boundary Conditions (PBCs) for displacement have been implemented. These PBCs produce a uniform elastic stress state across the domain in the pre-plastic deformation period.

Within the FDM code the domain edges may be handled in different ways depending on how the dislocation content interacts with the boundary. The first case, in this work termed the *open coundary condition*, is the case when the dislocation density is free to leave the simulation domain by travelling up to the edge-most gridpoint and proceeding unperturbed. As the Finite Difference grid has no points outside the domain, it is necessary for the numerical scheme to always look inwards at the domain edges regardless of the Upwind direction. The density information is lost as the density leaves the domain. This is analogous to the case when a single crystal is deformed and edge dislocations that reach the edge of the crystal disappear to become physical steps on the exterior.

The second case is the *closed boundary condition* where the dislocation density is stopped at the edge of the domain. This is achieved within the FDM code by installing the condition $v_g = 0$, for the duration of a simulation, at grid-points along the edges. The domain edge then becomes a hard barrier to slip, causing dislocation density to pile-up against it. This is similar to the situation when a grain is part of an agglomerate and the neighbouring grain has non-complementary orientation meaning that dislocations cannot slip across the grain-boundaries. The analogy is not exact in this case as the model does not account for the external tractions applied by these neighbouring grains within the Abaqus setup, only for the obstacle effect on dislocation slip in the FDM.

5.4.3   Microstructure using Obstacle files

The material domain within the FDM code exists as a bulk γ matrix, initiated at all elements, which can be overlayed with γ' particles in the form of obstacle elements. These obstacle elements are assigned a State Dependent Variable (SDV) flag which causes the UMAT to specify a different set of stiffness constants to the bulk material when calculating the local stress states.

Within the FDM code this obstacle flag also causes specific velocity conditions to be set for dislocation density at flagged grid-points. After the calculation of the local velocity from the motive force in Section 4.3, the initial condition $v_g = 0$ is set at all obstacle points. This causes moving density to pile up against the γ' elements as they act as hard obstacles to slip. The velocity condition is removed when the shear stress exceeds the threshold given in eqn 4.4.11.

The obstacle locations are generated using a placement code which produces a random distribution of particles for a specified radius r and volume fraction ϕ_L (see Fig. 5.4.1). The minimum resolution for an obstacle is the size of the FE element. As the elements within this work are 100 nm square then the particles are modelled as planar cross-sections of cuboidal shapes with a minimum radius of $r = 50nm$. TEM observations have shown that secondary particle radii can range from 40nm - 500nm [14][13], allowing all but the smallest possible secondary particles to be modelled. The tertiary particles, much smaller still, are instead included through the mean-field line tension effect detailed in Section 4.3.2.

$\phi = 0.35$, r = 50nm $\qquad$ $\phi = 0.35$, r = 100nm $\qquad$ $\phi = 0.35$, r = 150nm
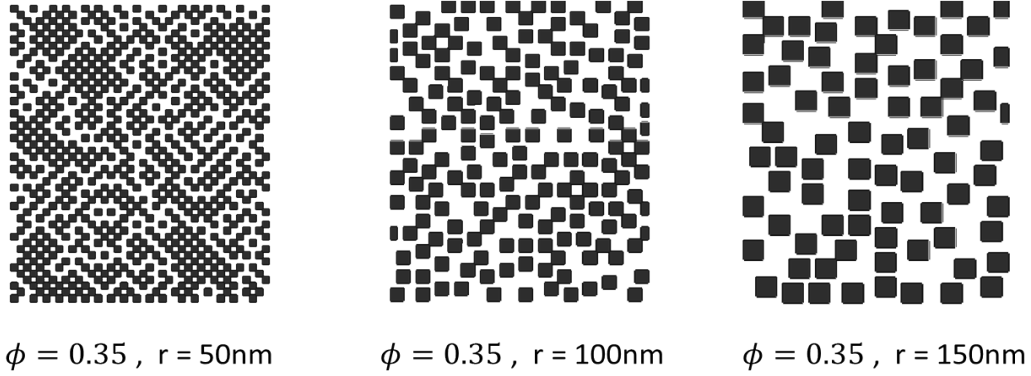
Figure 5.4.1: Example 2D distributions of uniformly sized particles for constant volume fraction $\phi = 0.35$ and differing radii r

5.4.4 Dislocation sources

Source operation

Dislocation sources are assigned to a given element in the same way as γ' obstacles, using an SDV flag. Each source element is assigned a Frank-Read source length l_{FR} from a random distribution with an average value of 76.2 nm ($300b$) ± 12.7nm ($50b$). This value is used within generation threshold equation (eqn (4.5.3)) to determine the shear stress above which a source will activate and begin emitting dislocation density. Using the typical model conditions within this work ($T = 973$K, $b = 0.254$ nm) the average shear stress source generation threshold becomes 46.3 MPa.

A nucleation time t_{nuc} applies to a Frank-Read source, signifying the time spent for the dislocations to bow out to a critical distance value. As the local glide velocity increases from 1 ms^{-1} to 100 ms^{-1} then the corresponding nucleation time decreases from 37.5 ns to 0.375 ns. This time period is interpreted within the model as the waiting time between individual generation events i.e after a generation an activated source will go inactive for a time equal to t_{nuc}.

Because the nucleation time at any instance changes with the local dislocation velocity at the source, which is in turn related to the stress in that element, then the period of time that source

remains inactive is changing dynamically with each time increment as the local conditions change. To handle this then the waiting time since the last generation, t_{wait}, is recorded for each source. The changing nucleation time is also tracked for each source at each increment. When the waiting time exceeds the nucleation time $t_{wait} > t_{nuc}$ then the source will generate again. If the local nucleation time changes between two increments then the lower of the two nucleation times is used for the comparison.

The amount of density ρ_{source} added to an element per generation event is 10^{14} m^{-2}. This was established by defining a unit cell for the mean area that contains one γ' particle as being 100nm^2: from such a definition the density of a single dislocation in this cell is on the order of 10^{14} m^{-2}. This value aligns with the SEM and TEM observations of nickel-based superalloys LEK 94 and CMSX-4 which have seen densities of $5\times10^{13} \sim 5\times10^{14}$ m^{-2} at γ/γ' boundaries [134][135][136], and also with density values produced in recent CDD models for this type of alloy [107]. Further observations of slip bands in deformed nickel-based superalloys have seen band widths of $\sim$ 100nm [130][131], which ties neatly with the dimensions of the unit cell (as at least one dislocation must have been present in these bands).

As the tetragonal element size in this model is also $\Delta x = \Delta y = 100$ nm, the ρ_{source} density over this element area leads to the value $\rho_{source}\Delta x\Delta y = 1$. By analogy to previous planar DDD models which average dislocation densities through the number of edge dislocations N divided by the height Y_0 and width X_0 of the domain $\rho = \frac{N}{X_0 Y_0}$ (e.g. Van Der Giessen and Needleman in 1995 [94]), this ρ_{source} value is equivalent to creating one single positive edge dislocation in an element per generation event. The total dislocation density in the domain ρ_{tot} can then be calculated using

$$\rho_{tot} = \frac{1}{X_0 Y_0} \iint_{N_e} \rho(\underline{\boldsymbol{X}})\Delta x\Delta y \; d^2\underline{\boldsymbol{X}} \tag{5.4.2}$$

where N_e is the collection of elements composing the domain. This approach has been adopted in 2D DDD/CDD comparison work before [124] and resultant flow stress curves and dislocation density profiles have shown to be comparable. Other CDD models have tied quasi-discrete FR source generation density to the minimum resolution of the model, with Sandfeld et al [137] choosing 8×10^{12} m^{-2} as this constituted the shortest dislocation loop length available in their 2.5D model. Further values for initial element densities have ranged from 1×10^{14} to 2×10^{16} m^{-2} depending on

the simulation domain [102][106][132].

Generally the timestep between increments adapts to be less than the nucleation time. However, in instances when the timestep is larger than the nucleation time then the amount of density generated at a source element is scaled up by $\frac{\Delta t}{t_{nuc}}$ to account for multiple generation events in a single increment.

Source location

The work of R. A. Varin *et al.* [63] has cited grain boundary sources as the key source of plastic deformation in metal polycrystals. This work further states that any model of grain boundary sources must satisfy two criteria: first, to generate at applied shear stresses of between $\frac{G}{1000}$ and $\frac{G}{400}$; second, to be capable of generating a large number of dislocations from a single source. The sources within this work meet both of the above criteria, with the quoted shear stress range translating to 55-140 MPa for standard model conditions and each source able to generate as frequently as permitted by the nucleation time.
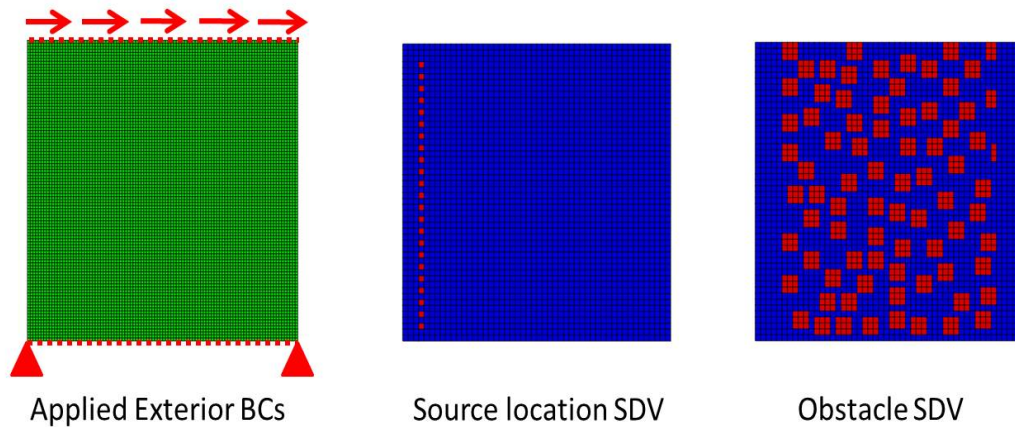
Figure 5.4.2: Example of applied boundary conditions, and SDVs used, for a simulation of a 5 μm grain with coarse particles of 150nm radius and positive-edge sources on the left-hand side.

Sources are assigned to elements near the domain edge. As it is positive edge type dislocations that

have been predominantly modelled, then the positive sources have been located on the left-hand side of the grains. A dislocation with a positive Burgers vector will move from left to right along the slip plane so this source positioning allows for maximum potential slip across the grain before the dislocation meets the opposite grain wall. Figure 5.4.2 shows the Finite Element setup of the boundary conditions and SDVs for a simulation with 150nm particles.

In all instances sources have been spaced at least 100nm apart, so as not to physically overlap or grossly interfere with each other. Source proximity can however have a significant effect on source operation as the repulsive stress fields of new dislocations may reduce the local stress at nearby sources; the effect of spacing and number of sources has been investigated in Section 6.2.

5.5 Material Parameters

The material parameters for this work have been sourced from literature. The aims of this work are to generate the general physics appropriate to the broader class of precipitate strengthened nickel-based superalloys, rather than to emulate a specific alloy. As such the chosen material constants are assumed to be representative of typical first/second generation alloys from this class, and the numerical investigation will focus more directly on the influence of different microstructural features on dislocation evolution (a common approach adopted for dislocation modelling for these materials [83][97][107][108]). Details of other assumptions, along with the constants and parameter ranges used for all simulations in the results section, are provided below.

5.5.1 Stiffness of Matrix and Particles

The elastic stiffness constants that describe the elastic stress-strain relation of a crystal exist as a fourth rank stiffness tensor $\underline{\underline{\underline{C}}}$. Making use of the isotropy in FCC crystals this tensor can be reduced to the second rank tensor $\underline{\underline{C}}$, which applies more readily to a 2D plane strain setup:

$$\underline{\underline{C}} = \begin{bmatrix} C_{11} & C_{12} & C_{12} & 0 & 0 & 0 \\ C_{12} & C_{11} & C_{12} & 0 & 0 & 0 \\ C_{12} & C_{12} & C_{11} & 0 & 0 & 0 \\ 0 & 0 & 0 & C_{44} & 0 & 0 \\ 0 & 0 & 0 & 0 & C_{44} & 0 \\ 0 & 0 & 0 & 0 & 0 & C_{44} \end{bmatrix} \tag{5.5.1}$$

The three distinct components of this tensor C_{11} C_{12} and C_{44} may be measured experimentally using Acoustic Emission Transmission (AET) [138] or dynamic resonance technique [139], often giving quite different results for similar alloy compositions depending on the method used [140].

More recently there have been efforts to calculate these constants from first principles using Density Function Theory (DFT) and a number of different solvers. Generally the calculated values of C_{11} and C_{12} come in marginally higher than experimental values. In 2018 Luan *et al.* [141] used the Cambridge Sequential Total Energy Package (CASTEP) software to determine a room temperature C_{11} value for Ni$_3$Al that was more than 15 GPa greater than the experimental value of 224 GPa.

The shear component C_{44} in this case was better aligned with the experimental value and within 2 GPa. The constants change with temperature, and so valid definitions over the operational temperature range of a given superalloy are required in order to study temperature effects within the model.

In some literature [140] the experimental data is taken from samples containing agglomerates of grains, making the findings unsuitable for the modelling of a single grain with this model. The discrete precipitate regions in the domain also require separate constants. No single literature source was found that contained extensive data for both the γ and γ' phases of a nickel superalloy over the temperature range under investigation (773K-1273K). Furthermore, in many instances the material history is not presented and experiments were carried out only at room temperature or very high temperature ($\sim$ 1273K), which would have required an undesirable linear interpolation between two data points from multiple authors. The matrix and precipitate data was therefore collected seperately from papers which did cover the required range. The matrix data was sourced from the experimental work of L. Di Masso et $al.$ [138] who tested single crystal CMSX-6 superalloy at high temperature using ultrasound reflection. CMSX-6 is a typical particle strengthened alloy used with aircraft turbine manufacture [142] [143], and so is an appropriate choice for use as the base of a general two-phase model. The values for the precipitate were taken from S. V. Prikhodko et $al.$ [144], who tested a similar temperature range for single crystal ordered Ni$_3$Al, a constituent of the second phase. A polynomial line was fitted to these results to yield a function of temperature which could interpolate stiffness constants for subsequent simulations.

For the bulk matrix material the temperature dependence of the stiffness was calculated as:

$$
\begin{aligned}
C_{11} &= -2\mathrm{E}^{-5} \ T^2 \ -1.89\mathrm{E}^{-2} \ T \ +241.16 \\
C_{44} &= -1\mathrm{E}^{-5} \ T^2 \ -1.53\mathrm{E}^{-2} \ T \ +129.17 \\
C^* &= -9.2\mathrm{E}^{-3} \ +49.33 \\
C_{12} &= -\left(2C^* - C_{11}\right)
\end{aligned}
\tag{5.5.2}
$$

where temperature T is in units of Kelvin and the constants are expressed in GPa.

For the γ'-precipitate the same functions were calculated as:

$$C'_{11} = -1\text{E}^{-5}\, T^2\, -1.74\text{E}^{-2}\, T\, +235.31$$

$$C'_{12} = -1\text{E}^{-5}\, T^2\, -5.30\text{E}^{-3}\, T\, +153.12$$

$$C'_{44} = -4\text{E}^{-6}\, T^2\, -2.54\text{E}^{-2}\, T\, +131.64 \qquad (5.5.3)$$

5.5.2 Dislocation transport parameters

In this work both the internal characteristics of the material domain and the applied external conditions are altered to investigate how this affects the trends in deformation behaviour. A control configuration of the system was required in order to base the comparisons in the following FDM results sections. This configuration is created using the *control parameters*. For all simulations that are presented, any model parameter that is not explicitly defined in the text or figure caption is assumed to take the control value.

The control parameters are given in Table 5.5.1. Some parameters, including Burgers vector magnitude, jog height, activation energy and anti-phase boundary energy have been kept constant universally, while others such as grain size and temperature are varied in later results sections. Most results are presented for a variety of jog spacings between 100 - 1000b (25.4 - 254nm), as experimental observations of jog spacing are seen to vary significantly depending on the work history of an alloy [145] [146]. A spacing between dislocation sources of 200nm was used as standard as this was found to produce a good plastic response.

To maintain accuracy within these simulations, the Finite Difference timestep within the model is required to be less than 2 ns (see Section 5.4.1): a limitation due to the high glide velocity over a short domain. Because this velocity scales with the local stress, it does not change significantly for a lower applied strain rate, and so the small FD timestep must be maintained in all simulations. For low strain rates, when the timescale for the deformation increases, more timesteps are required to reach a given strain and so the simulation becomes more computationally expensive (e.g taking over 3 weeks to produce the 0.01 s^{-1} curve). To reduce this computational expense this work uses a standard strain rate of 100s^{-1}.

A value of 2.56x10³ Pa⁻¹s⁻¹ has been used for the dislocation mobility parameter M. This was based upon both the simulations of Dongsheng Li et al [115] and the experimental work of Urabe and Weertman [116], which were considered in Section 4.2.2 . This value is half of that predicted by eqn (4.2.4), but is far closer to the measured values for this type of FCC alloy, and produces velocities within the expected range [25].

Table 5.5.1: Details of the control parameters (used in all simulations unless stated otherwise)

Parameter	Value	Reference
b (m)	$2.54{\times}10^{-10}$	[113]
ν	0.33	[147]
a_v (m^3)	$1.64{\times}10^{-29}$	Calculated as $\frac{4}{3}\pi\left(\frac{b}{2}\right)^3$
$D_{s,0}$ (m^2s^{-1})	10^{-4}	[148]
Q (kJ)	310	[113]
E_{APB} (J)	0.2	[113]
h_{jog} (m)	$2.07{\times}10^{-10}$	Calculated as $\frac{\sqrt{2}}{\sqrt{3}}b$
λ_{jog} (m)	$2.54{\times}10^{-8}$	[145] [146]
T (K)	973	-
μ [at 973K] (GPa)	54.69	[138]
Material density ϱ (gcm^{-3})	7.98	[143]
v_{sound} (ms^{-1})	$2.61{\times}10^3$	Calculated as $\sqrt{\frac{\mu}{\varrho}}$
M $(\mathrm{Pa}^{-1}\mathrm{s}^{-1})$	$2.56{\times}10^3$	[115]
Grain size d (m)	$5{\times}10^{-6}$	-
L_{FR}	$250b \leftrightarrow 350b$	[149]
Source spacing (m)	$2{\times}10^{-7}$	-
Number of sources	23	-
Generation density ρ_{source} (m^{-2})	10^{14}	Section 5.4.4
Applied strain rate $\dot{\varepsilon}$ (s^{-1})	100	-

Chapter 6

Full-field Simulations I: Pure Matrix

Assumed geometry for this chapter

Within this chapter the numerical results from Abaqus FE simple shear tests are presented for the case of a single crystal domain containing only γ phase. The model geometry is in plane-strain as depicted in Fig. 5.2.2, with the X_{Length}/Y_{Length} edge dimensions set to 5 μm (except in Section 6.6).

The control parameters for the simulations are established in the previous Section 5.5.2. These parameters are taken as the default while individual parameters are varied in each section. The default applied strain rate rate was 100s^{-1} and the temperature was 973K. As this setup describes a crystal of only the bulk matrix phase, these simulations will be referred to as either *Pure-Matrix* or *Open-Matrix* interchangeably.

Results analysis

Results will be presented largely in the form of domain-averaged (macro) flow stress curves. If the microstress and microstrains at position $\underline{\boldsymbol{X}}$ are $\underline{\underline{\boldsymbol{\pi}}}(\underline{\boldsymbol{X}})$ and $\underline{\boldsymbol{\epsilon}}(\underline{\boldsymbol{X}})$ respectively, then the macro-value counterparts can be given by the volume average over the domain Ω

$$\underline{\underline{\boldsymbol{\sigma}}} = \frac{1}{V_\Omega} \iiint_{N_e} \underline{\underline{\boldsymbol{\pi}}}^{\infty}(\underline{\boldsymbol{X}}) \, d^3\underline{\boldsymbol{X}} \qquad\qquad \underline{\underline{\boldsymbol{\epsilon}}} = \frac{1}{V_\Omega} \iiint_{N_e} \underline{\boldsymbol{\epsilon}}(\underline{\boldsymbol{X}}) \, d^3\underline{\boldsymbol{X}} \qquad\qquad (6.0.1)$$

where V_Ω is the volume of the domain and N_e is the collection of elements that compose it. As this model is applied within a plane-strain setup then the area average over the 2D simulation domain is used to calculate the macrostress. (Shear stress $\tau \equiv \sigma_{12}$ is plotted against applied shear strain).

6.1 Penetrable and Impenetrable Grain Boundaries

The effect of imposing closed and open $\underline{\underline{\alpha}}$ flux boundary conditions on the flow stress at 973K and $100s^{-1}$ is shown in Fig. 6.1.1 for a 5μm square grain. For both cases yield occurs after 0.36 % applied strain with a shear stress of 170 MPa. The open boundary grain has a post-yield behaviour that is almost ideally plastic - running on to 3% strain with only a small stress increase of ~ 25 MPa. The closed boundary grain shows considerable hardening post-yield, with the stress increasing by ~ 400 MPa. The hardening rate in latter case is linear. The contrast between the two simulations is stark as the dislocation content flows unobstructed out of the open boundary domain but is caused to pile-up on the grain wall of the closed boundary domain. In this instance the stress field from the large static dislocation content produces two mechanisms for hardening within the grain. Firstly, the motive force upon a dislocation approaching the pile-up is reduced due to the repulsive stress from the pile-up, lowering the velocity of the mobile dislocation. Secondly, the dislocation backstress will also lower the effective stress at the dislocation sources behind the pile-up, causing fewer generation events within the grain. A combination of slower moving dislocations and less dislocation content available within the grain significantly lowers dislocation activity and so also the plastic shear rate.

Fig. 6.1.2 shows the total dislocation source activity within the grain during these simulations. In both instances initial generation events are seen to occur at $\sim 0.1\%$ strain, followed by a period of inactivity until yield. Activation of the dislocation sources occurs at the generation stress threshold (see Section 5.4.4), thereafter dislocations are emitted and propagate at a jog-controlled velocity. For this simulation, the jog-controlled velocity after initial generation is low and the dislocation stress fields render the sources inactive until the density field can be advected away. Once the stress has built to $\sim$170 MPa the jog-controlled velocity of the emitted field ahead of the sources is large enough and the density begins to move across the domain more effectively. At this point the sources can resume operation and generation events begin to occur at a steady rate in both simulations. As expected the rate of generation is lower for a grain with an impenetrable boundary, due to the back stress acting on sources as dislocation pile-ups develop.
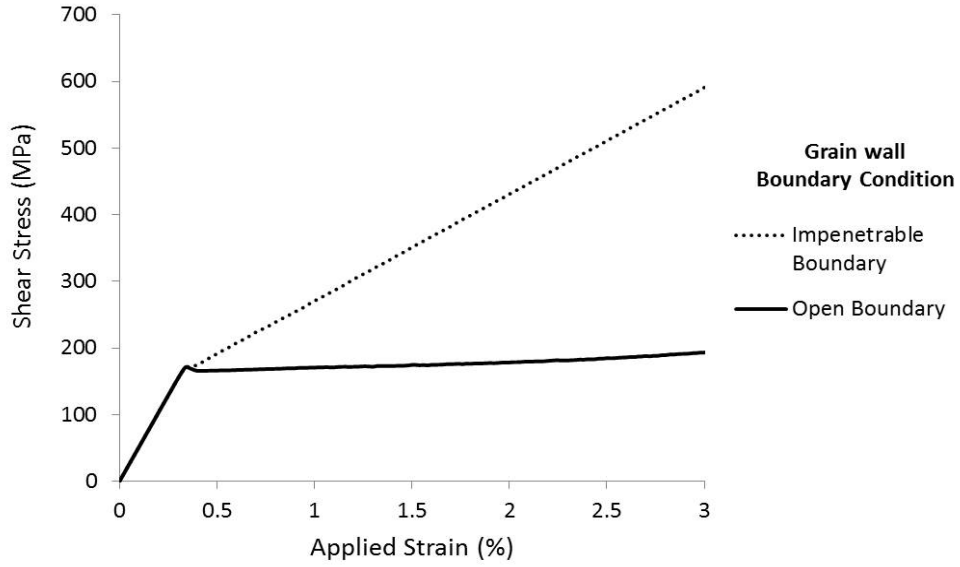
Figure 6.1.1: Flow stress response for identical grains with open or closed grain-wall boundary conditions ($\lambda_{jog} = 25nm$).
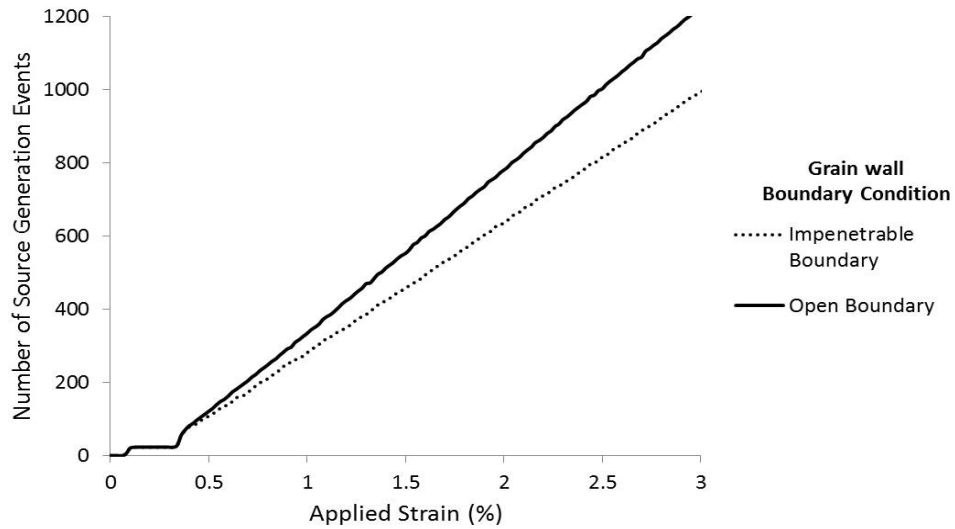

Figure 6.1.2: Number of dislocation generation events during deformation for identical grains with open or closed grain-wall boundary conditions ($\lambda_{jog} = 25nm$).

6.2 Effect of Dislocation Sources on Flow Stress Behaviour

6.2.1 Number of sources

The effect of dislocation source concentration within a grain was investigated by varying the number of grain-boundary sources on the domain wall. Fig. 6.2.1 shows slip band formation after 3% applied strain for the source spacings ranging between 200nm and 1 μm. Regions of plastic deformation are clearly defined and seperated by interstitial elastic regions with no dislocation activity which have F_{12}^p values of 0.
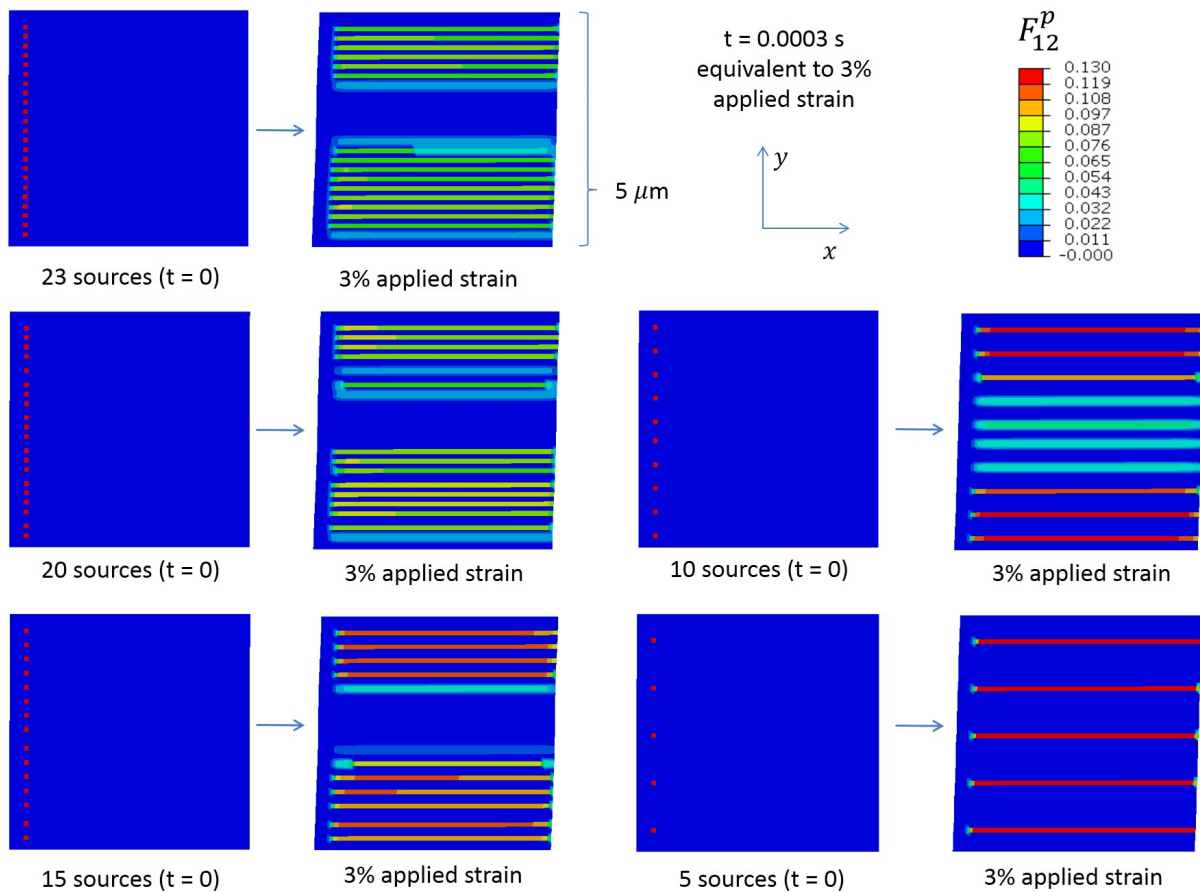
Figure 6.2.1: Plasticity maps (showing the shear component of the plastic deformation gradient tensor) for simulations with a differing number of sources placed across the left-hand grain wall ($\lambda_{jog} = 25$nm)

The average magnitude of the F_{12}^p values within the slip bands increases as the number of sources is reduced. This is expected as the same strain is applied to all grains, but the number of slip bands available to share the plastic deformation is reduced. In the simulation with only 5 available sources the plastic deformation in each band is the largest, with the individual sources generating at the highest observed rate and the 5 slip bands sharing the plastic shear evenly. As the number of sources is increased the plastic shear is spread over more bands and the deformation sharing becomes less even. In the 10 source simulation the slip bands near the top and bottom of the domain contain more slip activity than those in the middle.

Fig. 6.2.2 shows the variance of the local shear stress ($\pi_{12}^\infty + \pi_{12}^d$) along the left-hand domain boundary. It can be seen that the stress undulates with changing height such that the minima correspond with the locations of the boundary sources, since the plastic shear reduces the elastic strain in this vicinity, dropping the local stress. The maxima fall within the elastic domains between the slip bands. Both the minima and maxima follow a trend that they are lowest towards the middle of the grain, aligning precisely with the regions of low plasticity in Fig. 6.2.1. The minima vary over a small stress range of 110-140 MPa, occurring just below the threshold at which a dislocation will accelerate through the jog-drag and cause yield (see Section 4.2.2). The maxima, however, in the regions without the mitigating effect of plasticity, vary over a much wider stress range and the absolute stress values increase as source number is reduced. For the 10 and 5 source case, where there is wide enough spacing to resolve stress changes between slip bands, it can be seen that the stress is highest directly adjacent to the slip band and forms a local minima in the centre of the elastic region.
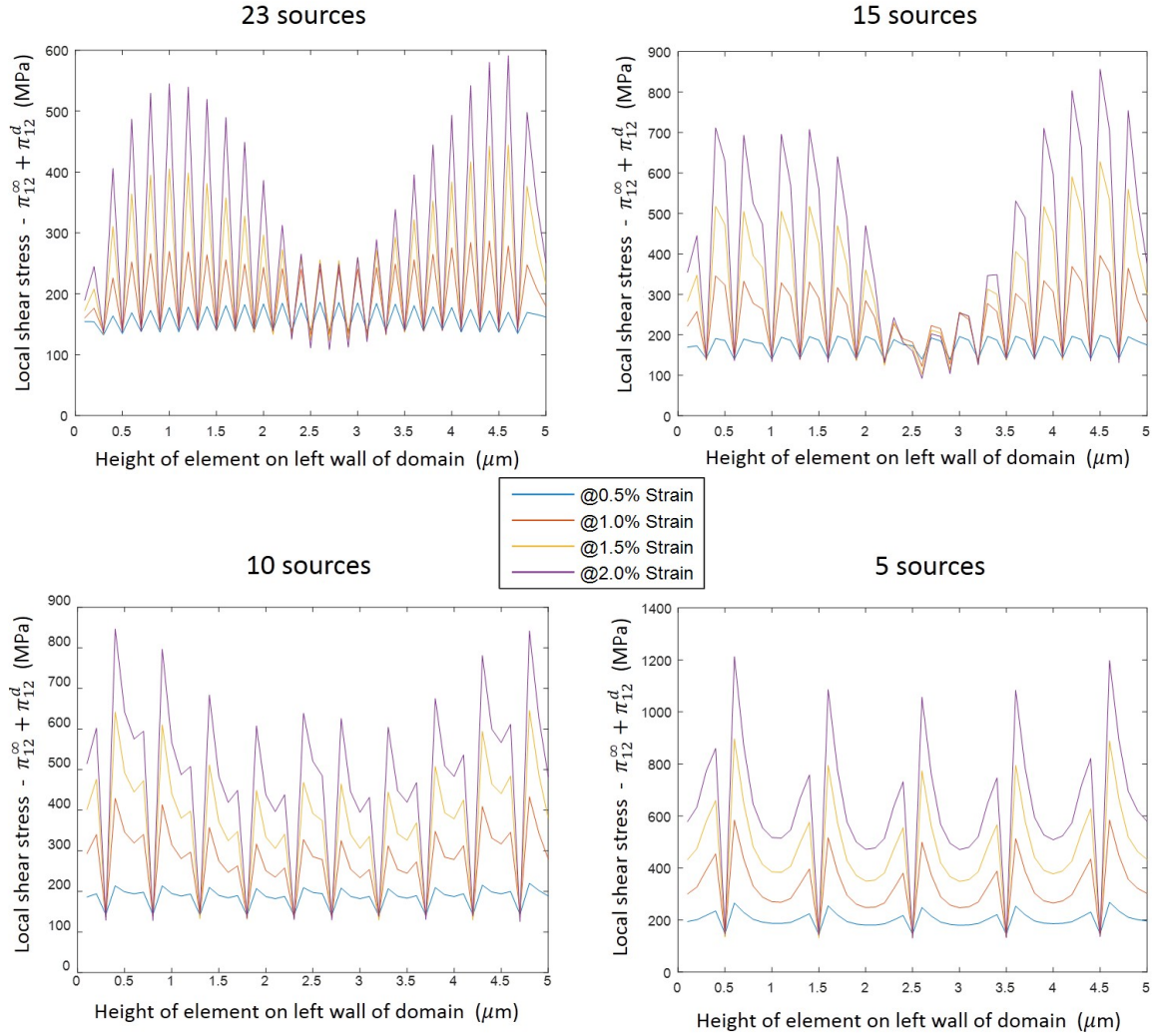
Figure 6.2.2: Shear stress fields for a verticle cross section of the domain, taken level with the dislocation sources, for increasing applied strain, when different numbers of sources are present.

The accompanying flow stress behaviour and source generation count for these simulations is shown in Fig. 6.2.3. The simulations all yield at the same point, but softening post-yield is shown to increase with source concentration. When fewer sources are present the domain must still accommodate the same amount of deformation, associated with the fixed strain rate, but with less plasticity available due to reduced source activity this leads to an increase in the strain hardening rate. The 23 source simulation showed the most ideally plastic behaviour and so was used as the control setup for all simulations in later sections. It has been shown in Fig. 6.2.1 that the amount

of sources present does not necessarily equate to the total active slip bands at a given time, but the use of 23 evenly spaced sources allows the maximum opportunity for slip to occur during deformation without sources occupying adjacent elements and negatively impacting source operation. This choice of maximum source density is justified by the fact that the 2D model deals with a single slip system, where in reality further out-of-plane slip systems would offer more opportunity for plastic flow.

The total dislocation generation within the grain is shown in Fig. 6.2.4 where it can be seen that the greater dislocation source activity corresponds with softer flow stress curve. It is also evident that the amount of dislocation generation does not scale linearly with the number of sources available. For the 5 source simulation the total generation after 3% applied strain (620 events) is approximately half of the generation for the simulation with 23 sources (1248 events). This result is consistent with the higher flow stress for the 5 source grain, but implies that the individual sources are generating at a greater rate than those in the 23 source grain. Averaging to find the number of generations by an individual source in each of these simulations gives 124 for the 5 source case, 87 for the 10 source, 69 for the 15 source, 59 for the 20 source and 54 for the 23 source. This implies that when fewer dislocation sources are available within a grain, those sources will generate more often than in a grain with higher source density.

The data in Fig. 6.2.2 is consistent with this observation, with the average stress at the dislocation sources being lower for the simulations with higher source density: 137.9 MPa for the 23 source case and 145.9 MPa for the 5 source case, at 0.5% strain.
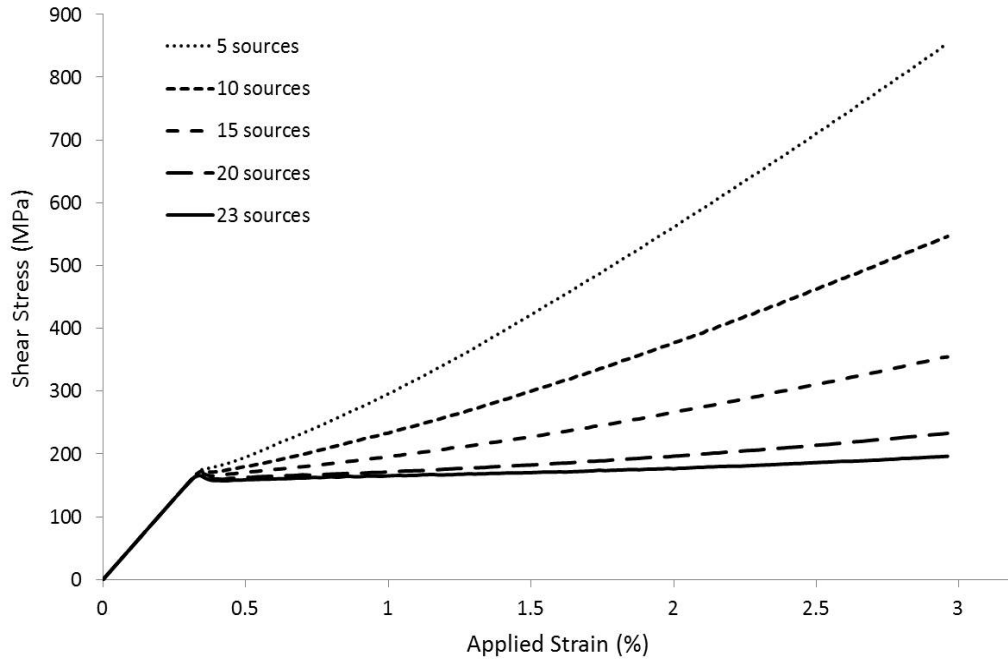
Figure 6.2.3: Flow stress response for the a grain with a differing number of sources placed across the left-hand grain wall ($\lambda_{jog} = 25nm$).
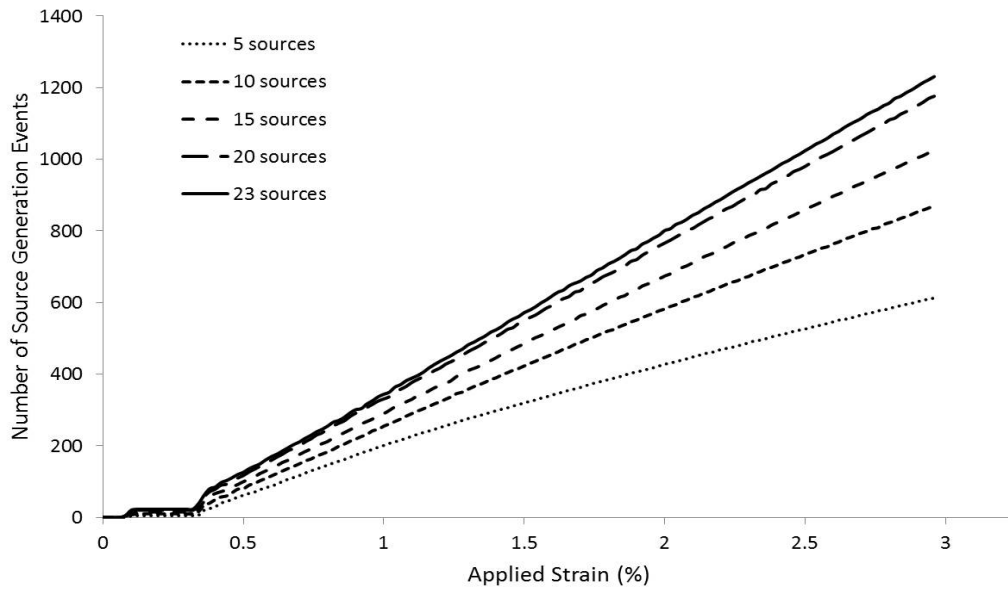
Figure 6.2.4: Number of dislocation generation events for the a grain with a differing number of sources placed across the left-hand grain wall ($\lambda_{jog} = 25nm$).

106

6.2.2 Distribution of sources

By keeping the number of sources uniform, and changing only their location, the influence of the distribution of slip bands on the deformation kinematics of the computation domain can be investigated. Fig. 6.2.5 shows the slip activity for three distinct arrangements of 10 boundary sources within a 5 micron grain. The initial domain shape is indicated by the dotted area, deviation from this original state naturally increases with applied strain, as does F_{12}^{p}. Shear deformation in the FE model is greatest where the dislocation activity is high. This is best observed in arrangements B and C when the slip bands are grouped together more closely; in these cases there is an elastic region at the top of the grain where no sources are active and a plastic region below where the grain walls are seen to slope at a greater angle. The source spacing for arrangement A is 500nm, for arrangement B is 300nm and for arrangement C is 200nm.
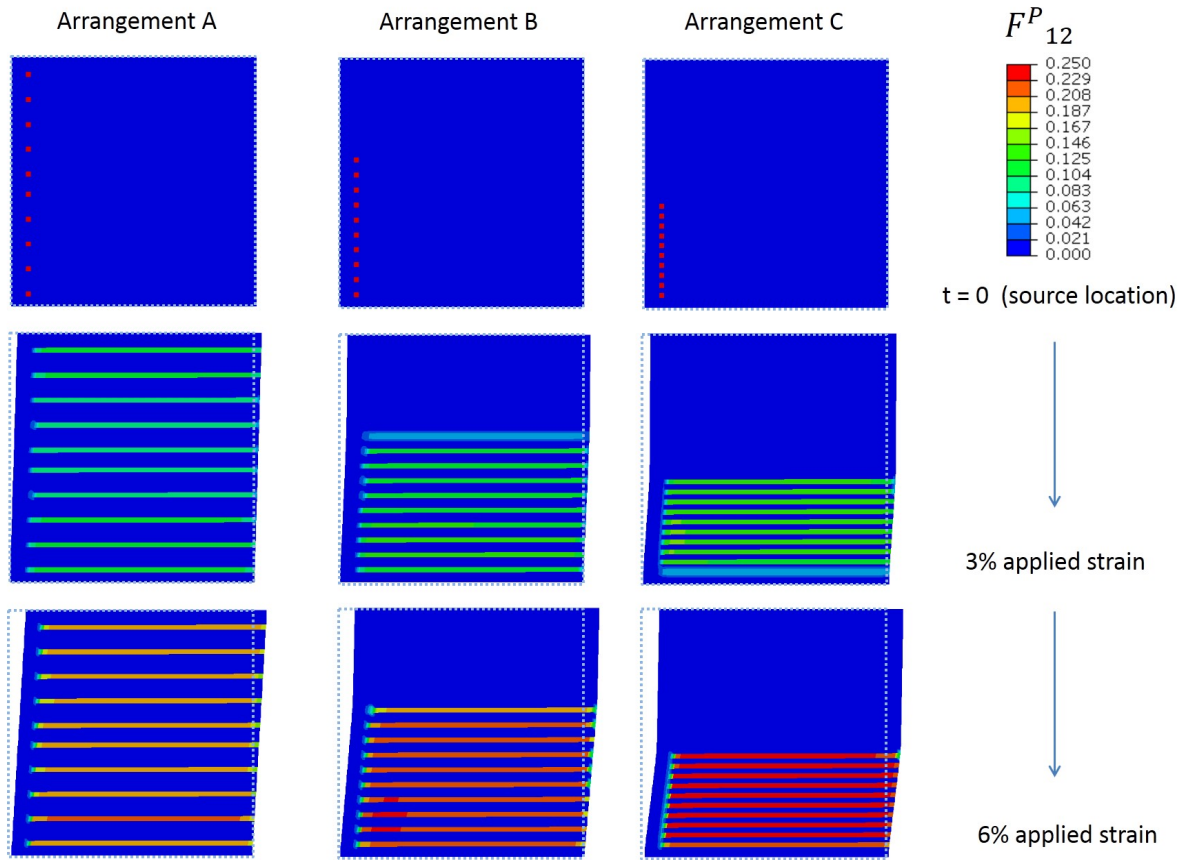
Figure 6.2.5: Plasticity maps evolving with applied strain (showing the shear component of the plastic deformation gradient tensor) for simulations with different placement of sources ($\lambda_{jog} = 25$nm): Initial state is illustrated by the dotted square.

Non-uniform deformation also effects the flow stress of the crystals, plotted in Fig. 6.2.6, with the highest flow stress response occurring when the sources are spaced evenly 500nm apart. In the simulations where the sources are arranged in closer proximity to each other the curves have increasingly soft responses. Each time the source spacing is increased the corresponding increase in flow stress becomes smaller, until the difference between the curves with 400nm and 500nm spaced sources is relatively small. Each curve shares the same yield point, after which the differences become apparent, in agreement with Fig. 6.2.5 a higher level of plasticity is shown in Arrangement B and C, causing lower stress at a given applied strain. At high strains of $> 4\%$ the curves begin to show a similar hardening rate.
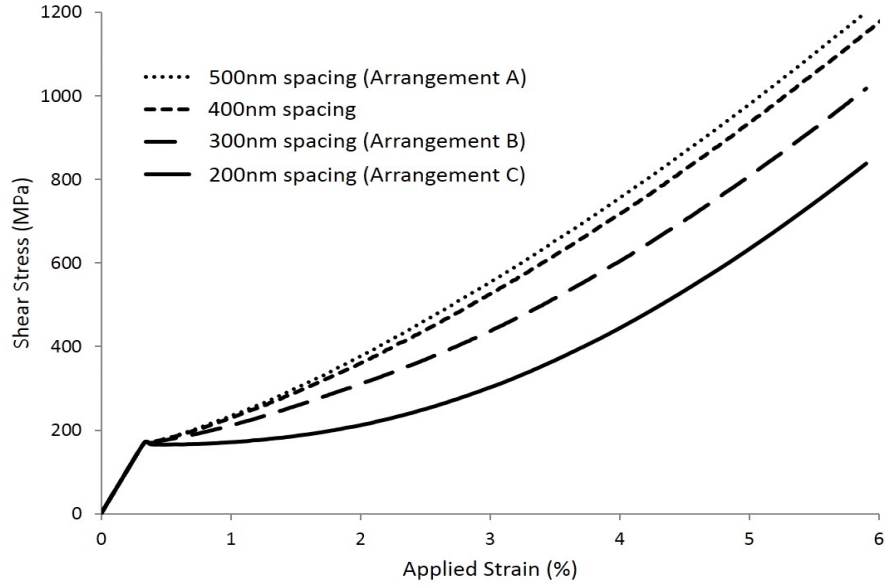
Figure 6.2.6: Flow stress response grains with a differing placement of 10 sources across the left-hand grain wall $(\lambda_{jog} = 25nm)$.

The source activity plot in Fig. 6.2.7 has the inverse trend from the flow stress plots, with the evenly spaced sources generating less frequently. As each simulation contains the same number of sources, the curves are comparable without the need for averaging. Following the yield strain of 0.36% the sources in closer proximity to one another begin generating at a higher rate. The increase in rate moving from $300 \rightarrow 200$nm source spacing is considerably larger than the increase moving from $500 \rightarrow 300$nm, which implies that the phenomenon is non-linear with source spacing and relates to close-range interactions of the dislocations. When greater dislocation content is generated, there is greater plastic shear created and consequently the softer observed flow stress responses.
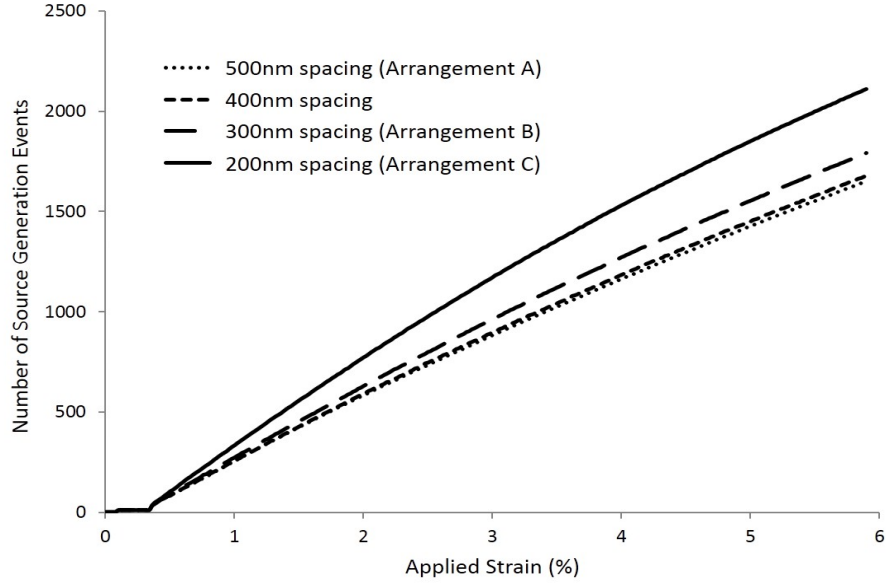
Figure 6.2.7: Number of generation events for the a grain with a differing placement of 10 sources across the left-hand grain wall ($\lambda_{jog} = 25nm$).

6.3 Effect of Jog Spacing

As described in eqn (4.2.5) and illustrated in Fig. 4.2.1, the jog-controlled glide velocity increases exponentially with motive force and jog spacing until the latent phonon drag from the crystal takes over as the limiting factor for dislocation mobility. This rapid dislocation acceleration within the jog-controlled glide scheme, from near-stationary to phonon-controlled speeds (> 100 ms^{-1}) is shown to be closely associated with the macro yield of the grain.
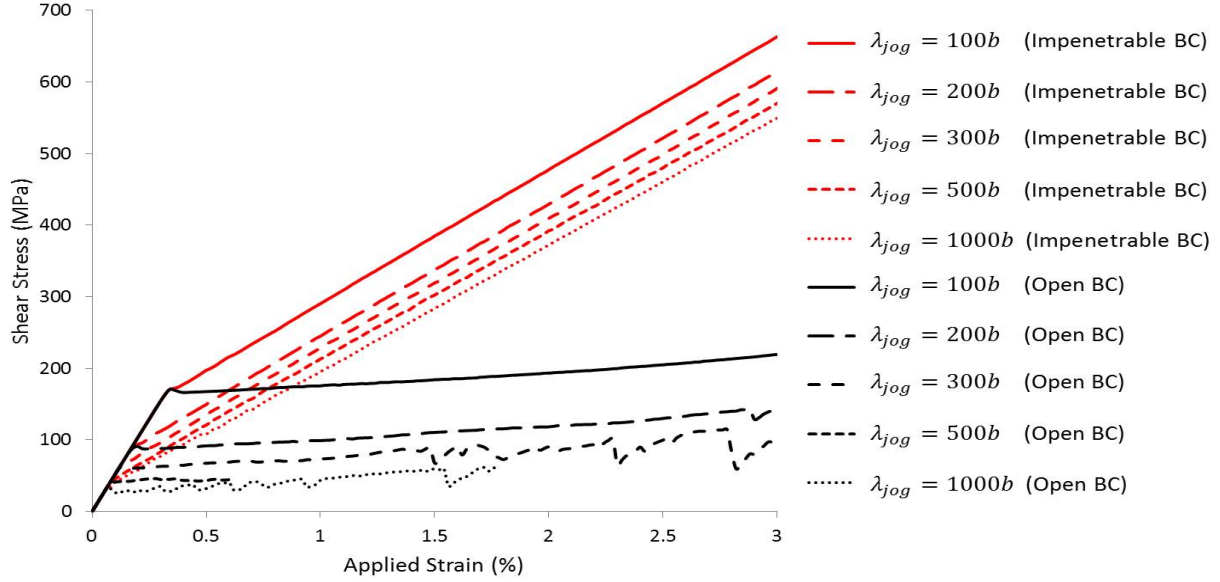
Figure 6.3.1: Flow stress response when varying the jog spacing within the matrix, for both Open and Closed grain-wall boundary conditions.

Fig. 6.3.1 shows flow stress curves for simulations with both open (black) and closed (red) boundary conditions and differing values of jog spacing, which are kept constant for the duration of the deformation. The yield points for the simulations are unchanged by the domain boundary condition, with the post-yield behaviour following the example in Section 6.1, but yield is shown to increase significantly as jog spacing reduces. This is understandable as the closer jog spacing means a higher density of jogs upon a dislocation line which reduces the effective dislocation mobility.

For the open boundary simulations with $\lambda_{jog} > 100b$ the post-yield flow stress behaviour is not as smooth as the $100b$ (25nm) case. The curves contain small fluctuations around an average value which occur due to the heterogeneous source activity. Small drops in flow stress correspond to periods when the shifting dislocation stress fields arrange in such a way that multiple sources generate large dislocation content at the same time. After this the local stress drops at the sources, ceasing operation and allowing the curve to recover. This behaviour is more evident in the simulations with wider jog spacing, as the dislocation velocity is greater and so the plastic shear created by any arbitrary dislocation content is greater. At the widest jog spacings of $500b$ (127nm) and $1000b$ (254nm) the bursts of sudden plasticity caused the model to end prematurely, leading to the

curtailed curves. These fluctuations are not witnessed in the closed boundary simulations as the pile-up of dislocations leads to much lower velocities. As an example, the dislocation glide velocity at 1% strain in the central element of the central slip band for $\lambda_{jog} = 1000b$ simulations can be compared: with open boundaries the value is 10.1 ms^{-1}, with closed boundaries the velocity is 0.03 ms^{-1}.

Plotting 0.1% yield stress vs jog spacing, in Fig. 6.3.2, reveals the exponential dependency of the macro yield upon the jog content. For jog spacings above $\sim 500b$ (127nm) the yield stresses are relatively low, ranging from 30-40 MPa. Narrowing below this value the added drag upon the dislocation lines strengthens the material considerably, almost tripling the yield stress as the jog spacing reduces from $300b$ (76nm) to $100b$ (25nm).
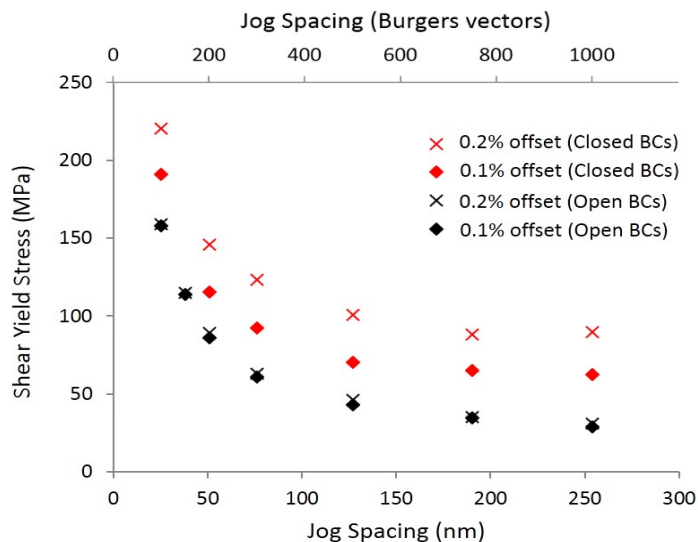
Figure 6.3.2: Yield stress vs jog spacing for open-matrix simulations.

It is significant that for every simulation in this work the source generation stresses range between 39 - 55 MPa. This means that in simulations when $\lambda_{jog} < 500b$ (127nm) the first dislocation density that is generated must face a waiting period before reaching a stress where the jog-drag is overcome and it may accelerate to gliding speed. Consequently the jog spacing (and not the generation threshold) is seen to control the plastic yield in these single phase crystals. For simu-

lations when $\lambda_{jog} > 500b$ the dislocation density may immediately begin to glide after generation, producing slip bands rapidly as individual source activate. Here the source threshold stress dictates yield, and causes a more gradual slip band development which is discussed further in Section 8.1.1.

6.4   Effect of Temperature

Fig. 6.4.1 shows the effect of temperature upon a single phase, single crystal (with open boundary conditions). The shear modulus (gradient of the pre-yield curve) is seen to reduce with an increase in temperature, from 54.19 GPa at 773K to 48.79 GPa at 1173K. The yield stress is also reduced by this temperature increase. The 0.1% offset yield stress is twice reduced by 31 MPa as the material temperature is increased in increments of 200K, which implies a linear relationship between the variables within single phases. The softening of the high temperature material is naturally expected, however the scale of the softening is greatly increased when dealing with multi-phase materials where microstructural features can vary dramatically with temperature (see Section 7.3.4). It is possible that there are less emphasised temperature effects here than observed in experiment because quantities like grain size and jog spacing are kept constant.
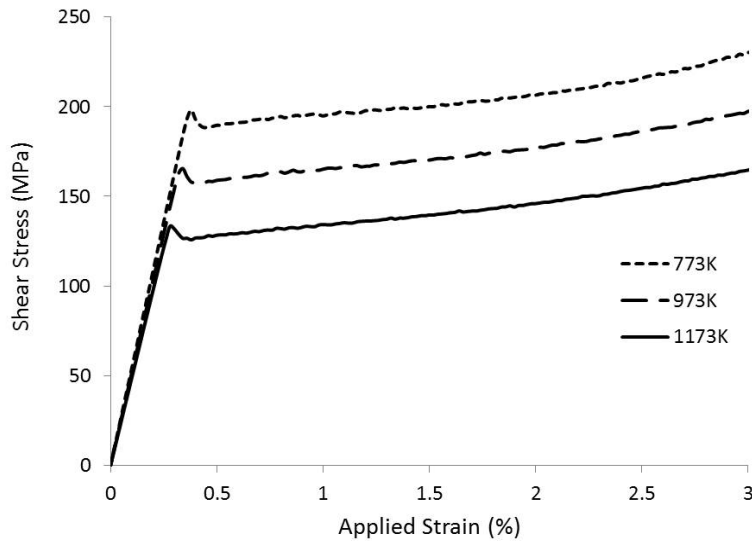
Figure 6.4.1: Flow stress response when varying the temperature of the material ($\lambda_{jog} = 25nm$).

6.5   Effect of Strain Rate

Varying the velocity boundary condition on the top face of the domain will effectively alter the strain rate of the applied simple shear system. By varying the velocity between 500μms^{-1} and 0.05μms^{-1} the simple shear strain rate is varied between 10^2 s^{-1} and 10^{-2} s^{-1} for a 5μm domain. Fig. 6.5.1

shows the simulated flow stress responses for these conditions. The post-yield behaviour is linear in all cases, with the yield stress decreasing uniformly by 20 MPa for each order of magnitude the strain rate is reduced. This means for this investigation a log proportionality is predicted for strain rate and yield.
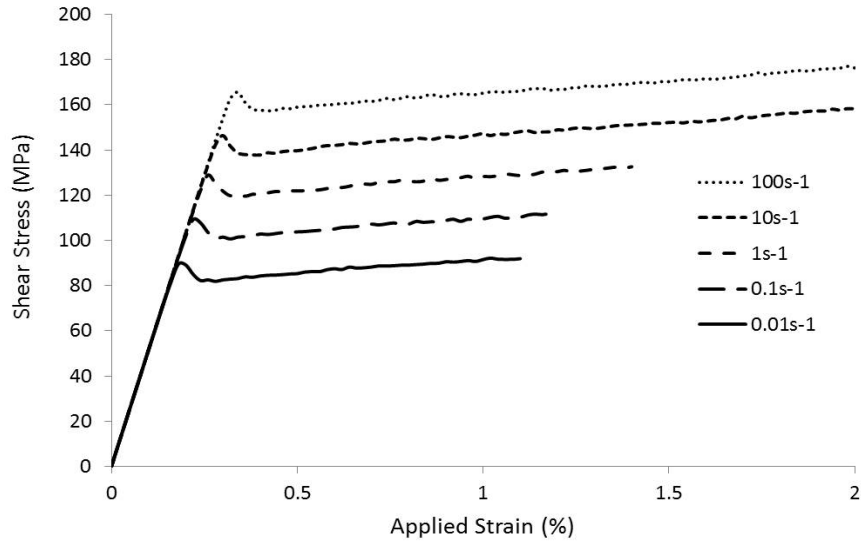

Figure 6.5.1: Flow stress response when varying the applied Strain Rate of the Boundary Conditions ($\lambda_{jog} = 25nm$)

It is expected from literature that lower strain rates should produce lower flow stress responses. The rationale for this phenomenon is that with a lower applied strain rate there is more time available for time-dependent mechanisms like glide and climb to occur while progressing towards a given strain, and more plastic flow is observed. This model has partially captured this behaviour, with greater plasticity in the lower strain rate simulations, however a change in curve shape is expected in the literature. Sharp yield features typically occur for strain rates >1 s^{-1} and give way to a smooth yielding for lower deformation rates [150]. Within Fig. 6.5.1 all curves contain the same sharp yield features which are evidence of a sudden burst of plasticity entering the matrix.

6.6   Effect of Grain Size

The effect of computational domain size on the yield stress will now be investigated for the case of impenetrable boundaries, as no effect is observed for open boundary conditions. Simulations were carried out for jog spacings of $300b$ (76nm) and $100b$ (25nm) to discern whether differing jog content will effect Hall-Petch strengthening. Only the x-dimension was varied while the y-dimension was maintained at 5μm.

Predictions of the 0.1 and 0.2% offset yield stress are shown in Fig. 6.6.1(a) as a function of domain size. For domain sizes between 5 - 12.5 μm the yield stress appears to follow a linear decrease with grain size; the larger grain sizes of 15 - 30 μm do not follow this trend however, revealing a non-linear relationship. Plotting the same offset stresses against (domain size)$^{-0.5}$ in Fig. 6.6.1(b) gives a more obvious linear trend. The R^2 coefficients for the points are 0.962 for 0.1% offset and 0.993 for 0.2% offset, justifying that the relationship is of Hall-Petch type: i.e $\tau_y \propto \frac{1}{\sqrt{d_g}}$ [151] where τ_y is the shear yield stress and d_g is grain size (diameter).
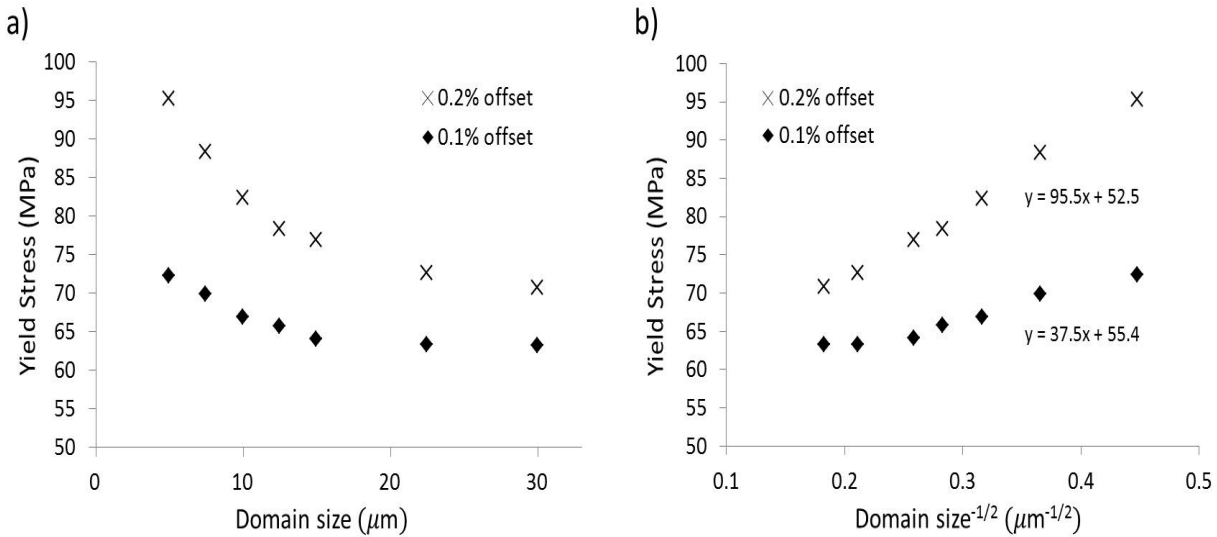
Figure 6.6.1: a) Yield stress vs the domain/grain size using impenetrable boundaries ($\lambda_{jog} = 76nm$). b) Yield stress vs the inverse root of the grain size, displaying the equations for a linear fit to the data.
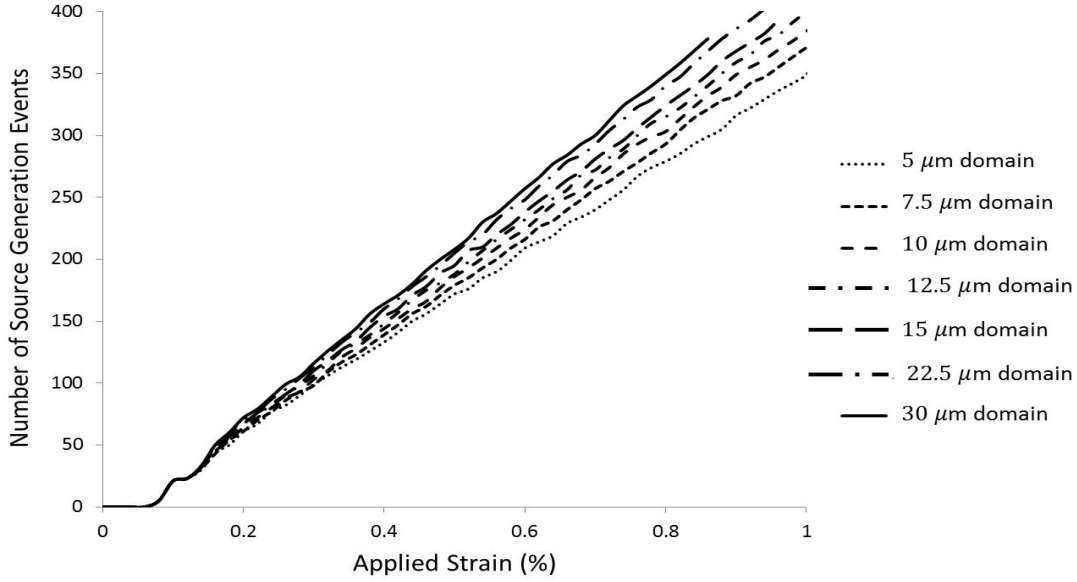
Figure 6.6.2: Number of source generation events when varying the grain dimensions using impenetrable boundaries ($\lambda_{jog} = 76nm$).

Rationale for the grain size hardening effect can be found through considering the number of generation events within each grain. This is displayed in Fig. 6.6.2. It can be seen that the generation rate increases with domain size and will therefore result in a reduction in the flow stress. As already stated, the boundary source generation rate can be affected by pile-up stresses, which vary with an inverse square of the distance from the end of the pile-up. The larger the domain, the greater the distance between pile-up and source and therefore the backstress acting on the source is lower.

The dislocation shear stress fields π_{12}^d evolution with applied strain for the 5μm and 15μm domains are shown in Fig. 6.6.3. The magnitude of the stresses can be seen to evolve with the applied strain as a result of the increasing dislocation content. Initially at 0.3% strain the dislocation stress fields are small and confined close to either the left hand boundary, near the dislocations being generated at the sources, or the right hand boundary near the pile-ups. As more dislocations join the pile-ups, at higher applied strains, the dislocation stresses ($\sim$ 100 MPa) build along the right hand boundary of both domains. To the left of these pile-ups, reaching back across the domain is the repulsive stress field; this is best observed in the 15 μm domain at 0.9% strain as the large

117

blue region dominating more than half the grain. The effect of this repulsive stress will be to lower the velocity of dislocations in the system and, by association, to increase the nucleation time of the dislocation sources. It can be seen that for the 5 μm grain the repulsive field in the locale of the sources is greater at any given strain than it is for the 15 μm domain. This is naturally due to the shorter distance between the sources and the pile-ups, and shows that the repulsive stress fields are an important factor in generation activity.

The dislocation density α_{13} and the shear component of the plastic deformation gradient F_{12}^p for these same simulations are shown in Figs. 6.6.4 and 6.6.5 respectively. The dislocation density is greatest at the right-hand boundary edge where the applied stress field holds the dislocations in large pile-ups. These pile-up grow gradually larger with strain. Some small amounts of density ($\sim 10^{14}\mathrm{m}^{-2}$) equivalent to a single dislocation may be seen on the left side of the domain at higher strains, where dislocation sources have recently finished generating and the density has not yet moved away. The plastic deformation is shown also to increase with strain and it is greatest along the slip bands that end in the largest pile-ups. This is understandable as more dislocations will have have passed along these bands and so the cumulative shear will have been greater.
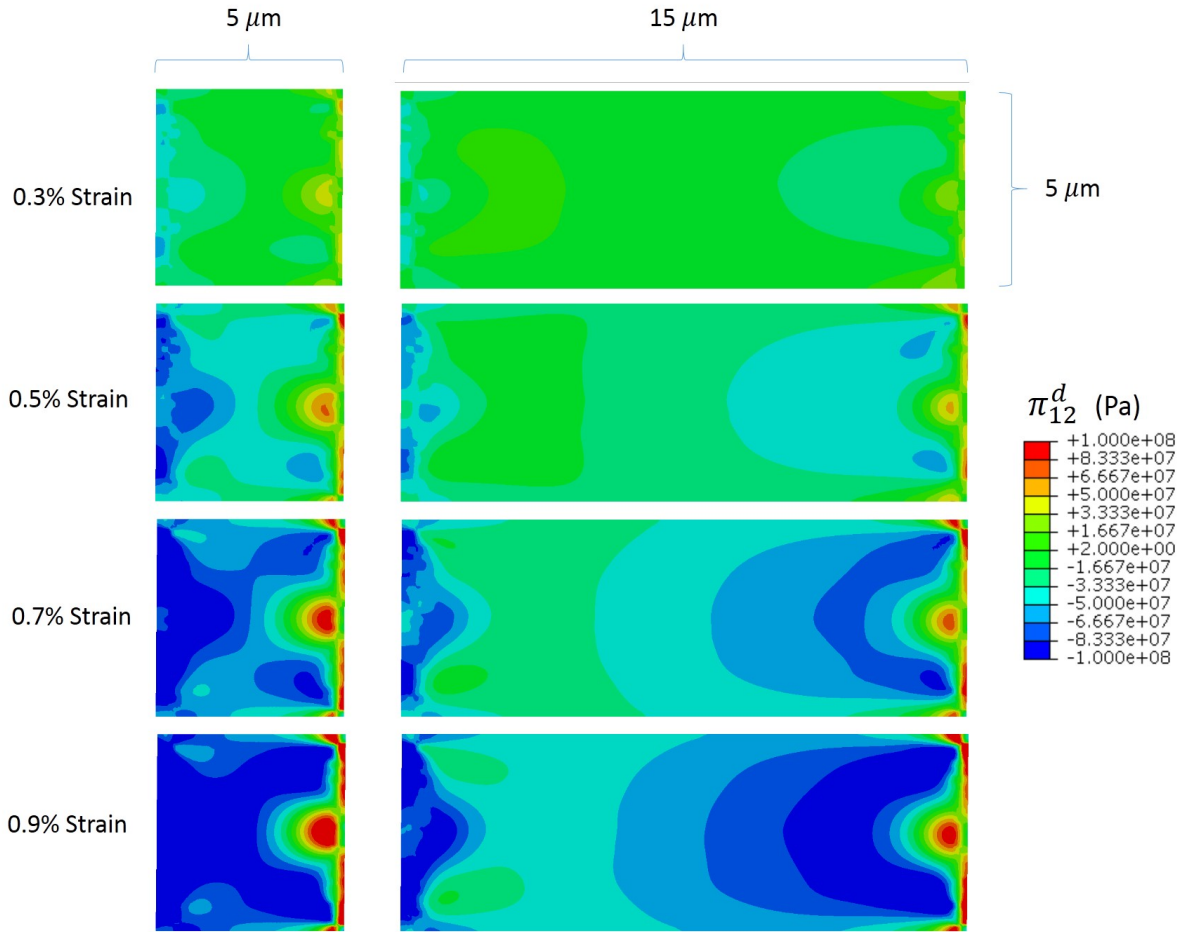
Figure 6.6.3: Evolution of the dislocation stress fields, at increasing applied strains, for grains of size 5 μm and 15 μm. Dislocations emit from the left boundary and pile-up on the right. $(\lambda_{jog} = 76nm)$.
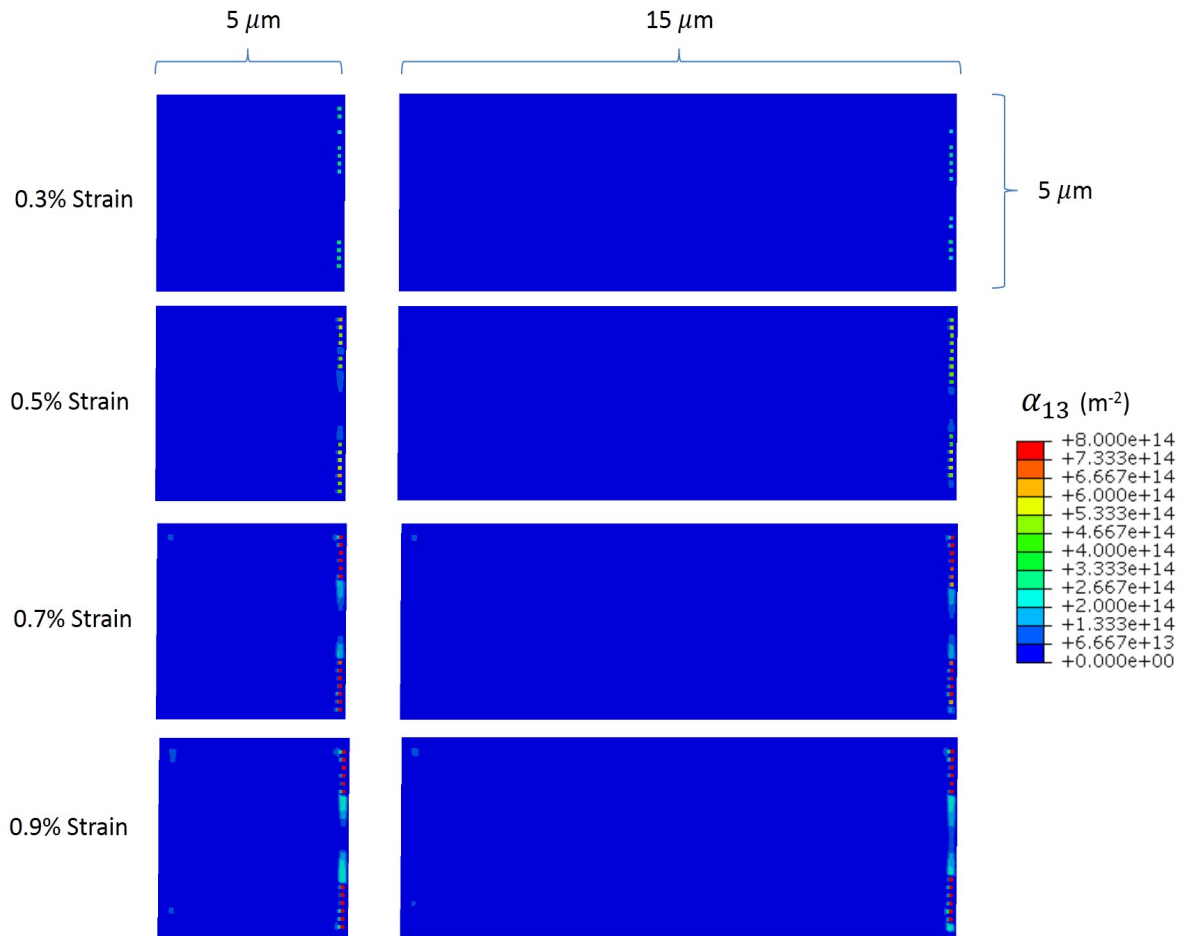
Figure 6.6.4: Evolution of the dislocation density field, at increasing applied strains, for grains of size 5 μm and 15 μm. Dislocations emit from the left boundary and pile-up on the right. ($\lambda_{jog} = 76nm$).
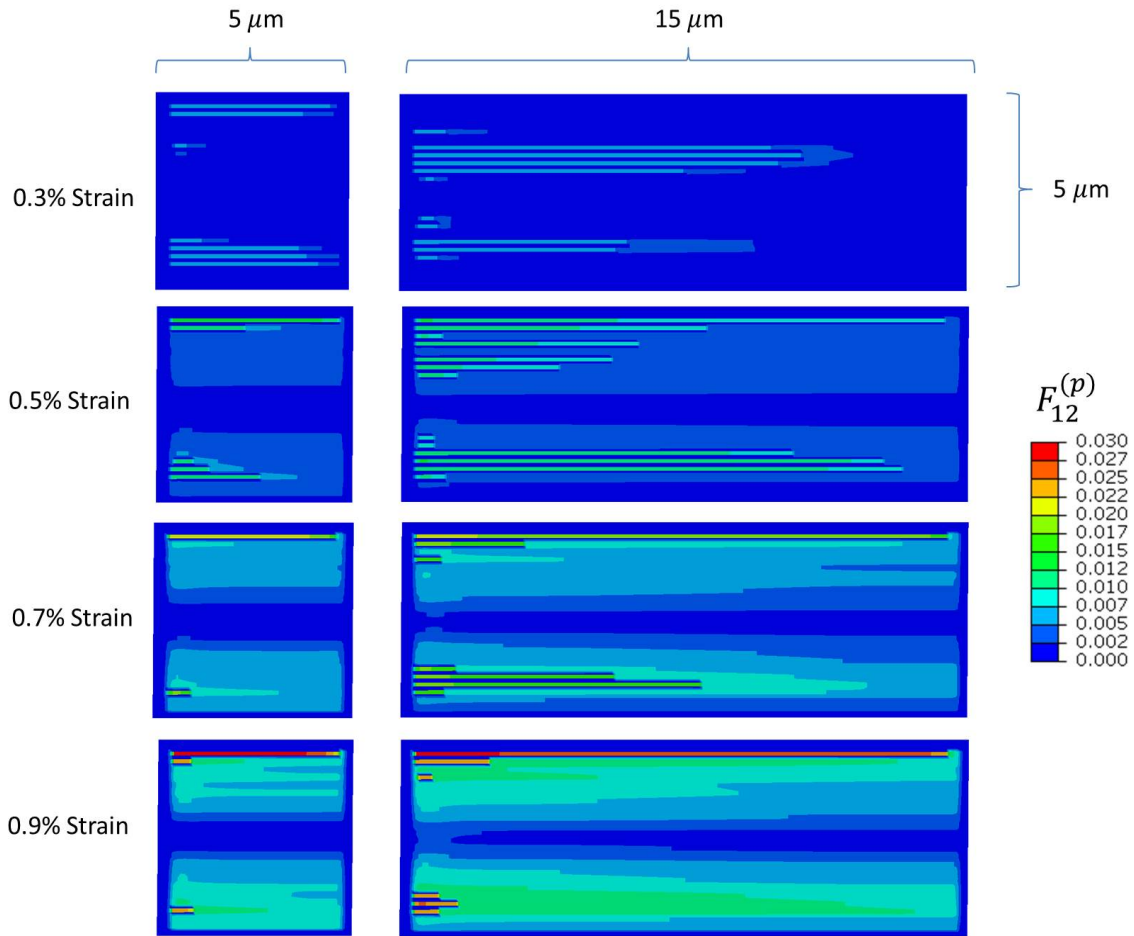
Figure 6.6.5: Evolution of the plasticity F_{12}^p, at increasing applied strains, for grains of size 5 μm and 15 μm. Dislocations emit from the left boundary and pile-up on the right. ($\lambda_{jog} = 76nm$),
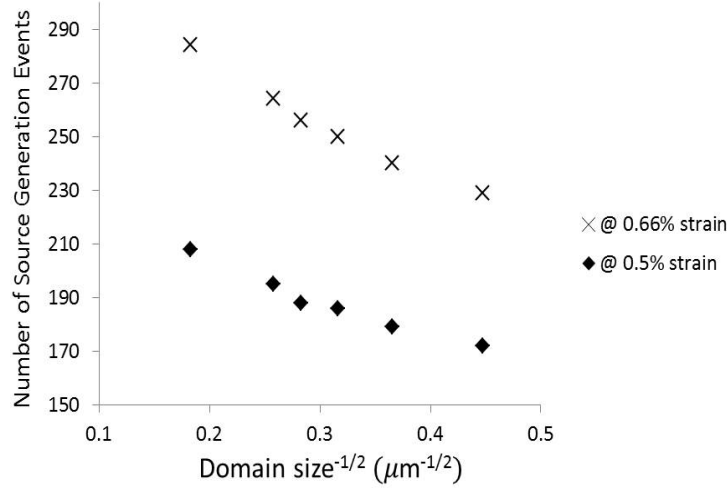
Figure 6.6.6: Number of generation events vs the domain/grain size using impenetrable boundaries ($\lambda_{jog} = 76nm$).

Fig. 6.6.6 shows the number of generation events plotted against (domain size)$^{-0.5}$ for two set shear strain levels. It can be seen that this relationship is also linear. This suggests that the Hall-Petch behaviour can be linked directly to the declining dislocation source activity within the grain. The R^2 coefficients are 0.9605 and 0.9722 for the 0.5% and 0.66% strain data respectively.

For a narrower jog spacing similar trends are observed. The yield offset plot in Fig. 6.6.7(a) follow the same trends as for the wider jog spacing, but with less variation in yield stress across the simulations. The difference between the yield stress of the $5\mu m$ and $15\mu m$ grains at 0.2% offset is 12.2 MPa for the $\lambda_{jog} = 25nm$ case, as opposed to 18.3 MPa for the $\lambda_{jog} = 76nm$ case. Fig. 6.6.7(b) maintains the linear Hall-Petch relationship seen for the wider jog spacing, but with shallower gradients on the linear fit. The R^2 values are 0.958 and 0.972 for the 0.1% and 0.2% yield offsets respectively.
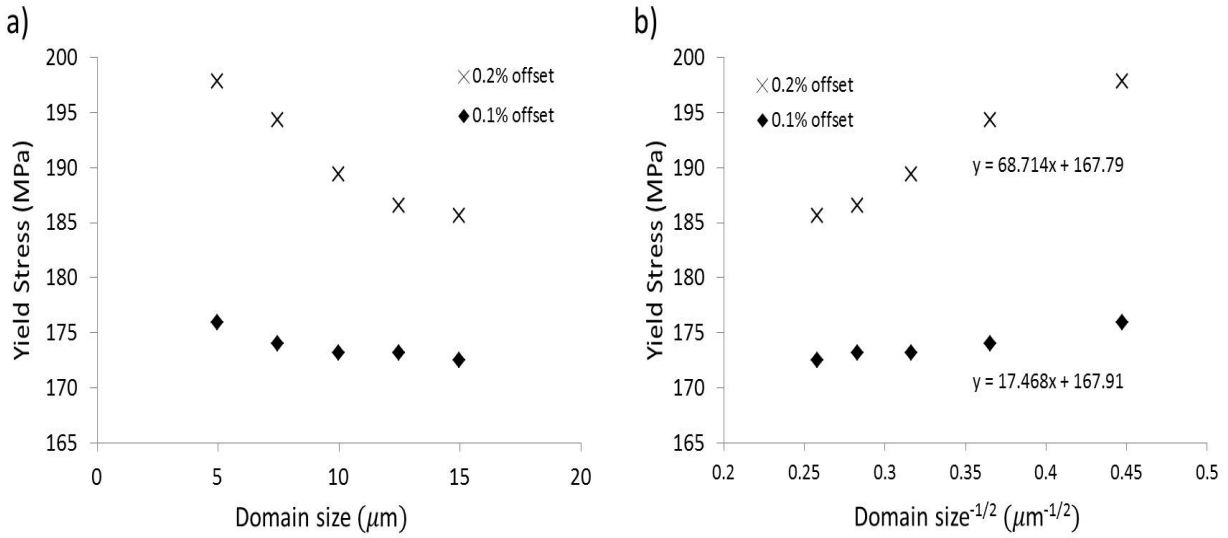
Figure 6.6.7: a) Yield stress vs the domain/grain size using impenetrable boundaries ($\lambda_{jog} = 25nm$). b) Yield stress vs the inverse root of the grain size, displaying the equations for a linear fit to the data.

The number of generation events for these simulations is plotted against (domain size)$^{-0.5}$ in Fig. 6.6.8. The linear relationship applies again for these variables, though the generation rate is different. Fewer dislocation generation events occur by 0.66% strain in the narrow jog spacing simulations than by the same point in the wider jog spacing simulations, which is understandable as the yield point is later for the narrow jog spacing, leaving a shorter period of time for sources to generate. The R^2 coefficients are 0.946 and 0.9901 for the 0.66% and 1% strain data respectively.
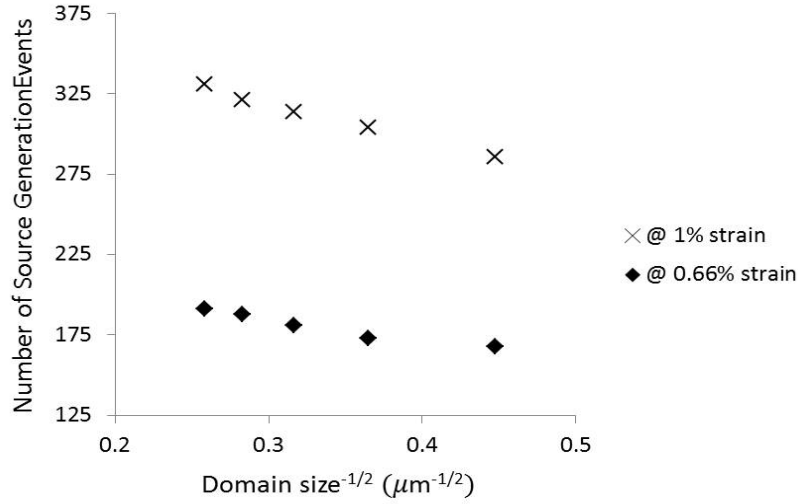
Figure 6.6.8: Number of generation events vs the domain/grain size using impenetrable boundaries $(\lambda_{jog} = 25nm)$.

In the simulations within this section it has been shown that Hall-Petch behaviour can be reproduced in a single slip model. The prerequisite is only that a hard grain boundary should exist that results in the formation of stable dislocation pile-ups. Full field simulations presented in this section illustrate how the repulsive stress arising from piled-up dislocations will reduce the mobilities of the advancing dislocation field and consequently reduce the resultant stress $(\pi_{12}^{\infty} + \pi_{12}^{d})$ acting on sources. This will in turn lower the generation rate of the source by either dropping below the generation threshold or increasing the nucleation time (see eqn (4.5.2)). For a smaller domain size the distance between pile-up and boundary source is naturally smaller, so the generation rate is reduced to a greater extent, and the material is plastically harder.

Chapter 7

Full-field Simulations II: Particle-Matrix

Assumed geometry for this chapter

This chapter will build on the previous chapter by presenting results from another set of FE simple shear tests (in plane-strain) with second phase particles now introduced to the simulation domain. The geometry is a square single crystal as depicted in Fig. 5.4.2, with the precipitate particle positions handled discretely element-by-element using an *obstacle* state dependent variable. The obstacles disrupt the dislocation flux as described in Section 5.4.3. The simulation domain again is 5μm square and the control parameters are adopted unless otherwise stated (see Table. 5.5.2). These tests had a default applied strain rate rate of 100s^{-1} and temperature of 973K (apart from benchmarking Section 7.4).

For disc nickel-based superalloys the γ' have a multimodal size distribution. The present study will focus on full field simulations representative of a unimodal and bimodal γ' strengthened alloy. For the latter, the small particles have a mean radius $r_s = 10$nm while the large particles have a radius of $r_L > 50$nm. Due to the size difference between the fine and large particle populations in the bimodal distribution, only the large particles will be spatially resolved in the computational domain. The small particles are treated implicitly by the line tension force on the dislocation field.

7.1 Unimodal Fine Particle Distribution

The effects of introducing a distribution of tertiary particles to the domain has been investigated. TEM images of NR3 high temperature disc alloy have shown the spacing of tertiary particles to vary widely over a short distance [20]; in some areas the smallest tertiaries may cluster while in others they are spread sparsely in the gaps between the larger secondaries. Edge-to-edge tertiary spacings of $\lambda_s = 25$, 35 and 45nm have been used in these simulations as being approximate averages of the distributions observed.

Fig. 7.1.1 shows flow stress curves for hypothetical systems containing only fine particles of mean radius $r_s = 10$nm, with different particle spacings. In the $\lambda_{jog} = 300b$ or $1000b$ (dotted green or black) curves it can be seen that the fine particles have increased the yield stress of the metal by impeding the dislocation flow, while for the very narrow $100b$ jog spacing all the curves follow an identical profile with no effect produced by the tertiaries. In the former cases, once the critical stress for cutting the tertiaries is reached a sharp drop in flow stress follows the plastic yield: this drop is more pronounced compared to the post-yield behaviour seen in single phase simulations. The reasoning for this stress drop is due to the high shear rates which occur following the release of the small particle line tension. The dislocations accelerate from stationary to gliding speed more rapidly than previously seen, as the stress regime following cutting is high enough to discount the drag from widely spaced jogs. For the very narrow $100b$ jog spacings (overlapping red curves), the jog spacing is still the dominant yield controlling factor, yielding at $\sim$160 MPa. As the small particles are cut between 105 and 155 MPa then the effect of the line tension is not observed in these systems.

Where fine particles do effect yield, the yield stresses are seen to increase with reduction to the particle spacing. This has been more clearly indicated in Fig. 7.1.2. There is negligible difference between the yield stress of the $\lambda_{jog} = 300b$ and $1000b$ simulations for a given fine particle spacing, evidencing that the particle cutting threshold is the dominant slip-limiting factor in these cases. At the narrow $100b$ jog spacing, when the jog drag is still the dominant slip-limiting factor, the yield is almost unchanged by the presence of a unimodal distribution of small particles.

The cause of the particle-spacing strengthening effect is apparent when considering the work re-

quired to cut a particle: the magnitude of this work changes only with particle cross-section (meaning in this investigation the work is always the same), but the work is performed by a length of dislocation line equivalent to the centre-to-centre particle spacing. As the length of dislocation line is reduced then the shear stress must be increased to maintain the same work. Through equation (4.4.4) it can be seen that this will increase the threshold stress at which the cutting takes place. The calculated shear stress cutting thresholds for the spacings of 25nm, 35nm and 45nm are 156 MPa, 125 MPa and 105 MPa respectively, which is reflected by the yield points of each system.
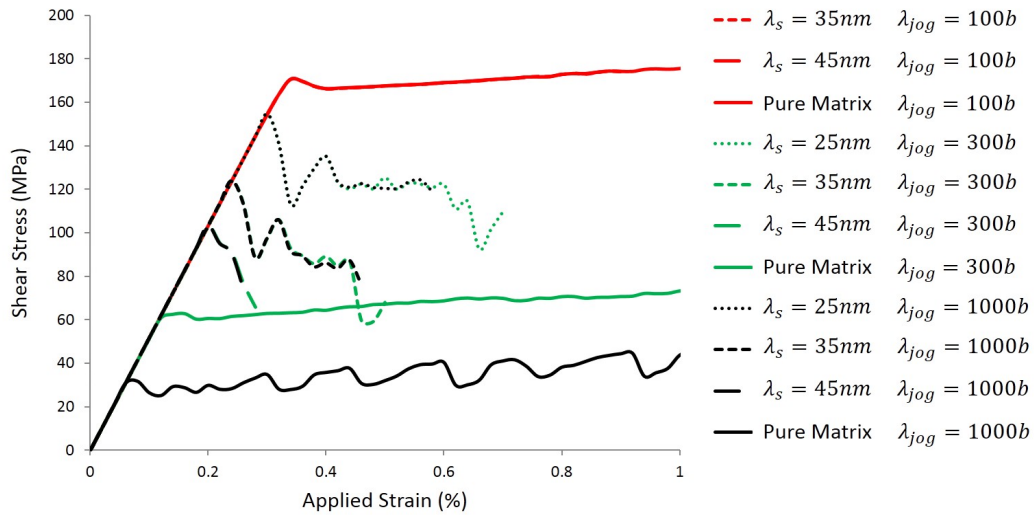
Figure 7.1.1: Flow stress response for a matrix containing fine particles $r_s = 10$nm, with varying particle spacing λ_s.
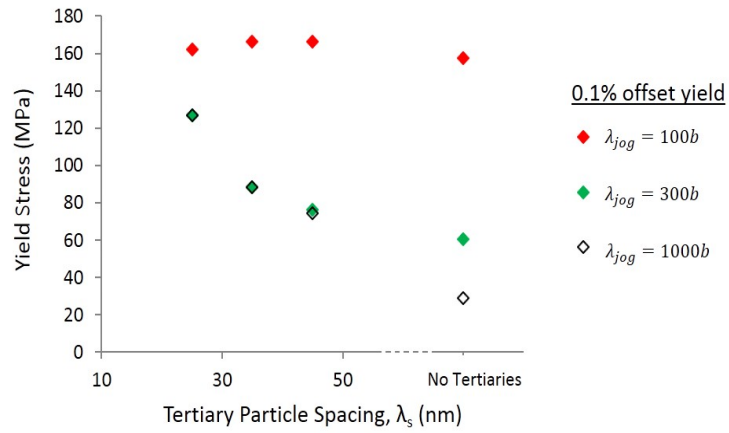
Figure 7.1.2: Yield stress vs fine particle spacing for the simulations within this section.

7.2 Unimodal Large Particle Distribution

7.2.1 Effect of γ' volume fraction

Observed volume fractions for transgranular large particles in nickel-based superalloys typically range between $\phi_L = 0.0$ and 0.5. Simulations investigating the influence of γ' volume fraction on the flow stress behaviour will now be presented. These assumed a unimodal particle dispersion with radius of $r_L = 50$nm at $700°$C.

The flow stress curves for unimodal dispersions with volume fractions of $\phi_L = 0.15$, 0.25, 0.35 and 0.45 are presented in Fig. 7.2.1. The inclusion of particles is seen to greatly increase the strength of the material compared to the γ matrix solutions, with yield stress increasing with volume fraction. The particle distribution used in each simulation has been included as an overlay on the left-hand plasticity map for each volume fraction. In each case, at the macro-yield point, the plasticity maps show short bands of plastic shear in the vicinity of the sources, which are quickly pinned by the precipitates. These initial shear bands have a negligible effect on the macroscale deformation behaviour. As the stress increases the pinning particles are sheared and the slip bands progress through the distribution towards the right edge of the domain, triggering the macro plastic yield. The first slip bands can be viewed at yield offsets of 0.02-0.06% in the figure and are seen to occur in different locations for each particle distribution; forming at the areas of greatest initial micro-shear after dislocation pile-ups have grown sufficiently for their stress fields to cut the leading particle. For lower volume fractions these localised shear bands may reach a greater length before hitting the first particle, and so typically contain more dislocation content in the particle boundary pile-up.

The number of slip bands appears to correlate with the γ' volume fraction. At the 0.1% yield stress there are 5 full slip bands formed for $\phi = 0.15$, while 4 bands formed for the $\phi = 0.25$ and 3 bands for $\phi = 0.35$. The softening is manifested through significant, discrete (~ 25 MPa) drops in flow stress as the applied strain increases. These align precisely with instances of increased dislocation generation in active bands or the cutting of particles to develop new bands. For higher volume fractions of 50nm particles the distribution becomes more homogeneous and less discrete phenomena are observed, thus a smoother flow stress curve is produced.
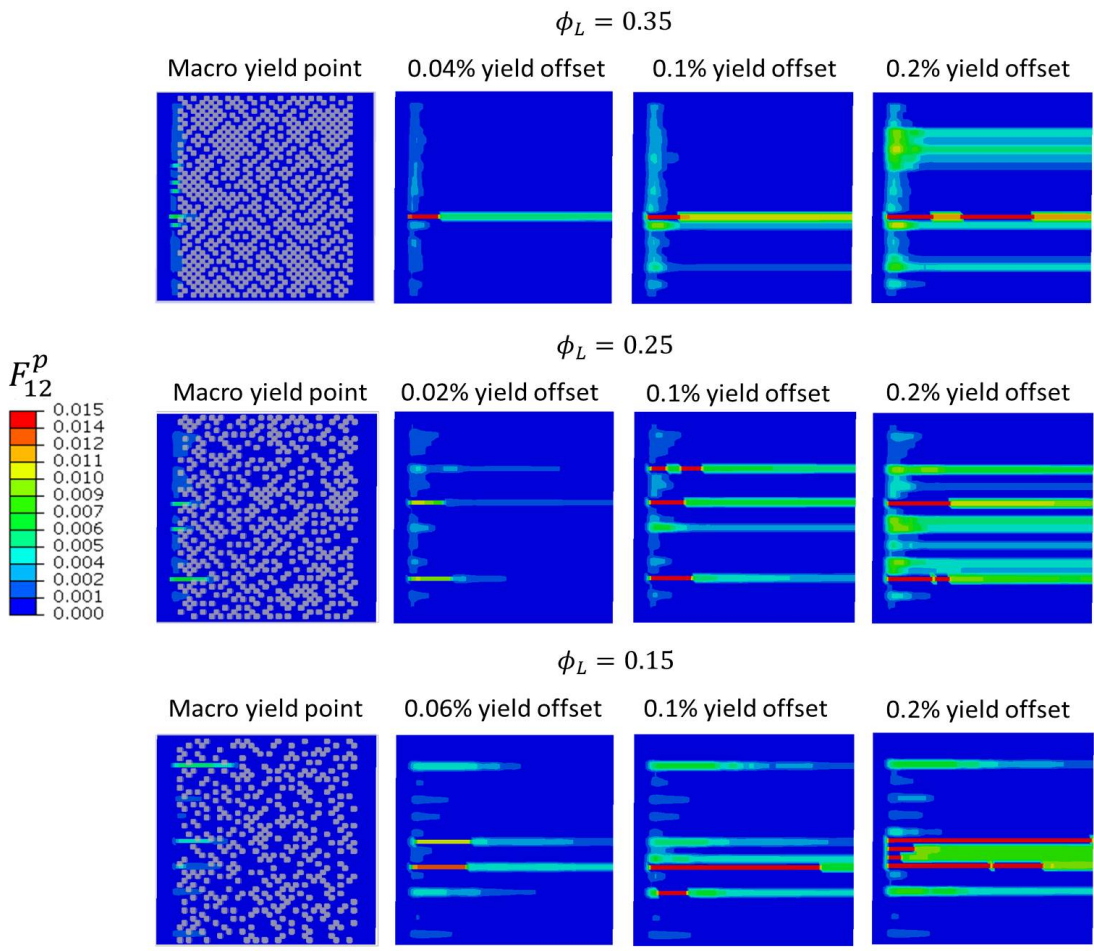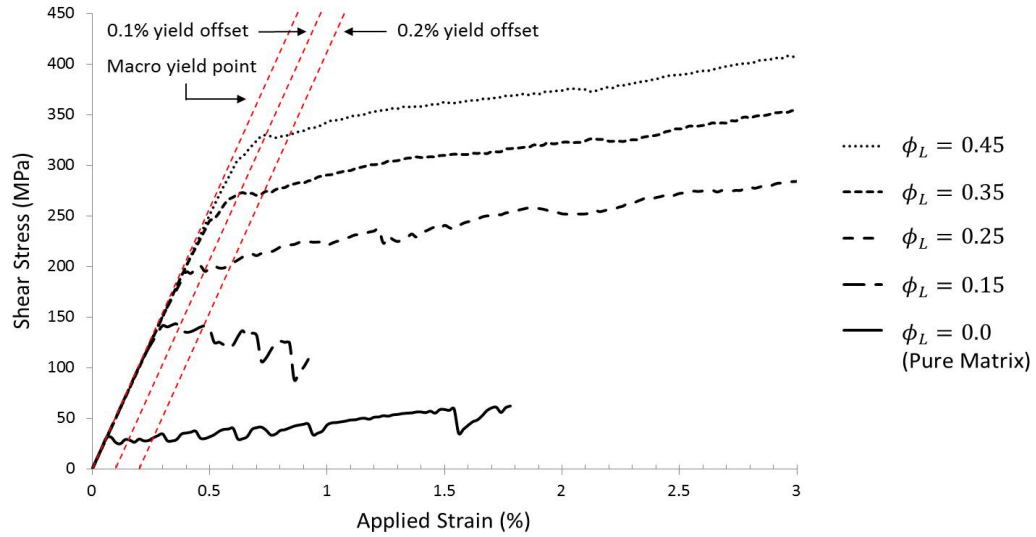
Figure 7.2.1: Flow stress curves and corresponding maps of plastic development over the yield period, for a unimodal γ' dispersion alloy containing $r_L = 50$nm particle distributions at different volume fractions ($\lambda_{jog} = 254$nm / $1000b$).

130

It is significant here that, regardless of the precipitate fraction in the domain, new slip bands tend to form in the vicinity of existing bands. These bands clump to form larger shear bands, showing short range interaction between bands. This behaviour was noted in single-slip deformation of the CMSX-4 alloy [27] displayed in the EBSD strain maps in Fig. 2.1.4, and is being reproduced here as an emergent property of the model.

Figs 7.2.2 and 7.2.3 show the effect of jog spacing on the unimodal dispersion flow stress. The most noticeable effect of jog spacing is the increased jerky character of the flow stress response with decreasing separation of jogs. The reason for this is linked to how jog spacing influences the slip band development in each case. For the wide jog spacing of $1000b$ the jog-drag is overcome at shear stresses 40-60 MPa before the particle cutting threshold, and so the micro-shear bands (evidenced in the plasticity maps) are allowed to form between the dislocation sources and particles. The dislocation sources are unobstructed and so generate density steadily. This leads to localised pile-ups which gradually cut their adjacent particles and form slip bands one by one, giving a slower macro-yield behaviour. For the narrower jog spacing the jog-drag immobilises the dislocations at the sources, preventing the micro-shear bands and pile-ups from developing, and restricting further generation. At the particle cutting threshold the line-tension is released and, with the increased motive force, the dislocations can overcome the jog-drag, rapidly accelerating from the sources to the domain edge without obstruction. In this instance multiple slip bands form at the same time, and multiple dislocation sources activate in unison, causing plastic events which register on the macro-scale flow stress curve.

Using the example of the $\phi = 0.35$ distribution: for $1000b$ jog spacing the first plastic bands are observed at 0.4% applied strain and the first plasticity within a particle is observed at 0.52%. The cutting of the initial particles is accompanied by 25 dislocation generations over a 0.02% strain increment. For $100b$ jog spacing the first plastic bands are observed much later at 0.52% applied strain and the first plasticity within a particle is observed at 0.58%. Following the cutting of the initial particles 46 dislocation generations occur over a 0.02% strain increment. This shows that the yield is delayed by narrower jog spacings, eventually occurring over a shorter strain interval and with increased dislocation generation rate.
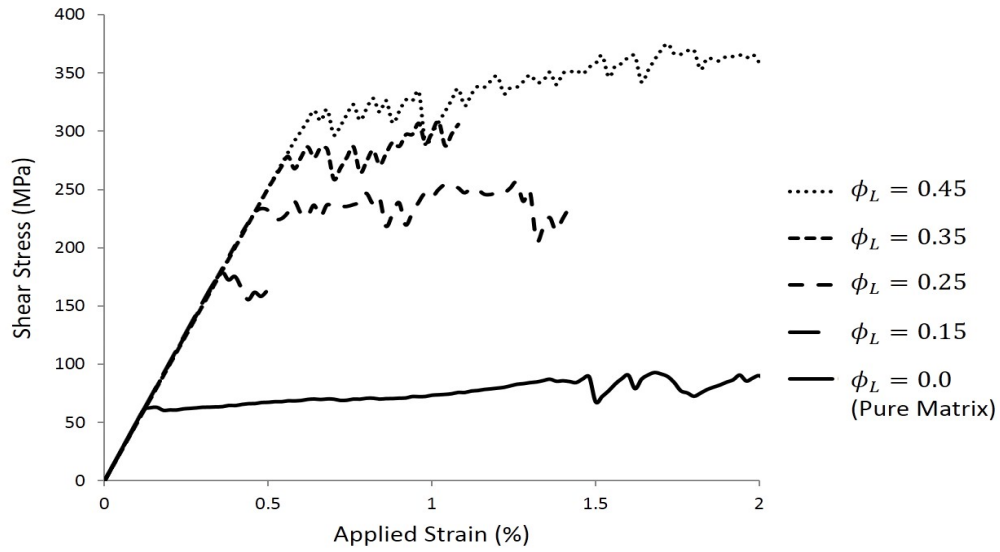
Figure 7.2.2: Flow stress response for a unimodal γ' dispersion alloy with varying volume fraction and constant radius of 50nm ($\lambda_{jog} = 76$nm / $300b$).
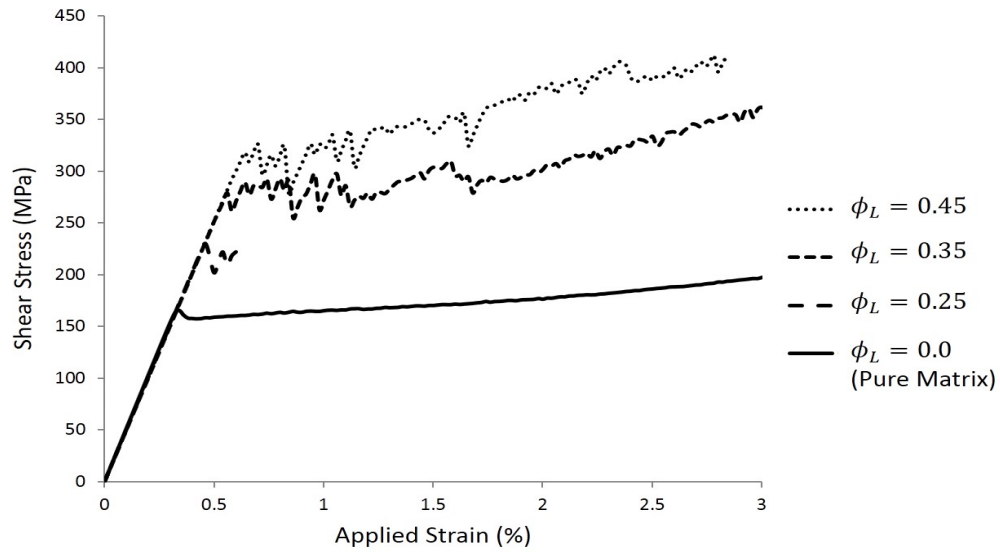

Figure 7.2.3: Flow stress response for a unimodal γ' dispersion alloy with varying volume fraction and constant radius of 50nm ($\lambda_{jog} = 25$nm / $100b$).
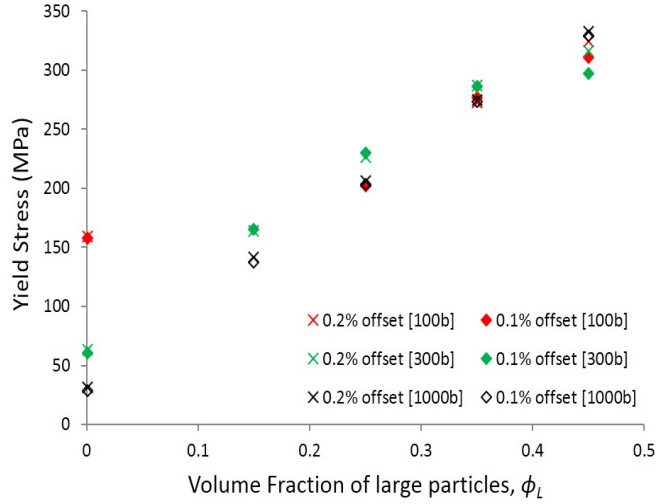
Figure 7.2.4: Yield stress vs volume fractions for the simulations within this section.

The increase in yield stress with volume fraction of particles is displayed in Fig. 7.2.4 for all jog spacings. A linear relationship is predicted in each case for $\phi_L \geq 0.15$, except for a deviation in the 0.1% offset yield stress for the $\phi_L = 0.45$ / $\lambda_{jog} = 300b$. This is associated with the formation of a new slip band at 0.7% applied strain, lowering the flow stress for a brief period over the 0.1% yield offset.

The volume fraction strengthening effect derives from the γ' shearing conditions. An increase in the cutting stress is created by an increase in volume fraction as the inter-particle spacing is reduced. The effect of particle spacing on cutting threshold has been discussed in the previous section. Table 7.2.1 shows the particle spacing and cutting threshold for the distributions used in the simulations above, calculated using the methodology discussed in Section 4.4.2. Comparing the yield stresses predicted in Fig. 7.2.4 with the cutting thresholds in this table it can be seen that there is good agreement for the narrower jog spacings at low volume fraction. For the wide jog spacing at low volume fraction the yield is predicted lower than the cutting threshold, as heterogeneous dislocation stress fields cause local yield to be reached earlier than the bulk domain.

Table 7.2.1: Details of particle spacings and associated cutting thresholds for the 50nm particle distributions used in this section

Volume fraction	Edge to edge spacing	Centre to centre spacing	Cutting threshold
ϕ_L	λ_L (nm)	λ_L^* (nm)	τ_c(MPa)
0.15	105.2	186.8	172.1
0.25	63.1	144.7	222.1
0.35	40.7	122.3	262.8
0.45	26.2	107.9	298.0

7.2.2 Effect of Particle Size

In this section particle size effects are investigated at constant volume fraction $\phi_L = 0.35$. Again the case is presented for three different jog spacings.

Numerical results for these cases are shown in Figs. 7.2.5, 7.2.6 and 7.2.7. From these results it is evident that the smaller particles result in a higher flow stress, though the magnitude of the effect that the particle radii have on yield stress varies significantly across the figures. For the widest jog spacing of $1000b$ the particle radius has the greatest effect on the yield strength. A difference of 75 MPa is observed between the 0.1% offset yield of 50nm and 100nm particles. For narrower spacings of $300b$ and $100b$ the same yield differences are 42 MPa and 3 MPa respectively. This model suggests that unimodal systems with large jog content may see less strength benefit from particle refinement than others. Differences in curve shape are also observed as the dislocation density interacts with the simulated microstructure. In Fig. 7.2.5 flow stress undulations related to shear avalanches are observed when the particle radius is increased.

A direct comparison of the $r_L = 100$nm particle distribution with different jog spacings is presented in Fig. 7.2.8, illustrating that for the coarser particle systems the yield stress increases with jog spacing. This strengthening effect of the jog spacing is noticeably different for the two-phase system (solid lines) and the pure matrix system (dotted lines).
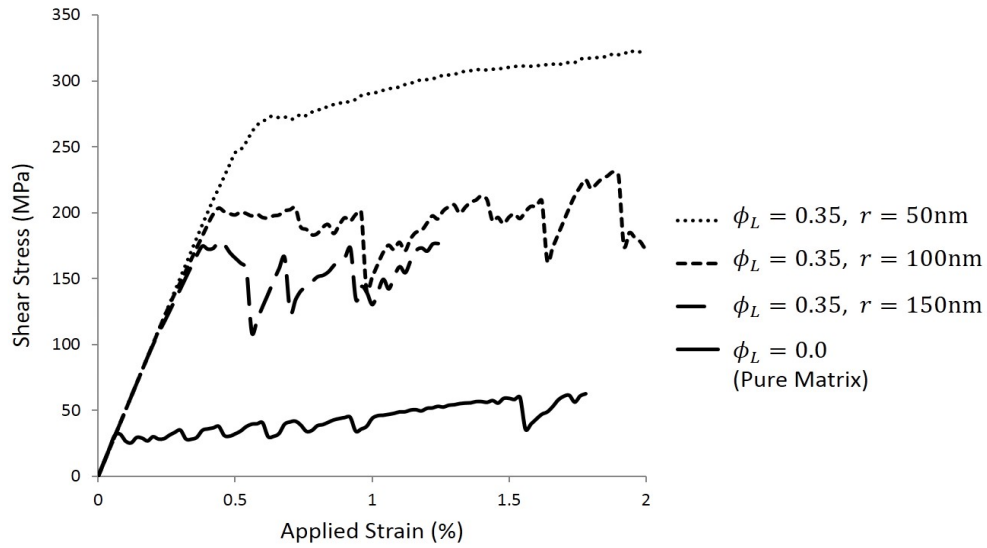
Figure 7.2.5: Flow stress response for a unimodal γ' dispersion alloy with constant volume fraction but varying radius ($\lambda_{jog} = 254$nm / $1000b$).
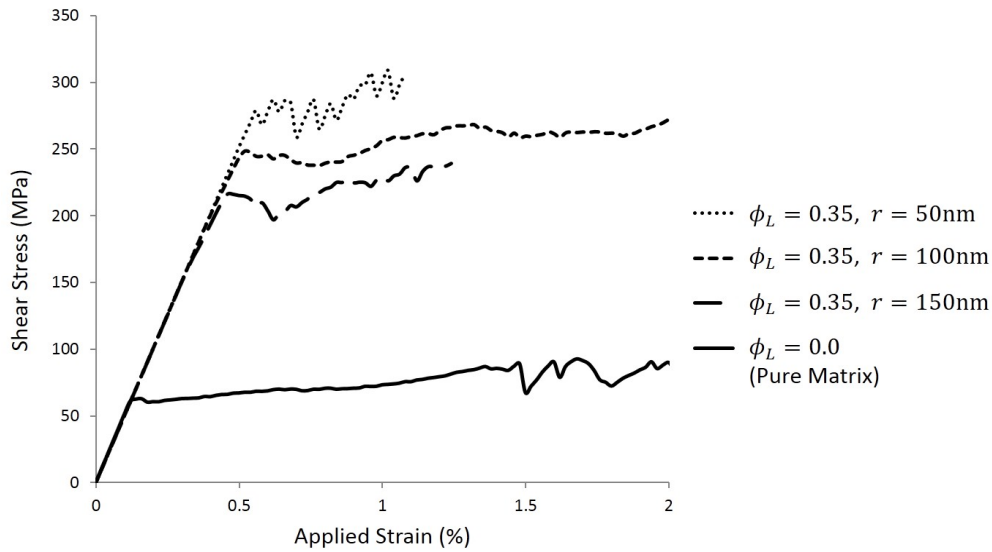

Figure 7.2.6: Flow stress response for a unimodal γ' dispersion alloy with constant volume fraction but varying radius ($\lambda_{jog} = 76$nm / $300b$).
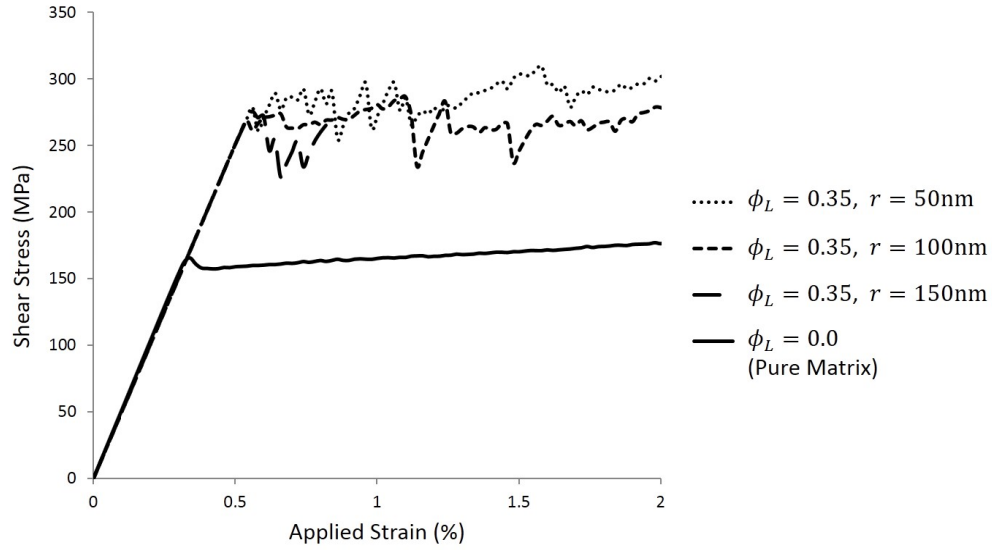
Figure 7.2.7: Flow stress response for a unimodal γ' dispersion alloy with constant volume fraction but varying radius ($\lambda_{jog} = 25$nm / $100b$).
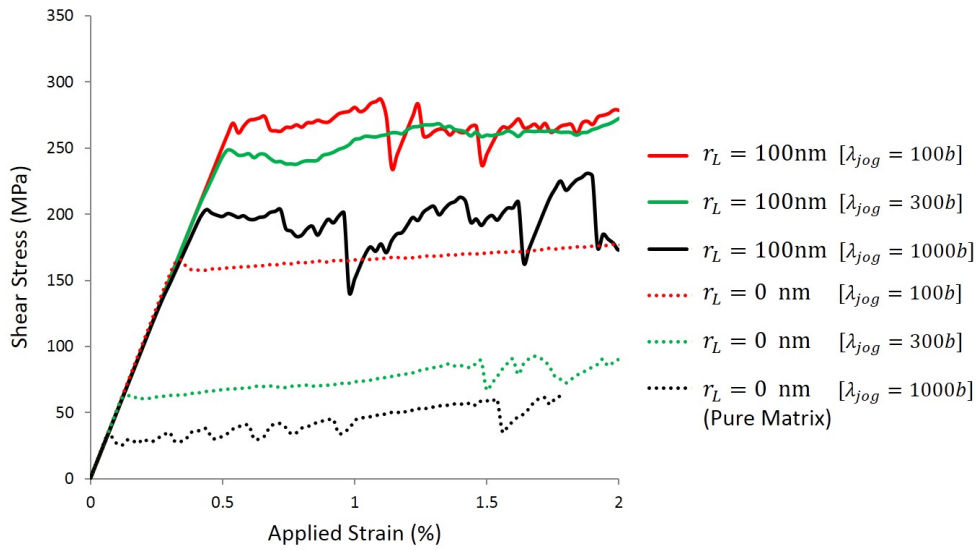

Figure 7.2.8: Flow stress response comparison for both wide and narrow jog spacings, for a unimodal γ' dispersion alloy with constant volume fraction but varying radius.

The evolution of both dislocation density α_{13} and the shear component of plastic deformation gradient F_{12}^{p} can be seen in Fig. 7.2.9 for a system with 100nm radius particles. (These images

correspond to the solid red and green flow stress curves plotted in Fig. 7.2.8). For the $\lambda_{jog} = 76$nm system, at 0.5% strain, before the macro yield, the density can be seen piling up against the particle distribution at the left side of the domain and causing micro-shear bands between the sources and the particles. By 1.0% those initial particles have been cut and the density is seen spread across the domain, piling up against other particles along the path of the slip band. At this point a jerky-glide dislocation motion is occurring within the model as the mobile density glides through the γ phase then waits at the edges of the γ' precipitate for the stress to rise high enough to shear and proceed. The locations of the waiting dislocation density corresponds with the developing slip bands within the F^p_{12} maps.

A slower slip band development is seen for the $\lambda_{jog} = 25$nm system. At 0.5% strain the initial dislocation density is held near the sources by the stronger jog-drag. Consequently there are no micro-shear bands created, no pile-ups at the particles and less dislocation density in the domain because the sources are impeded. At 1.0% strain some slip bands have fully developed, however there are fewer present than at the equivalent time in the previous system and they are concentrated at the top half of the domain. By 1.5% strain more slip bands have activated at the bottom of the domain and their positions match those of the wider-spaced jog system. The total F^p_{12} in the domains has become roughly equivalent at this point. The macro-scale flow stress behaviour matches well with these images, as the $100b$ (solid red) curve in Fig. 7.2.8 is seen to undergo a large shear avalanche shortly after 1.0% strain when the lower slip bands activate in unison. The flow stresses of the two systems become much closer after this point.

$r_L = 100$nm, $\lambda_{jog} = 300b$ (76nm)   Strain

$r_L = 100$nm, $\lambda_{jog} = 100b$ (25nm)   Strain
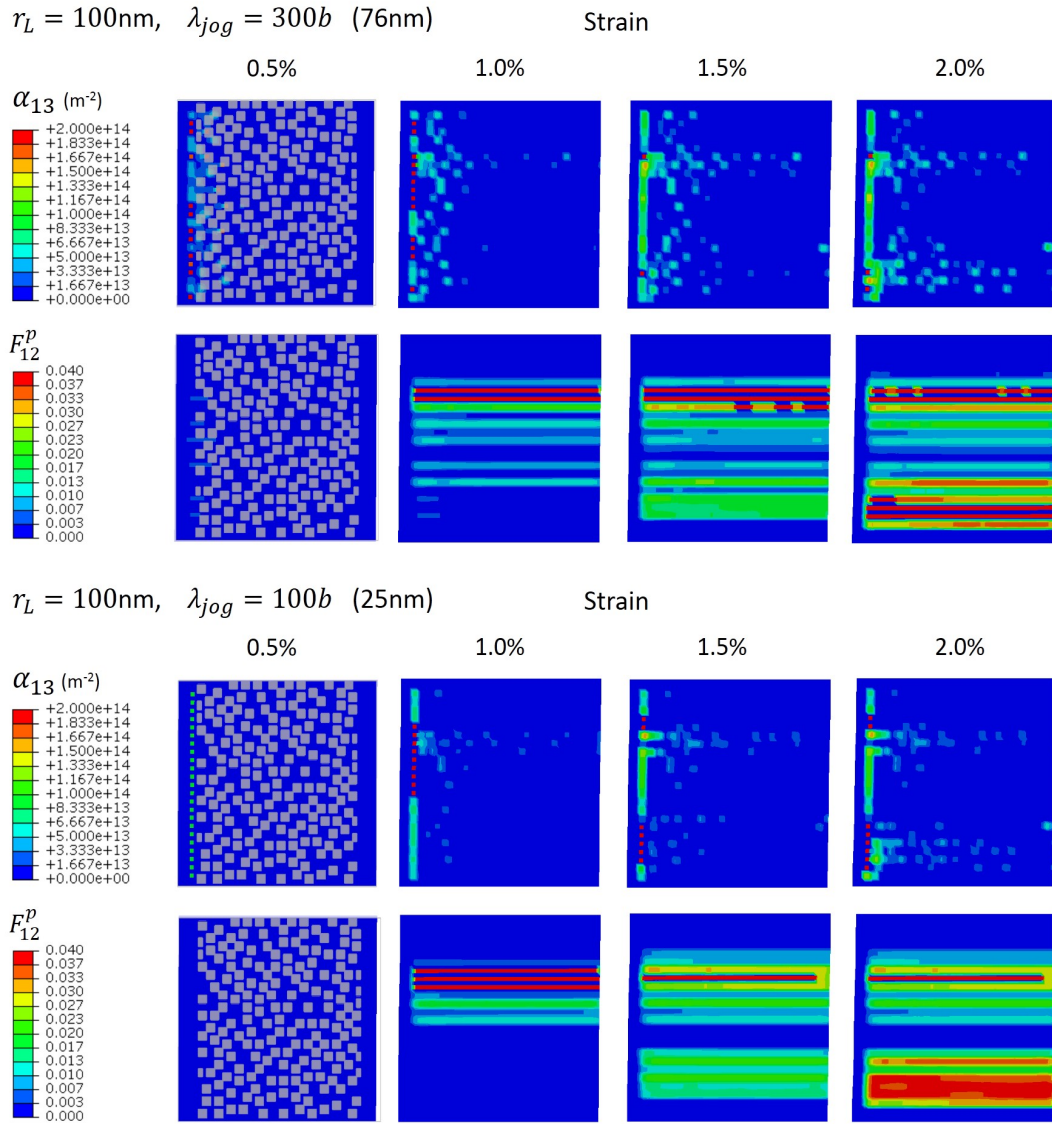
Figure 7.2.9: Evolution of dislocation density α_{13} and plastic deformation F^p_{12} (slip bands) with increasing strain, for a 5μm domain with a unimodal distribution of secondary particles $r_2 = 100$nm.
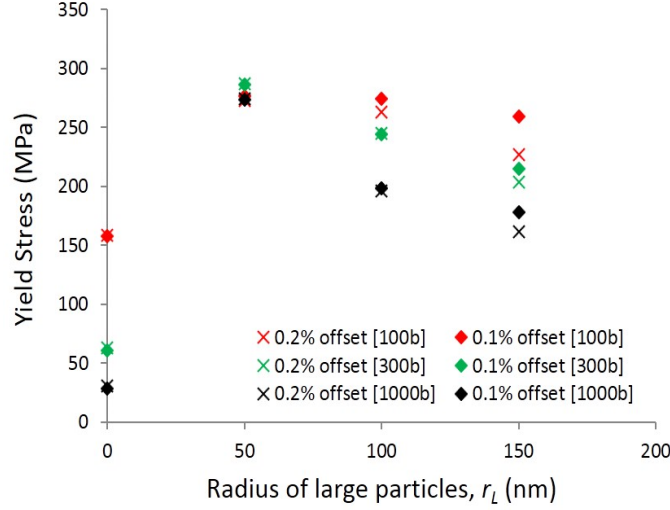
Figure 7.2.10: Yield stress vs volume fractions for the simulations within this section.

The yield stress vs particle radius is shown in Fig. 7.2.10 for constant volume fraction $\phi_L = 0.35$. The relationship between yield stress and particle size appears non-linear for lower jog spacings. This results matches well with the reuslts of experimental tension tests of M. Preuss *et al.* [30], performed at 750°C upon RR1000 samples with controlled secondary particle size. Despite the lower strain rate in the mentioned work the trend in yield stress vs secondary particle size appears as predicted by the FDM model. In both cases the fine secondary γ' shows the highest yield stress at all tested conditions.

It should be noted that if the yield stress was derived entirely from the shear cutting threshold in eqn (4.4.4) then the particle size would have no effect on yield at constant volume fraction. Assuming lattice square spacing is used to calculate the inter-particle space, a given increase in particle size is balanced by the increase in the spacing of the dispersion: giving the same cutting threshold stress in each case. This is demonstrated in Table 7.2.2. The differing yield stresses arise in this model from the line tension of the dislocations, which increases when the particles are closer together. The macro yield stresses in the flow stress curves may also occur lower than the calculated cutting stress threshold, as they represent the average of the applied stress π_{12}^{∞} across the domain, whereas locally at the matrix/particle boundaries the total internal stress field $\pi_{12}^{\infty} + \pi_{12}^{d}$ can be higher.

139

Table 7.2.2: Details of particle dispersion and associated cutting threshold for this section

Particle radius	Mean radius when intersected by plane	Edge to edge spacing	Centre to centre spacing	Cutting threshold
r_L (nm)	R_L (nm)	λ_L (nm)	λ_L^* (nm)	τ_c(MPa)
50	40.8	40.7	122.3	262.8
100	81.6	81.3	244.6	262.8
150	122.5	122.0	367.0	262.8

7.3 Bimodal Distributions of Particles

Until now a unimodal particle dispersion has been considered within an FDM framework for the prediction of the flow stress. In real applications, disc nickel-based superalloys are given complex heat treatments that are designed to generate in multimodal γ' size distributions. The aim of the following sections is to study the effects of a bimodal dispersion on the flow stress in the context of the proposed FDM theory.

As a representative γ' dispersion of a disc nickel alloy, the following size distribution for small particles has been used: volume fraction $\phi_s = 0.03$, radius $r_s = 10$nm, spacing $\lambda_s = 35$nm. In what follows, simulations will use these dispersion parameters for the small particles and assess the effect these particles have when introduced to the large particle dispersions considered in the previous sections.

7.3.1 Effect of large particle volume fraction

Fig. 7.3.1 shows the flow stress curve for particle distributions with and without small particles, with $\lambda_{jog} = 1000b$. Large particle radius is kept at 50nm. The fine γ' have the effect of increasing the flow stress while introducing a more gradual yield behaviour. Fig. 7.3.2 shows the yield stress increase when moving from the unimodal large particle system to the bimodal case. The yield strength of the bimodal system appears to rise linearly with volume fraction of large particles, but at a higher gradient than for the unimodal case: the increase in the 0.1% offset yield when the fine particles are added is 53 MPa at $\phi_L = 0.25$, 69 MPa at $\phi_L = 0.35$ and 82 MPa at $\phi_L = 0.45$.
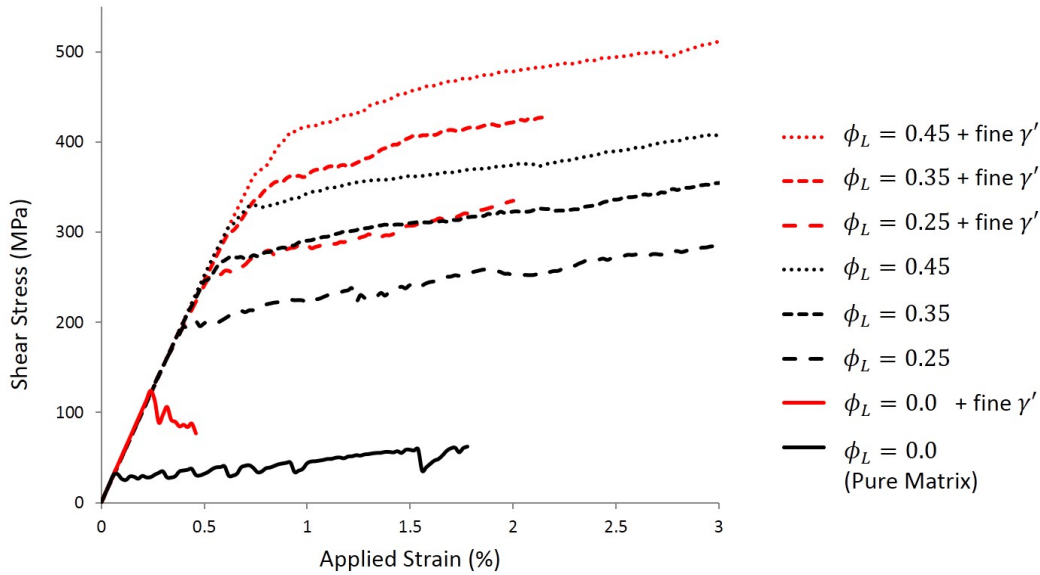
Figure 7.3.1: Flow stress response for a matrix with different unimodal or bimodal particle distributions and large particle radius of 50nm (λ_{jog} = 254nm / 1000b).
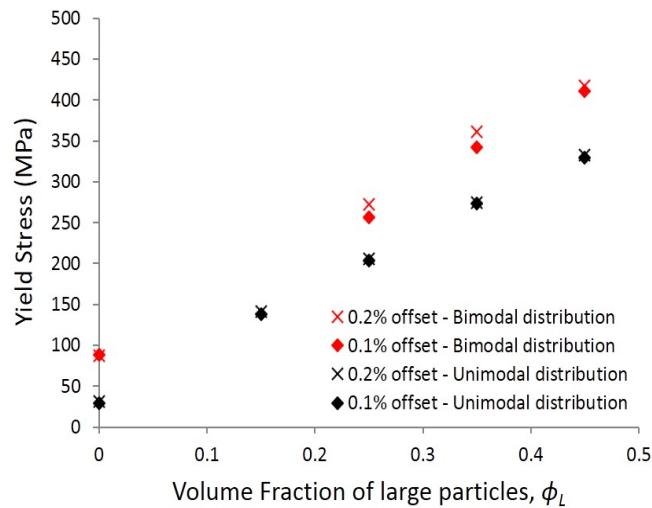

Figure 7.3.2: Yield stress vs volume fraction of large particles, with and without the presence of fine γ' (λ_{jog} = 254nm / 1000b).

The flow stress plots for the same distributions with jog spacing λ_{jog} = 300b are presented in Figs. 7.3.3. There is an immediate difference between the flow stress curves of the unimodal

and bimodal simulations, as the jerky curves with discrete shear avalanches (black lines) become smoother in the presence of fine γ' (red lines). The yield behaviour is also more gradual as the slip bands develop more slowly. Fig. 7.3.4 plots the dislocation source activity for the simulations corresponding to these flow stress curves. Comparing the two it can be seen that the macro-yield points in the flow stress curves occur at the same applied strain as the onset of continuous dislocation generation in the source activity curves. The presence of fine γ' particles is observed to delay the point at which the sources begin to generate and also reduce the rate of generation, this occurs through the increased cutting threshold and additional line tension which lowers the motive force on the dislocation. The combination of these effects means the abrupt plastic bursts from the unimodal curves are no longer seen.

Fig. 7.3.5 displays the linear relationship between yield stress and increasing large particle volume fraction for the bimodal dispersion. The strengthening effect of the fine particles is greater for the narrower jog spacing: the increase in the 0.1% offset yield when the fine γ' are added is 82 MPa at $\phi_L = 0.25$, 115 MPa at $\phi_L = 0.35$ and 168 MPa at $\phi_L = 0.45$. Comparing to Fig. 7.3.2, the effect of jog spacing on yield stress is shown to be greater for a system containing fine precipitates. For unimodal distributions (black markers) the strength increase moving from $\lambda_{jog} = 1000b$ to $300b$ averages at 25 MPa, while for bimodal (red markers) the same increase averages at 56 MPa.
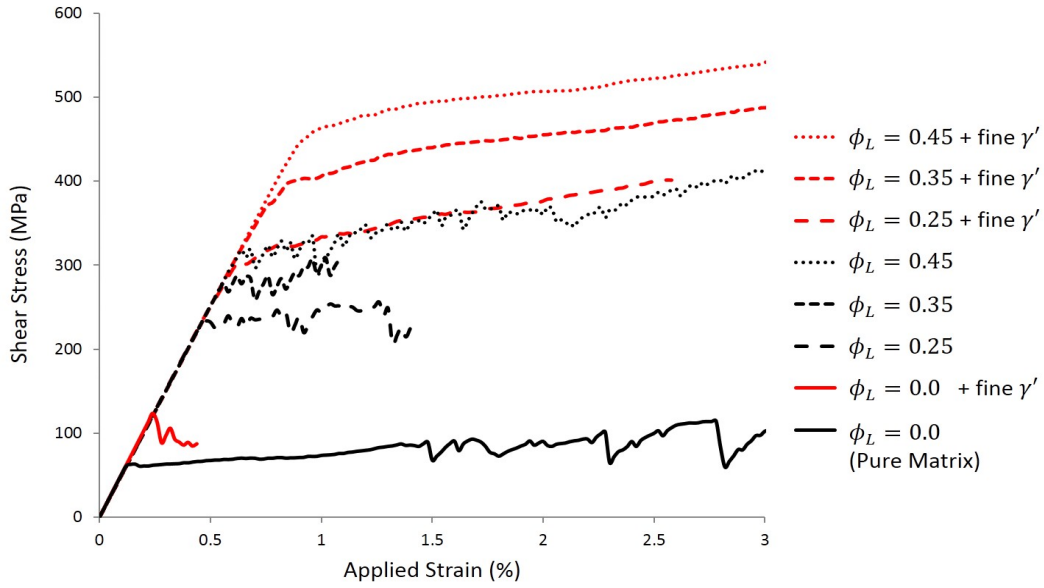
Figure 7.3.3: Flow stress response for a matrix with different unimodal or bimodal particle distributions and large particle radius of 50nm ($\lambda_{jog} = 76$nm / $300b$).
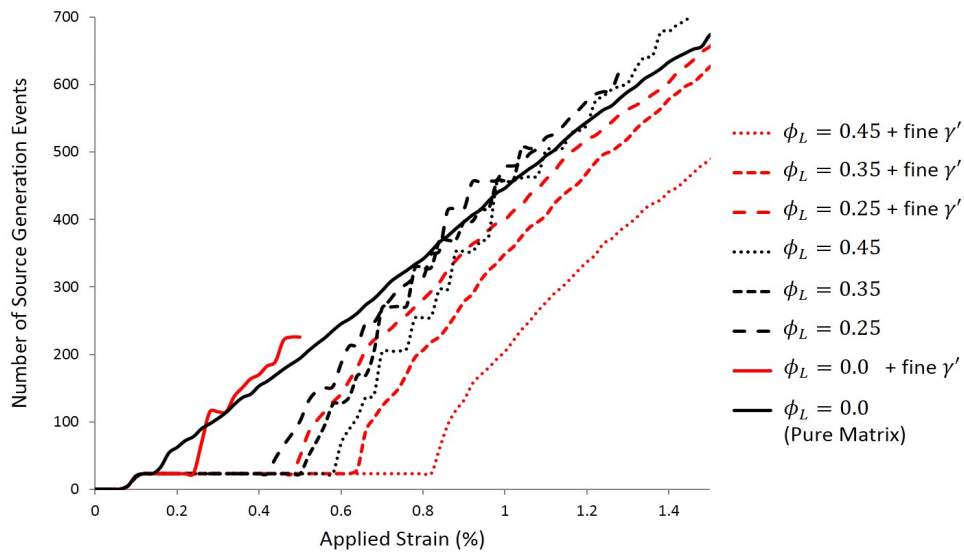

Figure 7.3.4: Number of dislocation generations in the domain for a matrix with different unimodal or bimodal particle distributions and large particle radius of 50nm ($\lambda_{jog} = 76$nm / $300b$).
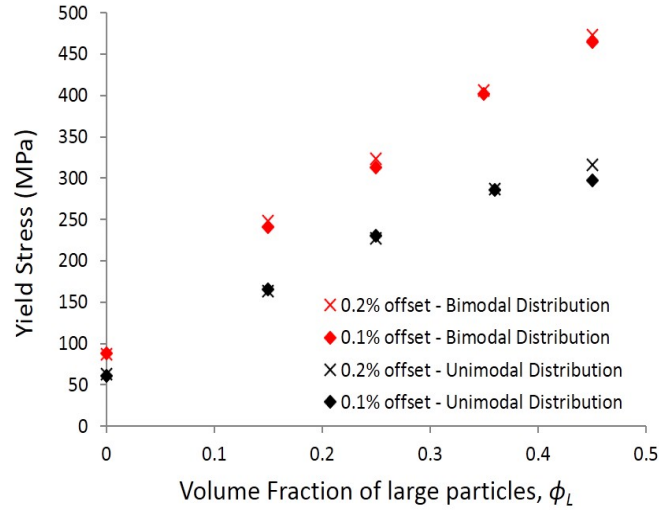
Figure 7.3.5: Yield stress vs volume fraction of large particles, with and without the presence of fine γ' ($\lambda_{jog} = 76$nm / $300b$).

Figs. 7.3.6 and 7.3.7 contain the flow stress and yield stress plots for the same distributions with a narrow jog spacing of $\lambda_{jog} = 100b$. Domain strength still increases with the introduction of small particles, but the smooth curves from the previous figures are not seen. The narrower jog spacing here is restricting plasticity sufficiently to stop the slow development of slip bands and keep the more abrupt shear avalanches occurring. The increase in the 0.1% offset yield when the tertiaries are added is 126 MPa at $\phi_L = 0.25$, 139 MPa at $\phi_L = 0.35$ and 143 MPa at $\phi_L = 0.45$.
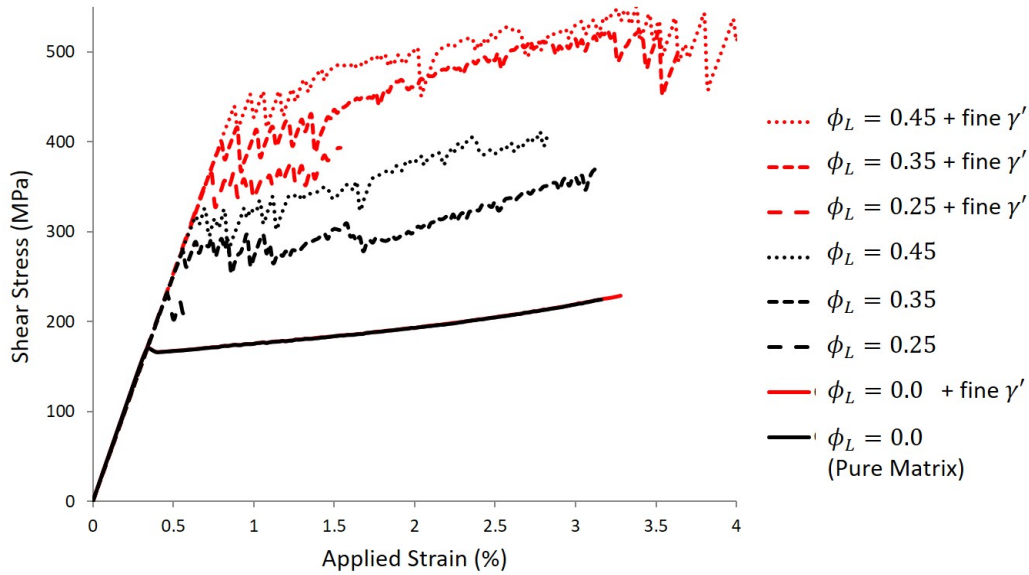
Figure 7.3.6: Flow stress response for a matrix with different unimodal or bimodal particle distributions and large particle radius of 50nm ($\lambda_{jog} = 25$nm / $100b$).
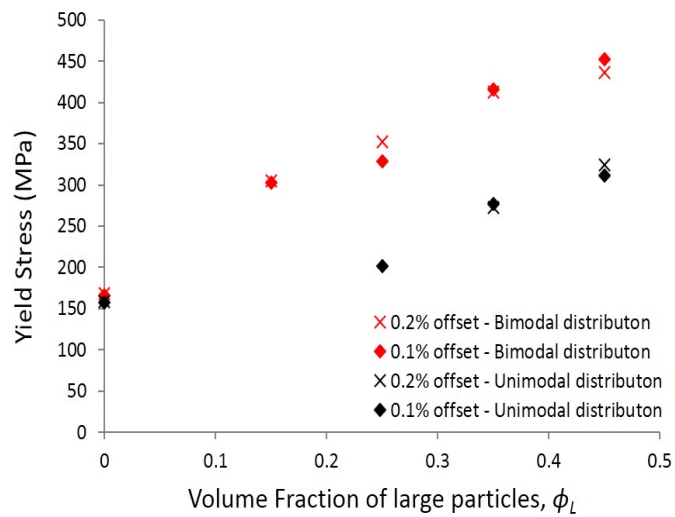

Figure 7.3.7: Yield stress vs volume fraction of large particles, with and without the presence of fine γ' ($\lambda_{jog} = 25$nm / $100b$).

7.3.2   Effect of large particle size

In Figs. 7.3.8 and 7.3.9 tertiary particles are added to different size distributions of the large particles with a constant volume fraction of $\phi_L = 0.35$. The yield stresses, which had appeared to decrease linearly with increasing particle size in the unimodal case (black lines), no longer follow a linear trend in the bimodal case (red lines). The 0.1% offset yield difference between the 150nm and 100nm radius distributions is 34 MPa, while the difference between the 100nm and 50nm radius distributions is almost three times larger at 95 MPa. The interstitial fine γ' increase the shear stress cutting threshold at which the large particles are cut and also act as the dislocation pinning spacing in low stress regimes. The combination of multiple possible spacings for the line tension (see eqn (4.3.15)), each dependent on the local stress and whether the particle type at a given element may be sheared, create this non-linear emergent behaviour.
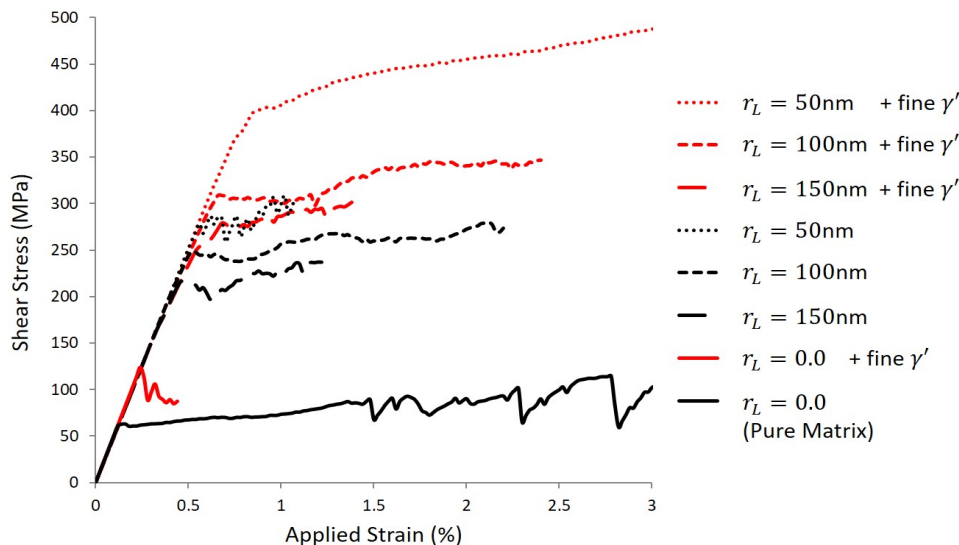

Figure 7.3.8: Flow stress response for a matrix with different unimodal or bimodal particle distributions and large particle volume fraction of $\phi_L = 0.35$ ($\lambda_{jog} = 76$nm / $300b$).

For the narrow $100b$ jog spacing case, in Figs. 7.3.10 and 7.3.11, the addition of fine γ' widens the gap between the flow stress curves for different large γ' radii. In the unimodal case (black) the yield stresses are relatively similar and do not follow a clear trend, but with the introduction of the distribution of fine particles the yields follow a linear trend, decreasing with increasing particle size. There is increased work hardening when the precipitate radius is smaller, as this distribution

146
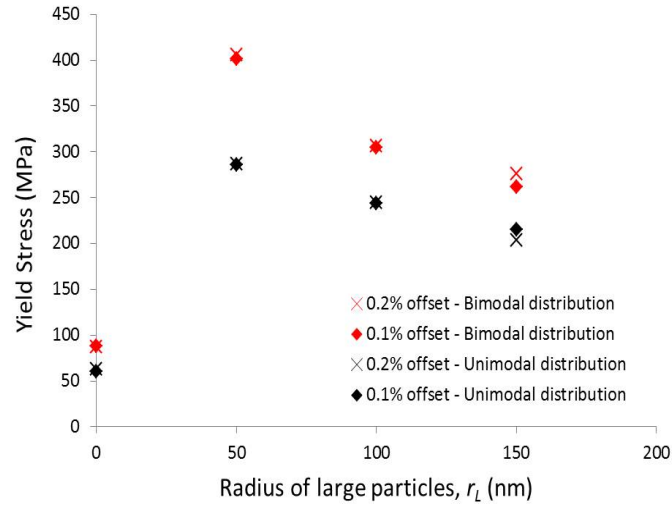
Figure 7.3.9: Yield stress vs radius of large particles, with and without the presence of fine γ' ($\lambda_{jog} = 76$nm / $300b$).

provides more impediment to both slip band development and dislocation movement.

The changing trend of the yield stresses depending on the jog spacing in the system is an emergent property of the model, arising non-trivially through competing mobility and line tension terms and the subsequent effect on internal dislocation stress fields and source generation rates.
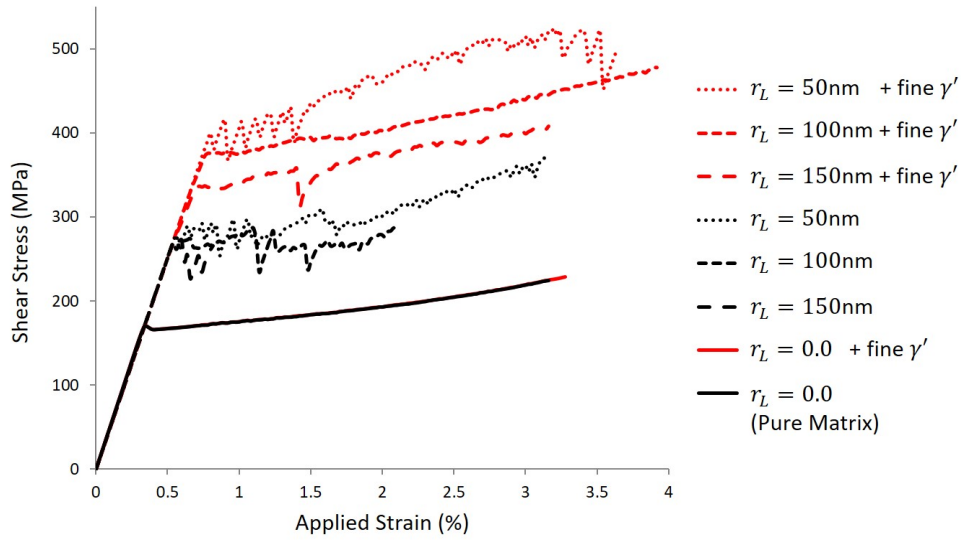
Figure 7.3.10: Flow stress response for a matrix with different unimodal or bimodal particle distributions and large particle volume fraction of $\phi_L = 0.35$ ($\lambda_{jog} = 25$nm / $100b$).
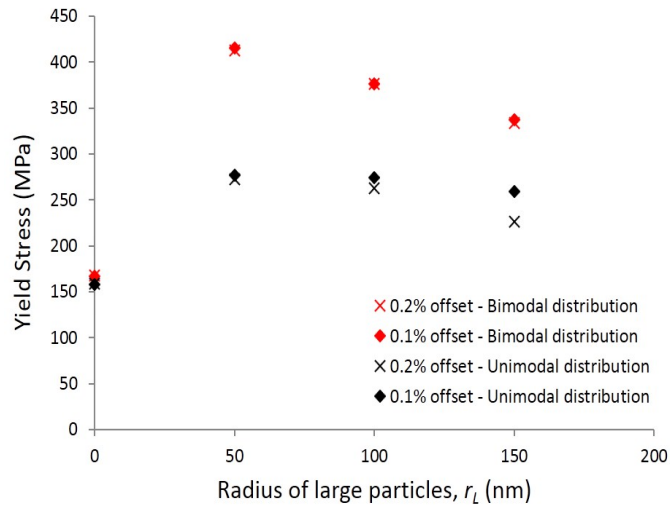

Figure 7.3.11: Yield stress vs radius of large particles, with and without the presence of fine γ' ($\lambda_{jog} = 25$nm / $100b$).

7.3.3 Trimodal dispersions

This section will present results corresponding to bimodal and trimodal γ' dispersion. For simplification of the model set-up, the large particle populations investigated in the previous section will be decomposed into two size populations. The large particle volume fraction will remain constant at $\phi_L = 0.35$, with individual particles radii being either 50nm or 100nm. The fine particles of $r_s = 10$nm cannot be resolved spatially in the current computational domains and will be treated as in the previous section. Fig. 7.3.12 shows the dispersions analysed.

1 – 0% 50nm 0% 100nm (open matrix) **2** – 100% 50nm 0% 100nm **3** – 75% 50nm 25% 100nm

**4** – 50% 50nm 50% 100nm **5** – 25% 50nm 75% 100nm **6** – 0% 50nm 100% 100nm
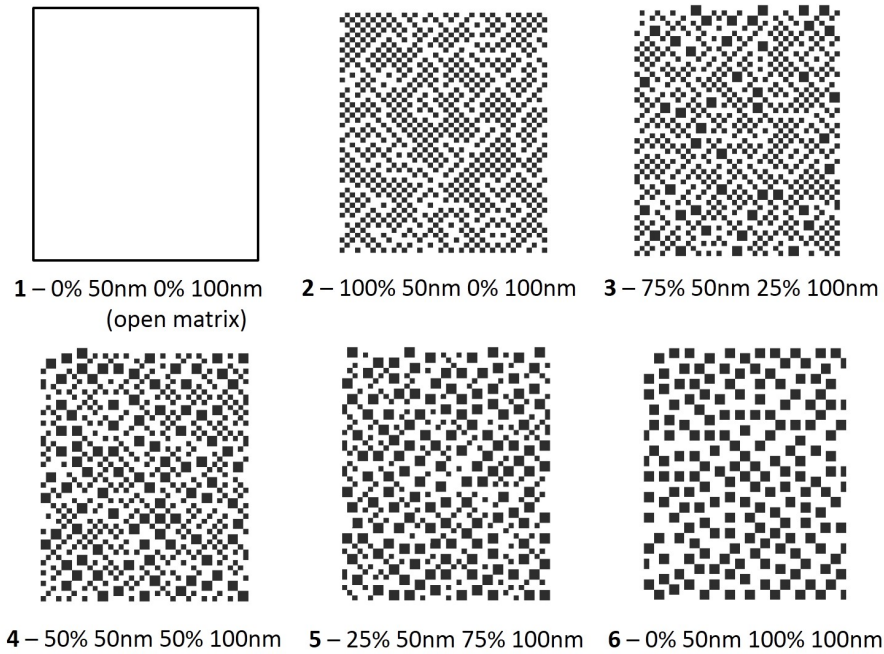
Figure 7.3.12: Key for the particle distributions implemented within this section.

Figs. 7.3.13 and 7.3.14 show the flow stress curves for the combined 50 and 100nm particle distributions, both without and with the presence of the fine 10nm particles. For Fig. 7.3.13, the case without the small tertiaries, a variety of different curve shapes are produced: Dist. **2** ($\hat{r}_L = 50$nm) and Dist. **3** ($\hat{r}_L = 62.5$nm) show the jerky curve progress that indicate significant shear avalanches occur during the deformation; Dist. **4** ($\hat{r}_L = 75$nm) and Dist. **5** ($\hat{r}_L = 82.5$nm) show smooth curves with gradual yielding that has been associated in the previous sections with micro-shear bands in early deformation; Dist. **6** ($\hat{r}_L = 100$nm) has a smooth curve, but with an abrupt yield at 250 MPa, making it most similar in shape to pure matrix curve, but with a

149

higher yield point. Those distributions with a mixture of particle sizes (**3**, **4** and **5**) show a higher flow stress response than those composed of a single uniform size. The highest strength is seen in Dist. **3** ($\hat{r}_L = 62.5$nm) which contains mainly 50 nm particles with 25% of larger 100nm particles.

In Fig. 7.3.14, when fine particles are included in the domain, the flow stress curves become smooth for each distribution. The shear avalanches from Dist. **2** ($\hat{r}_L = 50$nm) and Dist. **3** ($\hat{r}_L = 62.5$nm) are no longer seen, replaced by a gradual yielding. All yield points are increased from the previous case and Dist. **3** ($\hat{r}_L = 62.5$nm) retains the highest flow stress for applied strains above 1%. A key difference with the inclusion of fine γ' is that the bimodal Dist. **2** ($\hat{r}_L = 50$nm) shows higher yield than the trimodal Dist. **4** ($\hat{r}_L = 75$nm) and Dist. **5** ($\hat{r}_L = 82.5$nm).
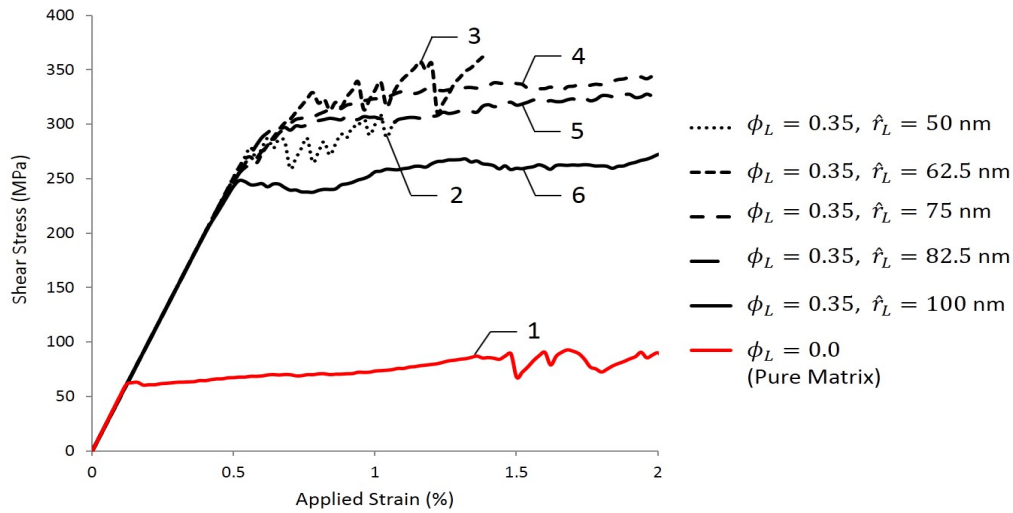

Figure 7.3.13: Flow stress response for particle distributions in Fig. 7.3.12, with constant volume fraction $\phi_L = 0.35$ ($\lambda_{jog} = 76$nm / $300b$).
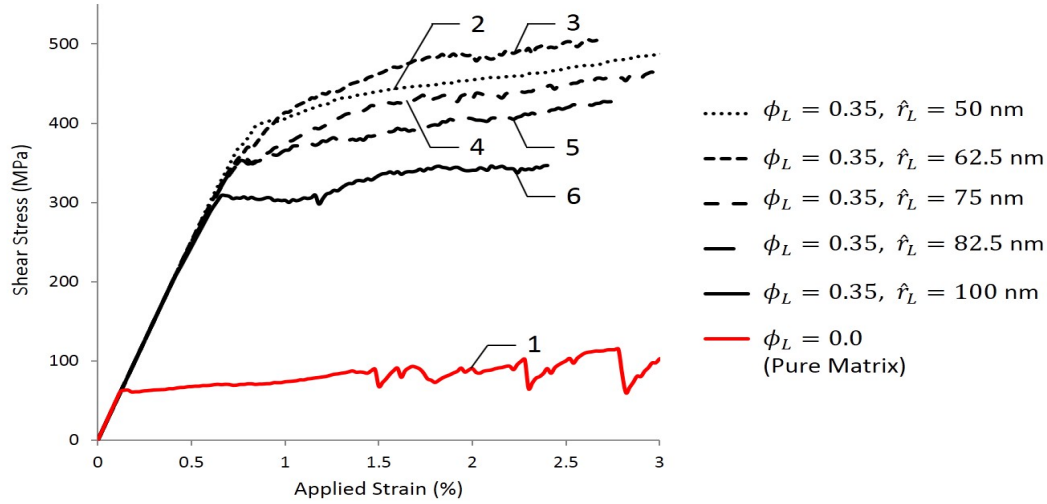
Figure 7.3.14: Flow stress response for particle distributions in Fig. 7.3.12, with constant volume fraction $\phi_L = 0.35$ and fine γ' ($\lambda_{jog} = 76$nm / $300b$).

The yield stress vs distribution number is presented in Fig. 7.3.15. Those flow stress curves that showed more gradual yield behaviour are reflected in this plot by the larger distance between 0.1 and 0.2% offset. Contributions to the yield stress in this model include the line tension that acts upon a dislocation segment from out-of-plane interactions and the obstructions caused by in-plane particles which must be overcome. The line tension is calculated as a mean field effect which is inversely proportional to the average particle spacing for the distribution $\hat{\lambda}_L$. This average spacing decreases moving from Dist. **6** → **2**, meaning Dist. **2** ($\hat{r}_L = 50$nm) has the highest line tension acting on a dislocation segment, followed by Dist. **3** ($\hat{r}_L = 62.5$nm). The cutting threshold calculation also uses this average particle spacing, but the particle radius value used is appropriate to the individual obstacle being cut in each instance (not the mean radius). Table 7.3.1 lists the mean particle spacings and cutting thresholds for the particles present in each distribution. For Dist. **3** ($\hat{r}_L = 62.5$nm) it can be seen that introducing a small quantity of larger 100nm particles to a domain with low particle spacing means the cutting threshold for the large particle rises significantly. This provides the increased strength observed in these simulations. Dist. **6** ($\hat{r}_L = 100$nm), by contrast, has a large particle spacing and a lower cutting threshold, giving it the lowest yield strength in both unimodal and bimodal situations.

151
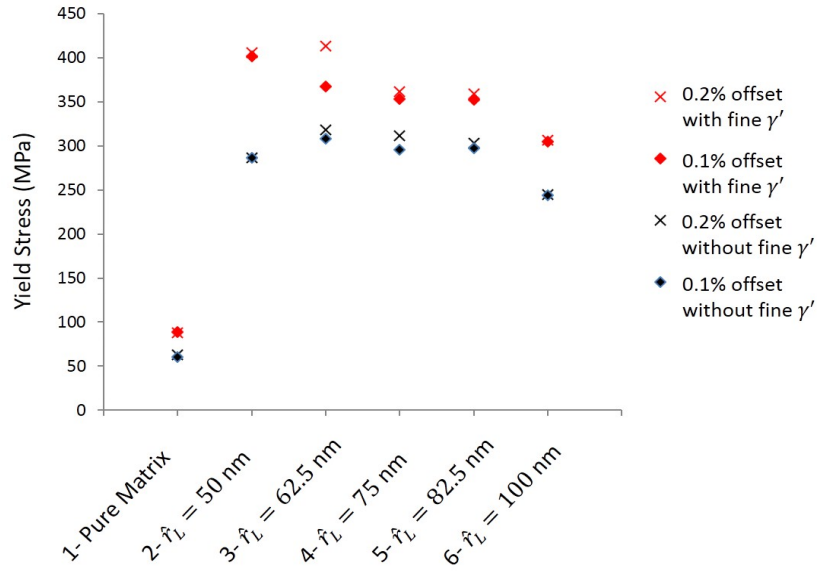
Figure 7.3.15: Yield stress vs particle distribution for the simulations within this section.

Table 7.3.1: Details of large particle dispersion and associated cutting threshold for this section (without fine γ')

Dist. number	Mean radius in distribution $\hat{r}_L$ (nm)	Mean edge to edge spacing $\hat{\lambda}_L$ (nm)	Distribution composition	Cutting threshold τ_c (MPa)
2	50	40.7	$r_L = 50$nm (100%)	262.8
3	62.5	50.8	$r_L = 50$nm (75%)	257.5
			$r_L = 100$nm (25%)	515.0
4	75	61.0	$r_L = 50$nm (50%)	214.5
			$r_L = 100$nm (50%)	429.1
5	82.5	67.2	$r_L = 50$nm (25%)	195.0
			$r_L = 100$nm (75%)	390.1
6	100	81.2	$r_L = 100$nm (100%)	262.8

7.3.4 Influence of temperature

Temperature is shown to have a significant effect on the deformation behaviour of superalloys at $> 700°$C. Amongst other properties, thermal conditions can influence the elastic stiffness constants of the material, the dynamics (both glide and climb) of the dislocation content and the microstructure. As these influences each apply concurrently it is difficult to experimentally separate the contribution to the deformation behaviour of the changing microstructure and the temperature-dependent thermophysical parameters. However, through the proposed computation mechanics approach it is possible to isolate these factors.

In Fig. 7.3.16 flow stress prediction at a number of different temperatures are presented for the

same γ' dispersion parameters. For these constant γ' dispersion simulations the effect of temperature on the predicted flow stress is not significant. The shear modulus for the domain (gradient of the pre-yield curve) is shown to decrease marginally with rising temperature, beginning at 52.72 GPa for 500°C and ending at 45.85 GPa for 1000°C. The 0.1% offset yield drops by only 25 MPa over the same temperature increase.
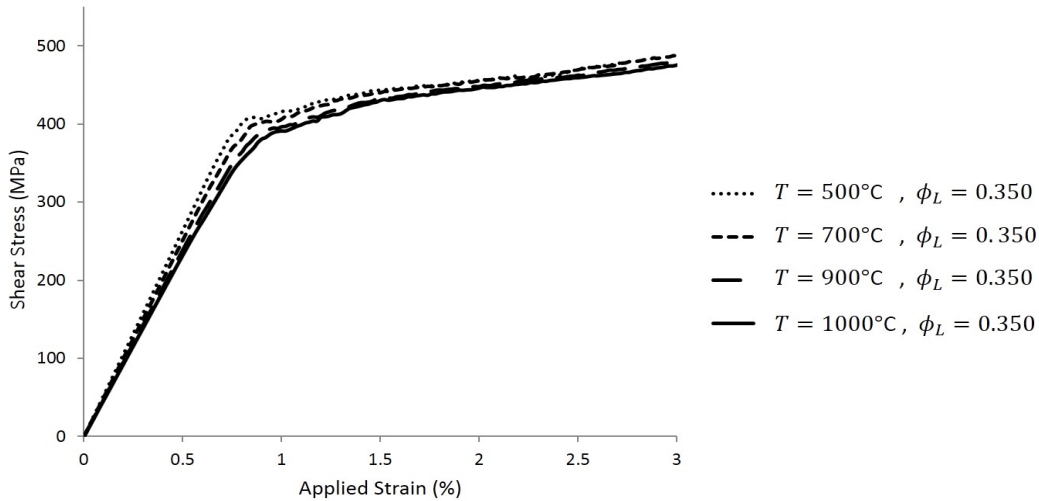

Figure 7.3.16: Flow stress response for a nickel-based superalloy at different temperatures, for a constant bimodal dispersion with parameters $r_L = 50$nm / $\phi_L = 0.35$ and $r_s = 10$nm / $\phi_s = 0.03$. ($\lambda_{jog} = 76$nm / $300b$).

In real alloys, the γ' dispersion will change with increasing temperature and eventually complete dissolve at the solvus temperature. The work of Dyson in 2009 [84] has described a formula by which the equilibrium volume fraction of precipitate phase ϕ_p within a superalloy may be predicted at a given equilibrium temperature T, if the γ' solvus temperature T_{solvus} is known. This is based on a lever-rule representation given by

$$C_0(T) = 17 \; exp\Big(\frac{-7250}{T_{solvus}}\Big)$$
$$C_e(T) = 17 \; exp\Big(\frac{-7250}{T}\Big)$$
$$\phi_p = \frac{C_0 - C_e(T)}{0.23 - C_e(T)} \tag{7.3.1}$$

where C_0 is the concentration of γ' formers and C_e their total equilibrium matrix solute concentration. The numerical constants were chosen to fit experimental data for seven different superalloys,

including CMSX-4. Employing this formula, the volume fraction of γ' has been determined and plotted in Fig. 7.3.17 for two solvus temperatures of 1100°C and 1060°C . The fraction of precipitate is shown to be relatively stable (for both solvus temperatures) up until a temperature of $\sim$ 700°C, whereby it falls away rapidly towards a pure-matrix state.

Computational domains were constructed based on particle distributions with a solvus temperature of $T_{solvus} = 1100$°C or 1060°C between 500°C - 1000°C. In practice the size of the γ' particles will also decrease with increasing temperature. However, this will not be considered in the present calculations and the particle radius of the large particles will be taken as 50nm for all simulations reported in this section.
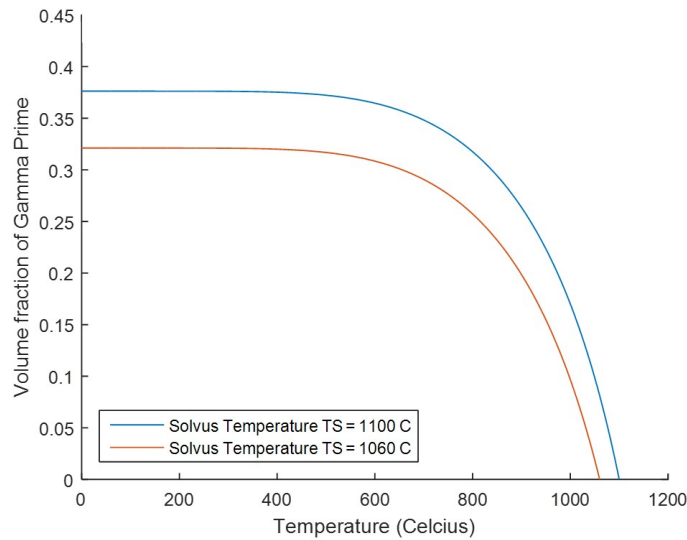
Figure 7.3.17: Predicted Volume Fractions verse temperature for two different solvus temperatures.

Fig. 7.3.18 shows the predicted flow stress curves at a number of temperatures. In this model setup the alloy strength varies considerably, dropping 195 MPa over the temperature range investigated. Comparing this to the 25 MPa drop seen for the simulations with a constant particle fraction indicates that the shifting microstructure is a more dominant factor in controlling softening at high temperature than the thermophysical properties. The curves for 500°C and 600°C are of similar shape with close yield points ($<$ 9 MPa apart). This follows with the fact that the volume fraction changes by only 0.007 over this range. At 700°C the curve starts to soften as the volume fraction of

precipitate is reduced by another 0.015. After this point the volume fraction falls away increasingly rapidly with each incremental temperature increase, and the yield stress of the domain follows this drop-off. At 1000°C, when the volume fraction takes its lowest value of $\phi_L = 0.17$, the curve shows signs of shear avalanches as slip bands develop, this occurs at 0.6%, 1.4% and 2.1% applied strain.
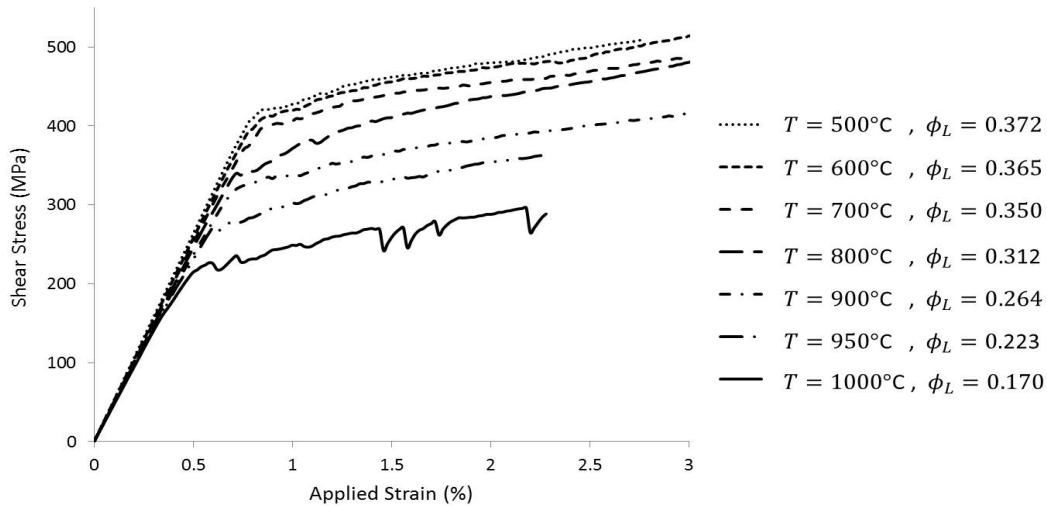
Figure 7.3.18: Flow stress response for a nickel-based superalloy with temperature-appropriate volume fractions for a T_{solvus} of 1100°C. ($\lambda_{jog} = 76$nm / $300b$).

When the solvus temperature is reduced to $T_{solvus} = 1060$°C, the flow stress curves in Fig. 7.3.19 follow the same trend as the previous case, softening increasingly with temperature. The volume fraction of γ' present at a given applied temperature is lower for the lower T_{solvus} value, which creates flow stress curves with lower yields. The drop in volume fraction is largest between 900°C and 1000°C, falling from $\phi_L = 0.199$ to 0.097. At this low volume fraction there are significant shear avalanches after the yield point, when the first particles are cut, this introduces fast dislocation reactions which require prohibitively small time steps to stabilise in the FD implicit scheme. For this reason the final curve is curtailed early after yield.
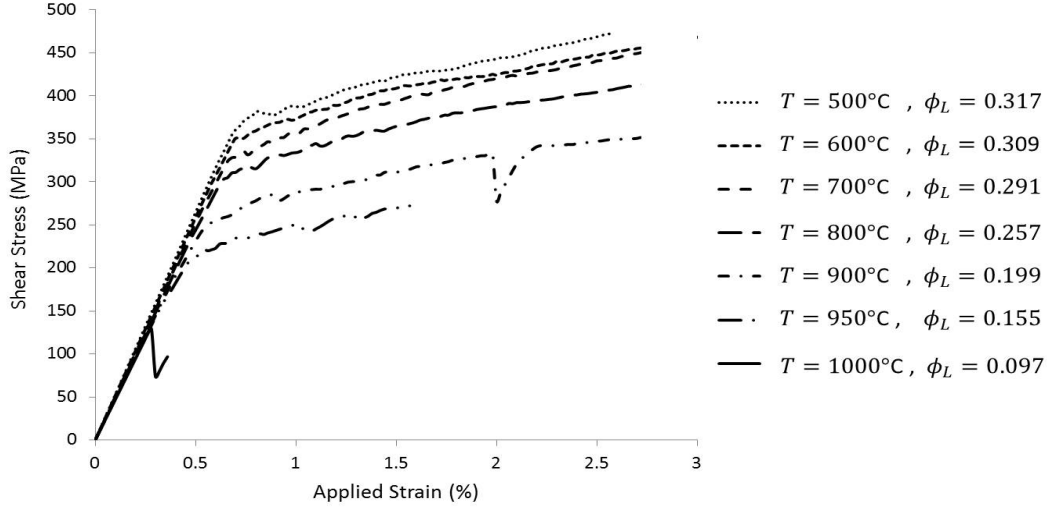
Figure 7.3.19: Flow stress response for a nickel-based superalloy with temperature-appropriate volume fractions for a T_{solvus} of 1060^oC. ($\lambda_{jog} = 76$nm / $300b$).

The yield stresses from the curves for $T_{solvus} = 1100°C$ and $1060°C$ are plotted against temperature in Fig. 7.3.20. The figure also contains the yields from the simulations with constant $\phi_L = 0.35$ and the pure-matrix case, all taken from domains with a jog spacing of $300b$. Trend lines (using a linear or 4th-order polynomial fit) are added for ease of interpretation. It is clear that the yield stress decreases linearly with temperature for systems where the microstructure remains unchanged (green and blue lines), and that this softening seems negligible in comparison to the effect when the microstructure is changed (red and black line). For the realistic volume fraction simulations the yield stresses decrease in a linear manner between $500°C$ and $700°C$, above this temperature the yields drop away rapidly as the solvus temperature is approached. The yield stress decreases with a curve shape which closely parallels the volume fraction over the same temperature range (from Fig. 7.3.17). For lower T_{solvus} the yield stresses drop away more quickly with temperature, and are lower in general. Note that if the changes to the particle size with increasing temperature were to be taken into account, the high temperature strength will be further reduced.

157
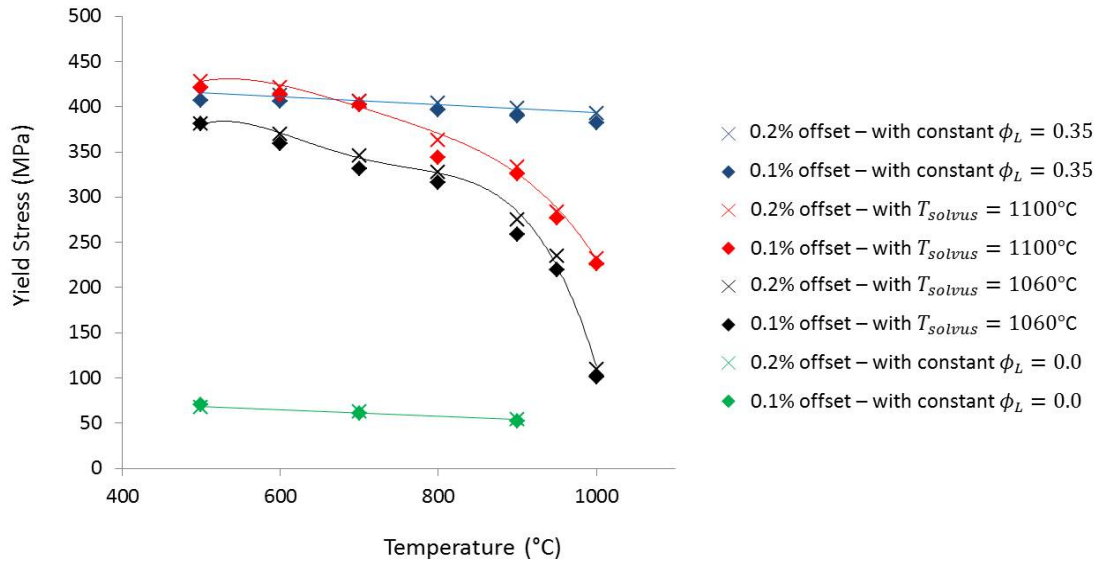
Figure 7.3.20: Yield stress vs temperature for a Nickel-Superalloy with temperature-appropriate volume fractions for different T_{solvus} ($\lambda_{jog} = 76$nm / $300b$).

7.4 Benchmarking Model Against Published Experiments

Single crystal shear testing of a nickel-based superalloy has been reported recently by G. Laplanche et al [41]. This work is atypical in that it reports flow stress curves rather than creep curves, and this has been discussed in context of similar shear creep tests by G. Eggler et al [152]. Laplanche's experiment involved the focused ion-beam (FIB) machining of sample pieces from larger crystals of known orientation, then the subsequent micro double shear (MDS) testing of those crystals with an in-situ SEM micromechanical test rig. An example specimen is shown in Fig. 7.4.1. The MDS method has been previously established, by the same group, for other materials and the exact geometry of the test specimens is provided in Fig. 1 of a paper by J.-K. Heyer et al [153].
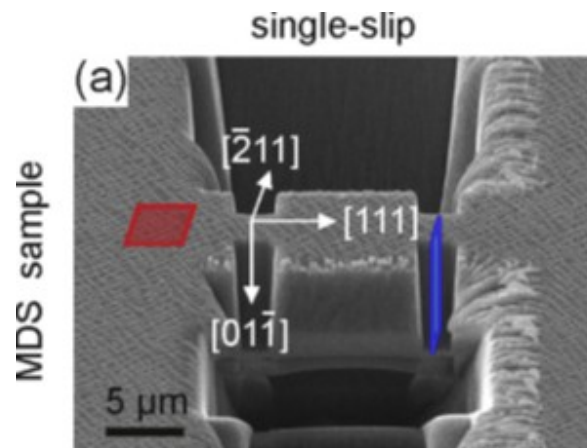
Figure 7.4.1: The MDS test specimen before deformation, showing the overlayed crystallographic orientation and shear area highlighted in blue. Reproduced from G. Laplanche et al [41].

The material in Laplanche's experiment was alloy ERBO/1, a variant of CMSX-4 [42], with micro-samples being taken from both interdendritic and dendritic regions of the casting. The elemental composition of the ERBO/1 alloy was listed as 5.8 wt.% Al, 9.4 wt.% Co, 6.2 wt.% Cr, 0.1 wt.% Hf, 0.6 wt.% Mo, 2.9 wt.% Re, 6.9 wt.% Ta, 1.0 wt.% Ti, 6.3 wt.% W, with Ni to balance. The material had two solution heat treatments at $1290°C$ (for 1h) and $1300°C$ (for 6h), followed by two precipitation heat treatments at $1140°C$ (for 4h) and $870°C$ (for 16h). The dendrite spacing was on average 500μm, and the composition of the γ channels/γ' precipitate was found to be almost constant across the dendritic/interdendritic regions [42]. The γ' particle content comprised of a

unimodal distribution of cuboidal particles, with a volume fraction of $\phi = 0.72$ in the dendritic regions and $\phi = 0.77$ in the interdendritic regions. The particles had an average edge length of 442nm ($r = 221$nm) and average spacing of 65nm.

A load was applied in the $[01\bar{1}]$ direction of the test specimens using a flat punch indenter with a constant displacement rate equivalent to 0.05s^{-1} (shear rate). This loading condition promoted $[01\bar{1}](111)$ single slip across the $24\mu\text{m}^2$ shearing surfaces. From the resultant load, shear displacement and shear zone width, a number of flow stress curves are published [41].

The data from these published curves has been extracted and used for comparison against the FDM model developed in this work. The FDM domain was set up as defined in Section 5.2.1 using a $5\mu\text{m}$ grain size to give a comparable $25\mu\text{m}^2$ shear surface and open boundary conditions for dislocation flux to emulate single crystal conditions. A constant shear strain rate of 0.05s^{-1} was applied to the edges of the domain (following Fig. 5.2.2) and single slip was induced in the $[\bar{1}10](111)$ system (equivalent to the experiment). Simulation domains were created using parameters representative of the dendritic/interdenritic microstructures reported above ($r = 221$nm, $\phi = 0.72/0.77$), an applied temperature of 298K and the standard 200nm FR source spacing from the previous chapters.

Fig. 7.4.2 shows flow stress curves for simulations with dendritic and interdendritic microstructural parameters (solid lines) alongside the corresponding experimental flow stress curves extracted from the literature (dotted lines) [41]. The experimental curves were reproduced by digitising the high-resolution images published alongside the original paper and replotting the data. Two experimental curves are provided from each region to give an idea of the experimental scatter. It can be seen that these simulations give a good agreement with the experimental data, with the predicted macro yield points occurring very close to the observed values for the dendritic and interdendritic material. The post-yield curve shape is quite good, mostly laying within the scatter of the provided experimental curves. The general agreement between predicted and measured flow stresses reflects that the experiments of Laplanche et al. have truly activated single slip (on $[01\bar{1}](111)$), matching the conditions currently being simulated. The simulation of dendrite material, with a lower volume fraction of γ', begins to macro yield at 548 MPa while the interdendritic simulation yields at 591 MPa:

this is consistent with the fact that the interdenritic material has a smaller particle spacing and thus a greater stress threshold for precipitate shearing and extra line tension on gliding dislocations.
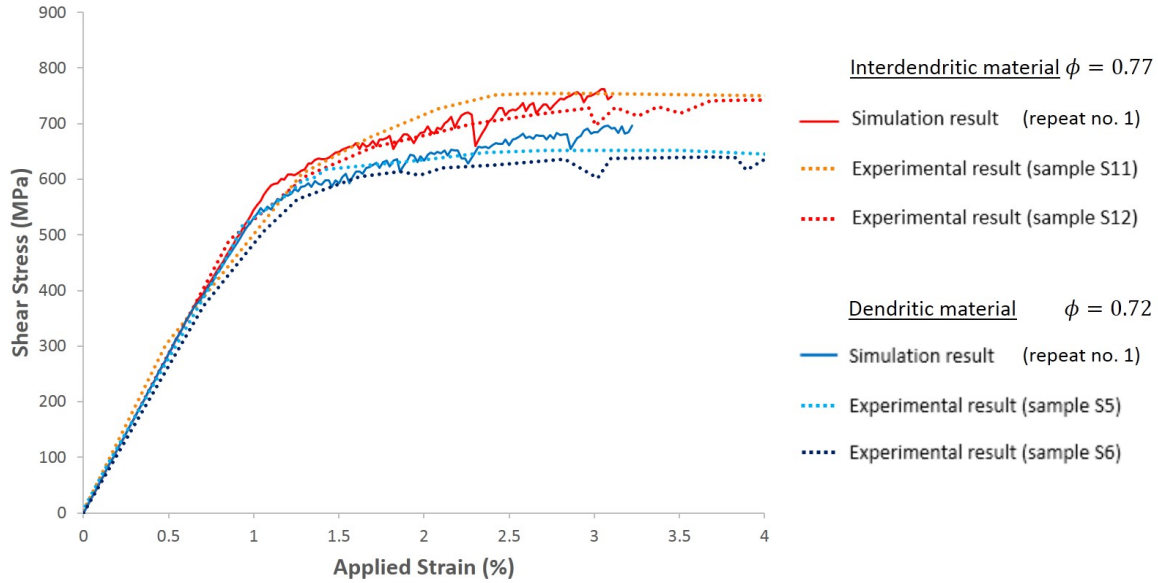

Figure 7.4.2: Comparison of model and experiment for simulations with dendritic and interdentritic volume fraction [41] ($r = 221$nm), loaded with a strain rate of 0.05^{-1} ($\lambda_{jog} = 76$nm / $300b$).

The graphics in Fig. 7.4.3 show the development of dislocation density α_{13}, and the accompanying plastic shear deformation gradient F^p_{12}, for the simulations from the previous plot. Images are provided for increasing applied strain levels. It can be seen that at the first strain level (1.06%) the dendritic material has a single slip band forming across the length of the domain, shearing through the γ' particles near the top of the domain. At the same strain level within the interdendritic material the particles are not yet sheared and only micro-slip bands are seen between the dislocation sources (left boundary) and the precipitates: this corresponds to the later yield point in the interdendritic simulation. At the next strain level (1.20%) both materials show two slip bands running across the full domain, however F^p_{12} is higher in the dendritic simulation, lowering the rate of stress increase. This is mirrored in the lower hardening rate observed in Fig. 7.4.2 (blue solid line) for this period. At the final strain level (1.64%) the interdendritic simulation has developed a higher number of slip bands, but each carries less F^p_{12} than those in the dendritic simulations. At this point both materials reach similar, constant hardening rates in the flow stress curves. In

161

general more dislocation density is seen in the dendritic simulations, leading to more plastic slip.
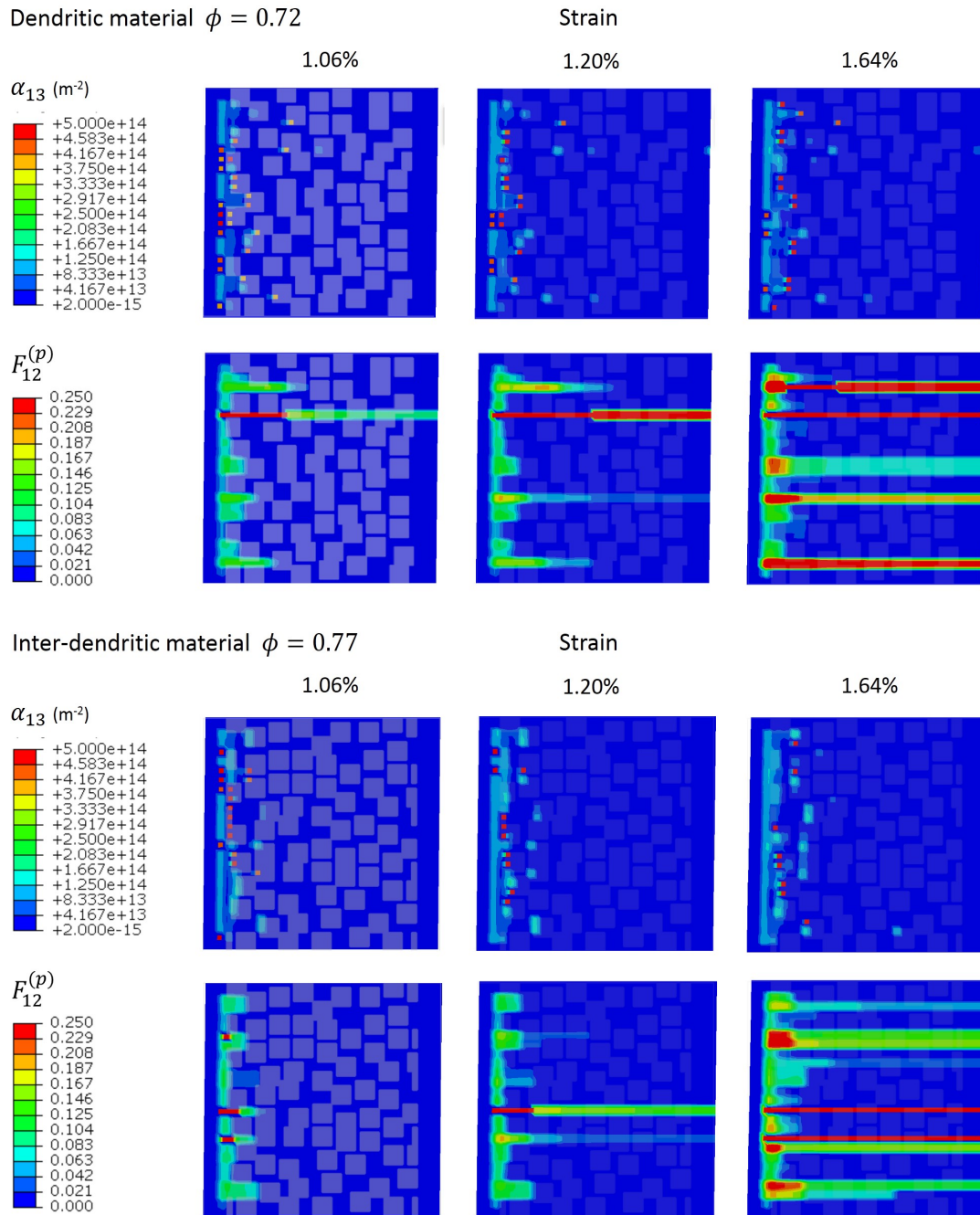

Figure 7.4.3: Maps of dislocation density α_{13} and plastic band evolution F_{12}^p, at given applied shear strains, for the simulated dendritic and interdendritic material domains. (Images taken from simulation repeat no. 1. Particle distributions are overlaid on the left-hand images.)

In Laplanche et al's [41] original analysis of their experimental curves, the stress value at which linear elastic behaviour ended was recorded as τ_{el}. The mean value of τ_{el} was **490 $\pm$ 20 MPa** for the dendritic curves and **490 $\pm$ 5 MPa** for the interdendritic curves. The stress at which a sudden deformation event (SDE) first occured was recorded as τ_{SDE}. Here a SDE was characterised by a significant strain increase in a short period of time. The mean value of τ_{SDE} was **630 $\pm$ 20 MPa** for the dendritic curves and **700 $\pm$ 40 MPa** for the interdendritic curves.

In order to compare against this analysis, three repeat simulations were performed for each material type (with different discrete particle distributions), the results from these simulations are provided in Table 7.4.1. This table includes the 0.1% yield stress τ_y, the stress when linear elastic behaviour ends τ_{el}, the stress when the first particles are sheared $\tau_{\gamma'shear}$, the stress before the first sudden deformation event τ_{SDE} and the stress drop during this event $\Delta\tau_{SDE}$. (As the FE boundary conditions apply a constant total strain rate to the simulation domain it was not possible to see the sudden strain increase from the experiments. It was possible, however, to see large stress drops associated with sudden slip band formation and this criteria for τ_{SDE} was used instead.)

Table 7.4.1: Stresses observed in shear simulations of dendritic/interdendritic CMSX-4 domains.

Dendritic

Repeat No.	τ_y (MPa)	τ_{el} (MPa)	$\tau_{\gamma'shear}$ (MPa)	τ_{SDE} (MPa)	$\Delta\tau_{SDE}$ (MPa)
1	548	380	484	636	23
2	554	383	515	639	14
3	496	373	452	-	-
average	**533 $\pm$ 32**	**378 $\pm$ 5**	**484 $\pm$ 31**	**638 $\pm$ 2**	**18 $\pm$ 6**

Interdendritic

Repeat No.	τ_y (MPa)	τ_{el} (MPa)	$\tau_{\gamma'shear}$ (MPa)	τ_{SDE} (MPa)	$\Delta\tau_{SDE}$ (MPa)
1	591	394	553	717	57
2	552	403	522	704	39
3	565	403	529	688	36
average	**569 $\pm$ 20**	**400 $\pm$ 5**	**535 $\pm$ 16**	**703 $\pm$ 14**	**44 $\pm$ 12**

From Table 7.4.1 it can be seen that the first deviation from linear elastic behaviour τ_{el} is underestimated by more than 90 MPa in all cases compared to experiment. This underestimate is likely because the numerical model can determine very minor yield phenomena associated with the small dislocation slip between sources and particles before precipitate shearing ($\tau < \tau_{\gamma'shear}$), as shown in the bottom left image of Fig. 7.4.3. The precipitate shearing stress $\tau_{\gamma'shear}$ occurred around ~ 100 MPa higher than τ_{el} for both materials and this quantity falls more in line with the experimental values of τ_{el}. The predictions for the stresses at which sudden plastic deformation occurs τ_{SDE} agree very closely with the experimental findings. In two of the dendritic simulations a plastic slip band was seen to develop rapidly, following the shearing of a line of precipitate particles, at domain shear stresses of 636 and 639 MPa respectively (the third repeat simulation saw no SDEs). These stress values line up comfortably within the 630 ± 20 MPa range observed in experiment. In the interdendritic material simulations a wider range of τ_{SDE} values were predicted, averaging at 703 MPa. This increased magnitude and widened range closely mirrors the real experiment, where τ_{SDE} was observed as 700 ± 40 MPa. Finally, the experimental analysis found significantly larger strain intervals for SDEs in the interdendritic material. This was associated with the higher stresses created in these samples. An equivalent behaviour was observed within the FE-FDM model, where the interdendritic domains saw much larger stress-drops $\Delta\tau_{SDE}$ following the SDEs. An example is clearly seen at 717 MPa of the solid red curve in Fig 7.4.2, where the $\Delta\tau_{SDE}$ is 57 MPa. The largest $\Delta\tau_{SDE}$ stress-drop in the dendritic simulations was 23 MPa. The greater size of the interdendritic stress-drops reflects the greater amount of plastic shear strain developed within a single event for those simulations. The experimental work states [41]: "*due to the higher γ'-volume fraction, higher stresses are required to initiate sudden deformation events (SDEs), which represent larger scale deformation processes.*". These phenomena were found not to be observed in tests of larger mm-scale samples [154], which implies that they are due to very localised (discrete) strain band formation.

Chapter 8

Emergent Behaviour I: Backstress Development

The heterogeneous development of slip bands within this model causes a redistribution of stresses across the domain. As each band forms the local plastic strain within it increases and by association the elastic stress in the slip band is reduced, effectively creating a softer material in the slipping region. To balance this the purely elastic zones between the slip bands will take more of the applied load, analogous to the dispersed phase in a composite material. By summing the local stresses $\underline{\underline{\pi}}^{\infty}(\underline{X})$ in the plastically active and inactive elements separately and dividing by the total volume, the homogenised stress contributions from the plastic zones $\underline{\underline{\sigma}}^{PZ}$ and the elastic zones $\underline{\underline{\sigma}}^{EZ}$ may be individually defined in the usual way as

$$\underline{\underline{\sigma}}^{PZ} = \frac{1}{V_{\Omega}} \iiint_{N_{plastic}} \underline{\underline{\pi}}^{\infty}(\underline{X}) \, d^3\underline{X} \qquad \underline{\underline{\sigma}}^{EZ} = \frac{1}{V_{\Omega}} \iiint_{N_{elastic}} \underline{\underline{\pi}}^{\infty}(\underline{X}) \, d^3\underline{X} \qquad (8.0.1)$$

where $N_{plastic}$ are the volume elements containing plastic strains and $N_{elastic}$ are the pure elastic volume elements. These regions are depicted in Fig. 8.0.1 for a simulation containing 5 sources. PZ or EZ are used to refer to the plastic or elastic zones respectively, and when used in sub-script or super-script indicate that the associated quantity pertains to this zone. The volume averaged stress state for the entire domain, that was defined in eqn (6.0.1) and used in previous results sections, is simply the summation of the homogenised stress contributions from each zone $\underline{\underline{\sigma}} = \underline{\underline{\sigma}}^{PZ} + \underline{\underline{\sigma}}^{EZ}$.

The partitioned stresses may also be represented by the volume average over the volumes of the

individual zones

$$\langle \underline{\underline{\pi}} \rangle_{PZ} \;=\; \frac{1}{V_{PZ}} \iiint_{N_{plastic}} \underline{\underline{\pi}}^{\infty}(\boldsymbol{X})\, d^3\boldsymbol{X} \qquad \langle \underline{\underline{\pi}} \rangle_{EZ} \;=\; \frac{1}{V_{EZ}} \iiint_{N_{elastic}} \underline{\underline{\pi}}^{\infty}(\boldsymbol{X})\, d^3\boldsymbol{X} \quad (8.0.2)$$

where $\langle \underline{\underline{\pi}} \rangle_{PZ}$ may be considered the effective stress within the slip bands. The expressions in eqns (8.0.1) and (8.0.2) are then related by the the volume fractions ϕ_* of the elastic and plastic zones within the domain

$$\underline{\underline{\sigma}}^{PZ} \;=\; \phi_{PZ}\, \langle \underline{\underline{\pi}} \rangle_{PZ} \qquad\qquad\qquad \underline{\underline{\sigma}}^{EZ} \;=\; \phi_{EZ}\, \langle \underline{\underline{\pi}} \rangle_{EZ} \qquad (8.0.3)$$

The volume averaged stress within the slip bands may be expressed as the averaged total stress of the domain minus some perturbation or *backstress* $\underline{\underline{\chi}}^{(S)}$ which accounts for the stress transfer away from the plastic zone

$$\langle \underline{\underline{\pi}} \rangle_{PZ} \;=\; \underline{\underline{\sigma}} - \underline{\underline{\chi}}^{(s)} \qquad\qquad (8.0.4)$$

$$\underline{\underline{\sigma}}^{PZ} \;=\; \phi_{PZ}\, (\underline{\underline{\sigma}} - \underline{\underline{\chi}}^{(s)}) \qquad\qquad (8.0.5)$$

The elastic backstress (or "internal stress" [84]) has been defined in this form in literature concerned with nickel-based superalloy creep [88] [155], developed over the last 30 years. However, using eqn (8.0.2) the effective stress and backstress may now be plotted directly for any simulation, using:

$$\underline{\underline{\chi}}^{(s)} \;=\; \underline{\underline{\sigma}} - \langle \underline{\underline{\pi}} \rangle_{PZ} \qquad\qquad (8.0.6)$$
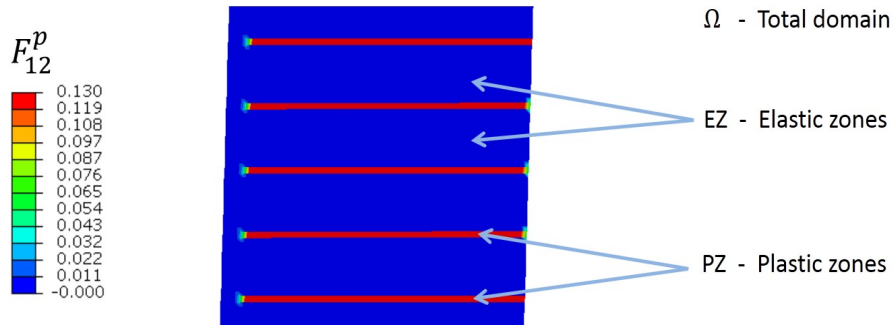
Figure 8.0.1: Elastic and Plastic zones within a domain with 5 sources.

8.1 Backstresses in γ-only Domains

8.1.1 Jog spacing

In Fig. 8.1.1 stress-strain curves are shown for the stress contributions from the plastically de-forming and purely-elastic zones of the single phase material, volume averaged across the whole Ω domain. Three jog spacing conditions are considered. During initial elastic deformation at low strains the elastic zone stress (dotted line) is equal to the total flow stress (solid line), as the entire domain is purely elastic at this stage. At yield the plastic zones are created and the plastic zone stress (dashed line) rises rapidly from zero. A corresponding fall is seen in the stress of the elastic zones as the plastic bands take on some of the total stress. For Fig. 8.1.1(a), where $\lambda_{jog} = 1000b$, once the plastic zones are created the stress within is seen to develop slowly with applied strain, increasing 7.3MPa over the following 1% strain.

For the narrower jog spacings of $300b$ (Fig. 8.1.1(b)) and $100b$ (Fig. 8.1.1(c)) the stress in the plastic zones stabilises at the initial value that is reached and does not develop significantly with increasing strain. Here the maximum of σ_{12}^{PZ} stress is reached within a single (0.02%) strain increment; during which the FE simulations show that slip bands form rapidly from every available source. The behaviour is captured in the plasticity maps (bottom) in Fig. 8.1.3. This is not the case for the $\lambda_{jog} = 1000b$ simulation, where slip bands are created over a range of strain increments (top Fig. 8.1.3), building slowly and causing a slower increase of σ_{12}^{PZ} stress. Slow slip band de-velopment is seen here as plastic yield occurs at stresses before the majority of dislocation sources are active (below the average source generation threshold of 46.3 MPa). At this point only the sources at the upper end of the Frank-Read length distribution (see Section 5.4.4) have activated, and further plastic bands will develop as and when the other sources reach generation stress.

For comparison, Fig. 8.1.2 display the data from Fig. 8.1.1 averaged over the individual plas-tic and elastic domain volumes. The pre- and post-yield curve trends for $\langle \underline{\underline{\pi}} \rangle_{EZ}$ and $\langle \underline{\underline{\pi}} \rangle_{PZ}$ in shear are similar to $\underline{\underline{\sigma}}^{EZ}$ and $\underline{\underline{\sigma}}^{PZ}$, with the plastic zone stress developing quickly then levelling off while the elastic zone stress steadily increases. With this representation, however, the stress within the elastic domains becomes greater than the total flow stress, while the plastic zone stress levels off

at roughly the yield stress. These values reflect the average elemental values of stress for each zone within the FE simulations. The backstress on the slip bands (from eqn (8.0.6)) is plotted in Fig. 8.1.4, showing backstress initiation tracking with the yield of the respective simulations. For $\lambda_{jog} = 300b$ and $100b$, after and initial peak the backstress increases steadily and at similar rates. As the total flow stress is increasing, it follows that the backstress increases proportionally for the effective plastic band stress $\langle \underline{\underline{\pi}} \rangle_{PZ}$ to remain saturated. Due to the differences in slip band development indicated in Fig. 8.1.3, the backstress for $\lambda_{jog} = 1000b$ does not fall in with the trend of the other two, and increases more slowly to match the plastic band development.
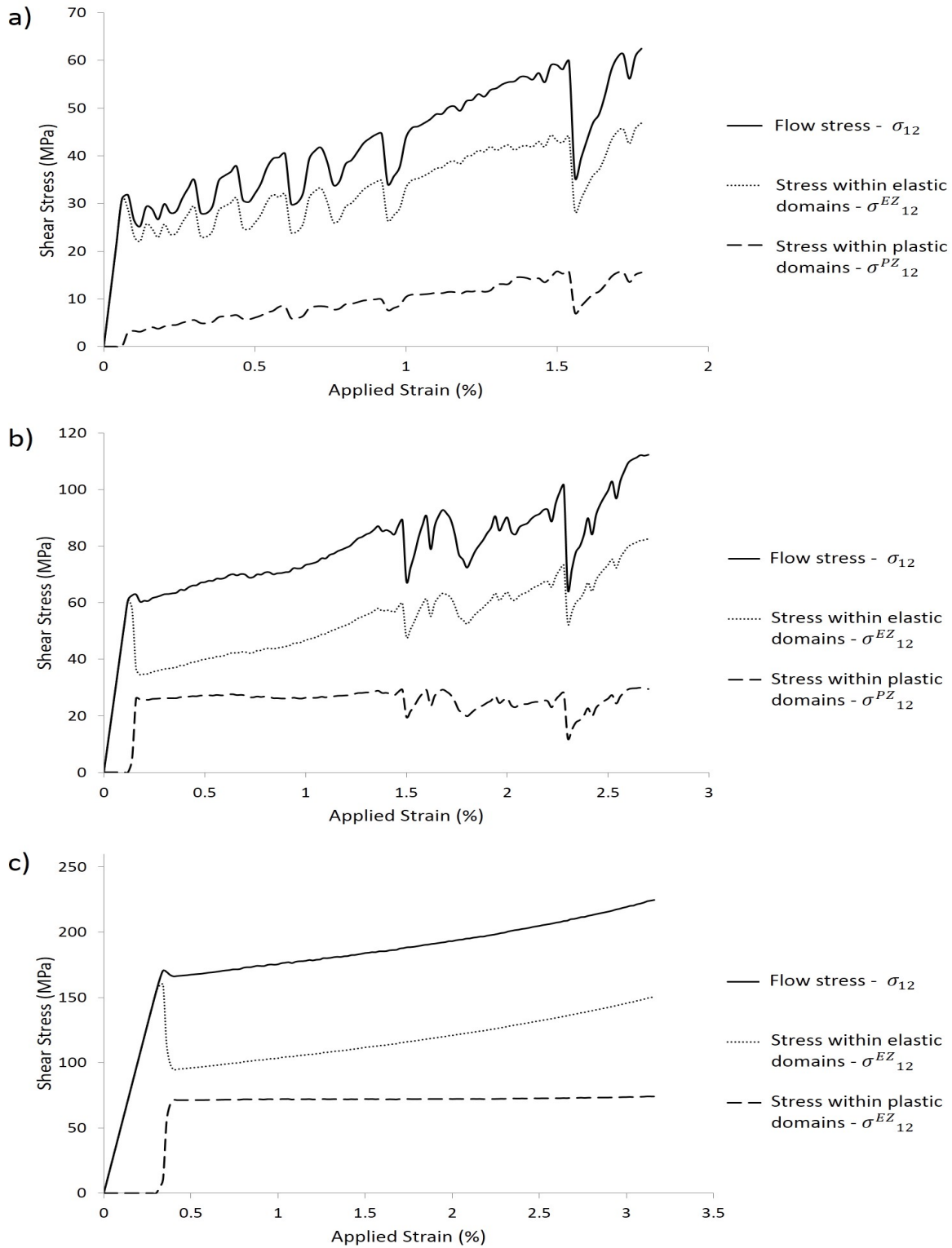
Figure 8.1.1: Flow stress response for a Pure-matrix domain, showing the stress contributions from the elastic/plastic regions: a) $\lambda_{jog} = 254$nm / $1000b$ b) $\lambda_{jog} = 76$nm / $300b$ c) $\lambda_{jog} = 25$nm / $100b$.
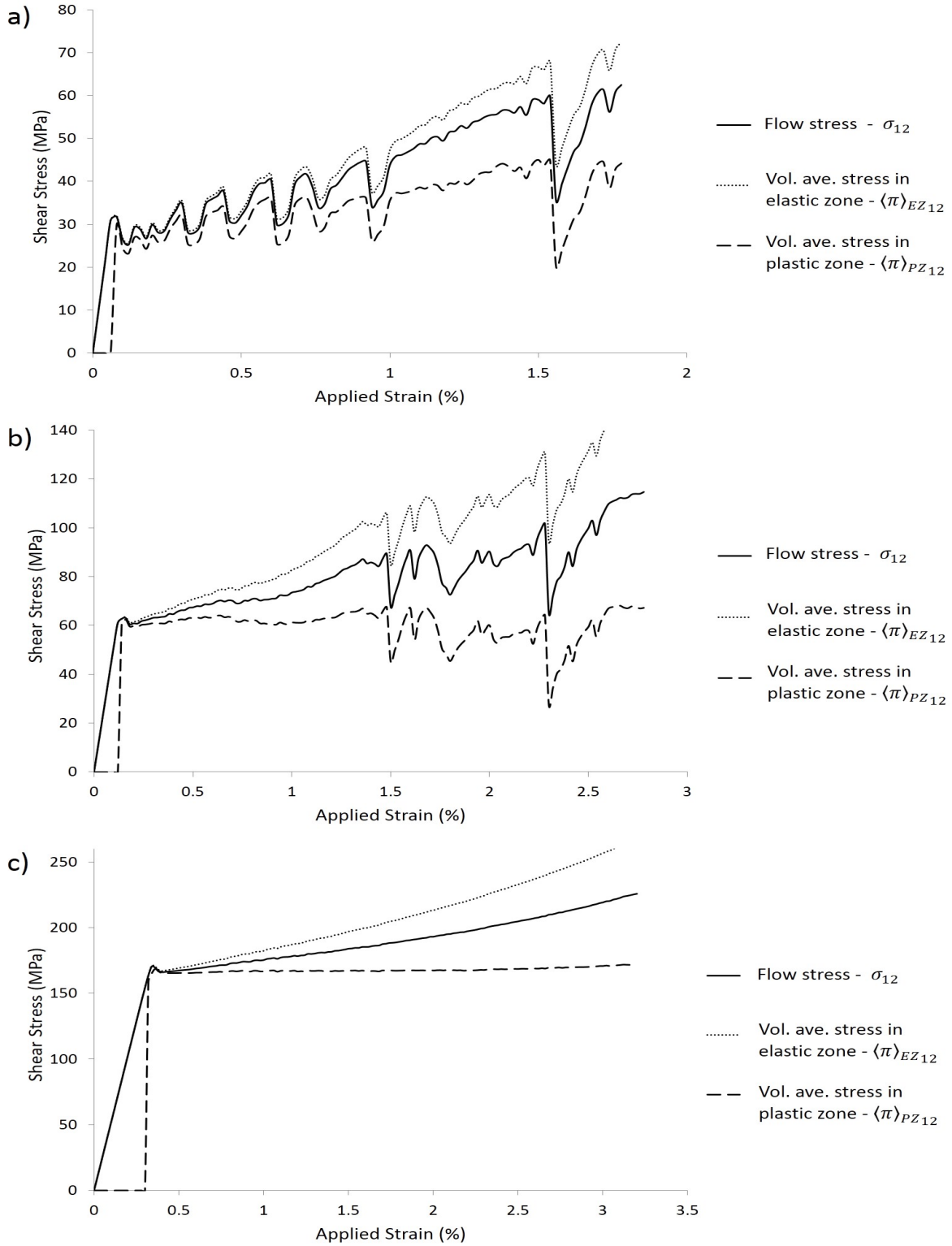
Figure 8.1.2: Flow stress response for a Pure-matrix domain, with stress contributions from the elastic/plastic regions averaged over the elastic/plastic domain volumes: a) $\lambda_{jog} = 1000b$ b) $\lambda_{jog} = 300b$ c) $\lambda_{jog} = 100b$.

170
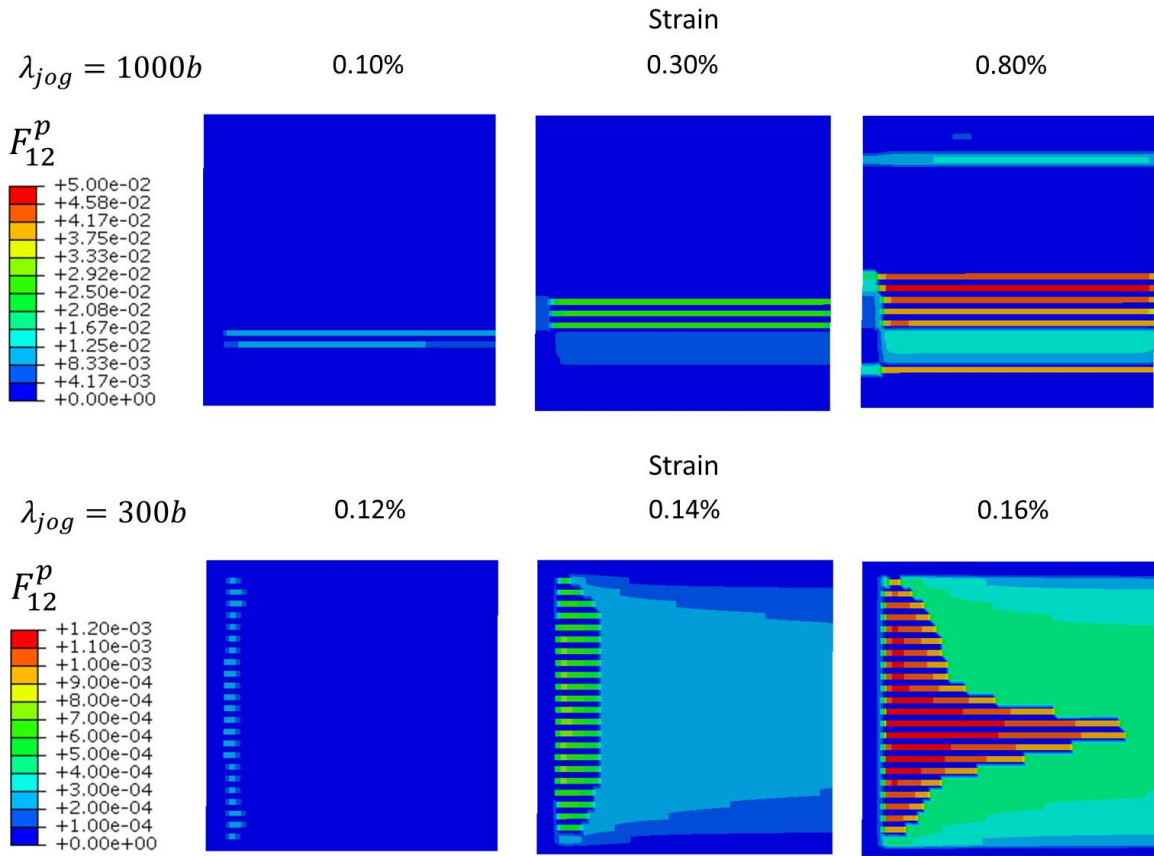
Figure 8.1.3: Plasticity maps showing different slip band development predicted for simulations using different jog spacing parameters.
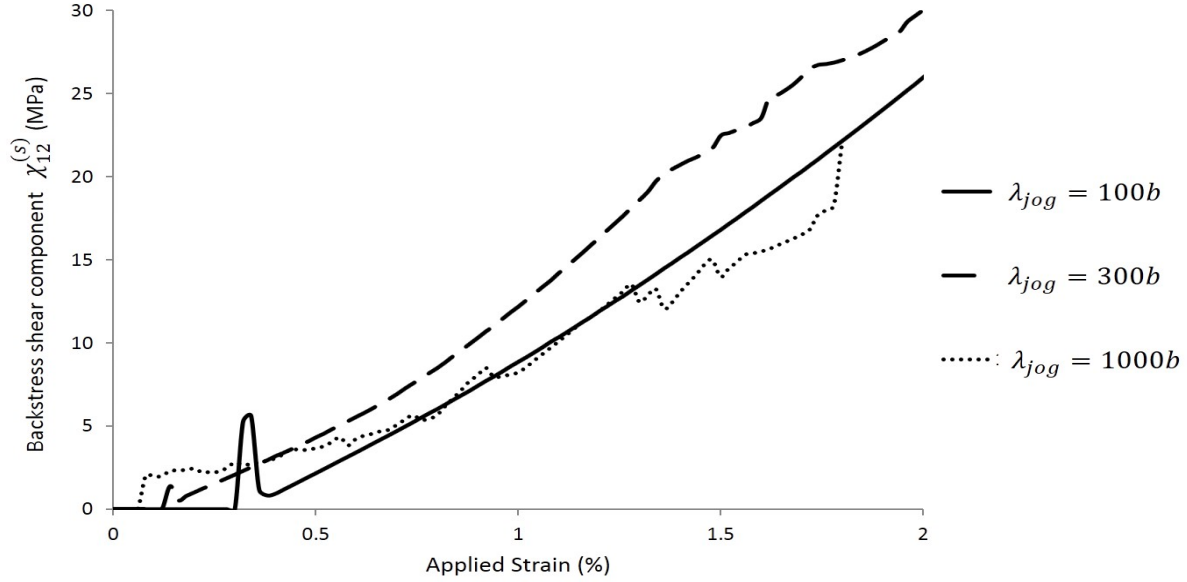
Figure 8.1.4: Backstress $\chi_{12}^{(s)}$ evolution with strain, for open matrix with different jog spacings.

8.1.2 Source distribution

Both the number and the positioning of boundary sources within the domain have been shown to have effect on the total plasticity produced within the simulations in Section 6.2. The simulations from this section are now further investigated with regard to the internal partitioning of stress.

Fig. 8.1.5 shows the stress partitioning for simulations containing different source numbers. The axis scales are the same in each case for ease of comparison. Despite similar yield points in the flow stress curves (solid lines), the plastic zones (dashed lines) are shown to clearly contain a larger contribution of the total stress when the source number is higher and there are more plastic bands available. Post-yield the plastic zone stress increases minutely in each case, meaning that the elastic zones accommodate the majority of the stress increase associated with hardening. Fig. 8.1.5(a), containing 20 sources, shows the elastic zone stress rise 47.0 MPa in the 2% strain following yield, while the plastic zone stress rises only 1.5 MPa in this interval. In Fig. 8.1.5(c), containing 5 sources, the elastic zone stress rises 491 MPa in the 2% strain following yield, while the plastic zone stress rises 24 MPa.

The stress partitioning at different strain intervals is shown in Fig. 8.1.6, plotted against the number of sources in the simulation. First taking Fig. 8.1.6(a) and considering the partitioning immediately after the yield point (diamond markers), it can be seen that the stress within the plastic zones rises linearly with source number. The elastic zone stress, meanwhile, declines linearly. After a further 2% applied strain (cross markers) the stresses in the elastic zones rise considerably, and no longer hold a linear relationship with source number. The stress in the plastic zones increases by a much smaller amount, levelling off at a value of 62 ± 2 MPa for source numbers ≥ 10 (the dashed blue line on the figure marks 62 MPa). This is significant as it suggests a saturation of the stress partitioned within the plastic domain once a threshold number of slip bands is reached. This could propose a criteria for an upper limit to the homogenised stress σ_{12}^{PZ} driving plastic flow.

Fig. 8.1.6(b) represents the stress partitioning as a percentage of the total stress in each zone plotted against the source number. For both yield and post-yield strain levels the percentage stress in the plastic zones is seen to rise linearly with source number. Mirroring this, percentage stress in elastic zones decreases with the negative gradient. In all cases the linear trendlines have R^2 values > 0.999.

The backstresses for this case are plotted in Fig. 8.1.7, showing similar shaped peaks at yield followed by a more rapid development of backstress $\chi_{12}^{(s)}$ when the number of sources (i.e slip bands) is lower.

Fig. 8.1.8 shows the stress-strain curves for simulations with 10 sources and different source placement. It can be seen that the stress gap between the plastic and elastic zones at yield does not change with source placement. Behaviour post-yield shows that the stress within the plastic zones increases at the greatest rate when the sources are further apart. For the case when source spacing is 200nm, in Fig. 8.1.8(a), the plastic zone stress is seen to decrease with increasing strain. It has already been shown in Fig. 6.2.7 that this setup with closely arranged sources produced increased dislocation generation in comparison to more distantly spaced sources; this increased generation evidently serves to increase shear rate in the slip bands and decrease the stress within the plastic zones - lowering σ_{12}^{PZ}.

Fig. 8.1.9 shows similar backstress evolution for each source spacing up until $\sim 1\%$ strain, where the rate of increase becomes greater for closer source spacing. In general at high strains the backstress is, therefore, larger at smaller source spacing.

As these backstresses influence the effective stress acting upon dislocations within the crystal, they will have direct effects upon the evolution of plasticity within a crystal, as stress is transferred away from the slip bands. In the context of nickel-based superalloys this effect would be even greater, due to mechanical yield being tightly linked to the stress at which dislocations will cut the precipitates. It is therefore a matter of high importance for superalloy deformation models to accurately capture the correct backstresses.
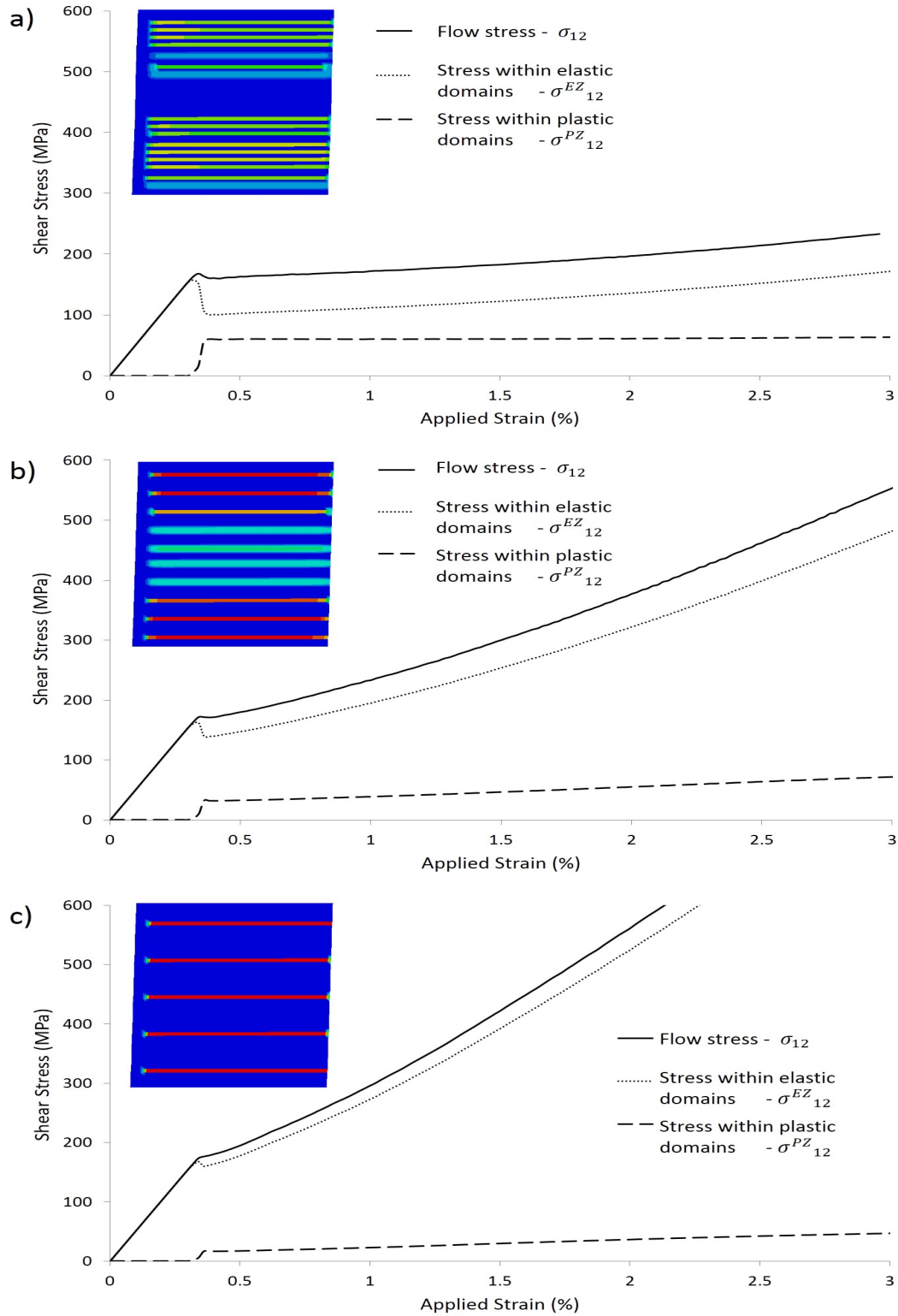
Figure 8.1.5: Flow stress response for a pure-matrix domain with different source numbers, showing the stress contributions from the elastic and plastic regions: a) 20 sources b) 10 sources c) 5 sources $(\lambda_{jog} = 25\text{nm} / 100b)$.

175
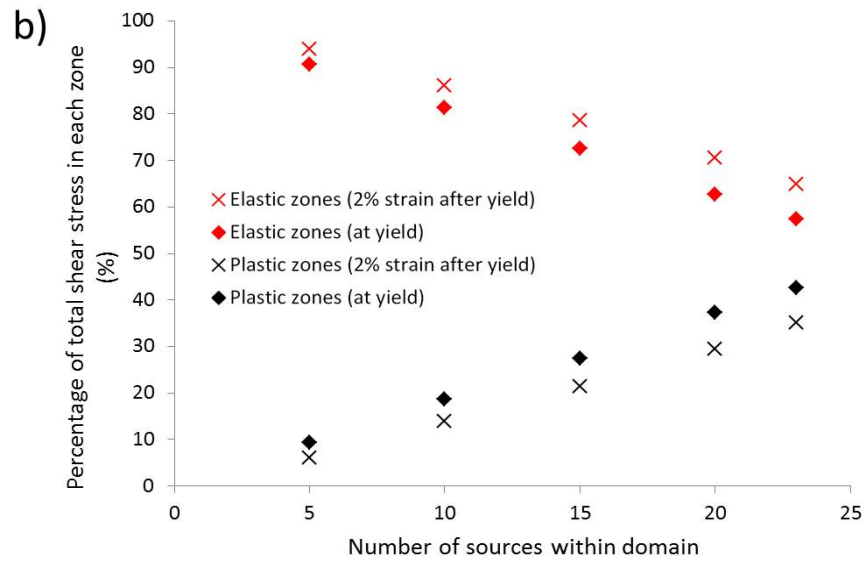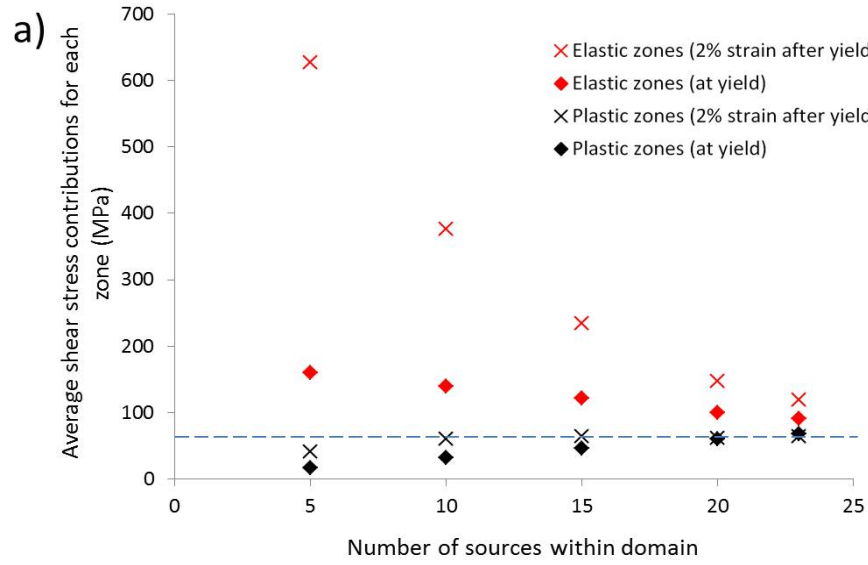
Figure 8.1.6: Stress partitioning measures at two strain levels, within a 5μm domain with different numbers of grain boundary sources ($\lambda_{jog} = 25$nm / $100b$).
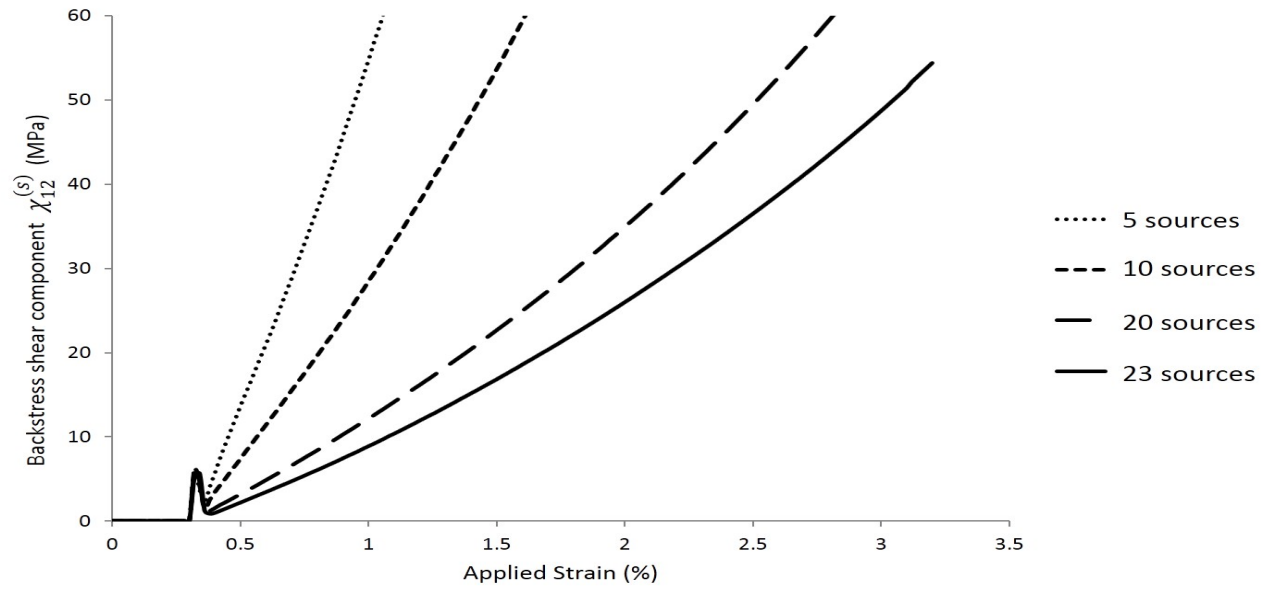
Figure 8.1.7: Backstress $\chi_{12}^{(s)}$ evolution with strain, for open matrix with different source numbers.
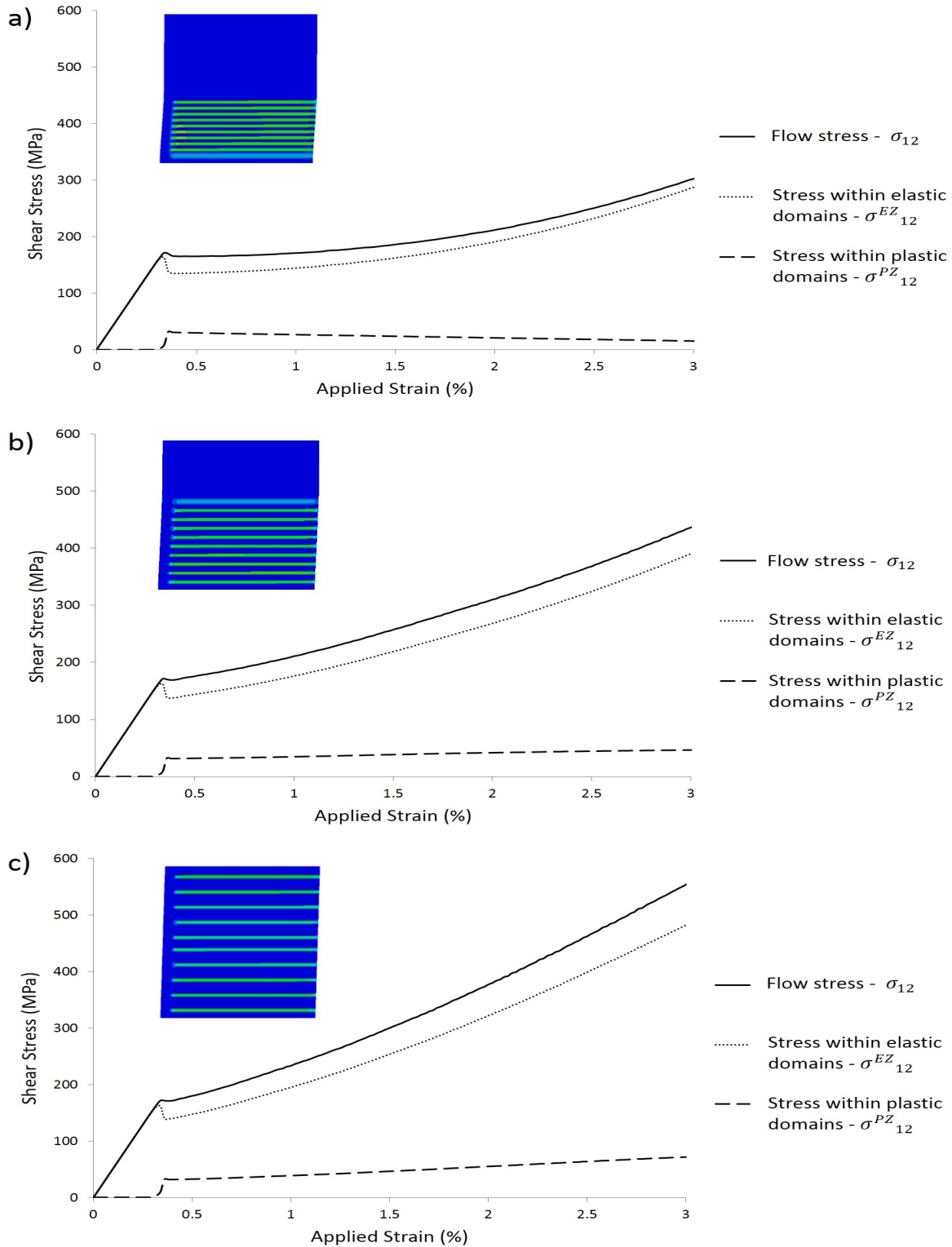
Figure 8.1.8: Flow stress response for a Pure matrix domain with 10 sources, showing the contributions from the elastic and plastic regions: source spacings a) 200nm b) 300nm c) 500nm ($\lambda_{jog} = 25$nm / $100b$).
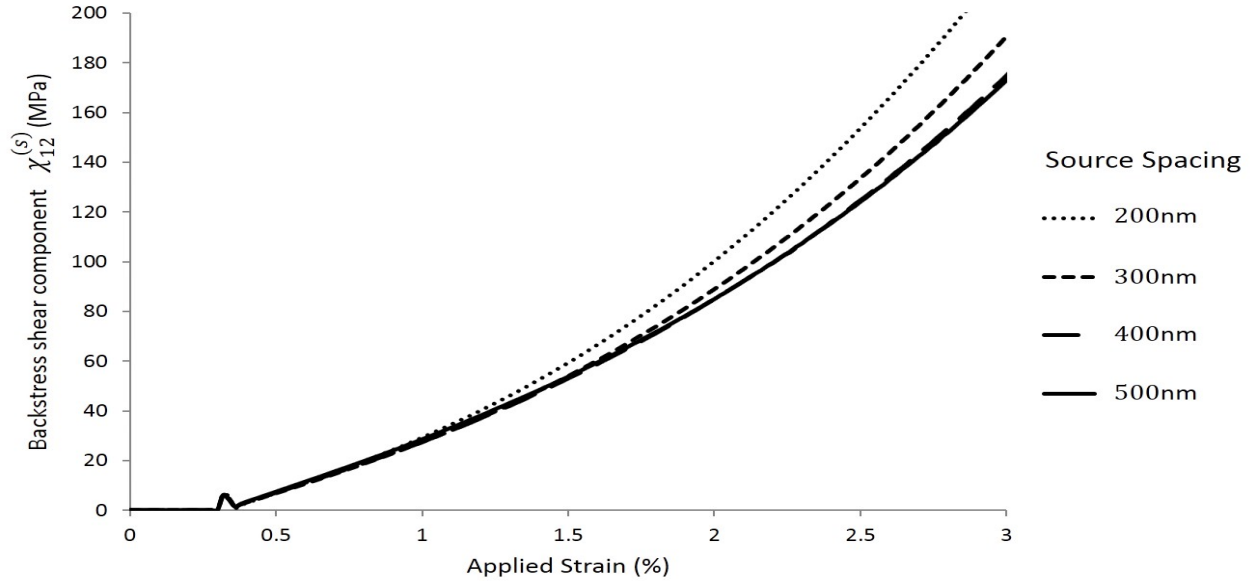
Figure 8.1.9: Backstress $\chi_{12}^{(s)}$ evolution with strain, for open matrix with different source locations.

8.2 Backstresses in γ-γ' Domains

In this section the presence of the second phase will be considered in relation to backstress development between elastic and plastic regions.

8.2.1 Volume fraction

Fig. 8.2.1 shows the stress-strain curves for simulations with 50nm large particles with different volume fractions and fine γ' ($\lambda_s = 35$nm / $r_s = 10$nm). These are the same simulations which produced the red curves in Fig. 7.3.3. The immediate difference from the open-matrix results in the previous sections is that the stress within the plastic zones develops over an extended period, rather than in a sharp rise. For Fig. 8.2.1(a) the stress within the plastic zones rises from zero to a stable value of 200 MPa during the strain interval from 0.80% to 1.38%. The stress develops in discrete jumps which correspond to periods of slip bands formation. In-between are short step-like intervals ($< 0.1\%$ strain) when slip bands stop forming and the stress stops increasing. Once the maximum number of slip bands is achieved the stress in the plastic zones saturates for all further strains.

Moving through sub-figures (a) to (c), decreasing the volume fraction of particles with each plot, the homogenised stress σ_{12}^{PZ} is seen to take a greater strain interval to reach its maximum value. In Section 7.2.1 it was noted that the simulations with lower volume fractions contained longer bands of localised shear in the period before particles were cut, it was also argued that these bands permitted dislocation pile-ups which in turn allowed the gradual cutting of particles and a slower yield. The slower yield can now be associated with a slow development of the plastic zone stress.

Fig. 8.2.2 plots the stress partitioning at plastic saturation as both an average stress contribution (a) and a percentage of the total stress in the domain (b). As the trend in (a) merely follows that of the total yield stress, increasing with volume fraction, and there is no strong trend in the total stress sharing in (b), it is assumed that within this model there is no connection between volume fraction of particles and the ultimate value of effective plastic stress in the domain. The addition of particles does not effect the fractional partitioning in these simulations.

The backstress development in Fig. 8.2.3 shows a wide peak at plastic initialisation which dies to a local minimum then begins to increase again steadily when the maximum plastic bands have been developed and the plastic zone stress is saturated. The interval between the first backstress peak and the period of steady increase decreases with increasing particle fraction, following the speed of development of plastic bands. The magnitude of the backstress during the interval is large ($\chi_{12}^{(s)} = 18 \pm 0.4$ MPa) for the low volume fraction of $\phi_L = 0.15$ but appears to converge towards a lower value ($\chi_{12}^{(s)} = 4.2 \pm 0.2$ MPa) as the fraction increases to $\phi_L = 0.45$. After moderate applied strains ($> 3\%$), when the backstress begins to increase again, the values begin to become similar for each case.
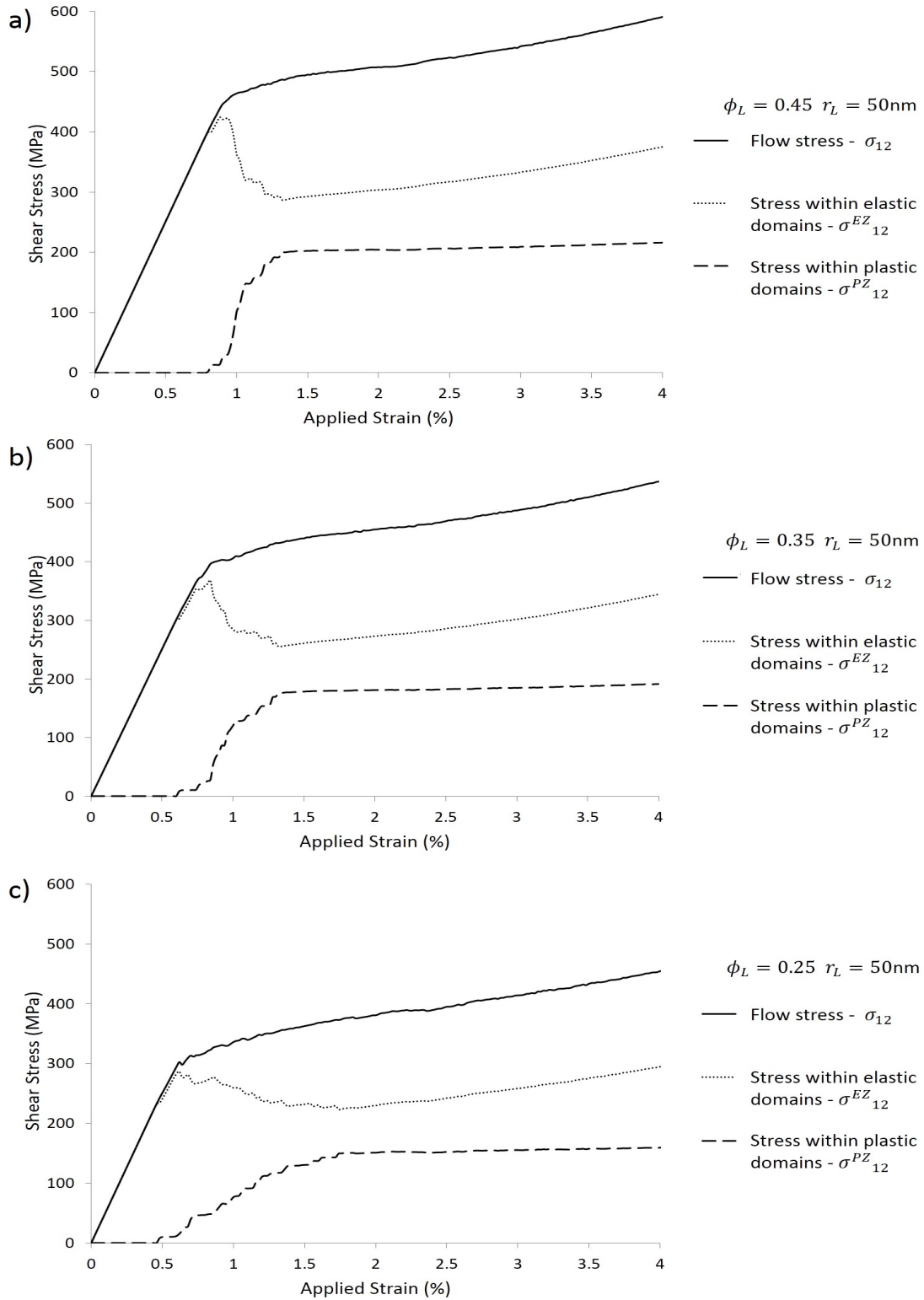
Figure 8.2.1: Flow stress response for bimodal distributions with large particle radius $r_L = 50$nm, showing the contributions from the elastic and plastic regions ($\lambda_{jog} = 76.2$nm / $300b$).
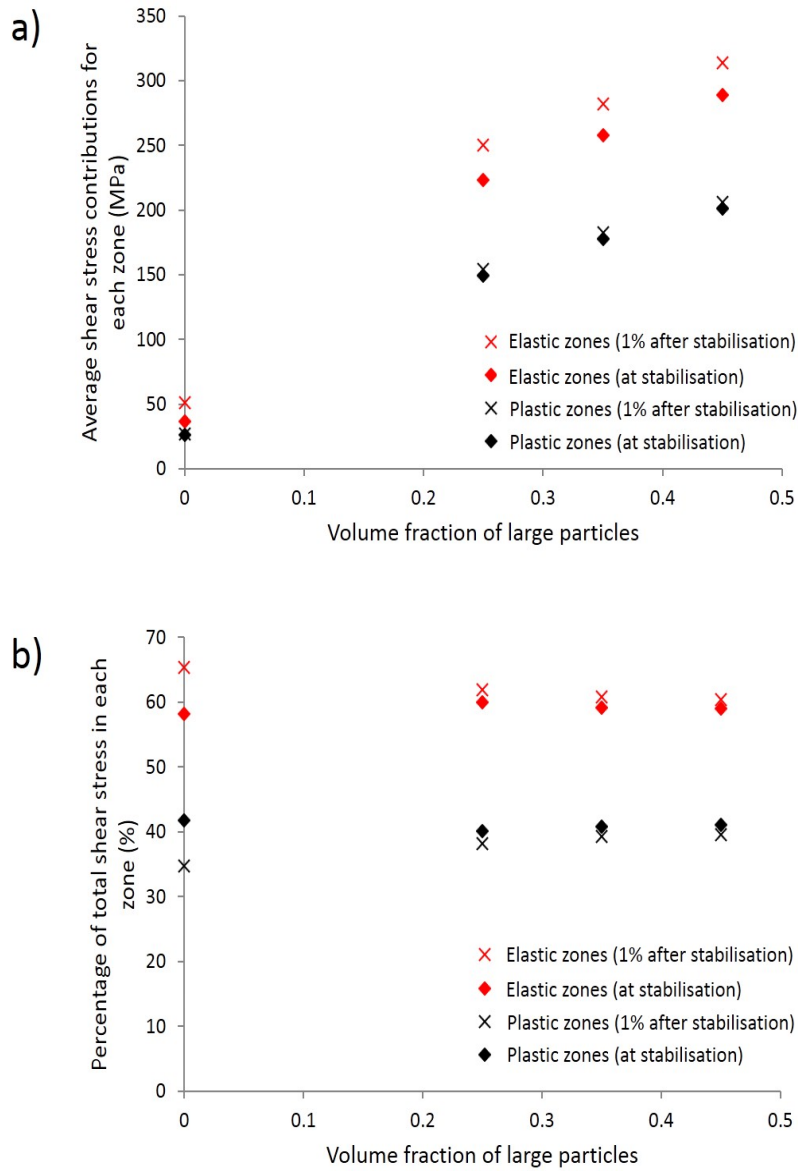
Figure 8.2.2: Stress partitioning measures at plastic saturation, for bimodal distributions with different secondary particle volume fraction ($\lambda_{jog} = 76.2$nm / $300b$).
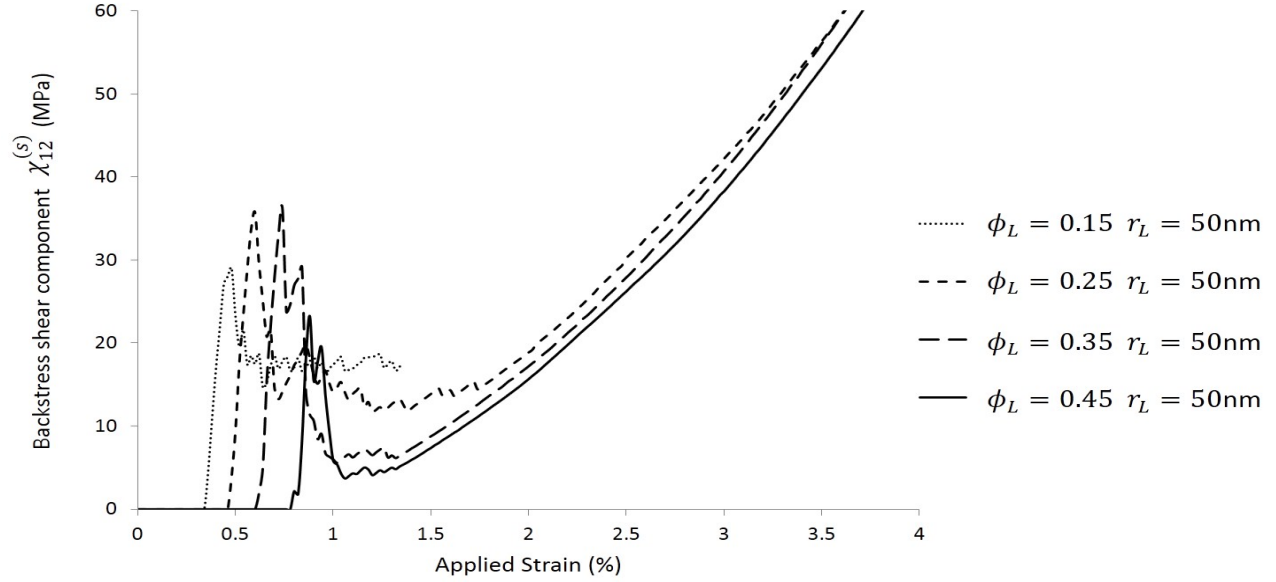
Figure 8.2.3: Backstress $\chi_{12}^{(s)}$ evolution with strain, for bimodal distributions with different large particle volume fraction ($\lambda_{jog} = 76.2$nm / $300b$).

8.2.2 Particle radius

Fig. 8.2.4 shows the stress-strain curves for simulations with varying large particle radii, constant secondary volume fraction ($\phi_L = 0.35$) and fine γ' ($\lambda_s = 35$nm / $r_s = 10$nm). These are the same simulations which produced the red curves in Fig. 7.3.10. The plastic zone stress is shown to evolve more slowly as the particle radius is increased, moving from sub-figure (a) to (c). The longest interval between plastic onset and plastic saturation within this results section is observed for Fig. 8.2.4(c) when the particle radius is at a maximum.

In Fig. 8.2.4(a) during the strain interval $0.7 - 1.4\%$, associated with the burst of plasticity immediately after yield, it can be seen that only the elastic domains are contributing to the oscillations that appear in the total flow stress curve. The elastic zone stress decreases in a jerky manner while the plastic domains have a comparatively smooth increase in stress during this period. As flow stress oscillations are a phenomenon directly concerned with changes in plastic shear, but the plastic zone stress does not oscillate noticeably during this time, it suggests that there is significant stress transfer occurring between the slip band and elastic domain. Further it appears that stable

183

plastic flow is maintained through passing stress back and forth to the elastic zones between slip bands.

Plotting the partitioning at plastic saturation point, using the same two methods as before, Fig. 8.2.5 is produced. The average stress contributions in (a) appear to follow the trend for decreasing yield stress with increasing particle radius, without exhibiting further relationship between the elastic and plastic zones. The percentage share of stress in each domain follows a very minor trend whereby the percentage stress in the plastic zones decreases 1.6% as the particle radius increases $50 \rightarrow 150$nm.

The backstresses plotted in Fig. 8.2.6 for different particle radii show a more consistent interval between the initial peak and the subsequent increase than for changing particle fraction. The height of the peak increases with particle size and the backstress between slip bands and elastic zones is shown to be larger at low strains ($< 2\%$), when the particles are larger. At higher strains the backstresses for each simulation become similar.
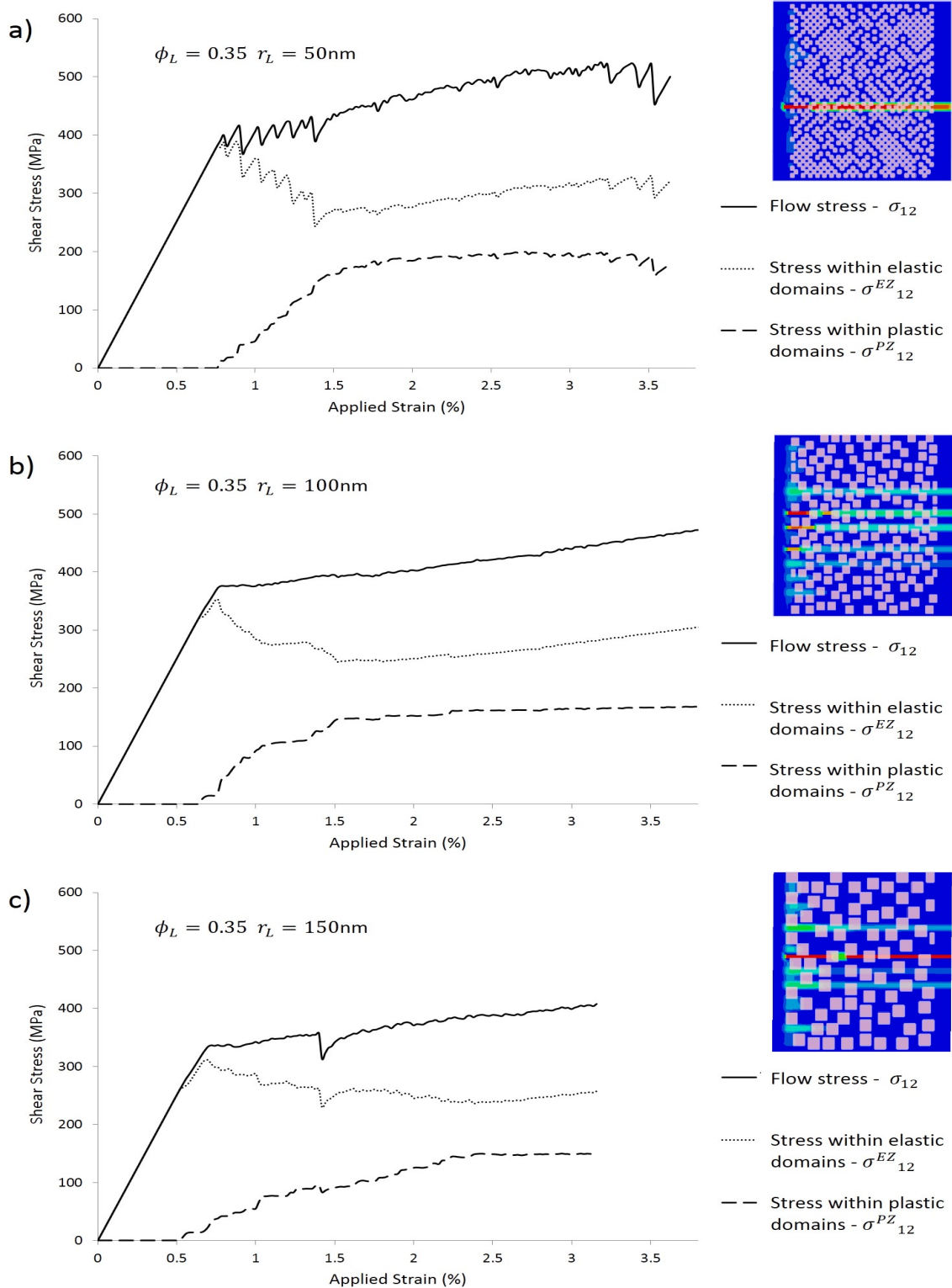
Figure 8.2.4: Flow stress response for bimodal distributions with constant large particle fraction $\phi_L = 0.35$, showing the contributions from the elastic and plastic regions ($\lambda_{jog} = 25$nm / $100b$).
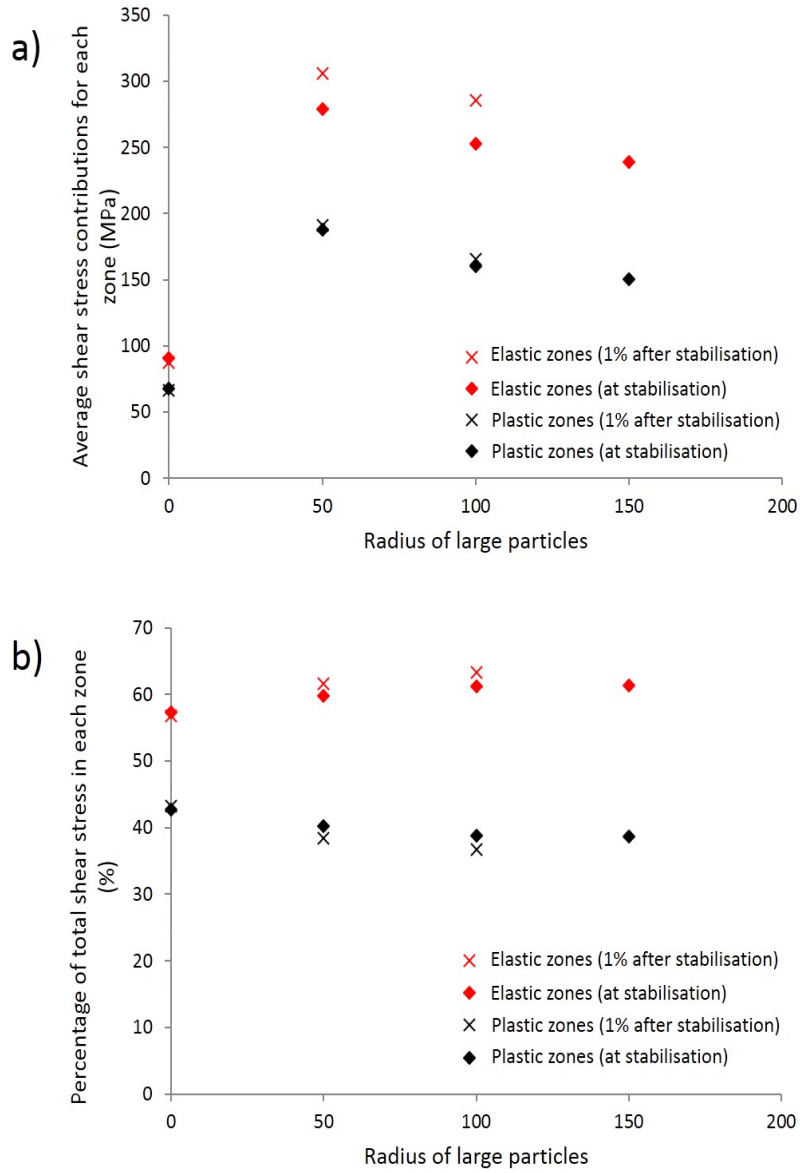
Figure 8.2.5: Stress partitioning measures at at plastic saturation, for distributions with different secondary particle radius (λ_{jog} = 25nm / 100b).
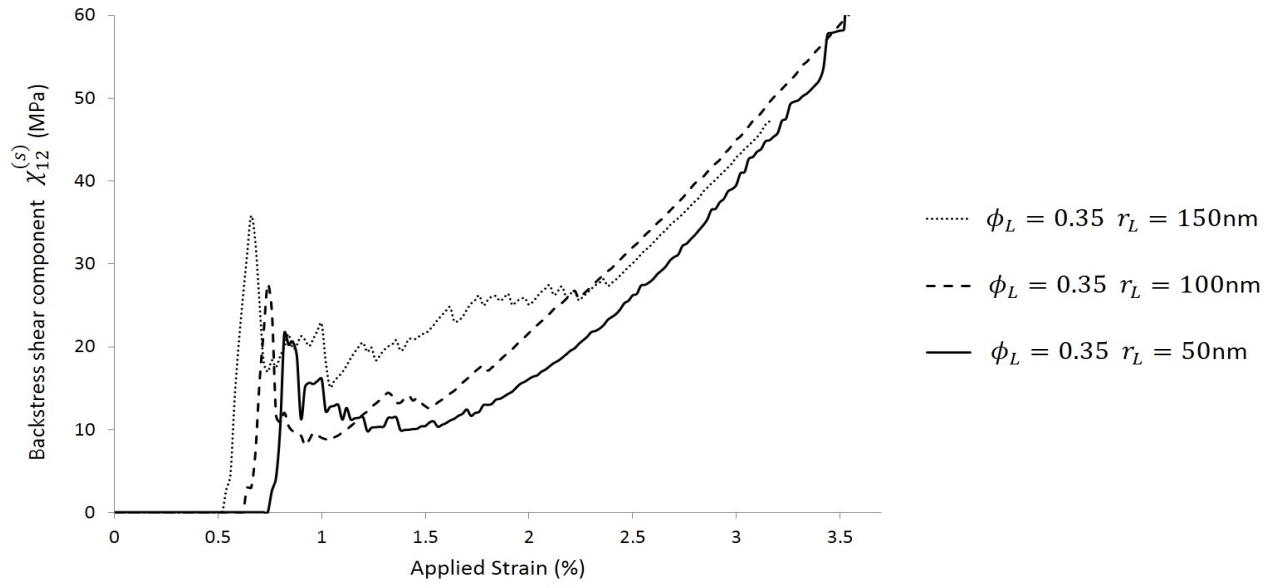
Figure 8.2.6: Backstress $\chi_{12}^{(s)}$ evolution with strain, for for bimodal distributions with different large particle radii ($\lambda_{jog} = 25.4$nm / $100b$).

Chapter 9

Emergent Behaviour II: Microstructure-Property relations

9.1 Yield Dependence on Microstructure

9.1.1 Varying particle distributions at constant temperature

Volume Fraction

Fig. 7.2.1 has shown a stark difference in slip band development can be caused through varying the volume fraction of a unimodal distribution of large γ' particles (radius 50nm). Slip bands were shown to form earlier when the precipitate fraction was lower; a phenomena observed due to the associated reduction to the threshold stress for particle cutting, the reduction to the line tension on a given dislocation segment and the increased space for dislocation pile-ups between sources and particles; all of which lower the yield stress. Fig. 8.2.3 has related slow slip band development to larger backstresses between elastic and plastic zones during the post yield period of these simulations.

The FDM model predicts a linear relationship between yield stress and volume fraction, which would not occur for a model with plastic yield dictated solely by the particle cutting stress. Fig. 9.1.1 displays this yield trend and line equation (black and green lines) with comparison to the calculated cutting stresses, which are best fit by a polynomial (blue line). The yield stress trend

line intercepts the vertical axis at approximately the yield stress of the open-matrix simulations. A simple relationship may be drawn, whereby if the yield stress of the particle-free matrix τ_y^0 is known for a material then the yield stress τ_y with a given particle fraction of small ($r_L = 50\text{nm}$) secondaries is predicted as:

$$\tau_y \;=\; c\,\phi_L \;+\; \tau_y^0 \tag{9.1.1}$$

where c is a material constant.
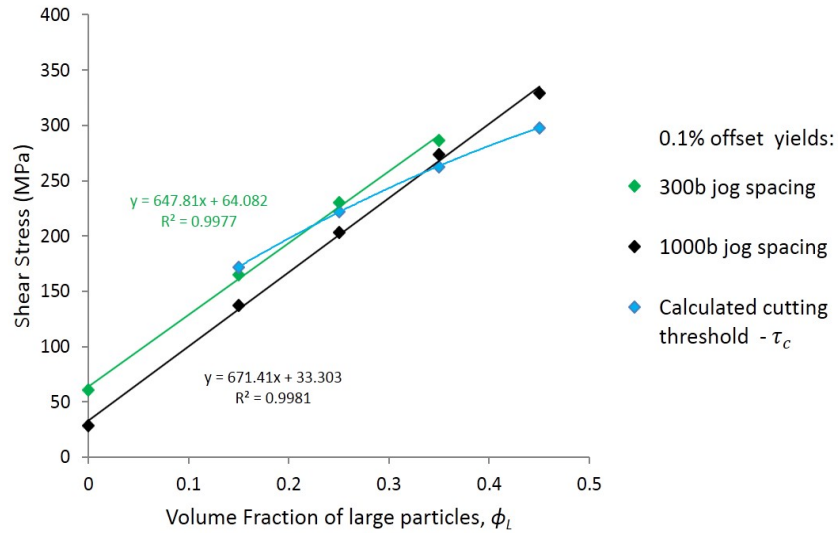
Figure 9.1.1: Comparison of simulation yield stress and calculated particle cutting stress for uni-modal distributions of 50nm particles.

Particle size

It has also been shown, in Fig. 7.2.10, that increasing the size of the large particles at constant volume fraction will lower the yield stress of the RVE. This effect was ascribed to the larger particle distribution having a larger inter-particle spacing and therefore less line tension acting on the dislocation segments in the γ matrix. This means the cutting stress may be achieved sooner. The increased space between the sources and pile-ups (which were depicted at the top of Fig. 7.2.9) is also a factor, allowing more dislocation generation to occur at lower stresses. The particle radii

had a notably larger effect on yield stress when the line tension from the particles was the dominant slip-limiting term within the matrix; this occurred when the jog spacing was widest ($\lambda_{jog} = 1000b$).

Again the FDM model predicted yields do not follow the calculated cutting stress of the particles, which is invariant at constant volume fraction. Fig. 9.1.2 displays this comparison. The trend is non-linear for $\lambda_{jog} = 1000b$, when dislocation mobility is not heavily tied to the transport of jogs, suggesting that above 150nm a further increase in particle size would not greatly diminish the yield stress. At the other end, this behaviour would imply a high upper boundary to the yield stress if the particles were made progressively finer than 50nm. This is most likely not the case, however, as the simulations with narrower jog spacing, with a significantly larger resistance to slip, would always be expected to yield at higher stress than those with $\lambda_{jog} = 1000b$. These data points (red and green) show a more linear relationship to particle radius, so yield stresses would not be expected to grossly exceed those values shown for 50nm with further particle refinement. This figure evidences how the combination of parameters effecting dislocation velocity can bring about different emergent behaviours in this model.
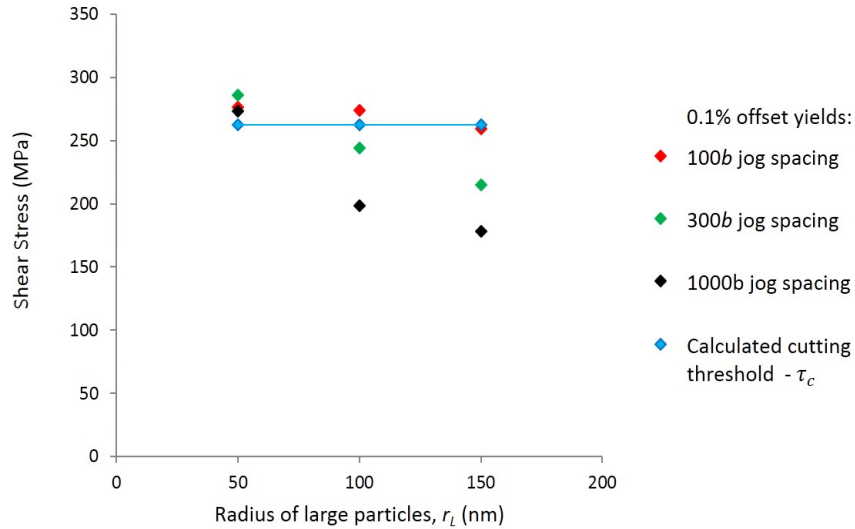

Figure 9.1.2: Comparison of simulation yield stress and calculated particle cutting stress for unimodal distributions with secondary fraction $\phi_L = 0.35$.

Bimodal dispersion of large (>50nm) and fine (<50nm) particles

The addition of a distribution of fine γ' particles ($\lambda_s = 35$nm / $r_s = 10$nm) to existing unimodal distributions of 50nm particles was shown by Figs. 7.3.2 - 7.3.7 to increase the yield strength by varying amounts, depending on the jog spacing and volume fraction of large particles in the domain. Fig. 9.1.3 plots the yield strength increases from fine γ' at 0.1% strain offset. It can be seen that for all jog spacings the yield stress increase rises proportional to the volume fraction of large particles present. The exact relationship changes with jog spacing, appearing linear for wide jog spacing ($1000b$, black). The fine γ' strength increase also increases with narrowing jog spacing, except for one anomaly at $\phi_L = 0.45$, when shear avalanches caused by $100b$ jog spacing cause the 0.1% yield stress to appear artificially lower. When the same fine distribution is added to unimodal distributions with different large particle radii, the strength increase falls away with increasing large particle size. This is shown in Fig. 9.1.4. Again the narrower jog spacing led to a greater strength increase from fine γ'. Both of these relationships show the trend that decreasing the large particle spacing, through either increasing volume fraction or refining the particles, causes a greater increase in fine γ' strengthening.
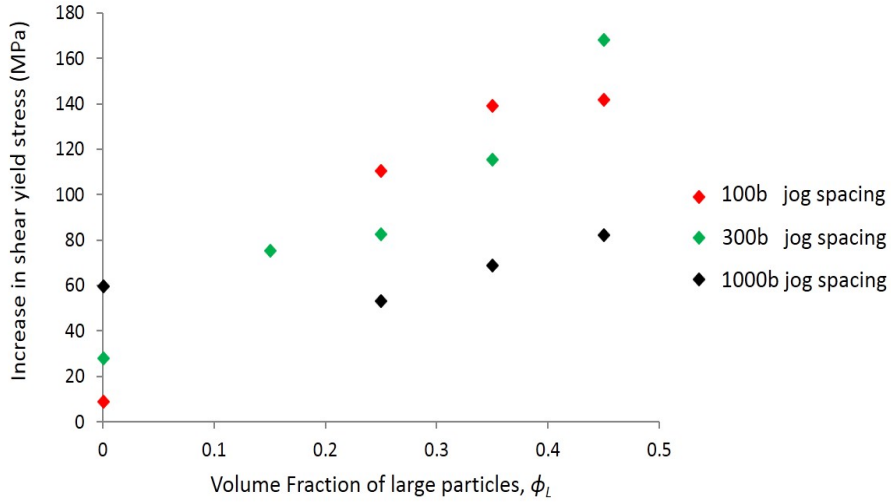
Figure 9.1.3: Predicted increase in 0.1% yield stress when moving from unimodal to bimodal particle distributions, for varying volume fraction of 50nm large particles.
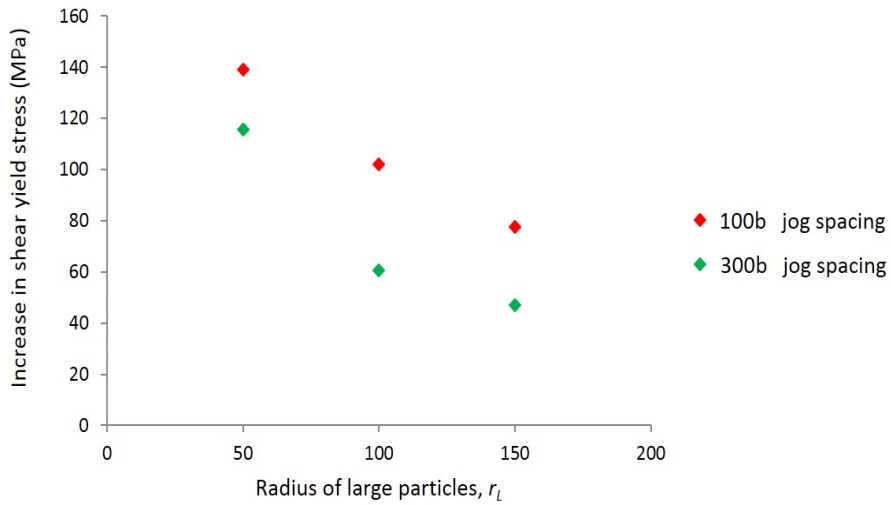
Figure 9.1.4: Predicted increase in 0.1% yield stress when moving from unimodal to bimodal particle distributions, for $\phi_L = 0.35$ large particles with varying radius.

The strengthening effect of the particles arrives through both the energy penalty for the advancing dislocation to create an anti-phase boundary as it shears the γ' and the extra line tension created by particles acting as pinning points before they are sheared. These separate strength contributions may be observed by running the FDM model with and without the line tension term

192

for dislocation motive force in eqn (4.3.16). The flow stress curves for this theoretical situation without line tension are plotted with blue lines in Fig. 9.1.5, next to the usual results in black. In Fig. 9.1.5(a), considering first the unimodal distribution when $\lambda_{jog} = 300b$, the 0.1% yield strength increase from the open matrix case (dotted black line) to the case with large particles and no line tension (solid blue line) is 152 MPa. Switching on the line tension term then further increases the yield strength by another 73 MPa (solid black line). The same process in Fig. 9.1.5(b), for $\lambda_{jog} = 100b$, shows a strength increase of 113 MPa for large particles without line tension, followed by a further increase of only 6 MPa when line tension is introduced. This result suggests that the main strengthening effect from large particles is due to the large associated cutting thresholds and that the lesser effect of the line tension from these particles diminishes when there are already existing slip-limiting factors with the matrix, i.e high jog concentration.
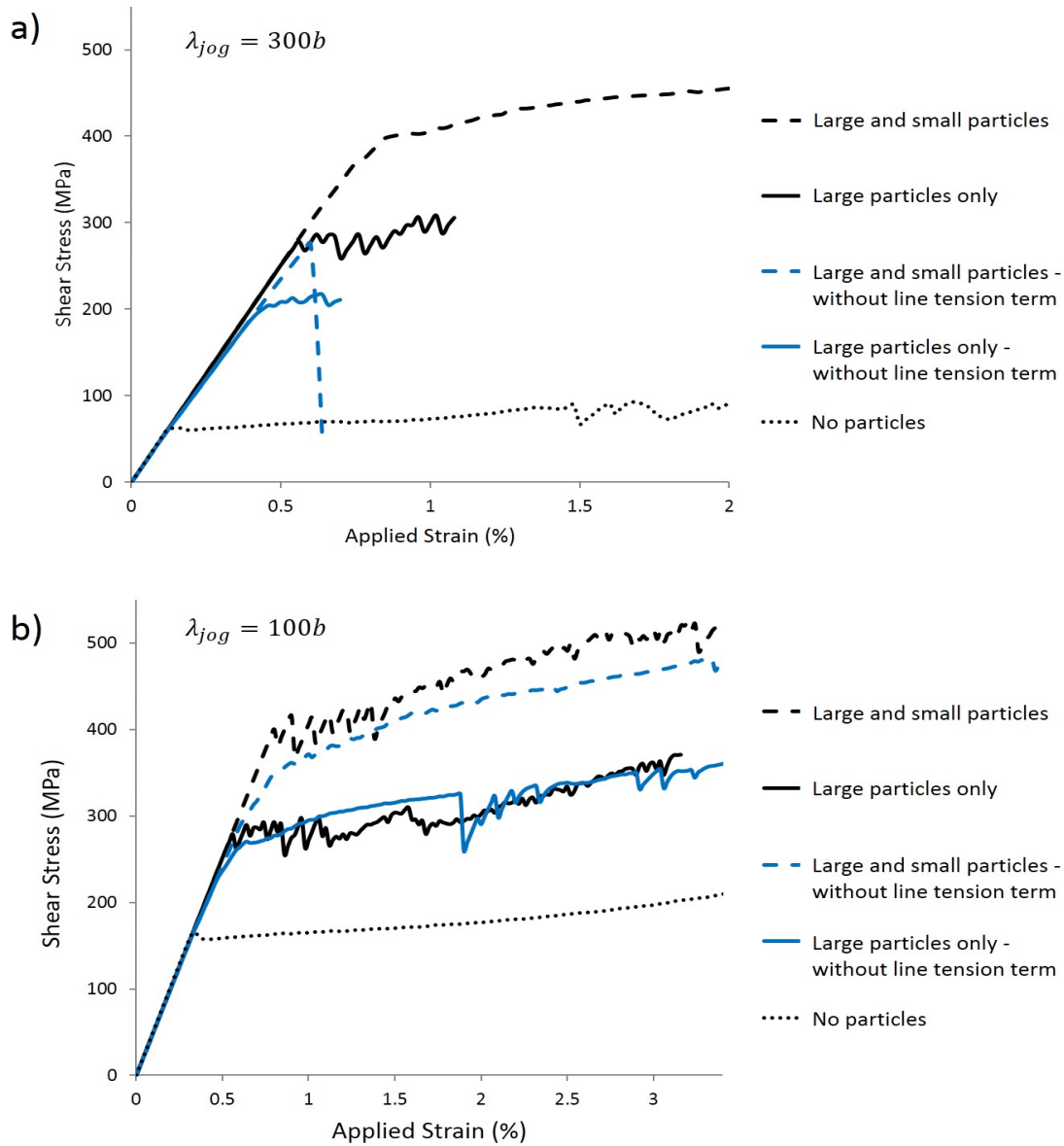
Figure 9.1.5: Flow stress curves for unimodal and bimodal particle distributions, with $\phi_L = 0.35$ / $r_L = 50$ nm, showing the influence of removing the out-of-plane line tension terms due to particles.

For the bimodal distributions in Fig. 9.1.5(a), the simulation without line tension (dashed blue line) unfortunately would not run stably within the FDM model. The cutting stress of 263 MPa for the large particle distribution and 125 MPa for the small particle distribution combine linearly in eqn (4.4.11) to form a shearing threshold of $\tau_c = 415$ MPa. At such high shear stress, without drag to temper the speed of the dislocations, the rapid acceleration when the waiting dislocation

194

density cuts the particles causes an improbably high shear rate which cannot be handled by this model setup. When the jog concentration is higher for Fig. 9.1.5(b), however, the acceleration is not so great and the bimodal simulation without line tension runs smoothly. Here the 0.1% yield strength increase from the open matrix case (dotted black line) to the bimodal distribution without line tension (dashed blue line) is 191 MPa. The further increase when the line tension is reactivated is 67 MPa. Where previously the line tension in a system with only large particles had little effect on the yield stress, here the effect is ×10 larger in the presence of fine γ' particles. This result suggests that an appreciable amount of the strengthening from fine γ' particles can arise through line tension on dislocation segments from the narrow particle spacing.

Bimodal dispersion of large particles (> 50nm)

Another emergent property demonstrated by the the FDM model is that the yield stress is highest for particle distributions containing mainly 50nm particles with a small amount of 100nm particles. This was shown in Fig. 7.3.15 where the 0.2% yield stress was highest for Dist. **3** (75% 50nm, 25% 100nm). The logic is presented that the separate strengthening effects of the inter-particle line tension and the particle cutting threshold reach a combined maximum for this type of distribution; utilising the low mean particle spacing $\hat{\lambda}_L$ to increase tension and the occasional larger particle with higher cutting threshold τ_c to form a hard barrier to slip. This behaviour could not be observed without the particles being discretely modelled and assigned with individual radii.

A full parametric study of the type in Fig. 7.3.15 could establish the exact ratio of $r_L = 50$nm/100nm particles that provides the highest yield stress for this system. It may therefore be possible in the future to use this type of model as a tool to inform alloy design processes towards increasing strength of superalloy systems. Within this limited study the trends show the ideal ratio lies somewhere between Dist. **2** (100% 50nm) and Dist. **4** (50% 50nm, 50% 100nm).

9.1.2 Varying particle distributions with increasing temperature

Within this model increasing the domain temperature was shown to produce a small and linear decrease in yield stress for systems with constant microstructure. By far the larger temperature effects were observed when the particle distribution was evolved with temperature, as shown in Fig. 7.3.20. This would suggest that for a γ/γ' system undergoing a temperature increase $500 \rightarrow 1000°C$ the associated decrease in the stiffness constants produced by eqns (5.5.2) and (5.5.3) do not significantly effect the flow stress of the lattice. Nor does the lattice drag coefficient in eqn (4.2.4) or jog-controlled velocity in eqn (4.2.5) effect dislocation motion enough to register more than a 25 MPa drop in stress. The yield stress reduction comes almost entirely from the change to the precipitate microstructure, increasing the particle spacing which lowers the cutting threshold and allows dislocations to shear through at lower stresses.

The curves for yield stress vs temperature in Fig. 7.3.20 (black and red lines) were best fit by high-order polynomials, however the shape is similar to the corresponding volume fraction profiles from Fig. 7.3.17. The FDM model predicts that the dependence of yield on volume fraction of γ' is strong enough that the volume fraction profile predicted by Dyson's formula in eqn (7.3.1) [84] may be overlayed upon a single yield point for a known temperature (with a complimentary x-axis scale) to produce a rough tool for yield prediction at other temperatures. This is demonstrated in Fig. 9.1.6, with the curve overlayed to cross the data point for $500°C$.
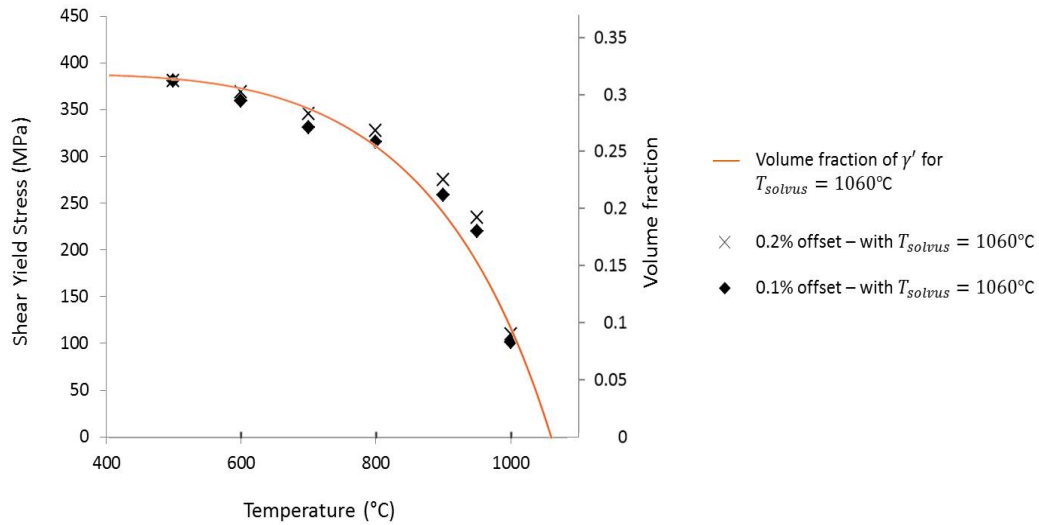
Figure 9.1.6: Axis 1: Shear yield stress vs temperature for a nickel-based superalloy with temperature-appropriate volume fractions for $T_{solvus} = 1060°$C ($\lambda_{jog} = 76$nm / $300b$). Axis 2: Volume fraction predictions for $T_{solvus} = 1060°$C.

It should be noted that, while dislocation climb velocity was included in this model, the model was loaded in shear and at high strain rate. This created a small force component f_2^∞ for driving the climb mechanism and provided little time for the vacancy diffusion required, which meant that dislocation climb played only a small role in the deformation in this work. If the simulations had not been restricted to a high strain rate due to computation time it is predictable that climb would have played an increased role in overcoming obstacles and so could have increased the effect of temperature at constant microstructure.

197

9.2 Post-yield Flows Stress Dependence on Microstructure

In some instances microstuctural parameters have been shown to have negligible effect on the initiation of plastic yield, but considerable effects on post-yield flow stress behaviour. Examples include penetrable/impenetrable grain boundary conditions, source distribution and domain size.

9.2.1 Opening/closing domain boundaries to dislocation flux

The difference between simulations with boundaries either fully open or impenetrable to dislocation flux is stark. It was shown in Fig. 6.1.1 that the use of closed boundaries introduces a hardening-type behaviour post-yield, which is attributed to the reduced generation rate revealed in Fig. 6.1.2. Later, in the discussion of domain size, the reduced source generation was shown to result from repulsive dislocation stress fields from boundary pile-ups, presented in Fig. 6.6.3. Similar modelling work by Hamid *et al* [105] in 2017 has previously concluded that the boundary conditions at grain boundaries have significant effect on the macroscale flow stress, but that the internal stress field from the dislocation pile-ups is negligible due to the rate at which this falls away across the grain. This work argues that the dislocation stress fields are not negligible, and that the two phenomena are linked through source activity.

All dislocation density generated was retained within the domain for these conditions, meaning the dislocation content at a given strain is equivalent to the number of generations that have occurred to that point during the simulation. Using this principle and averaging across the whole domain using eqn (5.4.2), the FDM model predicted a dislocation density of 1.14×10^{13} m^{-2} within the 5μm crystal after 1% applied strain, rising to 3.98×10^{13} m^{-2} after 3%.

With open boundaries (and no obstacles to hinder dislocation slip) no pile-ups are observed within the simulation domain and thus the only source of internal stress field is from the much lower density of mobile dislocations. This density is transient, existing for the short period between generation at one boundary and the moment it leaves the domain at the other boundary, and consequently it holds a smaller, steady value of $\sim 5 \times 10^{12}$ m^{-2} when the generation rate becomes steady post-yield. This impedes the sources to a lesser extent and allows more generation and greater shear rate within the open boundary domain.

The above values of dislocation density fall within typical norms for DDD simulations after similar deformation [103].

9.2.2 Source distribution

The number of sources was shown in Fig. 6.2.3 to have a profound effect on the flow stress of open boundary simulations, with curves showing hardening-type behaviour when the source number was lowered below ~20 for a 5 μm domain. The hardening in this case does not spawn from repulsive dislocation stress fields, but from the dislocation sources being unable to produce the required dislocation density for plastic deformation to entirely accommodate the increasing strain.

As the strain rate is the same in each simulation, then the total strain increase in the domain for a given time increment will also be the same. The dislocation sources, however, may only generate during this increment as often as their nucleation time t_{nuc} will allow (see eqn (4.5.3)). If the same plastic strain were to be maintained when the number of dislocation sources within a domain is reduced, then the average t_{nuc} of the remaining sources would be required to reduce also. As t_{nuc} is inversely proportional to glide velocity v_g, which has defined limits, then the required reduction in nucleation time may not necessarily be achieved. The surplus strain that is not accommodated plastically becomes elastic strain, which increases the stress state of the domain.

Fig. 9.2.1 demonstrates the non-linear relationship between the number of sources N_S within a domain and the average number of generations $\langle N_G \rangle_S$ each source performs. As expected, with less sources the number of generations per source increases. The relationship follows a power law:

$$\langle N_G \rangle_S = c \, N_S^{-m} \tag{9.2.1}$$

where c is a constant which increases approximately linearly for small strains ($\varepsilon < 4\%$), and m is an exponent that decreases approximately linearly for small strains ($\varepsilon < 4\%$).
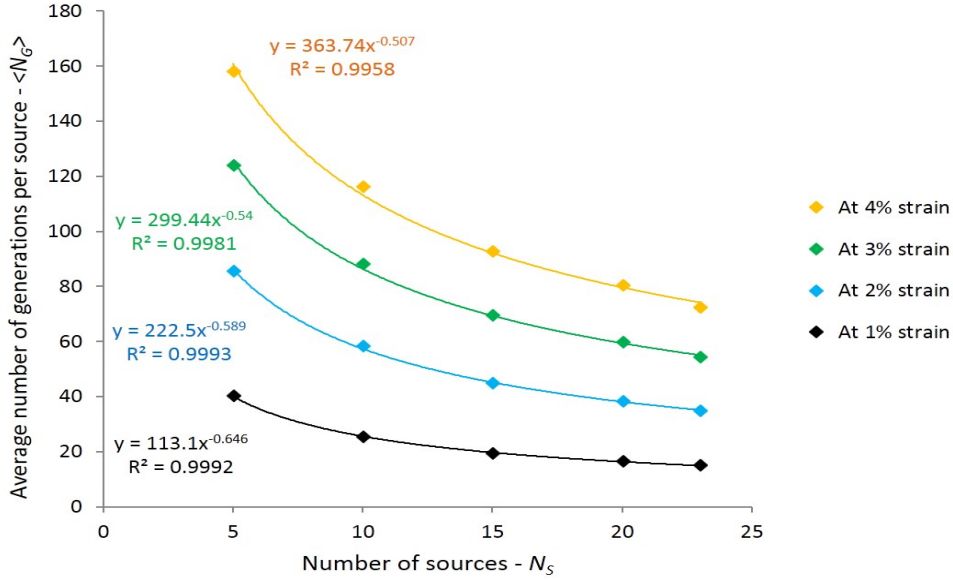
Figure 9.2.1: Average number of dislocation generation events per source vs the total number of sources within the domain, at varying strain levels within the simulation ($\lambda_{jog} = 25$nm / $100b$).

Relationships between the post-yield hardening and the number of sources in the domain may also be drawn. Considering the approximately linear sections of the flow stress curves between 2 and 4% in Fig. 6.2.3, the hardening modulus E_H for this period may be calculated. Plotting this modulus against the number of sources in the simulation, in Fig. 9.2.2, gives a log relationship. Plotting this modulus against the total number of generations N_G at 3% applied strain (during this hardening period) gives linear trend which intercepts the y-axis at approximately the shear modulus (i.e the modulus when no dislocations are present). The FDM model therefore provides trends that may associate source activity to hardening.

$$E_H \quad \propto \quad -ln(N_s)$$

$$E_H \quad = \quad a \, N_G \, + \, \mu \tag{9.2.2}$$

$$N_G \quad = \quad \langle N_G \rangle_S \, N_S \tag{9.2.3}$$

where a is a material constant and μ is the shear modulus.
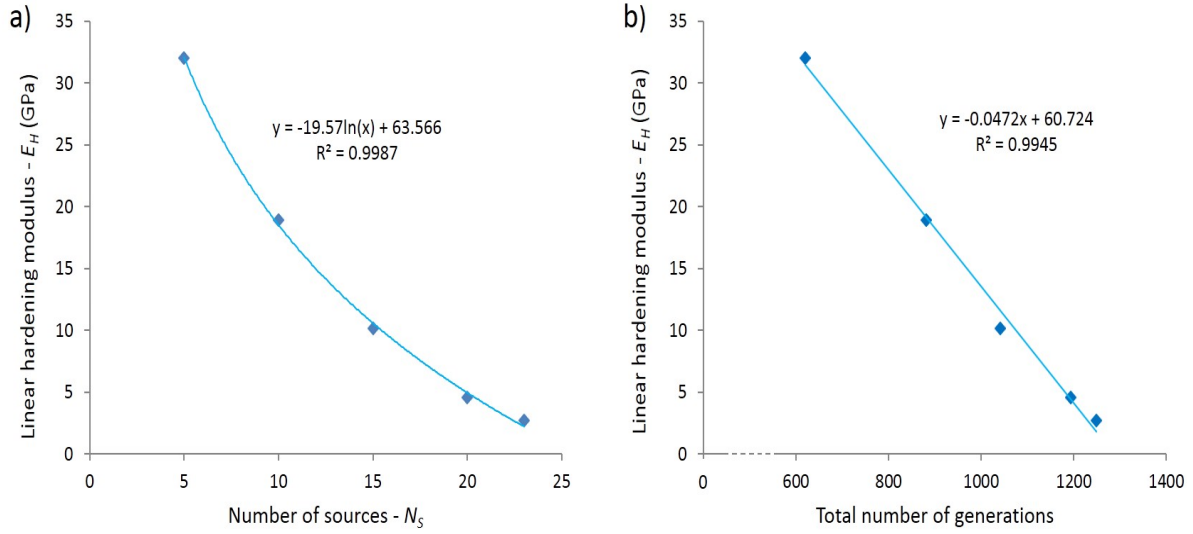
Figure 9.2.2: Modulus of the linear hardening of the flow stress for simulations with different source numbers plotted against: a) the number of sources in the simulation b) the total number of generation events. $(\lambda_{jog} = 25\text{nm} / 100b)$.

The spacing of sources has also been shown to effect generation rates when the total number of sources is constant. This was observed in Fig. 6.2.7. Here it was found that sources close to one another generated at higher rates than those spread apart. This interaction between sources was shown to occur over short range < 400nm, as increasing the spacing beyond this value caused very small decrease in generation events for the domain. The effect is assumed to relate to dislocation stress fields as the strength of these fields increases significantly over this range. The repulsive shear stress from a single dislocation, calculated with eqn (4.3.3), falls away 16.4 MPa $\rightarrow$ 10.9 MPa $\rightarrow$ 8.2 MPa $\rightarrow$ 6.6 MPa respectively as the distance from the dislocation increases 200nm$\rightarrow$300nm$\rightarrow$400nm$\rightarrow$500nm.

As all sources were aligned at exactly the same x-coordinate then the shear stress field of a newly generated dislocation on a given slip plane at (x_0, y_0) could not possibly have increased the stress state at the source above or below it at (x_0, y_1). This is a consequence of the shape of the shear stress field of an edge dislocation, given in eqn (4.3.3), which has no value directly above or below the singularity. It is however possible for the shear stress field from a newly generated dislocation

201

to effect a second dislocation that has previously been generated and has moved slightly away from its boundary source. The second dislocation would feel a repulsive stress and begin to increase velocity, moving away from it's source more quickly than if there had been no interaction. This would effectively increase the speed at which the space adjacent to a source is evacuated, allowing another generation to occur more quickly and meaning that t_{nuc} is reduced. This mechanism is illustrated in Fig. 9.2.3 where the stress field of new dislocation generated at $(1,3)$ provides a velocity increase to the dislocation at $(3,1)$ and $(4,5)$. The dislocation at $(4,5)$ also receives further velocity increase from the repulsion from the dislocation at $(2,7)$. In this manner the dislocations will move faster away from close-packed boundary sources, and these sources will be less impeded from further activity.
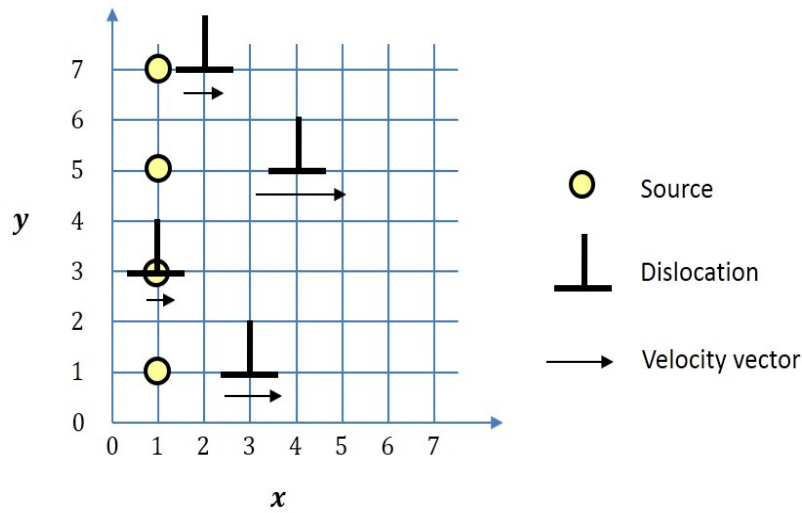
Figure 9.2.3: Illustration of how dislocations generated at neighbouring sources within the FDM model will increase the velocity of a given dislocation leaving a source.

9.2.3 Calculating Hall-Petch relationship constants

The Hall-Petch relationship proposes a link between yield stress σ_y and grain size d_g of the form [156][51]

$$\sigma_y = \sigma_{y,0} + \frac{k}{\sqrt{d_g}} \tag{9.2.4}$$

where $\sigma_{y,0}$ is taken to be a friction stress for dislocations pile-up in the pre-yielded grain and k is a constant for microstructural stress intensity.

In Section 6.6 grain-size dependency was discussed for pure-matrix domains with closed boundary conditions: here it was found that, while the stress at which the plastic deformation begins was the same in each case, rapid post-yield hardening led to different 0.1% offset yield stresses. These yield stresses followed the $\frac{1}{d_g}$ relationship and provided the following Hall-Petch constants (in shear form):

For $300b$ jog spacing

$$\tau_y(0.1\%) = 55.45 + \frac{37.52}{\sqrt{d_g}} \tag{9.2.5}$$

$$\tau_y(0.2\%) = 52.54 + \frac{95.52}{\sqrt{d_g}} \tag{9.2.6}$$

For $100b$ jog spacing

$$\tau_y(0.1\%) = 167.91 + \frac{17.47}{\sqrt{d_g}} \tag{9.2.7}$$

$$\tau_y(0.2\%) = 167.79 + \frac{68.71}{\sqrt{d_g}} \tag{9.2.8}$$

This result shows that the friction shear stress increases when the jog spacing is decreased and dislocations can move less easily. The microstructural stress intensity decreases for similar reduction in jog spacing.

9.3   Limitations of Current Model

Despite the potential of the macro-property predictive capabilities of this model there are also outstanding limitations that must be addressed:

One of the main limitations arrives through the numerical implementation, in that simulations are required to take place at high strain rates due to processing time restrictions. This lowers the amount of climb that can occur over the course of a given strain increment. Climb would be expected to assist dislocations in overcoming slip barriers, and so at lower strain rates (and high temperatures) a particle-matrix simulation would be expected to yield much earlier than at high strain rates. This behaviour has unfortunately not been captured within this work.

The effect that geometrically necessary dislocations (GND) will have on the evolution of the mobile density field has not been addressed in this work. GNDs are the dislocations required to accommodate the bending of the lattice planes to make deformation compatible, and this bending would be expected to effect the mobility of the dislocations which slip along these planes. Furthermore the local stress fields from GNDs should have an effect upon the mobile SSD population and influence the general density field evolution. As well as simplifying computer processing time, a single slip (and single crystal) arrangement was adopted within this model in order to reduce the potential effects of the missing GNDs; as the generated deformation gradients are not severe along the slip planes and the lattice rotations are minimal. In a real world polycrystal the effect should be much greater, as the dislocations piling at grain boundaries arrange into GNDs that accommodate the deformation. In the current state this model is therefore not appropriate for the modelling of polycrystal systems, and this will form a basis for future work.

A further limitation is that with only a single slip system there can be no sessile dislocations formed through interactions with dislocations from other slip planes. Sessile dislocations could be expected to act as a source of work hardening within simulations, as dislocation pile-up against the slip-barrier [157]. Multiple slip planes would also allow discrete, local jog formation to be modelled. An increase to the density of jogs within the RVE would be expected to create further hardening effect. For the same reason cross-slip cannot be captured in this model, and so Kear-Wilsdorf

locking and the subsequent anomalous yield behaviour in L1$_2$ ordered alloys cannot be observed with the current plane strain setup [158].

Gamma-prime misfit, and the related effects on dislocation motion and primary creep properties have also not been considered in the current model [159].

Finally a number of material parameters in this model have been taken from literature data for a specific nickel-based alloy (e.g. matrix stiffnesses C_{11}, C_{12} and C_{44} from CMSX-6 [138]) and adopted as representative of the wider alloy class in general. In order to allow better comparison against experimental results then such input parameters should be sourced from as similar an alloy as possible to the tested material.

Chapter 10

Conclusions and Future Work

10.1 Conclusion

The aim of this study was to produce a Field Dislocation Mechanics (FDM) formulation capable of interrogating the effects of microstructure on the evolution of a dislocation field within two-phase nickel-based superalloys, and the consequent deformation behaviour that emerges from the underlying physics. To this end a FDM theory has been presented for the transport of a continuous field of dislocations (eqn (5.1.1)). An implicit finite difference approach was then developed for solving this dislocation transport equation numerically in a plane strain setup, and coupled to a commercial finite element scheme, where the dislocation density tensor reacts to the applied stress field and microstructure. A square computational domain representative of a single crystal of a nickel-based superalloy was shear loaded at constant strain rate and high temperature ($100\mathrm{s}^{-1}$ and 973K) for various microstructural parameters, with slip bands being individually resolved. Inter-dislocation interactions were enabled through long range dislocation stress fields, which evolved heterogeneously across the simulation domain. Interaction with second-phase γ' particles was modelled both as an averaged drag effect from line tension and through cutting conditions on discrete obstacles.

Slip bands were found to evolve non-uniformly within two-phase simulations as a result of short range stress interactions between bands. This caused new bands to form near pre-existing bands, and reproduced the experimental observations of the strain maps in Section 2.1.3 as a behaviour emergent from the underlying physics. Sub-grain phenomena such as shear avalanches, from the

rapid generation or release of trapped dislocations, was shown to translate to stress drops within the average flow stress of the grain.

When applying shear loading to single crystal domains representative of generalised nickel-based superalloys, the FDM model has predicted a range of emergent properties at the grain-scale. The results have been mainly presented through the flow stress curves and plastic slip-traces from these domains. Conclusions from single-phase γ-matrix simulations, loaded at $100s^{-1}$ and 973K, include:

- Setting grain boundaries to be impenetrable to dislocation flux will result in increased hardening rate compared to open boundary solutions. This hardening can be directly associated with a reduction in dislocation generation, due to internal stress fields from dislocation pile-ups, and to a reduction in dislocation velocity (see Fig. 6.1.2 and Section 9.2.1).

- Impenetrable boundaries promote the emergence of a Hall-Petch dependency of shear yield stress on simulation domain size (see Fig. 6.6.1). Again this is related to repulsive stress field from dislocation boundary pile-ups reducing the generation activity of sources on the other side of the grain, thus in smaller domains the sources generate less frequently (see Fig. 6.6.2).

- The imposed jog concentration is seen to dominate the yield stress when the jog spacing is sufficiently narrow. In single-phase simulations the yield stress became jog-controlled for spacings below 127nm (see Fig. 6.3.2). In these cases fewer shear avalanche were observed.

- As the total number of dislocation sources within a domain was reduced the hardening rate in the domain proportionally increased following a log relationship (see Fig. 9.2.2).

- The generation activity of a given boundary source increases as the number of other sources in the domain is reduced (see Fig. 9.2.1). This increased activity does not necessarily offset loss in plasticity through source reduction, due to limitations in source nucleation time, thus the hardening is still observed.

- The spacing of dislocation sources can have a significant effect on generation activity, for a constant total source number. The closer packed sources were observed to generate more frequently and thus cause softer flow stress behaviour in the domain (see Figs. 6.2.6 and 6.2.7): with a 200nm source spacing producing considerably lower flow stress than 300nm or

400nm. This effect was related to the interacting dislocation stress field between slip bands, which decay rapidly over this same 200-300nm distance (see Section 9.2.2).

Conclusions following the extension to two-phase γ/γ' single crystal shear simulations, with controllable discrete precipitate particle microstructures, were as follows:

- Increasing the secondary γ' volume fraction, for a constant unimodal particle radius, causes the yield stress to increase linearly with volume fraction (see Fig. 9.1.1)

- Increasing secondary γ' particle radius (unimodal), for constant volume fraction, cause particles to be cut at a lower shear stress and reduces yield stress non-linearly. This relationship would not predicted directly by the precipitate shearing stress threshold alone (see Fig. 9.1.2).

- Precipitate distributions with a mix of discrete secondary particle sizes were capable of causing higher flow stress than a uniform particle field of either size, at constant volume fraction (see Fig. 7.3.14). This behaviour spawned from the combined effect of the mean particle spacing on both the dislocation line tension and the particle cutting stress threshold.

- Bimodal γ' distributions containing precipitates of typical tertiary and secondary size ranges were predicted to produce a higher yield stress than corresponding unimodal secondary distributions (see Fig. 7.3.6). This occurs through the increased drag effect from closer spaced particles and the additional stress required to cut the distribution. The latter was found to provide the main strength increase (see Section 9.1.1).

- A higher number of shear avalanches (more jerky flow stress curves) were observed in the two-phase simulations from domains with imposed jog spacings of 76nm or less (see Figs. 7.3.2, 7.3.5 and 7.3.7).

- Temperature effected the yield stress of two-phase structures primarily through the associated change in microstructure rather than the change to the lattice parameters (see Section 7.3.4). Yield stress is predicted to drop with increasing temperature at the same rate as the volume fraction of γ' drops (see Fig. 9.1.6).

- Stress is found to saturate within the slip bands shortly after yield in all simulations. The interval until saturation may be increased by introducing a distribution with large γ' particles or low volume fraction (see Fig. 8.2.1 and 8.2.4)).

- The backstress between the slip bands and the elastic regions of the domain may be calculated using local volume averages (see eqn (8.0.2); the largest backstresses were produced in domains with large γ' particles, low volume fractions or very few dislocation sources (see Chapter 8).

Finally, the model has been benchmarked against single crystal micro-shear tests (of a CMSX-4 type alloy) found in published literature [41]. Simulations of similar shear domains at room temperature and strain rate 0.05s^{-1} produced flow stress curves that compared well with these experimental results for both dendritic and interdendritic material types (see Fig. 7.4.2). The model predicted the onset of sudden deformation events (SDEs), due to rapid plastic shear avalanches, at average shear stresses of 638 MPa and 703 MPa for the two materials respectively. By comparison the experimentally observed values were 630 ± 20 MPa and 700 ± 40 MPa, showing very good alignment between prediction and reality. The model also yielded a prediction that the SDEs would be significantly more pronounced for the interdendritic material, which was again reflected in the experimental observations and offers good validation to this work.

Based on the portfolio of simulation results presented within this work, which have demonstrated a range of deformation features emergent from the underlying physics of dislocation-dislocation and dislocation-microstructure interaction, it is submitted that the objectives stated in Chapter 1 of this work have been met.

10.2   Future work

Further work is required to extend the numerical implementation to 3D. The general FDM formulation for SSD evolution would not need to be altered for this extension, but additional contributions from GNDs need to be included to accommodate large deformations, especially within polycrystals or when further slip systems are activated. The extension to 3D implementation will mean that multiple slip systems can be resolved, allowing mechanisms such as cross-slip and jog formation to be modelled through reaction terms on the transport equation.

In particular this would allow modelling of Kear-Wilsdorf locking within the γ' particles, as cross slip occurs between {111} and {010} planes, which would mean the anomalous yield behaviour typcial to disc nickel-based superalloys could be captured as a further emergent behaviour [158].

Gamma-prime misfit must also be introduced to this model in the future as this has been shown to have effect on dislocation motion and primary creep properties [159].

Finally, any future implementation would benefit greatly from improved processing parallelisation, possibly through extension of the FDM FORTRAN code to us MPI parallel programming methods. This would decrease processing wall-time and allow lower strain rate simulations to be carried out in a reasonable time frame.

10.2.1 Considerations for extension to multiple slip systems

G. Laplanche et al [41], referenced in Section 7.4, have also conducted MDS tests of crystals in the $[\bar{2}11](111)$ and $[010](100)$ orientations. The former orientation activated two FCC slip systems (double slip) with a Schmid factor of 0.87 while the latter activates up to eight systems (multiple slip) with a Schmid factor 0.41. Simulations of these orientations are not possible within the 2D plane strain setup of this work, as dislocation line tangents would not be orthogonal to the simulation plane, however the results of the experiments can be briefly discussed as a prelude to the future work for this model.

The double slip MDS experiments produced flow stress curves with similar linear elastic deviation stresses τ_{el} to the single-slip curves. In the dendrite material τ_{el} was 490 ± 10 MPa while in the interdendritic samples was 480 ± 10 MPa. The second value is 10 MPa lower than was previously recorded for the interdendritic material. A larger difference is seen in the post-yield deformation behaviour, where the double slip experiments show sudden deformation events (SDEs) occurring at stresses (τ_{SDE}) of 620 ± 30 MPa for dendritic samples and 610 ± 20 MPa for interdendritic samples. This represents a considerable change from single slip behaviour, as the sudden slip events in the interdendritic samples occur at average stresses 90 MPa earlier for a double coplanar slip arrangement. This also causes generally lower flow stresses in these samples. It is also noted that the strain increments over which the SDEs occur in the double slip experiments are one order of magnitude smaller than the single slip experiments for the dendritic samples, and two orders of magnitude smaller for the interdendritic samples. This is likely because with two slip systems activated any deformation can be spread across more potential slip bands and so the need for single slip bands to suddenly accommodate large strains is reduced.

The multiple slip MDS experiments, with eight activated slip systems, showed much higher flow stresses for both material types and considerable strain hardening post-yield. In both material types τ_{el} was 850 ± 10 MPa: this is associated with the reduced stress transfer onto the slip systems due to the reduced Schmid factor (less than half of the values from previous experiments). No sudden deformation events (or discrete shear steps) were observed in this setup, signifying that the extra slip systems share plastic deformation more evenly and avoid discrete plastic events. The average

shear stress at 1% plastic strain was found to be 950 MPa for both material types in this orientation. It is suggested that the dislocation interactions from different slip systems are having a larger effect on the deformation behaviour than the small microstructural differences in the materials [41].

The analysis of these experiments suggest that if the current single slip FDM model is extended to include further slip systems then generally higher flow stresses are to be expected when applying shear loads. The highly discrete stress-drop behaviour evidenced throughout this chapter, when particles are sheared and slip bands form (very clear in Fig. 7.2.8), would become less frequent and have smaller magnitudes. Further to the long-range dislocation stress fields, the model would require the addition of short-range dislocation interaction terms in order to capture the observed strain hardening from the multiple slip experiments. The correct material behaviour could not be expected without added dislocation generation/sink terms acting on the dislocation transport equation (eqn (5.1.1)), accounting for the multiplication and locking effects of dislocation content on these other slip systems.

Bibliography

[1] A.H. Cottrell. Commentary. a brief view of work hardening. volume 11 of *Dislocations in Solids*, pages vii – xvii. Elsevier, 2002.

[2] A. J. Kulkarni, K. Krishnamurthy, S. P. Deshmukh, and R. S. Mishra. Effect of particle size distribution on strength of precipitation-hardened alloys. *Journal of Materials Research*, 19(9):2765–2773, 2004.

[3] J. C. Stinville, N. Vanderesse, F. Bridier, P. Bocher, and T. M. Pollock. High resolution mapping of strain localization near twin boundaries in a nickel-based superalloy. *Acta Materialia*, 98:29–42, 2015.

[4] Baptiste Larrouy, Patrick Villechaise, Jonathan Cormier, and Olivier Berteaux. Grain boundary-slip bands interactions: Impact on the fatigue crack initiation in a polycrystalline forged Ni-based superalloy. *Acta Materialia*, 99:325–336, 2015.

[5] Enes Akca and Ali Gürsel. A Review on Superalloys and IN718 Nickel-Based INCONEL Superalloy. *Periodicals of Engineering and Natural Sciences (PEN)*, 3(1), 2015.

[6] Roger C. Reed. *The Superalloys fundamentals and applications*, volume 9780521859. Cambridge University Press, 2006.

[7] Tresa M Pollock, N Rene, N Rene, and N Rene. Nickel-Based Superalloys for Advanced Turbine Engines: Chemistry, Microstructure, and Properties. *Journal of Propulsion and Power*, 22(2):361–374, 2006.

[8] Atsushi Sato. *Nickel-Based Single Crystal Superalloys For Industrial Gas Turbines*. PhD thesis, University of Birmingham, UK, 2011.

[9] M. Gell, D. N. Duhl, D. K. Gupta, and K. D. Sheffler. Advanced Superalloy Airfoils. *Jom*, 39(7):11–15, 1987.

[10] P. Caron and T. Khan. Improvement of Creep strength in a nickel-base single-crystal super-alloy by heat treatment. *Materials Science and Engineering*, 61(2):173–184, 1983.

[11] R. Bowman. Superalloys: A Primer and History. `https://www.tms.org/meetings/specialty/superalloys2000/superalloyshistory.html`. Accessed: 2019-03-22.

[12] Aliou Niang, Julitte Huez, Jacques Lacaze, and Bernard Viguier. Characterizing Precipitation Defects in Nickel Based 718 Alloy. *Materials Science Forum*, 636-637:517–522, 2010.

[13] H. Y. Li, J. F. Sun, M. C. Hardy, H. E. Evans, S. J. Williams, T. J.A. Doel, and P. Bowen. Effects of microstructure on high temperature dwell fatigue crack growth in a coarse grain PM nickel based superalloy. *Acta Materialia*, 90:355–369, 2015.

[14] M. J. Anderson, A. Rowe, J. Wells, and H. C. Basoalto. Application of a multi-component mean field model to the coarsening behaviour of a nickel-based superalloy. *Acta Materialia*, 114:80–96, 2016.

[15] James Coakley, Hector Basoalto, and David Dye. Coarsening of a multimodal nickel-base superalloy. *Acta Materialia*, 58(11):4019–4028, 2010.

[16] P. W. Voorhees. The theory of Ostwald ripening. *Journal of Statistical Physics*, 38(1-2):231–252, 1985.

[17] N. Zhou, D. C. Lv, H. L. Zhang, D. McAllister, F. Zhang, M. J. Mills, and Y. Wang. Computer simulation of phase transformation and plastic deformation in IN718 superalloy: Microstructural evolution during precipitation. *Acta Materialia*, 65:270–286, 2014.

[18] I. M. Lifshitz and V. V. Slyozov. The kinetics of precipitation from supersaturated solid solutions. *Journal of Physics and Chemistry of Solids*, 19(1-2):35–50, 1961.

[19] S. K. Sondhi, B. F. Dyson, and M. McLean. Tension-compression creep asymmetry in a turbine disc superalloy: Roles of internal stress and thermal ageing. *Acta Materialia*, 52(7):1761–1772, 2004.

[20] D Locq, P Caron, S Raujol, A Coujou, and N Clément. On the Role of Tertiary Gamma Prime Precipitates in the Creep Gebahior at 700C of a PM Cisk Superalloy. *Superalloys 2004 (Tenth International Symposium)*, pages 179–187, 2004.

[21] D. Locq and P. Caron. On Some Advanced Nickel-Based Superalloys for Disk Applications. *AerospaceLab*, (3):1–9, 2011.

[22] R.J. Mitchell, Mark Hardy, Michael Preuss, and Sammy Tin. Development of γ' morphology in p/m rotor disc alloys during heat treatment. In *Superalloys 2004*, pages 361–370, 01 2004.

[23] J. Gayda. Dual microstructure heat treatment of a nickel-base disk alloy. Technical report, Glenn Research Centre, Cleveland, 2001.

[24] J. Gayda, T.P. Gabb, and P.T. Kantzos. The Effect of Dual Microstructure Heat Treatment on an Advanced Nickel-Base Disk Alloy. *Superalloys 2004 (Tenth International Symposium)*, pages 323–329, 2004.

[25] D. Hull and D.J. Bacon. Movement of Dislocations. In *Introduction to Dislocations*, pages 47–70. Pergamon Press, Oxford, third edition edition, 2011.

[26] Wael Z. Abuzaid, Michael D. Sangid, Jay D. Carroll, Huseyin Sehitoglu, and John Lambros. Slip transfer and plastic strain accumulation across grain boundaries in Hastelloy X. *Journal of the Mechanics and Physics of Solids*, 60(6):1201–1220, 2012.

[27] Bo Chen, Jun Jiang, T. Ben Britton, Yongjun Guan, Jinwen Zou, and Fionn P.E. Dunne. Crystal plasticity modelling and HR-DIC measurement of slip activation and strain localization in single and oligo-crystal Ni alloys under fatigue. *International Journal of Plasticity*, 88:70–88, 2016.

[28] R. Jiang, F. Pierron, S. Octaviani, and P. A.S. Reed. Characterisation of strain localisation processes during fatigue crack initiation and early crack propagation by SEM-DIC in an advanced disc alloy. *Materials Science and Engineering A*, 699(February):128–144, 2017.

[29] E. Nembach. *Particle strengthening of metals and alloys.* John Wiley & Sons, New York, 1997.

[30] M. Preuss, J. Quinta da Fonseca, R. Moat, E. Knoche, M. Daymond, and B. Grant. The Effect of γ' Particle Size on the Deformation Mechanism in an Advanced Polycrystalline Nickel-Base Superalloy. In *Superalloys 2008*, number 010, pages 405–414, 2012.

[31] Thomas H. Courtney. *Mechanical Behavior of Materials*. Waveland Press, Inc., Illinois, 2nd edition edition, 1990.

[32] U. F. Kocks. A statistical theory of flow stress and work-hardening. *Philosophical Magazine*, 13(123):541–566, 1966.

[33] R. B. Schwarz and R. Labusch. Dynamic simulation of solution hardening. *Journal of Applied Physics*, 49(10):5174–5187, 1978.

[34] A. W. Zhu and E. A. Starke. Strengthening effect of unshearable particles of finite size: A computer experimental study. *Acta Materialia*, 47(11):3263–3269, 1999.

[35] V Mohles, D Rönnpagel, and E Nembach. Simulation of dislocation glide in precipitation hardened materials. *Computational Materials Science*, 16(1-4):144–150, 1999.

[36] Lais Mujica Roncery, Inmaculada Lopez-Galilea, Benjamin Ruttert, David Bürger, Philip Wollgramm, Gunther Eggeler, and Werner Theisen. On the Effect of Hot Isostatic Pressing on the Creep Life of a Single Crystal Superalloys. *Advanced Engineering Materials*, 18(8):1381–1387, 2016.

[37] 'Cannon Muskegon Corporation'. ALLOY DEVELOPMENT. `https://cannonmuskegon.com/products/alloy-development/`. Accessed: 2020-02-22.

[38] 'Cannon Muskegon Corporation'. CMSX-4. `https://cannonmuskegon.com/products/alloy-development/`. Accessed: 2020-02-22.

[39] Ken Harris and Jacqueline B. Wahl. Improved single crystal superalloys, CMSX-4®(SLS)[La+Y] and CMSX-486®. *Proceedings of the International Symposium on Superalloys*, (Figure 1):45–52, 2004.

[40] Inmaculada Lopez-Galilea, Benjamin Ruttert, Junyang He, Thomas Hammerschmidt, Ralf Drautz, Baptiste Gault, and Werner Theisen. Additive manufacturing of CMSX-4 Ni-base

superalloy by selective laser melting: Influence of processing parameters and heat treatment. *Additive Manufacturing*, 30:1–12, 2019.

[41] G. Laplanche, N. Wieczorek, F. Fox, S. Berglund, J. Pfetzing-Micklich, K. Kishida, H. Inui, and G. Eggeler. On the influence of crystallography and dendritic microstructure on micro shear behavior of single crystal ni-based superalloys. *Acta Materialia*, 160:173 – 184, 2018.

[42] Alireza B. Parsa, Philip Wollgramm, Hinrich Buck, Christoph Somsen, Aleksander Kostka, Ivan Povstugar, Pyuck Pa Choi, Dierk Raabe, Antonin Dlouhy, Julian Müller, Erdmann Spiecker, Kathrin Demtroder, Jürgen Schreuer, Klaus Neuking, and Gunther Eggeler. Advanced scale bridging microstructure analysis of single crystal Ni-base superalloys. *Advanced Engineering Materials*, 17(2):216–230, 2015.

[43] D. Hull and D.J. Bacon. Chapter 1 - defects in crystals. In D. Hull and D.J. Bacon, editors, *Introduction to Dislocations (Fifth Edition)*, pages 1 – 20. Butterworth-Heinemann, Oxford, fifth edition edition, 2011.

[44] J. P Hirth and J. Lothe. *Theory of Dislocations*. Wiley, New York, 2nd editio edition, 1982.

[45] J W Morris. Chapter 4 : Defects in Crystals. *Materials Science*, pages 76–107, 2007.

[46] J. W. Christian. The stress dependence of dislocation velocity, and its relation to the strain rate sensitivity. *Acta Metallurgica*, 12(1):99–102, 1964.

[47] A N Gulluoglu and C S Hartley. Simulation of dislocation microstructures in two dimensions . I . Relaxed structures. 1(1):1–17, 1992.

[48] R. Sedláek, C. Schwarz, J. Kratochvíl, and E. Werner. Continuum theory of evolving dislocation fields. *Philosophical Magazine*, 87(8-9):1225–1260, 2007.

[49] D. Hull and D.J. Bacon. Elastic Properties of Dislocations. In *Introduction to Dislocations*, pages 63–83. Pergamon Press, Oxford, third edition edition, 2011.

[50] Doyl E Dickel, Katrin Schulz, Severin Schmitt, and Peter Gumbsch. Stress Correlations of Dislocations in a Double-Pileup Configuration : A Continuum Dislocation Density Approach - Complas XII. In *XII International Conference on Computational Plasticity. Fundamentals and Applications*, Barcelona, 2013. CIMNE.

[51] R. W. Armstrong. Dislocation pile-ups, strength properties and fracturing. *Reviews on Advanced Materials Science*, 48(1):1–12, 2017.

[52] H. Mughrabi. Dislocation wall and cell structures and long-range internal stresses in deformed metal crystals. *Acta Metallurgica*, 31(9):1367–1379, 1983.

[53] Shengxu Xia and Anter El-Azab. Computational modelling of mesoscale dislocation patterning and plastic deformation of single crystals. *Modelling and Simulation in Materials Science and Engineering*, 23(5), 2015.

[54] J. W Steeds and J. R. Willis. Dislocations in anisotropic media. volume 1 of *Dislocations in Solids*, pages 143–167. North-Holland Publishing Company, 1979.

[55] H. Föll. Defekte in Kristallen: Stress Field of an Edge Dislocation. `https://www.tf.uni-kiel.de/matwis/amat/def_ge/kap_5/illustr/i5_2_1.html`. Accessed: 2019-03-22.

[56] A. J. E. Foreman. The bowing of a dislocation segment. *The Philosophical Magazine: A Journal of Theoretical Experimental and Applied Physics*, 15(137):1011–1021, 1967.

[57] Daniel N Blaschke and Benjamin A Szajewski. Line tension of a dislocation moving through an anisotropic crystal. *Philosophical Magazine*, 98(26):2397–2424, 2018.

[58] Michael D. Sangid, Tawhid Ezaz, Huseyin Sehitoglu, and Ian M. Robertson. Energy of slip transmission and nucleation at grain boundaries. *Acta Materialia*, 59(1):283–296, 2011.

[59] Douglas E. Spearot and Michael D. Sangid. Insights on slip transmission at grain boundaries from atomistic simulations. *Current Opinion in Solid State and Materials Science*, 18(4):188–195, 2014.

[60] W. S. Blackburn. On the criterion for crack nucleation from a dislocation pile up. *Philosophical Magazine*, 17(146):431, 1968.

[61] A. G. Kunjomana and E. Mathai. Direct observation of Frank-Read sources in stoichiometric bismuth telluride crystals. *Journal of Materials Science*, 26(22):6171–6175, 1991.

[62] Hussein M. Zbib, Moono Rhee, and John P. Hirth. On plastic deformation and the dynamics of 3D dislocations. *International Journal of Mechanical Sciences*, 40(2-3):113–127, 1998.

[63] R.A. Varin, K.J. Kurzydlowski, and K. Tangri. Analytical treatment of grain boundary sources for dislocations. *Materials Science and Engineering*, 85:115 – 126, 1987.

[64] J. F. Nye. Some geometrical relations in dislocated crystals. *Acta Metallurgica*, 1(2):153–162, 1953.

[65] B. A. Bilby, R. Bullough, and E. Smith. Continuous distributions of dislocations: a new application of the methods of non-Riemannian geometry. *Proceedings of the Royal Society of London. Series A. Mathematical and Physical Sciences*, 231:263–273, 1955.

[66] E. H. Lee and D. T. Liu. Finite strain elastic—plastic theory with application to plane wave analysis. *Journal of Applied Physics*, 38:19 – 27, 02 1967.

[67] E. H. Lee. Elastic-plastic deformation at finite strains. *Journal of Applied Mechanics*, 36:27, 06 1968.

[68] T. Mura. Continuous distribution of moving dislocations. *Philosophical Magazine*, 8(89):843–857, 1963.

[69] Toshio Mura. Definition of eigenstrains. In *Micromechanics of defects in solids*, pages 1—-61. Martinus Nijhoff Publishers, The Hague, 1st editio edition, 1982.

[70] A. M. Kosevich. Dynamical theory of dislocations. *Soviet Physics Uspekhi*, 7(6):837–854, 1965.

[71] A. M. Kosevich and F. R. N. Nabarro. Crystal dislocations and theory of elasticity. In *Dislocations in Solids vol. 1*, pages 33—-142. North-Holland, Amsterdam, 1979.

[72] N. Fox. A continuum theory of dislocations for single crystals. *IMA Journal of Applied Mathematics*, 2(4):285–298, 1966.

[73] A. El-Azab. The boundary value problem of dislocation dynamics. *Modelling and Simulation in Materials Science and Engineering*, 8(1):37—-54, 2000.

[74] B. A. Bilby, R. Bullough, and Dora K. DeGrinberg. General theory of surface dislocations. *Discussions of the Faraday Society*, 38:61—-68, 1964.

[75] Amit Acharya. A model of crystal plasticity based on the theory of continuously distributed dislocations. *Journal of the Mechanics and Physics of Solids*, 49(4):761–784, 2001.

[76] Amit Acharya. Constitutive analysis of finite deformation field dislocation mechanics. *Journal of the Mechanics and Physics of Solids*, 52(2):301–316, 2004.

[77] Amit Acharya and Anish Roy. Size effects and idealized dislocation microstructure at small scales: Predictions of a Phenomenological model of Mesoscopic Field Dislocation Mechanics: Part I. *Journal of the Mechanics and Physics of Solids*, 54:1687–1710, 2006.

[78] ABAQUS UNIFIED FEA, Dassault Systèmes. `https://www.3ds.com/products-services/simulia/products/abaqus/`. Accessed: 2019-03-22.

[79] DEFORM-3D, Scientific Forming Technologies Corporation. `https://www.deform.com/products/`. Accessed: 2019-03-22.

[80] J. N. Reddy. *An Introduction to the Finite Element Method*. McGraw-Hill, Inc., New York, 3rd edition edition, 1993.

[81] J R KLEPACZKO. Physical-State Variables - the Key To Constitutive Modeling in Dynamic Plasticity. *Nuclear Engineering and Design*, 127(1):103–115, 1991.

[82] H. Mecking and U. F. Kocks. Kinetics of flow and strain-hardening. *Acta Metallurgica*, 29(11):1865–1875, 1981.

[83] H Basoalto, S K Sondhi, B F Dyson, and M Mclean. A Generic Microstructure-Explicit Model of Creep in Nickel-Base Superalloys. *Superalloys 2004*, 1:897–906, 2004.

[84] B. F. Dyson. Microstructure based creep constitutive model for precipitation strengthened alloys: theory and application. *Materials Science and Technology*, 25(2):213–220, 2009.

[85] James Coakley, David Dye, and Hector Basoalto. Creep and creep modelling of a multimodal nickel-base superalloy. *Acta Materialia*, 59:854–863, 2011.

[86] Hector Basoalto and Paul L. Blackwell. Slip Induced Strain Rate Sensitivity for Superplastic Material? *Materials Science Forum*, 735:31–36, 2013.

[87] Niels Saabye Ottosen and Matti Ristinmaa. 9 - introduction to plasticity theory. In Niels Saabye Ottosen and Matti Ristinmaa, editors, *The Mechanics of Constitutive Modeling*, pages 203 – 246. Elsevier Science Ltd, Oxford, 2005.

[88] J. E. Ion, A. Barbosa, M. F. Ashby, Dyson B.F., and M. McLean. *The Modelling of Creep for Engineering Design - I*. NPL REPORT DMA AIlS. The National Physical Laboratory, Teddington, Middesex, U.K, 1986.

[89] E B Marin and P R Dawson. On modelling the elasto-viscoplastic response of metals using polycrystal plasticity. *Computer Methods in Applied Mechanics and Engineering*, 165(1):1–21, 1998.

[90] S. Groh, E. B. Marin, M. F. Horstemeyer, and H. M. Zbib. Multiscale modeling of the plasticity in an aluminum single crystal. *International Journal of Plasticity*, 25:1456–1473, 2009.

[91] Shahriyar Keshavarz and Somnath Ghosh. Multi-scale crystal plasticity finite element model approach to modeling nickel-based superalloys. *Acta Materialia*, 61:6549–6561, 2013.

[92] Somnath Ghosh, George Weber, and Shahriyar Keshavarz. Multiscale modeling of polycrystalline nickel-based superalloys accounting for subgrain microstructures. *Mechanics Research Communications*, 78:34–46, 2016.

[93] C O Frederick and P J Armstrong. A mathematical representation of the multiaxial Bauschinger effect. *Materials at High Temperatures*, 24(1):1–26, 1966.

[94] A Van der Giessen and E Needleman. Discrete dislocation plasticity: a simple planar model. *Modelling and Simulation in Materials Science and Engineering*, 3(5):689–735, 1995.

[95] H. H.M. Cleveringa, E. Van Der Giessen, and A. Needleman. Comparison of discrete dislocation and continuum plasticity predictions for a composite material. *Acta Materialia*, 45(8):3163–3179, 1997.

[96] Hussein M. Zbib, Tomas Díaz De La Rubia, Moono Rhee, and John P. Hirth. 3D dislocation dynamics: Stress-strain behavior and hardening mechanisms in fcc and bcc metals. *Journal of Nuclear Materials*, 276(1):154–165, 2000.

[97] M Huang, L Zhao, and J Tong. Discrete dislocation dynamics modelling of mechanical deformation of nickel-based single crystal superalloys. *Int. J. Plast.*, 28:141–158, 2012.

[98] Haël Mughrabi. The effect of geometrically necessary dislocations on the flow stress of deformed crystals containing a heterogeneous dislocation distribution. *Materials Science and Engineering A*, 319-321:139–143, 2001.

[99] A ROY and A ACHARYA. Size effects and idealized dislocation microstructure at small scales: Predictions of a Phenomenological model of Mesoscopic Field Dislocation Mechanics: Part II. *Journal of the Mechanics and Physics of Solids*, 54:1711–1743, 2006.

[100] T. Hochrainer, M. Zaiser, and P. Gumbsch. A three-dimensional continuum theory of dislocation systems: Kinematics and mean-field formulation. *Philosophical Magazine*, 87(8-9):1261–1282, 2007.

[101] Stefan Sandfeld, Thomas Hochrainer, Michael Zaiser, and Peter Gumbsch. Continuum modeling of dislocation plasticity: Theory, numerical implementation, and validation by discrete dislocation simulations. *Journal of Materials Research*, 26(5):623–632, 2011.

[102] Thomas Hochrainer, Stefan Sandfeld, Michael Zaiser, and Peter Gumbsch. Continuum dislocation dynamics: Towards a physical theory of crystal plasticity. *Journal of the Mechanics and Physics of Solids*, 63(1):167–178, 2014.

[103] Stefan Sandfeld and Michael Zaiser. Pattern formation in a minimal model of continuum dislocation plasticity. *Modelling and Simulation in Materials Science and Engineering*, 23(6), 2015.

[104] Mehran Monavari, Stefan Sandfeld, and Michael Zaiser. Continuum representation of systems of dislocation lines: A general method for deriving closed-form evolution equations. *Journal of the Mechanics and Physics of Solids*, 95:575–601, 2016.

[105] Mehdi Hamid, Hao Lyu, Ben Jared Schuessler, Pui Ching Wo, and Hussein M Zbib. Modeling and Characterization of Grain Boundaries and Slip Transmission in Dislocation Density-Based Crystal Plasticity. *Crystals*, 7(6):152, 2017.

[106] Stefan Sandfeld and Giacomo Po. Microstructural comparison of the kinematics of discrete and continuum dislocations models. *Modelling and Simulation in Materials Science and Engineering*, 23(8), 2015.

[107] Ronghai Wu, Michael Zaiser, and Stefan Sandfeld. A continuum approach to combined γ/γ' evolution and dislocation plasticity in Nickel-based superalloys. *International Journal of Plasticity*, 95:142–162, 2017.

[108] Ronghai Wu and Stefan Sandfeld. A dislocation dynamics-assisted phase field model for Nickel-based superalloys: The role of initial dislocation density and external stress during creep. *Journal of Alloys and Compounds*, 703:389–395, 2017.

[109] I J Beyerlein and A Hunter. Understanding nanoscale dislocation mechanics using phase field dislocation dynamics. *Philos. Trans. R. Soc. A*, 374(2066):20150166, 2016.

[110] Y. Zeng, A. Hunter, I. J. Beyerlein, and M. Koslowski. A phase field dislocation dynamics model for a bicrystal interface system: An investigation into dislocation slip transmission across cube-on-cube interfaces. *International Journal of Plasticity*, 79:293–313, 2016.

[111] Stefan Sandfeld, Zoe Budrikis, Stefano Zapperi, and David Fernandez Castellanos. Avalanches, loading and finite size effects in 2D amorphous plasticity: Results from a finite element model. *Journal of Statistical Mechanics*, (P02011):1–17, 2015.

[112] Hector Basoalto. On a heterogeneous theory of crystal plasticity. Report P-41, PRISMM, Univeristy of Birmingham, 2016. PRISMM report.

[113] H. C. Basoalto and J. J. Little. A feld dislocation mechanics approach to slip band evolution in two-phase alloys. *pre-submission*, 2020.

[114] E. A. de Souza Neto, D. Perić, and D. R. J. Owen. Elements of Continuum Mechanics and Thermodynamics. In *Computational Methods for Plasticity: Theory and Applications*, chapter 3, pages 41–81. John Wiley & Sons, New York, 2008.

[115] Dongsheng Li, Hussein Zbib, Xin Sun, and Mohammad Khaleel. Predicting plastic flow and irradiation hardening of iron single crystal with mechanism-based continuum dislocation dynamics. *International Journal of Plasticity*, 52:3–17, 2014.

[116] N Urabe and J Weertman. Dislocation mobility in potassium and iron single crystals. *Materials Science and Engineering*, 18(1):41 – 49, 1975.

[117] Chansun Shin. *3D Discrete Dislocation Dynamics Applied To Dislocation-Precipitate Interactions*. PhD thesis, INSTITUT NATIONAL POLYTECHNIQUE DE GRENOBLE, 2004.

[118] Terrell L. Hill. *An Introduction to Statistical Thermodynamics*. Dover Publications, Inc., New York, 1st editio edition, 1986.

[119] U. F. Kocks, A. A. Argon, and M. F. Ashby. *Thermodynamics and kinetics of slip*. Pergamon Press, Oxford, 1st editio edition, 1975.

[120] Thomas Hochrainer. Thermodynamically consistent continuum dislocation dynamics. *Journal of the Mechanics and Physics of Solids*, 88:12–22, 2016.

[121] J. Friedel. *Dislocations*. Pergamon Press, New York, 1964.

[122] Beñat Gurrutxaga-Lerma, Daniel S. Balint, Daniele Dini, Daniel E. Eakins, and Adrian P. Sutton. Mobility Laws. In *Dynamic Discrete Dislocation Plasticity*, volume 47, pages 93–224. Elsevier Inc., 2014.

[123] A. A. Benzerga, Y. Bréchet, A. Needleman, and E. Van der Giessen. Incorporating three-dimensional mechanisms into two-dimensional dislocation dynamics. *Modelling and Simulation in Materials Science and Engineering*, 12(1):159–196, 2004.

[124] S. Yefimov, I. Groma, and E. Van der Giessen. A comparison of a statistical-mechanics based plasticity model with discrete dislocation plasticity calculations. *Journal of the Mechanics and Physics of Solids*, 52(2):279–300, 2004.

[125] K. Schulz, D. Dickel, S. Schmitt, S. Sandfeld, D. Weygand, and P. Gumbsch. Analysis of dislocation pile-ups using a dislocation-based continuum theory. *Modelling and Simulation in Materials Science and Engineering*, 22(2), 2014.

[126] A. M. Kosevich. Crystal dislocations and the theory of elasticity. volume 1 of *Dislocations in Solids*, pages 62–86. North-Holland Publishing Company, 1979.

[127] E. NEMBACH. *Particle strengthening of metals and alloys*. Wiley, New York, 1997.

[128] D. Hull and D.J. Bacon. Origin and Multiplication of Dislocations. In *Introduction to Dislocations*, pages 63–83. Elsevier, 2011.

[129] Louis Thébaud, Patrick Villechaise, Coraline Crozet, Alexandre Devaux, Denis Béchet, Jean Michel Franchet, Anne Laure Rouffié, Michael Mills, and Jonathan Cormier. Is there an optimal grain size for creep resistance in Ni-based disk superalloys? *Materials Science and Engineering A*, 716:274–283, 2018.

[130] L. Zhang, L. G. Zhao, A. Roy, V. V. Silberschmidt, and G. McColvin. In-situ SEM study of slip-controlled short-crack growth in single-crystal nickel superalloy. *Materials Science and Engineering A*, 742:564–572, 2019.

[131] Yumeng Luo, Jinxu Liu, Wenqi Guo, Qianran Yu, and Shukui Li. Dislocation Slip Behavior of Ni Single Crystal Under Dynamic Compression. *Journal of Dynamic Behavior of Materials*, 2:223–233, 2016.

[132] Stefan Sandfeld, Ekkachai Thawinan, and Christian Wieners. A link between microstructure evolution and macroscopic response in elasto-plasticity: Formulation and numerical approximation of the higher-dimensional continuum dislocation dynamics theory. *International Journal of Plasticity*, 72:1–20, 2015.

[133] D M Causon and C G Mingham. *Introductory Finite Difference Methods for PDEs Download free books at Introductory Finite Difference.*

[134] P. Nörtershäuser, J. Frenzel, A. Ludwig, K. Neuking, and G. Eggeler. The effect of cast microstructure and crystallography on rafting, dislocation plasticity and creep anisotropy of single crystal Ni-base superalloys. *Materials Science and Engineering A*, 626:305–312, 2015.

[135] L. Agudo Jácome, P. Nörtershäuser, J. K. Heyer, A. Lahni, J. Frenzel, A. Dlouhy, C. Somsen, and G. Eggeler. High-temperature and low-stress creep anisotropy of single-crystal superalloys. *Acta Materialia*, 61(8):2926–2943, 2013.

[136] N. Miura, Y. Kondo, and N. Ohi. The Influence of Dislocation Substructure on Creep Rate during Accelerating Creep Stage of Single Crystal Nickel-based Superalloy CMSX-4. In *Superalloys 2000*, pages 377–385, 2012.

[137] Stefan Sandfeld and Thomas Hochrainer. Towards Frank-Read sources in the continuum dislocation dynamics theory. *AIP Conference Proceedings*, 1389(2011):1531–1534, 2011.

[138] L. di Masso, B. Coluzzi, and F. M. Mazzolai. Ultrasonic Investigation of CMSX-6 Superalloy at Low and High Temperatures. *Le Journal de Physique IV*, 06(C8):C8–247–C8–250, 1996.

[139] W. Hermann, H.G. Sockel, J. Han, and A. Bertram. Elastic Properties and Determination of Elastic Constants of Nickel-Base Superalloys by a Free-Free Beam Technique. *Superalloys 1996*, pages 229–238, 1996.

[140] D. Dye, J. Coakley, V. A. Vorontsov, H. J. Stone, and R. B. Rogge. Elastic moduli and load partitioning in a single-crystal nickel superalloy. *Scripta Materialia*, 61(2):109–112, 2009.

[141] X. Luan, H. Qin, F. Liu, Z. Dai, Y. Yi, and Q. Li. The mechanical properties and elastic anisotropies of cubic ni3al from first principles calculations. *Crystals*, 8:115 – 126, 2018.

[142] J. Sieniawski A. Onyszko, K. Kubiak. Turbine blades of the single crystal nickel based cmsx-6 superalloy. *Journal of Achievements in Materials and Manufacturing Engineering*, 32, 01 2009.

[143] K. Harris, G.L. Erickson, J. Wortmann, and D. Froschhammer. Development of low density single crystal superalloy CMSX-6. In *7th World Conference on Investment Casting*, Munich, 1988.

[144] S.V. Prikhodko, J. D. Carnes, D. G. Isaak, H. Yang, and A. J. Ardell. Temperature and composition dependence of the elastic constants of Ni3Al. *Metallurgical and Materials Transactions A*, 30A:2403–2408, 1999.

[145] Mahendra Malu and John K. Tien. A theory for steady state creep based on the motion of interstitial type jogs. *Acta Metallurgica*, 22(2):145–151, 1974.

[146] Ning Tian, Sugui Tian, Huichen Yu, Ying Li, and Xianlin Meng. Microstructure and Creep Behavior of a Directional Solidification Nickel-based Superalloy. *High Temperature Materials and Processes*, 34(4):299–309, 2015.

[147] P. E. Aba-Perea, T. Pirling, P. J. Withers, J. Kelleher, S. Kabra, and M. Preuss. Determination of the high temperature elastic properties and diffraction elastic constants of Ni-base superalloys. *Materials and Design*, 89:856–863, 2016.

[148] C.L. Fu, R. Reed, A. Janotti, and M. Kremar. On the Diffusion of Alloying Elements in the Nickel-Base Superalloys. *Superalloys 2004*, pages 867–876, 2004.

[149] Bing Lin, Minsheng Huang, Liguo Zhao, Anish Roy, Vadim Silberschmidt, Gordon McColvin, Mark Whittaker, and Nick Barnard. 3D DDD modelling of dislocation–precipitate interaction in a nickel-based single crystal superalloy under cyclic deformation. *Philosophical Magazine*, 98(17):1550–1575, 2018.

[150] Lei Wang, Yang Liu, Xiu Song, Junchao Jin, and Beijiang Zhang. Tensile Deformation Behavior of a Nickel-base Superalloy under Dynamic Loads. In *13th International Conference on Fracture*, 2013.

[151] W.F. Smith and J. Hashemi. *Foundations of Materials Science and Engineering*. McGraw-Hill series in materials science and engineering. McGraw-Hill, 2003.

[152] G. Eggeler, N. Wieczorek, F. Fox, S. Berglund, D. Bürger, A. Dlouhy, P. Wollgramm, K. Neuking, J. Schreuer, L. Agudo Jácome, S. Gao, A. Hartmaier, and G. Laplanche. On Shear Testing of Single Crystal Ni-Base Superalloys. *Metallurgical and Materials Transactions A: Physical Metallurgy and Materials Science*, 49(9):3951–3962, 2018.

[153] J. K. Heyer, S. Brinckmann, J. Pfetzing-Micklich, and G. Eggeler. Microshear deformation of gold single crystals. *Acta Materialia*, 62(1):225–238, 2014.

[154] C. Mayr, G. Eggeler, G. A. Webster, and G. Peter. Double shear creep testing of superalloy single crystals at temperatures above 1000 °C. *Materials Science and Engineering A*, 199(2):121–130, 1995.

[155] Ramkumar Oruganti, Mallikarjun Karadge, Sachin Nalawade, Sivakumar Kelekanjeri, and Francesco Mastromatteo. *A New Approach to Modeling of Creep in Superalloys*, pages 473–479. John Wiley & Sons, Ltd, 2012.

[156] N. J. Petch. The cleavage strength of polycrystals. *The Journal of the Iron and Steel Institute*, 173(5):25–28, 1953.

[157] D. Hull and D.J. Bacon. Jogs and the Intersection of Dislocations. In *Introduction to Dislocations*, pages 141–160. Pergamon Press, Oxford, third edition edition, 2011.

[158] Y. M. Wang-Koh. Understanding the yield behaviour of L12-ordered alloys. *Materials Science and Technology (United Kingdom)*, 33(8):934–943, 2017.

[159] B.C. Wilson and G.E. Fuchs. The Effect of Composition, Misfit, and Heat Treatment on the Primary Creep Behavior of Single Crystal Nickel Base Superalloys PWA 1480 and PWA 1484. *Superalloys 2008*, pages 149–158, 2008.